University of Tehran

Print ISSN: 2322-2093

Online ISSN: 2423-6691

Volume 54, Number 2, December 2021

Civil Engineering Infrastructures Journal

CEIJ

Available online at
http://www.ceij.ir/

Civil Engineering Infrastructures Journal (CEIJ)

Volume 54, Number 2, December 2021

Civil Engineering Infrastructures Journal (CEIJ)
Semiannual Publication

Published by:

University of Tehran
College of Engineering

Indexed by:

Web of Science (ESCI)

Scopus

Civil Engineering Infrastructures Journal (CEIJ)
College of Engineering
University of Tehran
P.O. Box: 11155-4563
Tehran, Iran.
Tel/ Fax: +98-21-88956097
Email: ceij@ut.ac.ir
Web Site: www.ceij.ir

Editorial Board

Advisory Board

CONTENTS
Volume 54, Number 2, December 2021

Civil Engineering Infrastructures Journal 2021, 54(2): 205-223
DOI: 10.22059/CEIJ.2020.293429.1634

RESEARCH PAPER

Seepage and Stability Analysis of the Eyvashan Earth Dam under Drawdown Conditions

Komasi, M.[1]* and Beiranvand, B.[2]

[1] Assistant Professor, Department of Civil Engineering, University of Ayatollah Ozma Borujerdi, Borujerd, Iran.
[2] Ph.D. Candidate in Civil Engineering, Water and Hydraulic Structures, University of Qom, Qom, Iran.

Received: 03 Dec. 2019; Revised: 02 Apr. 2020; Accepted: 17 Apr. 2020

ABSTRACT: The rapid drawdown condition to control floods and irrigation is one of the things that may occur over the lifetime of the dam. Also, the stability of the dam at the rapid drawdown will be more important due to the faster reduction of the water level of the dam reservoir than the pore water pressure. In this study, the finite element method and GeoStudio software used to study the seepage from the body earth dam. Also, the complete elastic-plastic model of Mohr-Coulomb is considered in the analysis. In this study, the stability analysis of the Eyvshvan earth dam after rapid drawdown due water to release of the dam reservoir to downstream agricultural lands during drought crisis, is investigated. For the validation, first, the results of the pore water pressure instrument were compared with the results of numerical analysis. The results of multivariate regression analysis (coefficient of determination) showed very good agreement (R^2=0.98). The results showed that the phreatic line remains after 29 days from the start of the rapid drawdown of the reservoir, while half of the volume of the drained reservoir remains at 1842 masl (1/3 of the crest). The analysis of dam stability during rapid drawdown using both Morgenstern-Price and Bishop Methods showed that the most critical situation would occur after 42 days of discharge with a factor of safety (FoS) of 1.71, with no stability hazard and the upstream slope would be safe.

Keywords: Eyvashan Earth Dam, Factor of Safety, Geostudio, Pore Water Pressure, Rapid Drawdown.

1. Introduction

After the dam reservoir is filled (impounding) and the water penetrates the body of the dam, any rapid and slow drawdown in the reservoir may cause damage and cracks in the upstream slope of the dam. In this case, the drop in reservoir water's height is faster than the depletion of the pore water pressure body or foundation of the dam. The rapid drawdown of the reservoir water reduces the resistive force against the propulsion force. Because, firstly, the pressure on the upstream as a superconductor; secondly, the saturation line in the dam body is placed above the reservoir's surface, and the drainage cannot decompress the pore water pressure with the speed at which the reservoir water level decreases. Zedan et al. (2018) studied the

* Corresponding author E-mail: komasi@abru.ac.ir

behavior of the Khasa-Chai Dam using Geo-Slope software to find the factor of safety of the upstream slip surface during the drawdown conditions. The results of their studies showed that the water flux decreases fast relating to reservoir slow drawdown as the water in the rapid drawdown.

Sica et al. (2019) studied the rapid drawdown of Campolattaro Dam placed in a highly seismic area of Southern Italy, using FLAC2D software. Their studies showed that a seismic previously experienced by the dam further contribute to decreasing dam stability during the rapid drawdown especially during the first stages of reservoir reduction. Also, the faster the drawdown, the smaller the dam safety factor against stability (FOS) with more prominent effects of the initial (pre-drawdown) soil conditions. When the phreatic line (free surface) falls slowly or remains almost at the same position, it is considered as ”rapid” drawdown. The lag of the phreatic line or the rate of drawdown depends on four factors: permeability coefficient of the dam, rapid drawdown rate, pore active volume, and upstream slope. The exit gradient and the rate of flow at the downstream face decrease with time as the water in the reservoir drawdown which means the factor of safety against boiling increases with time (Abadjiev, 1994).

Nian et al. (2011) investigated the slope stability of homogeneous dams under rapid drawdown. In addition to the saturated and unsaturated analyzes, they also examined the stability of the upstream slope of the dam during the rapid drawdown. Lane and Griffiths (2000) produced operating charts for structure safety using FEM to provide a direct method to assess slope stability of the partial and complete submerged soil under the different rates of reservoir drawdown.

Numerous studies have reported the effects drawdown of dam slope stability using limit analyses, numerical analyses, and laboratory tests (Yan et al., 2010; Wang et al., 2012; Viratjandr and Michalowski, 2006; Gao et al., 2014; Alonso et al., 2016). All embankment dams are subject to some seepage passing through, under, and around them. If uncontrolled, seepage may be detrimental to the stability of the structure as a result of excess pore water pressures, or by internal erosion (Fattah et al., 2017).

López-Acosta et al. (2014) utilized the SEEP/W program, based on FEM, to study the influence of filter in the reduction of the soil erosion problems under drawdown conditions. Three filter types were analyzed at a drawdown rate of 1 m/day. The results showed better efficiency in reducing the pore water pressure when using two horizontal filters at the toes of the upstream and downstream slope. Zomorodian and Abodollahzadeh (2010) investigated the influence of horizontal drains on the upstream slope of rockfill dams in the condition of rapid drawdown using limit equilibrium and finite element methods. The development of pore water pressure, outpouring rate of flow, and factor of safety was inspected. The amount of water leakage and seepage in the dam was investigated by using the SEEP/W software and the static slope stability analysis by using the SLOPE/W software.

Zhang and Luo (2017) developed a simplified method to analyze the stability of a strain-softening slope for determining the subsidiary shear deformation under rapid drawdown. This method was based on a new algorithm and was verified to be effective in the stability evolutionary analysis of the strain-softening slopes caused by the dropping of the water level. The results showed that the behavior of the strain-softening and the initial level of water have a significant effect on the critical slip surface and the slope stability under the drawdown event.

The behavior of progressive failure is important to prevent the overestimation of the slope factor of safety. Stark and Jafari (2018) recently utilized the finite element method to investigate the reasons that caused the upstream slope failure of the San Luis Dam under a drawdown event. Alonso

and Pinyol (2016) calculated the distributions of the pore water pressure under rapid drawdown conditions using different approaches. They analyzed two real cases to study the effect of rapid drawdown. The first case study involved the Glen Shira Dam in Scotland. A similar analysis was performed for the upstream slope of the Glen Shira Dam, Scotland, and numerical results were compared with field measurements during a controlled drawdown. A key aspect of the case was the correct characterization of permeability of a representative soil profile. This case allows the validation of the computational results through comparison with field measurements. The upstream slope was covered by a rockfill filter for increasing the stability of the slope. A thin wall of reinforced concrete also used in the dam center. Another modeled case was the slope failure of the Canelles Reservoir in Spain after a reservoir drawdown event. The rainfall effect was also simulated in the model. The results showed that coupled flow deformation analysis is necessary for saturated and unsaturated soils to measure the distribution of the pore water pressure within the slope. Salmasi et al. (2015) used numerical simulation and GeoStudio software to measure the effect of relief wells on reducing the load on a homogeneous dam.

Bahrami et al. (2018) analyzed the static and quasi-static stability of the Narmab Dam and sensitivity analysis with GeoStudio Slope/w software. They found that according to static and quasi-static conditions, Narmab Dam is stable in all loading stages (end of construction, first impounding, and steady-state seepage). For static conditions of the end of construction, the sensitivity of adhesion is greater than the angle of the internal friction, but in other conditions, the sensitivity of the friction angle has more effects.

Boroomand and Mohammadi (2019) investigated the Alborz Dam seepage considering the uncertainty in soil hydraulic parameters. Their results showed that uncertainty in the hydraulic parameters of the Alborz Dam is notable, and the risk is important in this dam. It was also found that the quantity of seepage increases considerably when the dam is without clay core, therefore, the core is necessary to decrease the amount of seepage through the earth dam. Siacara et al. (2020) studied the reliability analysis of the rapid drawdown of an earth dam using a direct coupling.

In this paper, the rapid drawdown condition is investigated by instrument results and the finite element method for the Eyvashan earth dam. Changes in pore water pressure and stability during the rapid drawdown of the reservoir will be also studied.

2. Methodology

2.1. Eyvashan Earth Dam- Case Study

Eyvashan earth dam has 1.5 km distance from the upstream of the village of Eyvashan and about 57 km from Khorramabad in the coordinates of 48°49'2" and 33°28'31" degrees north, located on the Horod River. The area of the Horod river drainage basin up to the dam axis is 120 km^2. The dam is a rockfill earth dam type. The dam was designed with a maximum height of 68 m and a crest length of 650 m and a normal water level of 1864 masl (meters above sea level). It has a storage capacity of 52 million m^3. The upstream slope is 1 v: 2.5 h and the downstream local slopes are 1 v: 1.85 h and 1 v: 2.0 h. The area of the lake at a normal level is 2.3 km^2. Figure 1, presents the Eyvashan earth dam.

The construction site of the Eyvashan earth dam from the geological viewpoint of the rock bed includes conglomerate rocks that have outcrops in the boundaries of these rocks but deposited on the conglomerate rock in the bottom of the valley of alluvial sedimentary deposits. In terms of lithology, the conglomerate of the dam axis and the lake is composed of limestone, sandstone, slate, metamorphic rocks and igneous rocky parts with a silty-sandy and sometimes silt-clay matrix.

2.2. Instrumentation Sections of Eyvashan Earth Dam

The instrumentation of the Eyvashan earth dam in 4 sections with numbers 228-228, 229-229, 230-230 and 231-231 is considered in 0 + 249, 0 + 356, 0 + 477 and 0 + 546, respectively. In the present study, the characterization of the instrument installed in the section 229 of Eyvashan earth dam is investigated. In Figure 2, the position of the cross-sections and the section of the instrumentation 229 of the dam are shown. The highest level of instrumentation is related to the 229-229 cross-section with 7 levels and the least number of instrumentation levels related to the 231-231 section with 5 levels. The electrical piezometer embankment (EPE) on the maximum cross-section of the Eyvashan earth dam is shown in Figure 2.

2.3. Governing Equation for Seepage Analysis

The long-time steady-state and the transient analysis of the seepage are conducted by using numerical models. The numerical model of Seep/W is applied in which an instrument is using the finite element method to simulate the water flowing through porous media (Seep/W). Seep/W is used to simulate the groundwater movement in both the steady or transient states. The software is based on the flow of water in saturated and unsaturated soils and is based on Darcy's law, which may be expressed as a Eq. (1):

$$q=k.i \tag{1}$$

in which q: is the specific discharge, k: is the hydraulic conductivity, and i: is the gradient of the total hydraulic head.

The hydraulic conductivity in Eq. (1) is maintained at a constant value in the fully saturated soil, while it is modeled as various values for the unsaturated soil changing with the water content of the soil. The basis of the seepage equations is that the difference between the inflow and outflow values is equal to the water volume changes over time. Thus, the main equation governing seepage problems is expressed as follows:

$$\frac{\partial}{\partial x}(k_x\frac{\partial H}{\partial x})+\frac{\partial}{\partial y}(k_y\frac{\partial H}{\partial y})+Q=\frac{\partial \theta}{\partial t} \tag{2}$$

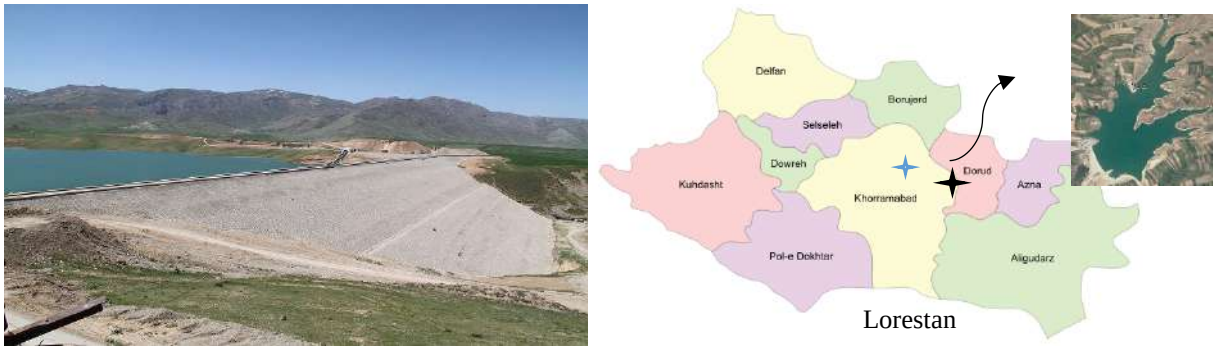

Fig. 1. Eyvashan earth dam

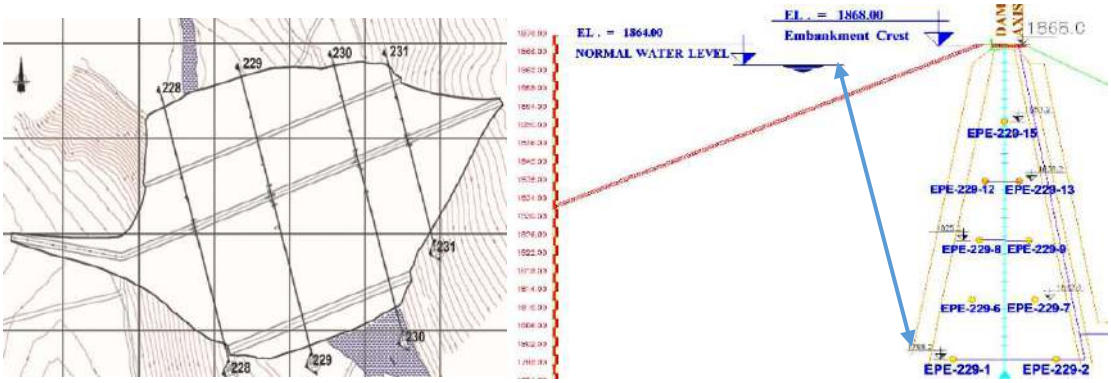

Fig. 2. Position of the instrument on the plan and maximum cross-section of the Eyvashan earth dam

in which ∂H: is the total head, $\underline{k_x}$: is the permeability coefficient in x-direction, k_y: is the permeability coefficient in y-direction, Q: is the leakage from boundary, $\partial\theta$: is the water content, and t: is the time.

If the steady-state of the outflow and inlet is constant at the equilibrium state, the main equation will be transformed into Eq. (3):

$$\frac{\partial}{\partial x}(k_x\frac{\partial H}{\partial x})+\frac{\partial}{\partial y}(k_y\frac{\partial H}{\partial y})+Q=0 \quad (3)$$

Mainly, this equation equates the water flux flowing through a two-dimensional elemental volume in x and y-directions plus the applied boundary flux to the volumetric water content with consideration to the time. The change in the volumetric water content is related to the changes in the stress state variables: $(\sigma - ua)$ and $(ua - uw)$, which σ: is the total stress, ua: is the pore air pressure, and uw: is the pore water pressure. It is assumed in Seep/W that the total stress in the soil is constant, which means there is no change in the variable of $(\sigma - ua)$. Also, the program assumes no change in the pore air pressure (ua). Therefore, the change in the volumetric water content of soil depends only on the change in the pore water pressure (uw). Changes in the volume of water by Eq. (4) are related to changes in the pore water pressure.

$$\partial\theta = mw.\gamma w.\partial(H-y) \quad (4)$$

in which mw: is the storage curve slope, γw: is the unite weight of water, H: is the total hydraulic head, and y: is the elevation.

By substituting Eq. (4) into Eq. (2), the general governing differential equation may be stated as (Seep/W):

$$\frac{\partial}{\partial x}(k_x\frac{\partial H}{\partial x})+\frac{\partial}{\partial y}(k_y\frac{\partial H}{\partial y})+Q = mw.\gamma w.\partial(H-y) \quad (5)$$

2.4. Governing Equation for Slope Stability Analysis

This section discusses the underlying theory used in the analysis of the stability of slopes in this research. The critical surface of failure may lie between the topsoil and a cylindrical surface in a finite slope. The shear strength on the critical surface consists of two components, soil cohesion, and frictional resistance. Slope/W uses the theory of finite equilibrium forces and torques to calculate the fracture stability coefficient. For the analysis based on effective stress, the shear strength is determined by Eq. (6):

$$\tau = c` + (\sigma_n - u).tan\varphi` \quad (6)$$

in which τ: is the shear strength, $c`$: is the effective cohesion, $\sigma_n$: is the total normal stress, $u$: is the pore water pressure and $\varphi`$: is the effective internal friction angle. Stability analysis includes landslide crossing the soil mass and segmentation with slices vertical. The slip surface may be circular, composite, or a straight line.

2.5. Monitoring of Electrical Piezometer Embankment (EPE)

In summer 2017, to prevent drying up of the river and occurrence of the environmental disasters, the provision of the environmental rights of the river, as well as to compensate for the shortage of water from Beiranshahr to the Pol-e Dokhtar city about 9.2 liters per second of water were released from the Eyvashan earth dam in 58 days. The Kashkan River forms an important part of the riverside stream of Karkheh River and includes about one-third of Lorestan province. The unprecedented drop in the Kashkan River discharge in this season is due to the absolute performance of the climatic factors, as well as the unprecedented planting of hydrophilic species, especially rice, which plumbs the water of the Kashkan River. Eyvashan earth dam has target lands with a network area of 2500 ha, and because its network has not been completed, there is the possibility of releasing water downstream and compensating for a shortage of 46 million m^3. Therefore, the results of the piezometers installed in the core of the Eyvashan earth dam in the conditions of rapid drawdown reservoirs were investigated within 58 days. The illustrated results in Figure 3 shows that volume of the reservoir at the level of 1864

masl is equivalent to 52 million m^3 and will decrease to 6 million m^3 after the rapid drawdown of the reservoir at the level of 1814 masl (dead volume). On the 1806 masl, two piezometers are located on the up and down core axis. At the beginning of the rapid drawdown in the reservoir, and the level of 1864 masl, the highest pore water pressure in the piezometer 229-1 (reservoir side) was 505 kPa and in the last reading after 58 days at the level of 1814 masl, it was reduced to 214 kPa. In the 229-2 piezometer, a uniform process and very small changes in pore water pressure are observed (127 to 70 kPa).

At the level of 1812 masl, two piezometers are located on the up and down Ax-core. Figure 4 shows that at the ow sbeginning of the rapid drawdown in the reservoir and at the level of 1864 masl, the maximum pore water pressure in the piezometers 229-6 (side of the reservoir) was 360 kPa, and at the last reading at the level of 1814 masl, it was reduced to 106 kPa. In piezometers 229-7, the results are mild and the pore water pressure has dropped from 79 to14 kPa.

At the level of 1825 masl, two piezometers are located on the up and down Ax-core. According to Figure 5 at the beginning of the rapid drawdown in the reservoir and at the level of 1864 masl, the maximum pore water pressure in the piezometers 229-8 (side of the reservoir) was 270 kPa, and at the last reading at the level of 1814 masl, it was reduced to 14 kPa. In piezometers 229-9, the results are mild and the pore water pressure has dropped from 43 to 3 kPa.

At the level of 1838 masl, two piezometers are located on the up and down Ax-core. IT can be seen if Figure 6 that at the beginning of the rapid drawdown in the reservoir and at the level of 1864 masl, the maximum pore water pressure in the piezometers 229-12 (side of the reservoir) was 149 kPa, and at the last reading at the level of 1814 masl, it was reduced to -242 kPa. The pore water pressure was read at the 229-13 piezometer and before the rapid drawdown of the reservoir -118, which decreased to -291 after 58 days.

At the level of 1851 masl, one piezometer was installed on the clay core ax. Figure 7 shows that the pore water pressure dropped to 59 kPa before the rapid drawdown in the reservoir and at the end of the 58 days, the drainage of the reservoir decreased to -375 kPa.

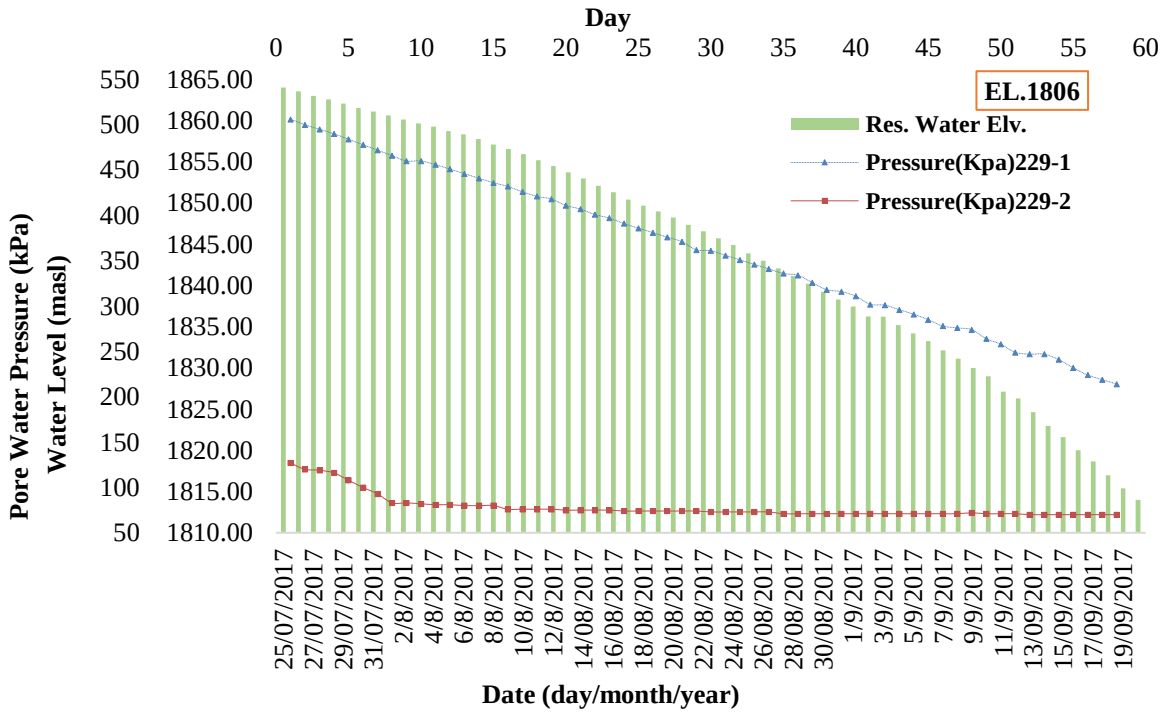

Fig. 3. Pore water pressure in the core of Eyvashan earth dam during rapid drawdown (EL.1806 masl)

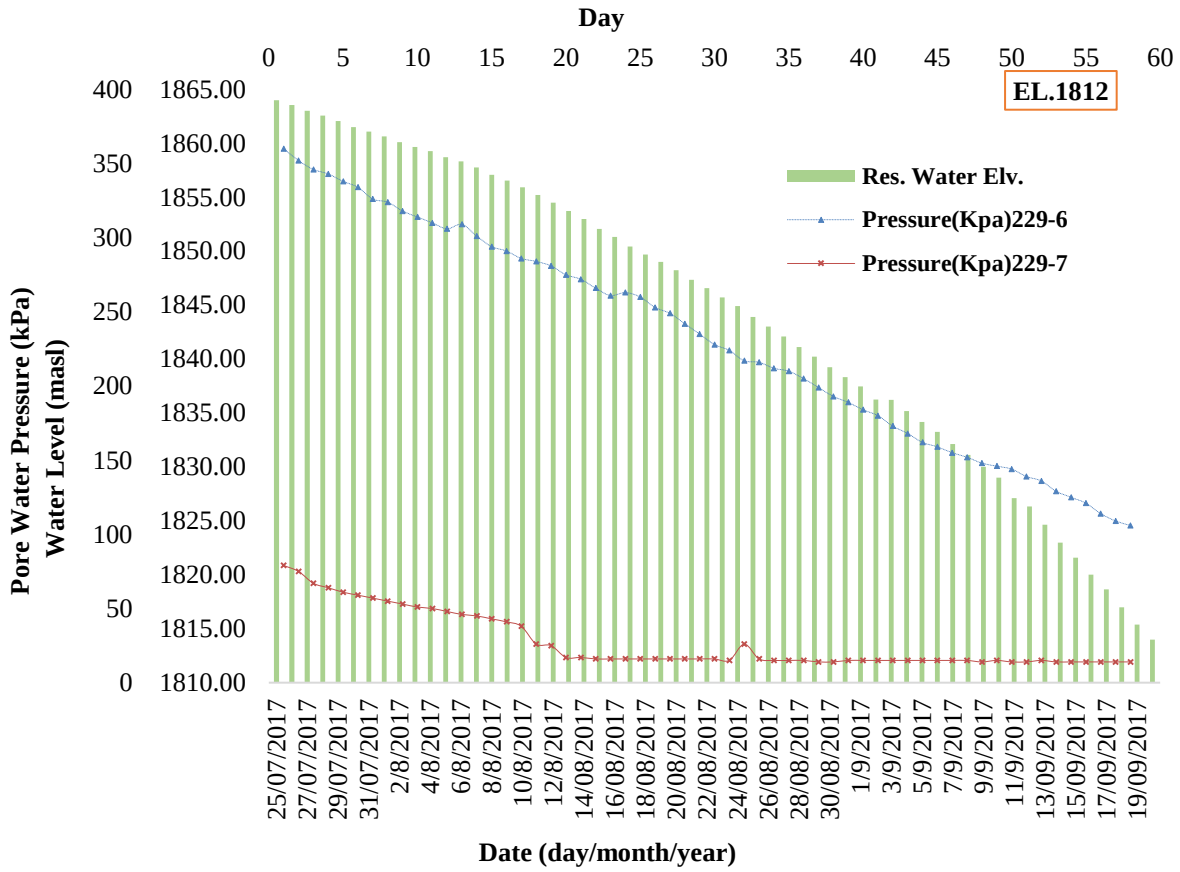

Fig. 4. Pore water pressure in the core of Eyvashan earth dam during rapid drawdown (EL.1812 masl)

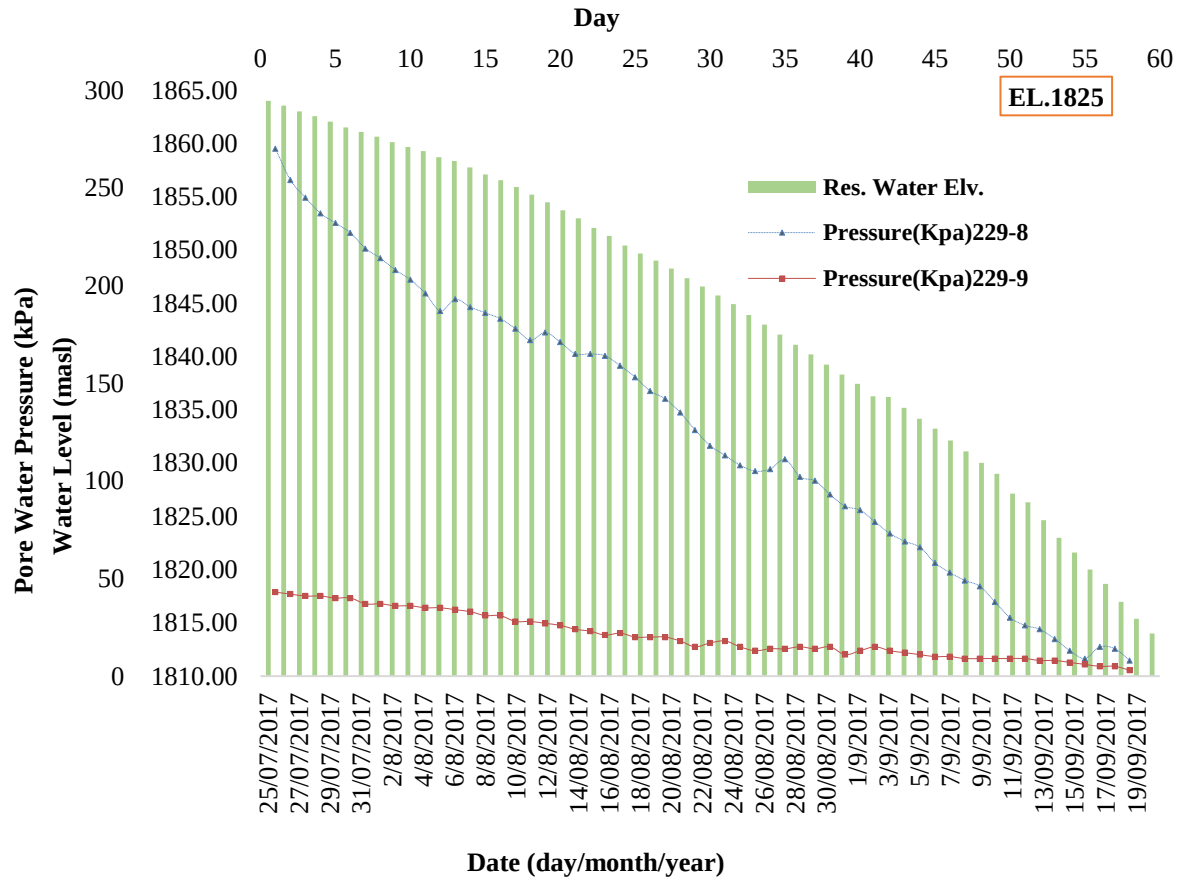

Fig. 5. Pore water pressure in the core of Eyvashan earth dam during rapid drawdown (EL.1825 masl)

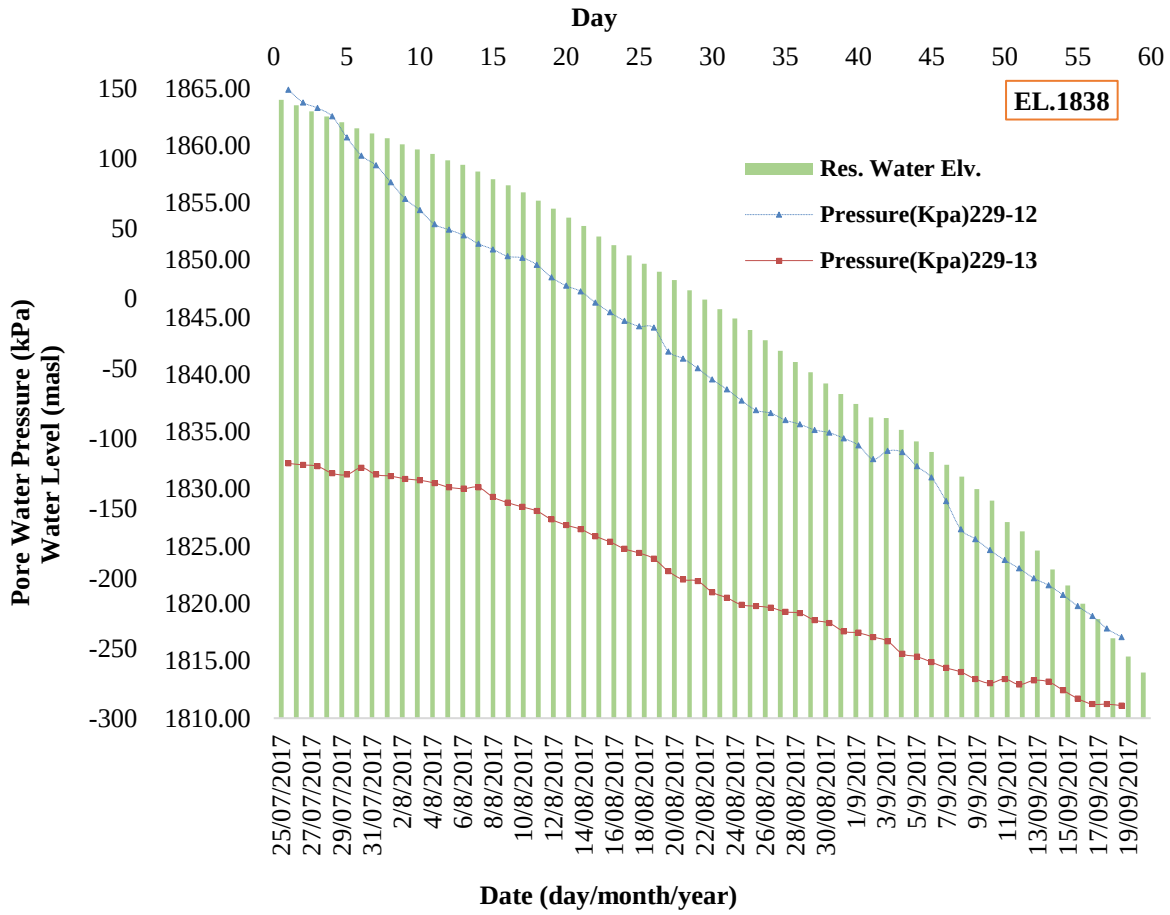

Fig. 6. Pore water pressure in the core of Eyvashan earth dam during rapid drawdown (EL.1838 masl)

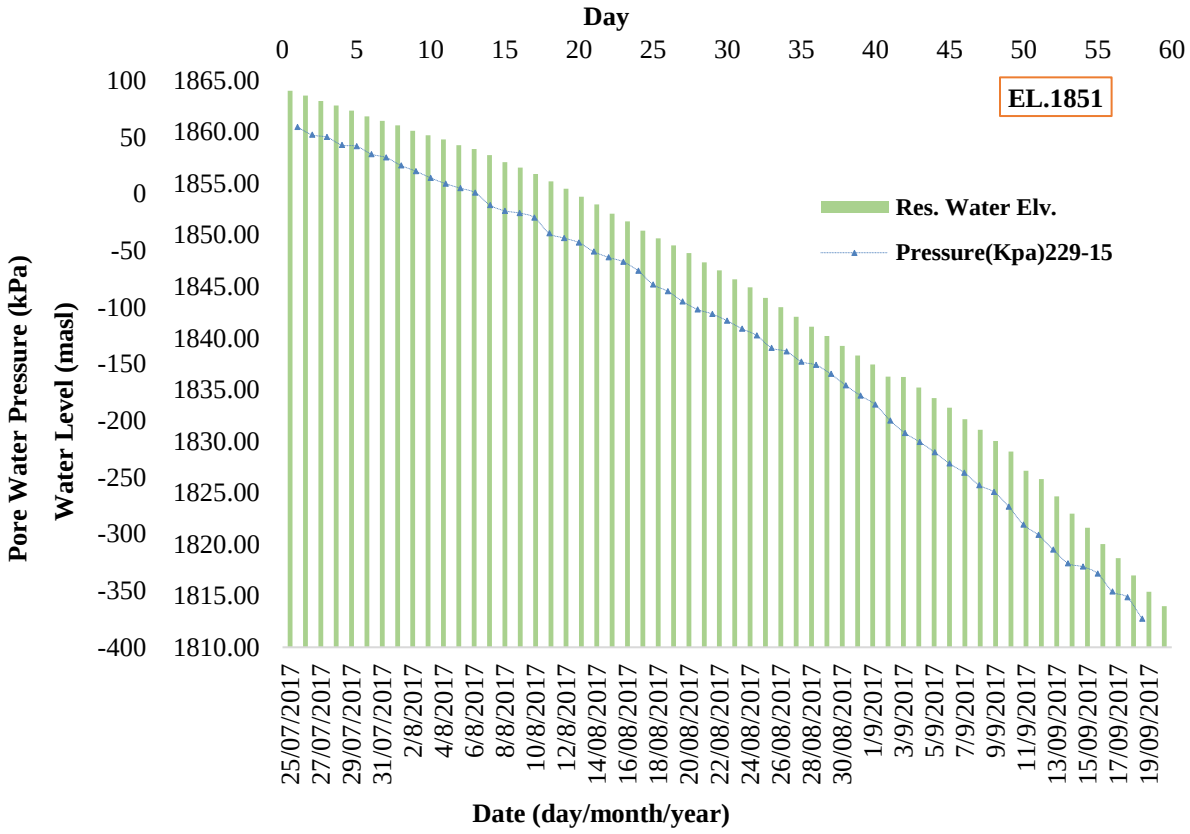

Fig. 7. Pore water pressure in the core of Eyvashan earth dam during rapid drawdown (EL.1851 masl)

3. Modeling and Analysis

To verify the data obtained from instrumentation readings, the pore water pressure on the Eyvashan earth dam was modeled using the GeoStudio software. Then the results of the numerical analysis were compared with the results of the observation. The behavior of the material of the dam body and the core in the analysis and the complete elastic-plastic model of Mohr-Coulomb were considered. The Mohr-Coulomb model is one of the simplest soil behavioral models. Since most soil parameters such as dough and elastic soil are present in this model, it is appropriate to model most soil behavioral conditions. In FEM based analysis, the selection of the proper shape of the element, element number, element size, etc. is crucial to minimize their effect in the calculation of the numerical results. Consequently, the mixed element (triangle and quadrilateral) have been considered. The number of elements and nods used in the main model was 2670 and 3105, respectively. Tables 1 and 2 show the parameters of the Mohr-Coulomb elasto-plastic model for various zones of the dam. For the drawdown analysis, the boundary condition is specified as a hydrostatic pressure for the dam reservoir. The hydrostatic pressure (water level) is 64 m on the upstream side and zero on the downstream side (dry). The displacement in the x-direction is specified as a fixed boundary condition on the left and the right of the ends of the foundation. Fixed x and y displacement condition is also specified at the bottom of the dam model. In the transient analysis, the boundary conditions for seepage vary in value over time (Figure 8). The rapid drawdown of the upstream water is simulated by lowering the water level from 64 m to 14 m in 58 days. Process and solution algorithm is described in Figure 9.

In this study, two steady and transient modes of modeling have been used. Before the rapid drawdown of the reservoir, a steady-state is used for modeling. The transient seepage analysis includes determining pore-water pressures during the drawdown and stability analysis of the upstream dam slope. For the analysis, each material was assumed to be homogeneous and isotropic. The steady-state results for the Eyvashan earth dam are shown in Figure 10a. The low permeability of both the core and the complete cut-off wall reduces the magnitude and velocity of the seepage, which keeps the total head and the phreatic level at the upstream at a constant value. Inside the core, the total head is suddenly reduced to a very low value, and the phreatic line drops. During the drawdown event, water occupying the soil voids begins to flow out of the dam.

For rapid drawdown modeling, transient analysis is used. The modeling was done in 58 days to match the actual results. Figure 10b shows the arrows indicating the flow direction for the case where the reservoir level has dropped to half of its initial level in fourteen days. The results showed that a substantial volume of water will seep out the dam starting from the core and the cut-off wall faces because of the low permeability of the core and the cut-off wall. The results of the numerical analysis of the Eyvashan earth dam indicate that the stagnant water level which has fallen without the water in the body, has the opportunity to evacuate. In this case, the hydrostatic pressure on the outer surface of the upstream slope is eliminated, while the overpressure of the pore water pressure remaining in the body remains.

Drawdown ratio is the most important factor affecting rapid drawdown. The drawdown ratio is shown as L/H, (L: reservoir water drop due to rapid drawdown, H: the normal water level) (Griffiths and Lane, 2000) (see Figure 11).

The drawdown rate is also the drainage drop of the reservoir water relative to the time indicated by R (cm or m/day) (Berilgen, 2007). United States Bureau of Reclamation (USBR) (1987) has proposed a critical drawdown rate of 0.5 ft (15 cm)

per day. In the transient analysis, the reservoir water level changes with time. Therefore, the head of water (H) specified at the upstream of the dam is dependent on time. The total head of water versus time illustrated in Figure 12, shows the initial and final values of the head. Moreover, the head versus time function shows the total head when the earth dam is under steady-state seepage, without any reduction in reservoir water level with time. Thus a constant total head of 138 m has been applied at time equals to zero. Moreover, to simulate a rapid drawdown condition, for loss of 50 m head in the reservoir over 58 days with a final head of 88 m, boundary condition has been applied in such a way that the reduction in reservoir water and pore-water pressures in the dam at a different time during the rapid drawdown process was modeled.

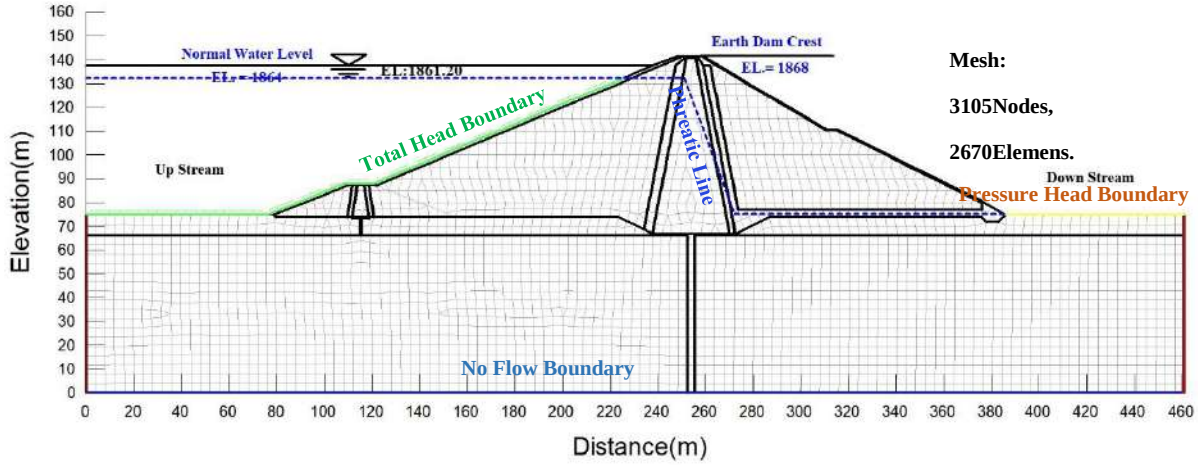

Fig. 8. Boundary conditions for the seepage analysis and the finite element mesh (Eyvashan earth dam)

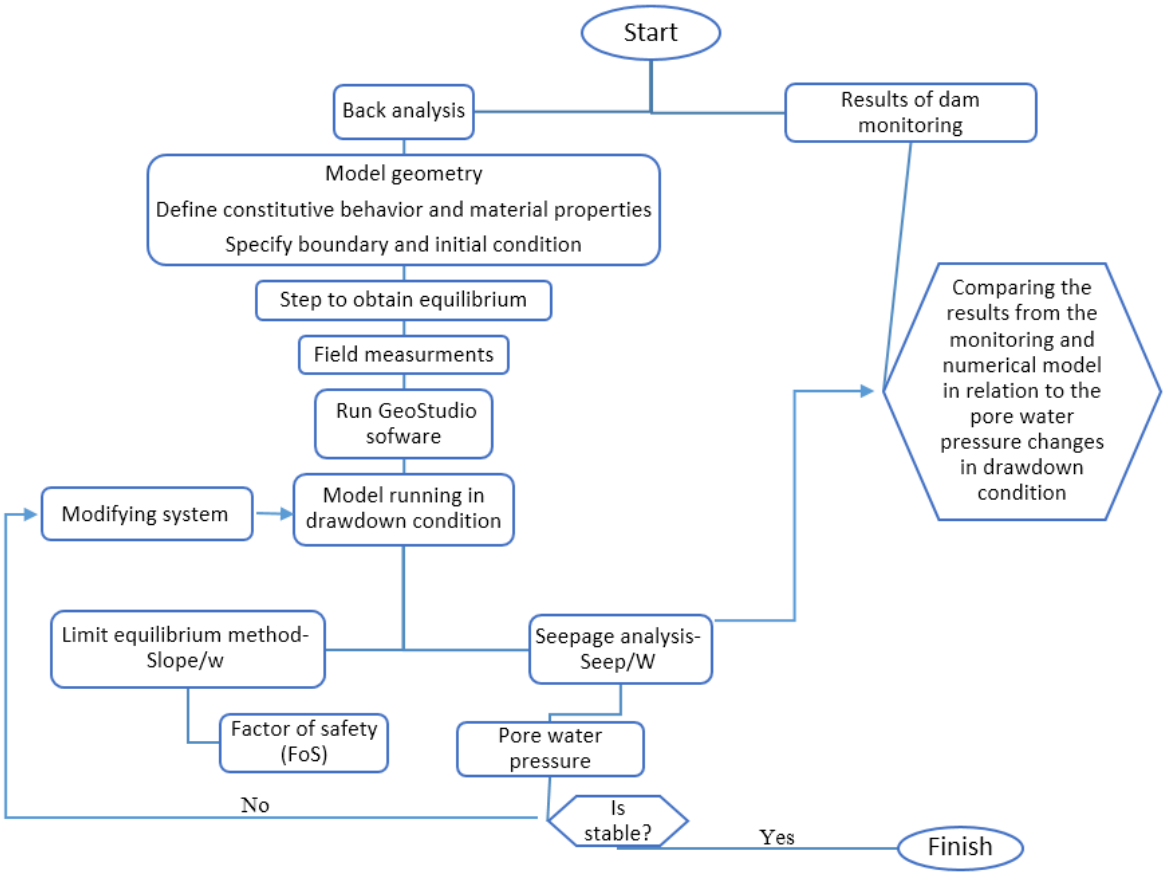

Fig. 9. Back analysis method and solution algorithm

Table 1. Initial amounts of material parameters in the body of the dam

Material	Mohr-Coulomb	Type material	Young's modulus E (MPa)	γ_{dry} (kN/m^3)	γ_{wet} (kN/m^3)	γ_{sat} (kN/m^3)	c, c′ (kPa)	
Core	Elasto-Plastic	Undrained Drained	35	17	20	21	63 28	11 24
Shell	Elasto-Plastic	Drained	70	22.5	23.8	24.5	-	-
Filter	Elasto-Plastic	Drained	45	19	21	22	-	-
Drain	Elasto-Plastic	Drained	55	20.5	22	23	-	-
Alluvium	Elasto-Plastic	Drained	500	21.5	-	23.2	-	-
Foundation	Elasto-Plastic	Drained	5000	25	-	25.5	-	-
Cut-off wall	Elasto-Plastic	Drained	2500	24	-	24	-	-

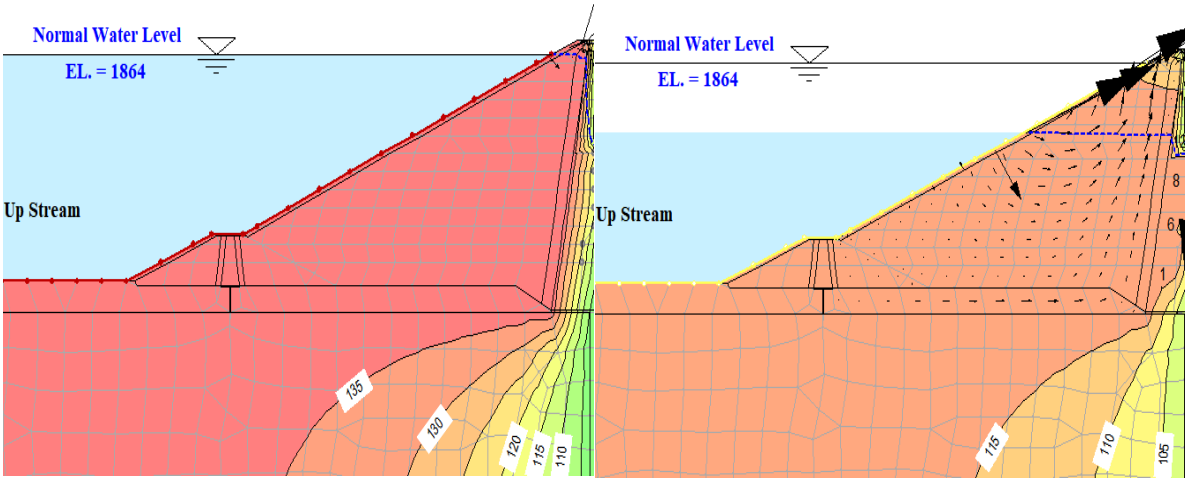

(a) **(b)**

Fig. 10. Total head contours (m) and flow directions of the water flux: a) Before the drawdown event; and b) after the reservoir is dropped to half in 42-day (GeoStudio)

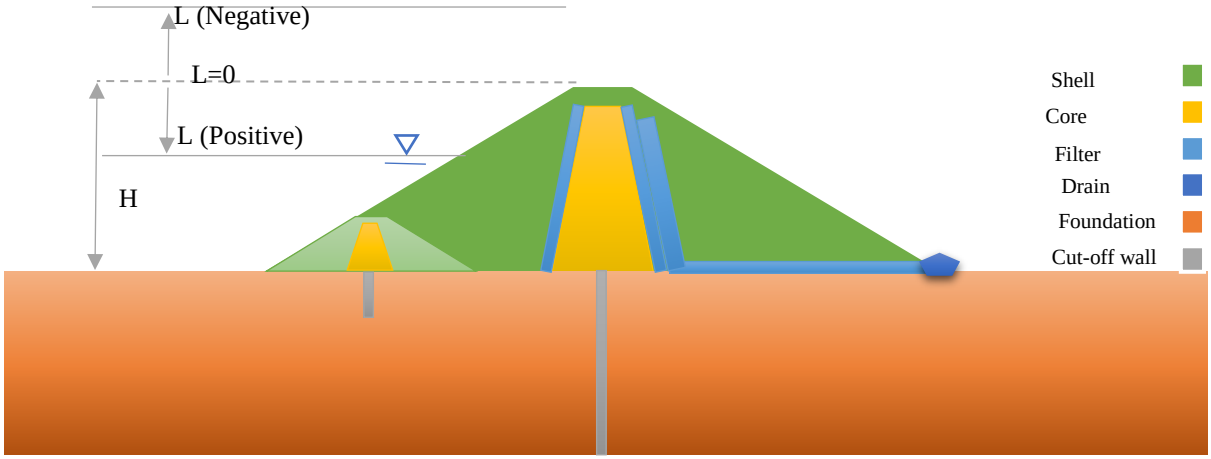

Fig. 11. Drawdown ratio (Eyvashan earth dam)

Table 2. Permeability of various materials of Eyvashan earth dam

Materials	k_x (m/sec)	k_y/k_x
Core	2.5×10^{-2}	0.2
Shell	1×10^{-3}	1
Filter	1×10^{-4}	0.5
Drain	2×10^{-2}	1
Alluvial	5×10^{-3}	1
Foundation	1×10^{-9}	1
Cut-off wall	1×10^{-7}	1

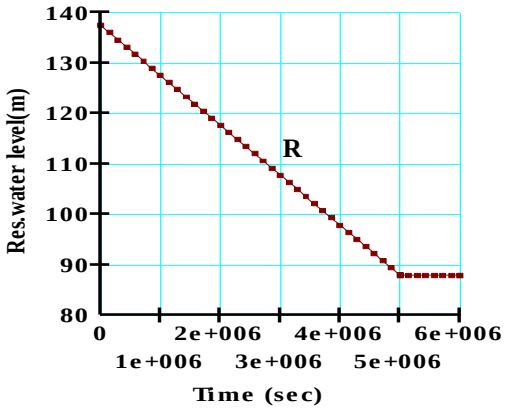

Fig. 12. Drawdown rate (head versus time), GeoStudio

4. Results and Discussion

4.1. Seepage Analysis

When the phreatic line (free surface) falls rapidly, almost in the same position, it is considered as rapid drawdown. The lag of the phreatic line or the rate of drawdown depends on four factors: drawdown rate, the permeability coefficient of the dam, pore water pressure, and upstream slope gradient. In cases where the reservoir water of the dam needs to fall quickly due to special conditions and on the other hand, the material on the slope of the dam is impermeable, the phreatic line does not fall so much and it causes instability. (Abadjiev, 1994). When the reservoir dam is rapid drawdown, pore water pressures in the dam core and body are reduced in two ways. There is an immediate elastic effect due to the removal of the total or partial water load and there is a slower dissipation of pore pressure due to drainage. It is assumed in this phenomenon that the reservoir has been maintained at a high level for a sufficiently long time so that the fill material of the dam is fully saturated and steady seepage established. In drawdown condition, the direction of flow is reversed, causing instability in the upstream slope of the embankment. The "instantaneous" drawdown is a hypothetical condition that is assumed and pore pressures along the sliding surface are determined by inspection of "instantaneous" pore water pressure at different points in the finite element mesh. The most critical condition of rapid drawdown means that while the water pressure on the upstream slope at the "full reservoir" condition is removed, there is no tangible change in the water content of the saturated soil within the dam (see Figure 13). This figure presents the water flux flowing out of the upstream face after the drawdown conditions, as a function of time during and after the drawdown event. The seepage now starts to exit the dam immediately after the drawdown starts for all the drawdown periods. Also, the seepage period is further prolonged and lasts for more than 58 days.

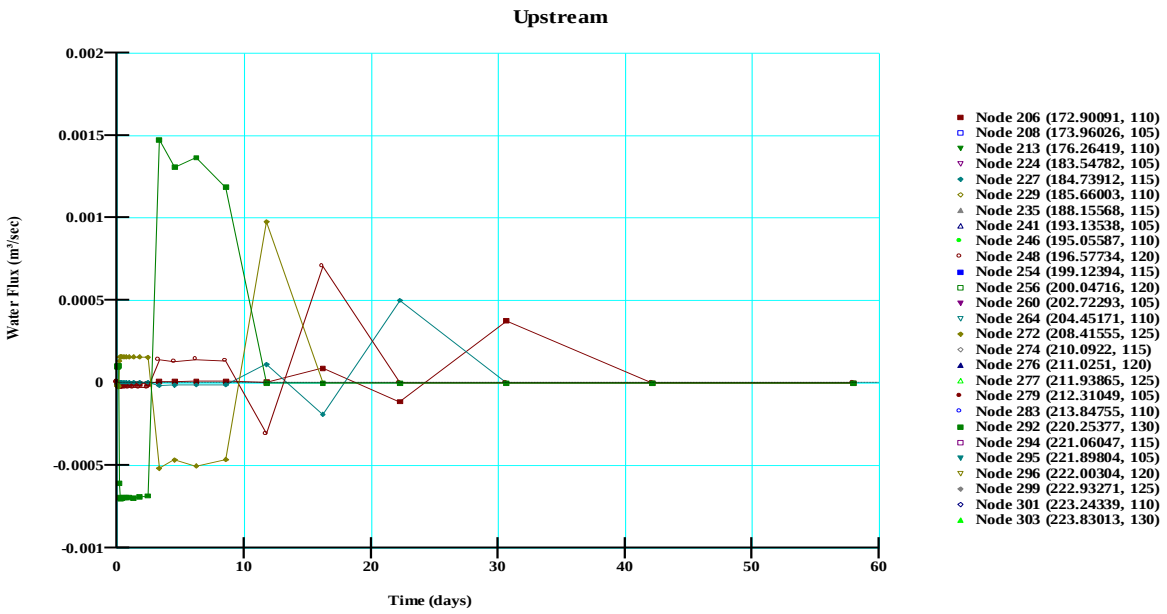

Fig. 13. The behavior of the water flux flowing out of the upstream face after the drawdown conditions

Figure 14 shows variations in pore water pressure during the rapid drawdown of the reservoir. In the conditions of the rapid drawdown of the reservoir of the Eyvashan earth dam and according to the modeling results performed based on the reality, the water level has decreased by 50 meters in 58 days (5011200 sec). The results show that the phreatic line remains constant after 29 days from the start of the rapid drawdown of the reservoir, while half of the volume of the drained reservoir remains at 1842 masl ($\frac{1}{3}$ of the crest dam). Throughout the time of the rapid drawdown of the reservoir, the pore water pressure has decreased. To accurately compare the results of numerical analysis with the actual results, the sections were precisely modeled on the actual position in the geostationary software. The results of the numerical analysis of the pore water pressure during the rapid drawdown of the reservoir based on time and at different levels are shown in Figure 15.

In addition, the results show that the water pressure graphs on the upstream of the core axis have been reduced more rapidly and steeper than the downstream sections. In Figure 16, variations in pore water pressure are shown in relation to the core height during the rapid drawdown at different sections of the dam core.

It is clear that at higher levels of the core, the pore water pressure drop is higher. In the upstream sections, the core has a higher drop than the downstream side, which is adjacent to the horizontal drain. To evaluate and compare the performance of the instrumentation and the GeoStudio model, multivariate regression used from the criterion of the coefficient of explanation (Eq. (7)).

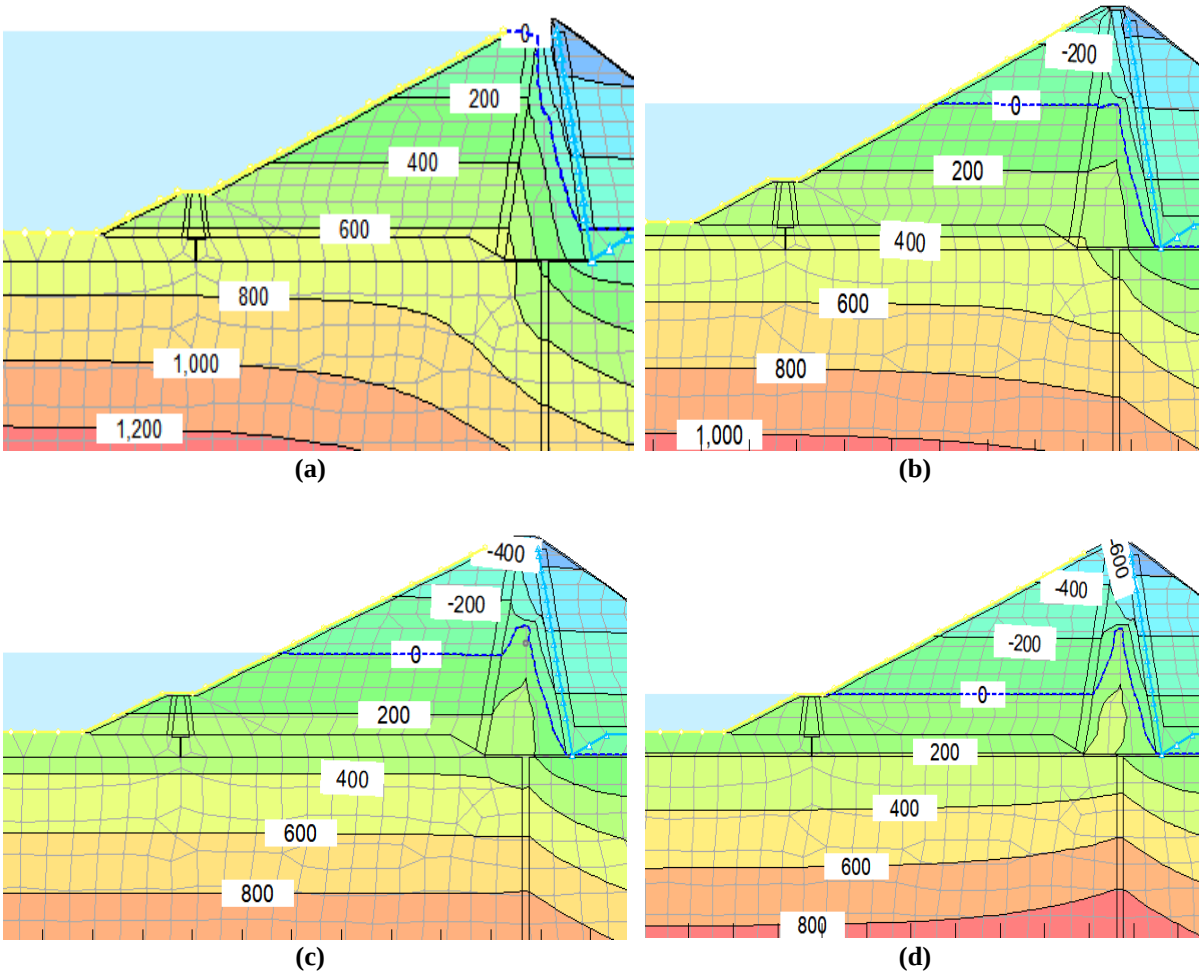

Fig. 14. Pore water pressure contours during drawdown (GeoStudio): a) Start drawdown; b) After 30 days; c) After 42 days; and d) After 58 days

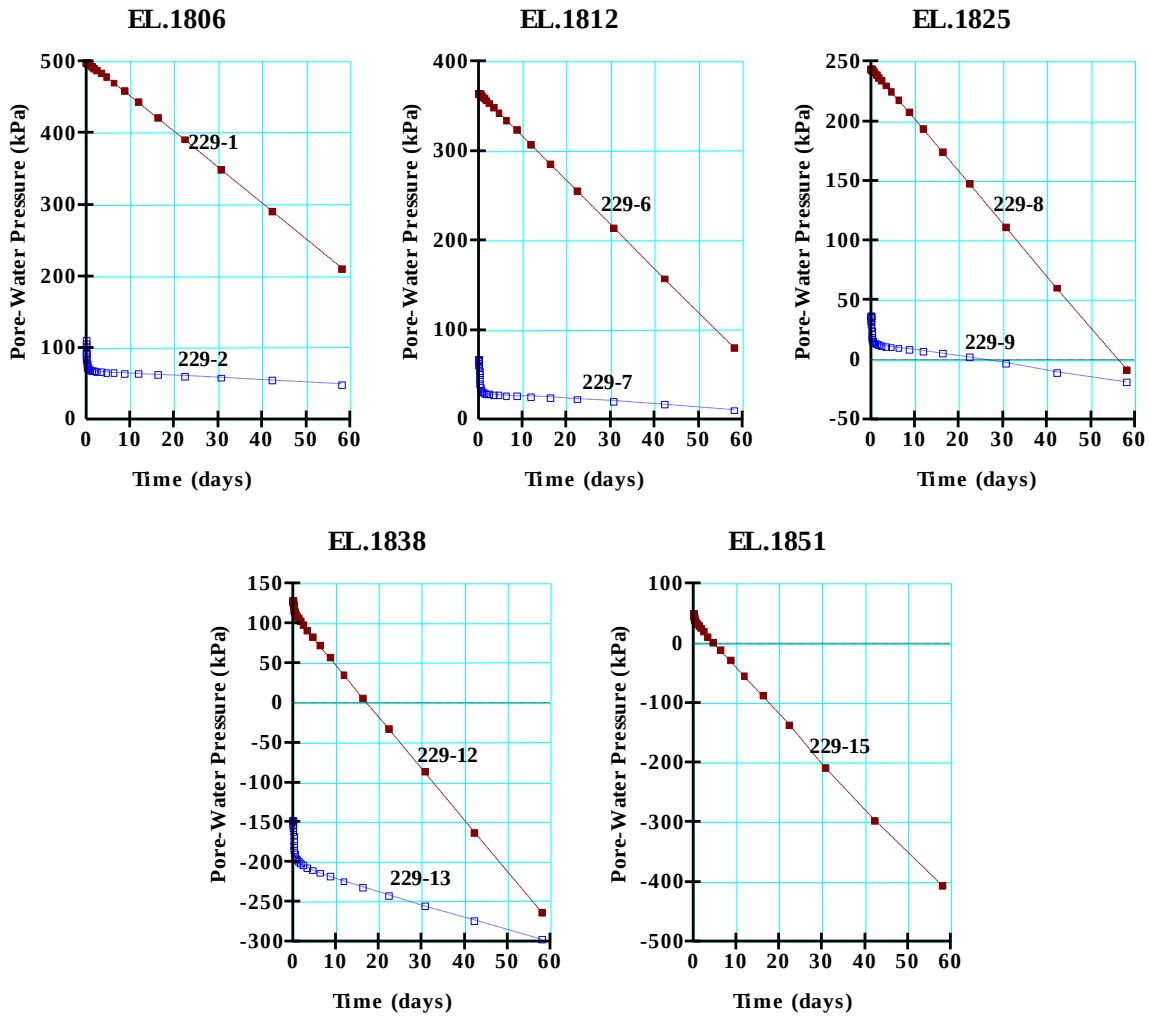

Fig. 15. Pore water pressure in the core of Eyvashan earth dam during rapid drawdown (GeoStudio)

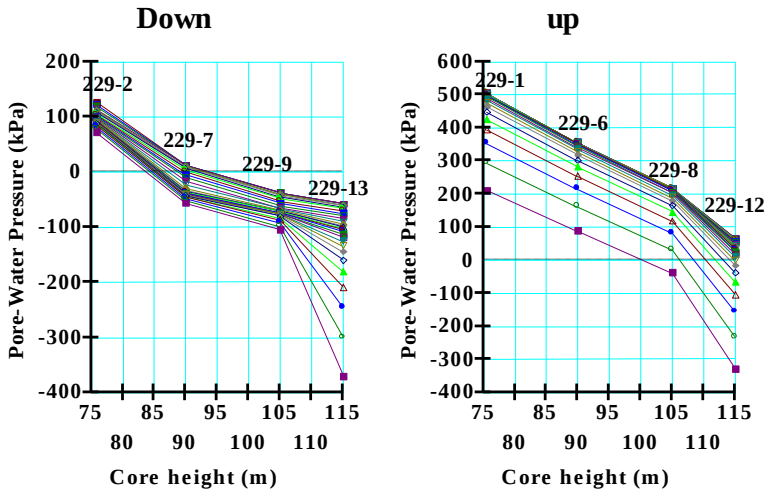

Fig. 16. Variations in pore water pressure relative to the core height during rapid drawdown

$$R^2=1-\frac{\sum_{i=1}^{n}(Pi-Oi)^2}{\sum_{i=1}^{n}(Pi-Oave)^2} \quad (7)$$

in which n: is the number of samples, O_i and P_i : are respectively the observed values and the predicted values, and O_{ave}: is the mean of observational values.

The explanatory factor shows that the regression line between the predicted and

measured values is close to the regression line with a slope of one. In the calculations, the closer R^2 to 1, the more efficient the model is. Indeed, if the value of R^2 is equivalent to 1, it shows a perfect fit, indicating a complete fit between the observational and predicted data. By applying Eq. (7) on the observed and predicted data, the coefficient of explanation for GeoStudio software was about 0.98 which showed the correspondence of the results of pore water pressure for Instrumentation and predicted values (see Figure 17).

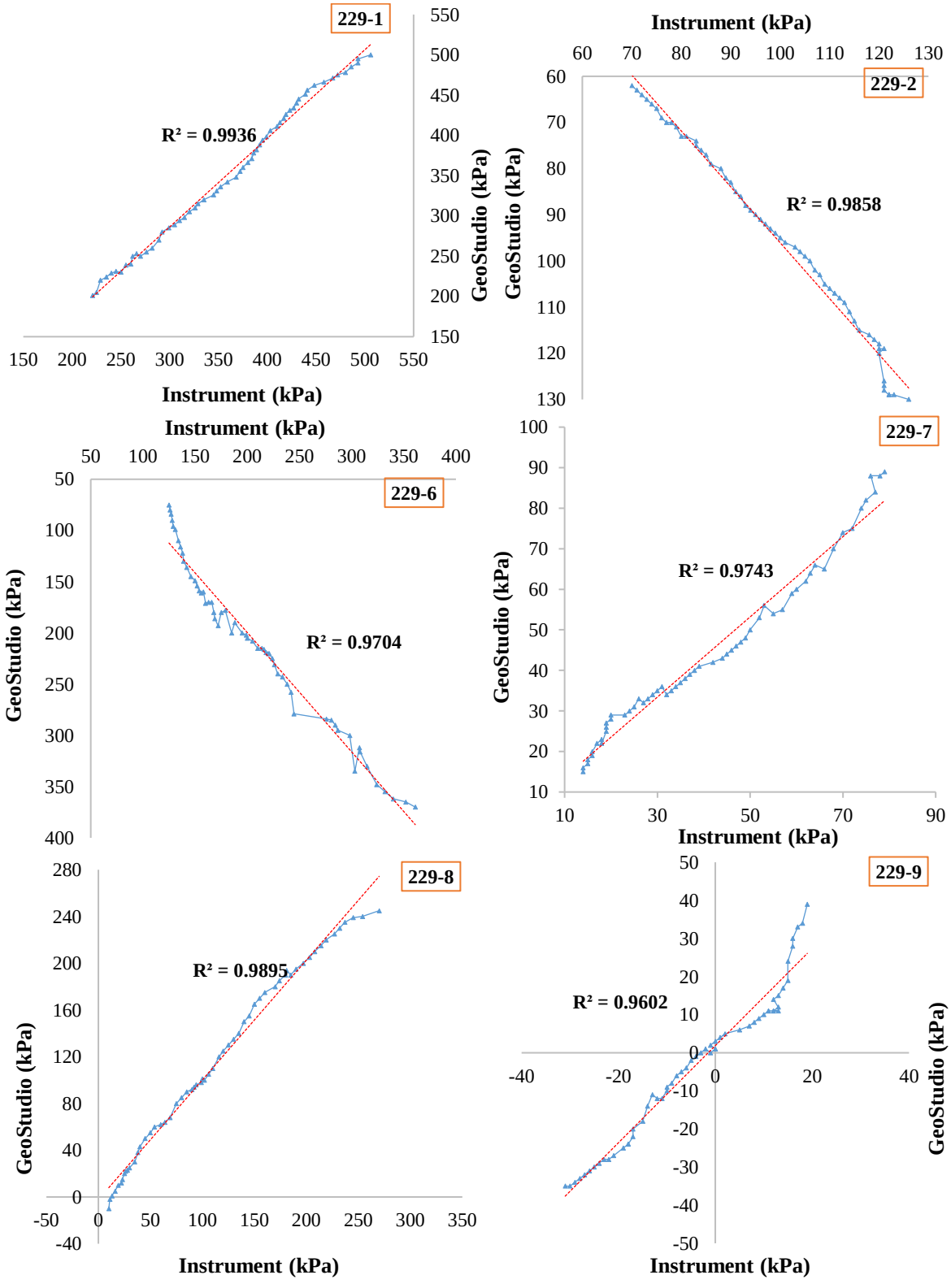

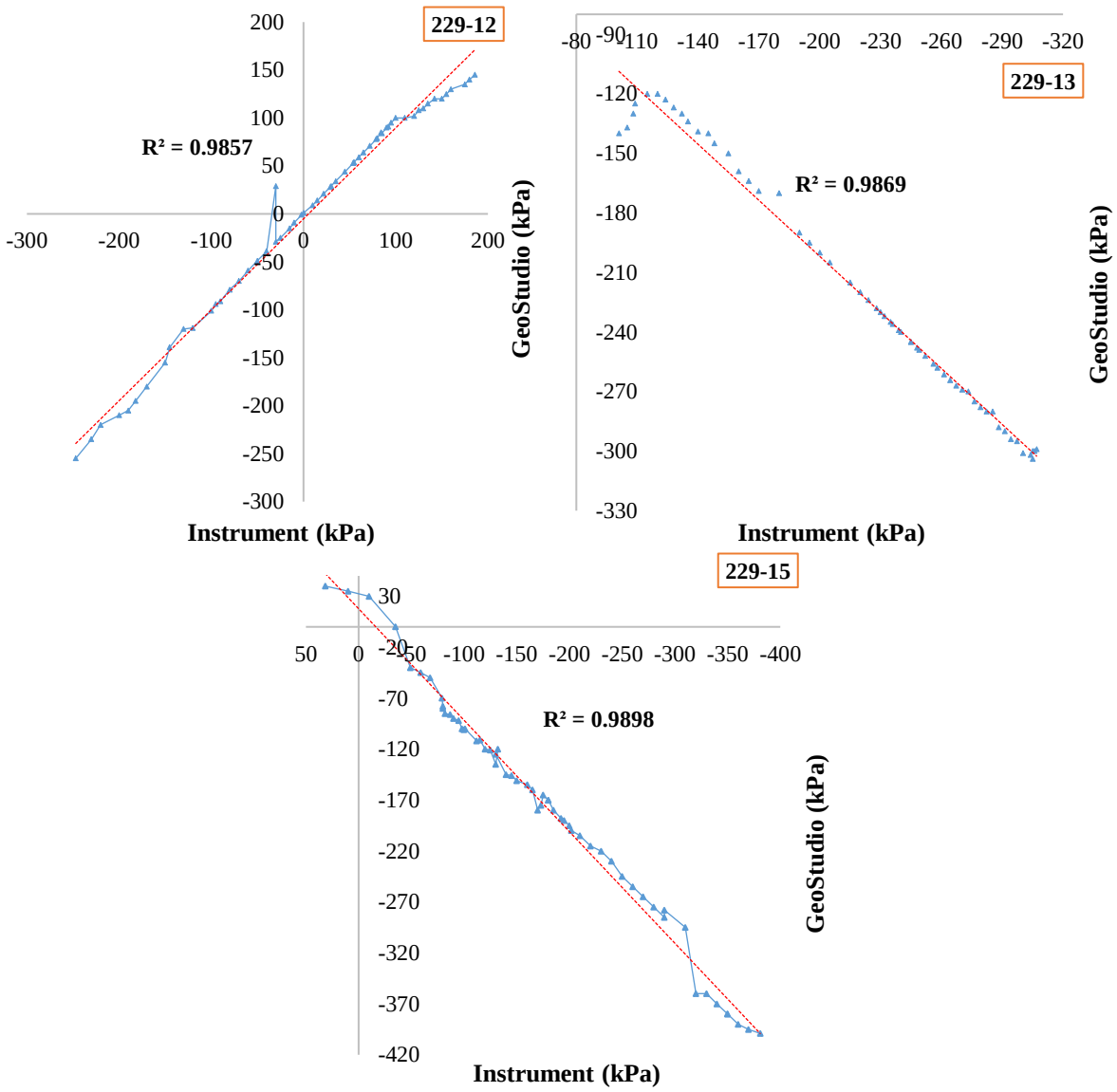

Fig. 17. Distribution diagram for the observed and predicted values (GeoStudio)

4.2. Slope Stability Analysis

The precise method of reservoir drawdown analysis is to use the transient analysis results. In this method, unlike the steady-state method, the exact amount of pore water in the drainage reservoir is used. With this method, the factor of safety can be obtained at different times of drainage of the reservoir. In the Eyvashan earth dam model, the reservoir dam has fallen from 64 to 14 m in 5011200 sec. In this type of analysis, the phreatic line decreases with time, which reduces pore water pressure over time and thus changes the amount of factor of safety. The factor of safety results has been computed using Morgenstern-Price and Bishop's usual methods as shown in Figure 18 for different conditions of water level (rapid drawdown). The minimum factor of safety in the Morgenstern-Price and Bishop methods for upstream slip surface at steady state was found to be 2.11 and 2.05, respectively.

The factor of safety gradually decreases as water in the reservoir decrease to 42 days of drawdown (water reservoir level 1830 masl) that a minimum factor of safety during drawdown falls above the value of (1.72 for both methods Morgenstern-Price and Bishop). Then, the factor of safety increases until the last day of rapid drawdown (58 days). So that at the time of

full discharge, the factor of safety will be 2.01 for the Morgenstern-Price method and 2 for the Bishop method. Therefore, according to the results of the stability of the upstream slope of the dam in a rapid drawdown mode (within 58 days), the dam will not have a problem in terms of stability in conditions drawdown. Figure 19 represents the factor of safety for different time intervals.

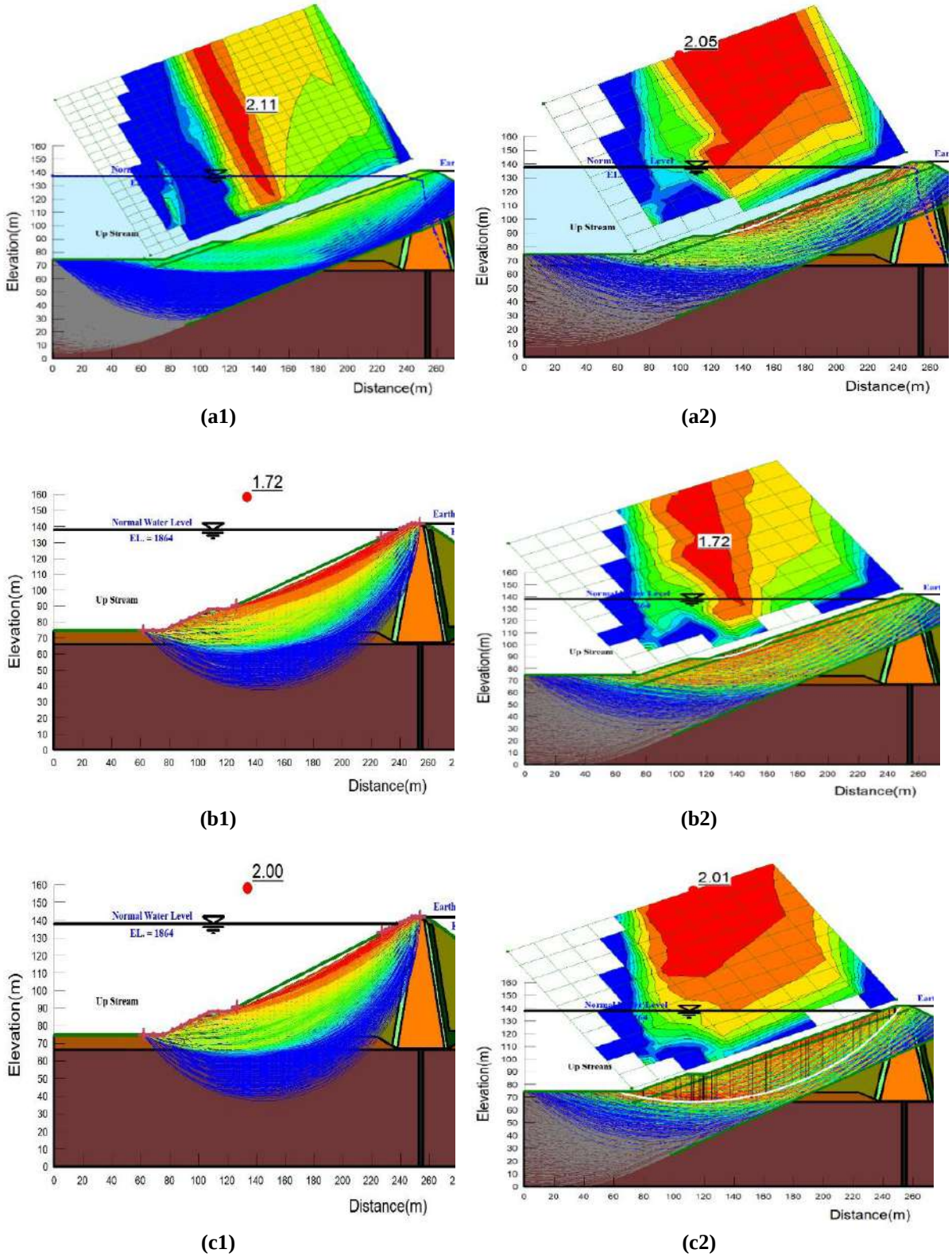

Fig. 18. Critical slope surface and factor of safety after rapid drawdown: a) Before drawdown; b) After 42 day; c) After 58 day (1: Morgenstern-Price; and 2: Bishop)

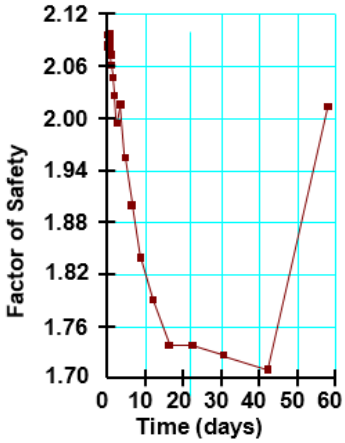

Fig. 19. Factor of safety results by using different methods for Eyvashan earth dam

As with the instantaneous drawdown analysis, the factor of safety decreases when the reservoir is drawdown. However, the Factor of Safety (FS) for the slow drawdown analysis does not drop below 1.72. According to Figure 19, FS is reduced until the dam reservoir drop is continued. But after the end of the rapid drawdown, it gradually increases and it reaches an amount of constant after a relatively long period. The reason for this is that after the end of the rapid drawdown, it takes a while before the phreatic line reaches its lowest level and the amount of pore water pressure is also fixed and in the analysis steady-state of the transient state analysis mode, the safety factor will remain constant.

5. Conclusions

In the conditions of the rapid drawdown of the reservoir of the Eyvashan earth dam and according to the modeling performed based on reality, the water level has decreased by 50 m in 58 days (5011200 sec). The results showed that the phreatic line remains constant after 29 days from the start of the rapid drawdown of the reservoir, while half of the drained reservoir volume remains at 1842 masl ($\frac{1}{3}$ of the crest). Throughout the time of the rapid drawdown of the reservoir, the pore water pressure has decreased. To accurately compare the results of numerical analysis with the actual results, the sections were precisely modeled on the actual position in the geostationary software. To evaluate and compare the performance of the instrumentation and the GeoStudio model, multivariate regression was used and the criterion of the coefficient of explanation. By applying R^2 on the observed and predicted data, the coefficient of explanation for GeoStudio software was about 0.98, which showed the correspondence of the results of pore water pressure for instrumentation and predicted values. The minimum factor of safety in the Morgenstern-Price and Bishop methods for upstream slope surface at steady state was found to be 2.11 and 2.05, respectively. The factor of safety gradually decreases as water in the reservoir decrease to 42 days of drawdown (water reservoir level 1830 masl) that a minimum factor of safety during drawdown falls above the value of 1.72 (for both Morgenstern-Price and Bishop methods). Then, the factor of safety increases until the last day of rapid drawdown (58 days) so that at the time of full discharge, the factor of safety will be 2.01 for the Morgenstern-Price method and 2 for Bishop Method. Therefore, based on the results of the stability of the upstream slope of the dam in a rapid drawdown mode (within 58 days), the dam will not have a problem in terms of stability in conditions drawdown.

6. References

Abadjiev, C.B. (1994). "Safety assessment and stability improvement of the upstream slope of earth dams", *Proceedings of the 18th ICOLD Congress*, Durban, South Africa, 1, 261-273.

Alonso, E.E., and Pinyol, N.M. (2016). “Numerical analysis of rapid drawdown: Applications in real cases”, *Water Science and Engineering*, 9(3), 175-182.

Bahrami, A., Teimouri, B. and Khalkhali, A.B. (2018). "Stability control of Narmab Dam and sensitivity analysis of reliability coefficients", *Civil Engineering Journal*, 4(9), 2197-2209.

Berilgen, M.M. (2007). "Investigation of stability of slope under drawdown condition", *Computers and Geotechnics*, 34, 81-91.

Boroomand, M.R. and Mohammadi, A. (2019). "Evaluation of earth dam leakage considering the uncertainty in soil hydraulic parameters ", *Civil Engineering Journal*, 5(7), 1543-1556

Fattah, M.Y. Omran, H.A. and Hassan, M.A. (2017). "Flow and stability of Al-Wand earth dam during the rapid drawdown of water in the reservoir", *Acta Montanistica Slovaca*, 1(22), 43-57

Lane, P.A. and Griffiths, D.V. (2000). "Assessment of stability of slopes under drawdown conditions", *Journal of Geotechnical and Geoenvironmental Engineering, (ASCE)*, 126(5), 443-450.

López-Acosta, N., Sánchez, M., Auvinet, G. and Pereira, J. (2014). "Assessment of exit hydraulic gradients at the toe of levees in water drawdown conditions", In: *Scour and Erosion*, 171-181.

Nian, T., Jiang, J., Wan, Sh. and Luan, M. (2011). "Strength reduction FE analysis of the stability of bank slopes subjected to transient unsaturated seepage", *Electronic Journal of Geotechnical Engineering*, 16, 165-177.

Salmasi, F., Mansuri, B. and Raoufi, A. (2015). "Use of numerical simulation to measure the effect of relief wells for decreasing uplift in a homogeneous earth dam", *Civil Engineering Infrastructures Journal*, 48(1), 35-45.

SEEP/W. (2016). "Seepage modeling with SEEP/W: *An engineering methodology*, GEO-SLOPE International Ltd.

Siacara, A.T. Beck, A.T. and Futai, M.M. (2020). "Reliability analysis of rapid drawdown of an earth dam using direct coupling", *Computers and Geotechnics*, 118, 1-16

Sica, S., Pagano, L. and Rotili, F. (2019). "Rapid drawdown on earth dam stability after a strong earthquake", *Computers and Geotechnics*, 116, 1-15

Stark, T.D., and Jafari, N.H. (2018). "San Luis dam case history: Seepage and slope stability analyses and lessons learned", In: *IFCEE 2018*, pp. 317-329.

United States Bureau of Reclamation (USBR), (1987). *Design of small dams*, Department of Interior, Col., USA.

Vanapalli, S.K. Fredlund, D.G., Pufahl, D.E. and Clifton, A.W. (1996). "Model for the prediction of shear strength with respect to soil suction", *Canadian Geotechnical Journal*, 3, 379-392.

Viratjandr, C. and Michalowski, R.L. (2006). "Limit analysis of submerged slopes subjected to water drawdown", *Canadian Geotechnical Journal*, 43(8), 802-814.

Wang, J.J. Zhang, H.P. Zhang, L. and Liang, Y. (2012). "Experimental study of heterogeneous slope responses to drawdown", *Engineering Geology*, 147, 52-56.

Yan, Z.L., Wang, J.J. and Chai, H.J. (2010). "Influence of water level fluctuation on phreatic line in silty soil model slope", *Engineering Geology*, 113(1-4), 90-98.

Zedan, A.J., Faris, M.R. and Abdulsattar, A.A. (2018). "Slope stability of an earth dam during drawdown conditions (Khasa Chai Dam) as a case study", *International Journal of Engineering and Technology*, 7(37), 17-21.

Zhang, G. and Luo, F. (2017). "Simplified stability analysis of strain-softening slopes under drawdown conditions", *Environmental Earth Sciences*, 76(4), 151.

Zomorodian, S.M.A. and Abodollahzadeh, S.M. (2010). "Effect of horizontal drains on upstream slope stability during rapid drawdown condition", *International Journal of Geology*, 4(4), 85-90.

Civil Engineering Infrastructures Journal 2021, 54(2): 225-251
DOI: 10.22059/CEIJ.2021.294057.1642

RESEARCH PAPER

Development of a Road-Condition Assessment System and Application to Road Maintenance Decision-Making

Miyamoto, A.[1]* and Ximenes, H.D.C.[2]

[1] Emeritus Professor, Yamaguchi University, Japan, and Visiting Professor of EPFL, Lausanne, Switzerland.
[2] M.Sc., Department of Civil Engineering, National University of Timor Leste, Dili, Timor Leste.

Received: 14 Dec. 2019; Revised: 14 Sep. 2020; Accepted: 14 Sep. 2020

ABSTRACT: The deterioration of existing road pavement surfaces over the years due to aging and the growing number of heavy vehicles has become an important issue. Roads require appropriate maintenance to keep providing the target service. Many efforts have been made by road engineers to maintain road pavement surfaces; however, there are some problems due to costs, including vehicle running costs. Therefore, there is a need for an efficient and low-cost system to facilitate evaluation of the serviceability of existing road pavement surfaces. This study aims to develop an efficient, rational and useful method or system that can be used to perform a visual assessment of the condition of not only the pavement but also road structures, including slopes, vegetation and equipment such as guardrails, curbs and guideposts. Such a system should be inexpensive and be IT-based by making use of new information and the latest technologies. In addition, a method based on an analytic hierarchy process is employed in the decision-making process to analyze a complicated decision problem based on video files obtained by the system.

Keywords: Analytic Hierarchy Process (AHP), Assessment System, Decision Making, Ippo-Campo, Road Condition, Road Network, Timor-Leste.

1. Introduction

Road networks are one of the most important key infrastructures that contribute to rapid economic growth. At the same time, there is an increasing demand for reasonable preventive maintenance, including repairs to the road pavement and other facilities within the road networks while the roads remain in service, despite limited budgets and human resources.

Regarding the road pavement, for example, the Maintenance Control Index (MCI) is used in Japan as an index for judging damage to asphalt pavements (Miyamoto et al., 2009). MCI parameterizes the cracking ratio, roughness and rutting depth, but it can also be used as an index based on two attributes or even just one attribute (CESFJ, 1993). MCI inspection of the road pavement is undertaken using a specially designed vehicle (Government of Japan, 2008).

In the United States, the current level of serviceability of a pavement is expressed using the Present Serviceability Index (PSI)

* Corresponding author E-mail: miya818@yamaguchi-u.ac.jp

developed by the American Association of State Highway and Transportation Officials (AASHTO) (AASHTO, 1993). Another useful index is the international roughness index (IRI) proposed as an indicator by the World Bank (Sayers, 1985), which mainly focuses on ride quality and the roughness of road surfaces, including but not limited to asphalt pavements. The IRI is an index defined by applying an algorithm to a measurement of the longitudinal profile.

For the indices mentioned above, the soundness of the road pavement is usually evaluated by using an inspection vehicle. Such a vehicle is capable of accurate quantitative evaluation, but its initial and operating costs are usually relatively high, and such vehicles tend to be used infrequently. Another constraint is that this inspection vehicle cannot measure the road width, radius of curvature and slope. In addition, there are many features of a road that must be regularly checked, such as road appurtenances and filled/cut slopes. Therefore, there is a need for an efficient and low-cost system to facilitate evaluation of the serviceability of an existing road pavement surface. This paper introduces a newly developed road condition assessment system (called Ippo-Campo) and its practical application to road maintenance decision-making. Ippo-Campo is a pavement maintenance evaluation system based on a moving vehicle and obtains data from a motion sensor, as well as video, sound and GPS data. It is a simple evaluation system that provides a systematic and consistent approach to the evaluation of the condition of a pavement surface. In addition, the video file produced by Ippo-Campo can be used for making a multi-criteria-based decision by using the analytical hierarchy process (AHP). This supports decision making with regard to complex sustainability issues and can help to recognize and define a problem in detail. The results of AHP provide a useful means of checking the consistency of evaluation measures and alternatives to reduce bias in decision-making. It is helpful for particular conditions and distress types and enables the prioritization of necessary repairs and maintenance work within limited budgets.

2. Research Significance

Road deterioration due to inadequate and untimely maintenance is likely to lead to an increase in the number of traffic accidents, reduced reliability of transport services and increased vehicle operating costs. Therefore, there is a need for an appropriate maintenance method to ensure that a road can provide a sustainable service (Modarres and Shabani, 2015; Zhao et al., 2018). The main aims of the work described in this paper are to apply a road condition assessment system to road networks in both Japan and Timor-Leste to confirm the effectiveness of the system and also to apply the system to decision making for road maintenance by using the AHP model for the road networks of Timor-Leste, which is a developing country, as a specific example.

3. Development of a Road-Condition Assessment System

3.1. Concept of the System

This section gives a brief overview of how data analysis is performed. Data are obtained using a three-dimensional motion sensor, a GPS system equipped with a gyro and an acceleration sensor, a high-resolution camera, and a microphone. Figure 1 shows the equipment installed in a vehicle. It takes about 20 min to install and start-up the measuring equipment. The system sensor acquires GPS log data. Thus, the acceleration, time (GMT), angular velocity, geomagnetic and orientation sensor information, an orbital plan view and satellite reception conditions can be recorded. The GMT time is very important for synchronizing the video information with the sensor information. In addition, items displayed on this screen can be selected independently, and the scale of the viewing area can be arbitrarily set

(Miyamoto et al., 2013). Figure 2 shows an example of the system's signal display. The noise from the car and the car's motion data, as obtained from the video and the motion sensor, are obtained from a car travelling along a selected road. The recommended speed of the car is 50 km/h to 60 km/h. It is possible for one person (the driver) to check the status of the installation of the equipment and capture the data (Hugo et al., 2014).

3.2. Configuration of the System

An evaluation of the road pavement condition using the Ippo-Campo assessment system and the obtained three-dimensional motion sensor, video and sound data involves several steps. Figure 3 shows an example of the system's menu screen. It was developed using Visual Basic in Microsoft Excel (Miyamoto et al., 2013). Figure 4 shows the configuration of the system functions. Motion sensor data, driving video data, sound data, subtitle data and GPS data are acquired by the system. By connecting these data, an evaluation of the road surface ("GOOD", "MODERATE" or "BAD") is output to an Excel file every second, together with the longitude, latitude, X and Y coordinates, point distance, etc. In addition, by linking the system with online maps by using the GPS data, the evaluation results can also be displayed on a map. Then, by converting the world geodetic system into latitude and longitude information, it is possible to reflect the results of the evaluation on road register map data (Hugo et al., 2014).

3.3. Determination of Threshold Values for the System

The determination of the threshold points for the pavement surface uses the standard deviation of the Z-axis acceleration signal. The threshold was decided by conducting a road surface measurement test as part of a cooperative study undertaken by Yamaguchi Prefectural Government and Yamaguchi University. The defined value was obtained by evaluating the data between the MCI and the Z-axis acceleration. The results assumed that the threshold levels for pavement management for the standard deviation of the Z-axis acceleration are: 0 to 0.4 for "GOOD", which is indicated in green and with the ○ symbol; 0.4 to 0.6 for "MODERATE", which is indicated in yellow and with the △ symbol; and more than 0.6 for "BAD", which is indicated in red and with the X symbol. Figure 5 shows the correlation between the MCI and the standard deviation of the Z-axis acceleration. The regression equation and correlation coefficient are derived from the relationship between the MCI standard and the obtained Z-axis acceleration data. It is assumed that the value of 0.4 for the standard deviation of the Z-axis acceleration is equivalent to an MCI of ≥ 6, which represents the "GOOD" condition of the road pavement. A value of 0.6 for the standard deviation of the Z-axis acceleration is equivalent to an MCI of ≥ 5, which represents the "MODERATE" condition of the road pavement. Moreover, a value of ≥ 0.6 for the standard deviation of the Z-axis acceleration is equivalent to an MCI of ≥ 5, corresponding to the "BAD" condition of the road pavement (Hugo et al., 2014).

Table 1 shows an example of the output data in an Excel file. Figure 6a shows an example of a video and subtitle file that illustrates the road situation using video, and Figure 6b shows an example of output data indicating the condition of the road as web map data, showing the road condition using three highlighted colors: red for bad, yellow for moderate, and green for good.

On the other hand, the Timor-Leste threshold was determined by using the average value for the data obtained from the measurement points by using the system, because Timor-Leste has no established method with which a comparison can be made. In addition, the Japanese thresholds (0.4 to 0.6) shown in Figure 5 are not applicable to Timor-Leste road surfaces because the conditions are completely

different. Therefore, we randomly selected a measurement point from the best road conditions in Timor-Leste and analyzed the obtained data using the system.

Fig. 1. Arrangement of measuring equipment installed in a car

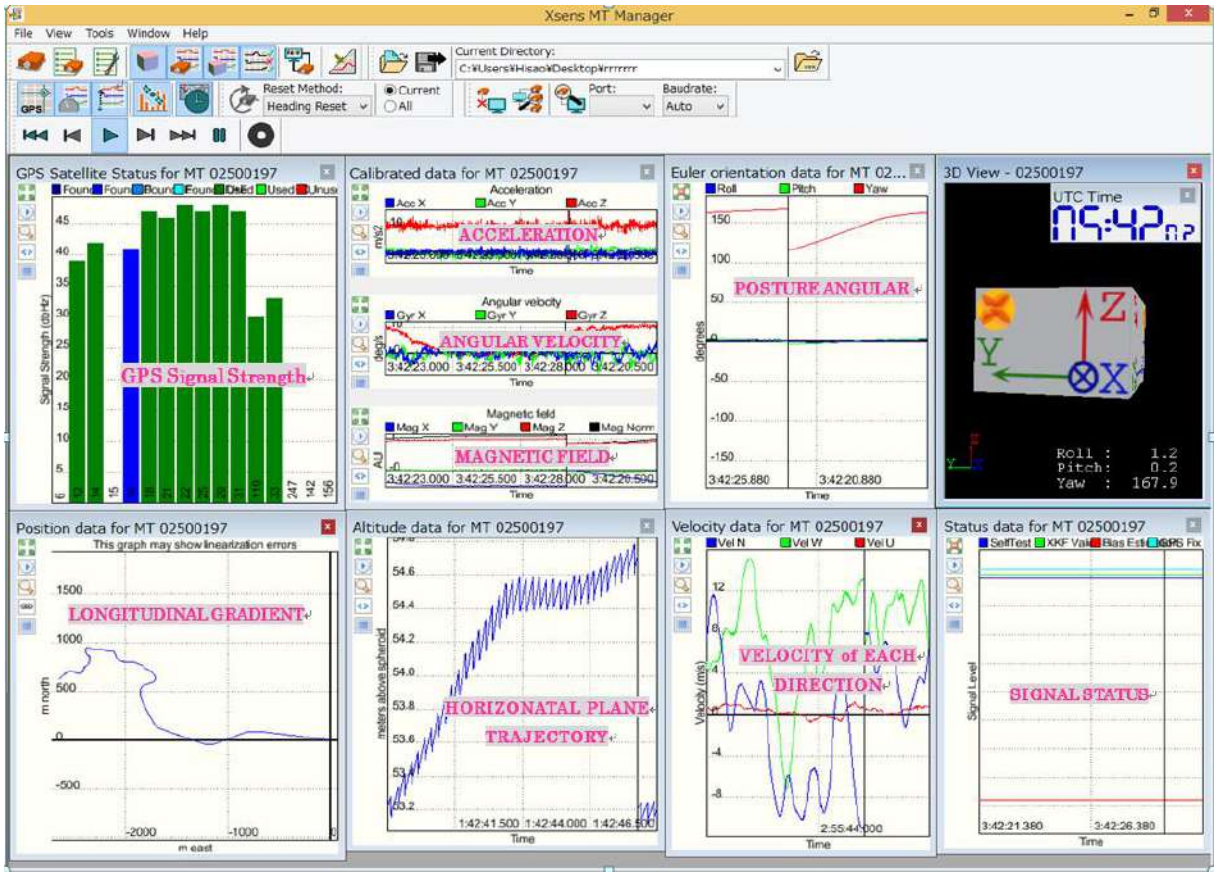

Fig. 2. Example of signal display in the system

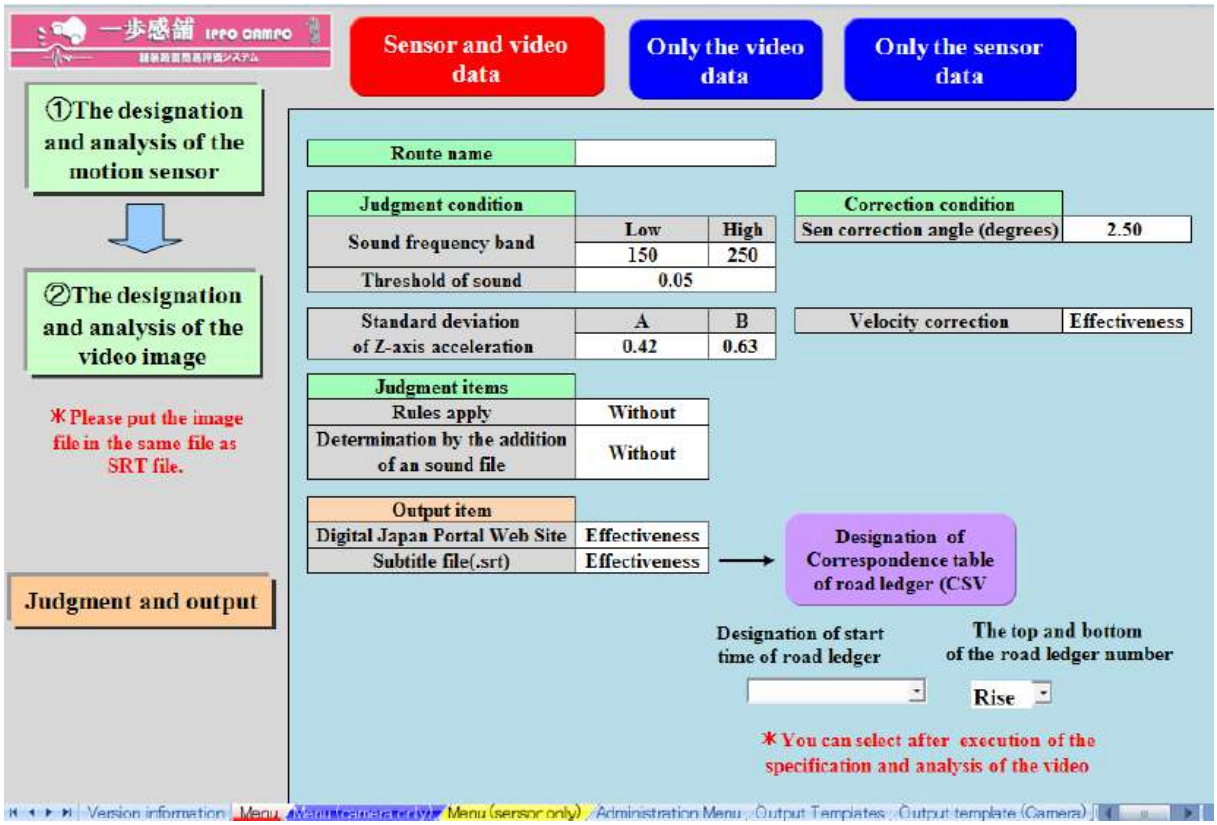

Fig. 3. Menu screen of the road condition assessment system

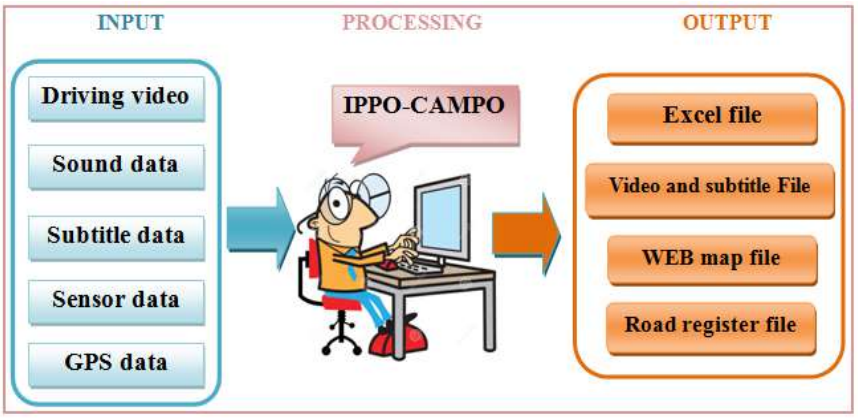

Fig. 4. Configuration of the system functions

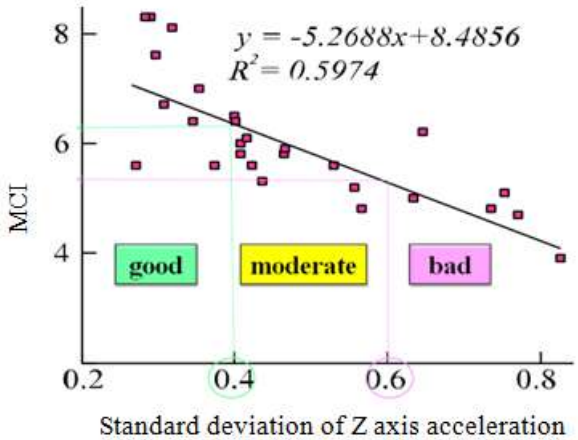

Fig. 5. Correlation between MCI and standard deviation of Z axis acceleration

Table 1. Example of output data of evaluation results in an Excel file

10	JST	Latitude	Longitude	Map	Point distance	Cumulative distance	Longitudinal gradient	Number of satellites	Judgment
553	2012/2/16 16:08:20	34.17839	132.0643	Map	14.07224488	6350.2716	−2	7	○
554	2012/2/16 16:08:21	34.17839	132.0642	Map	12.65927545	6362.930875	−2	7	△
555	2012/2/16 16:08:22	34.1784	132.064	Map	14.1230363	6377.053912	−1.3	7	△
556	2012/2/16 16:08:23	34.17841	132.0639	Map	14.12303446	6391.176946	−0.9	7	△
557	2012/2/16 16:08:24	34.17843	132.0637	Map	14.22408505	6405.401031	−0.7	7	×
558	2012/2/16 16:08:25	34.17845	132.0635	Map	15.61633777	6421.017369	−0.5	7	×
559	2012/2/16 16:08:26	34.17847	132.0634	Map	14.22407889	6435.241448	0.3	7	×
560	2012/2/16 16:08:27	34.17845	132.0635	Map	12.91129266	6448.152741	1	7	×
561	2012/2/16 16:08:28	34.17852	132.06331	Map	14.29311293	6462.445854	2.8	7	×

(a)

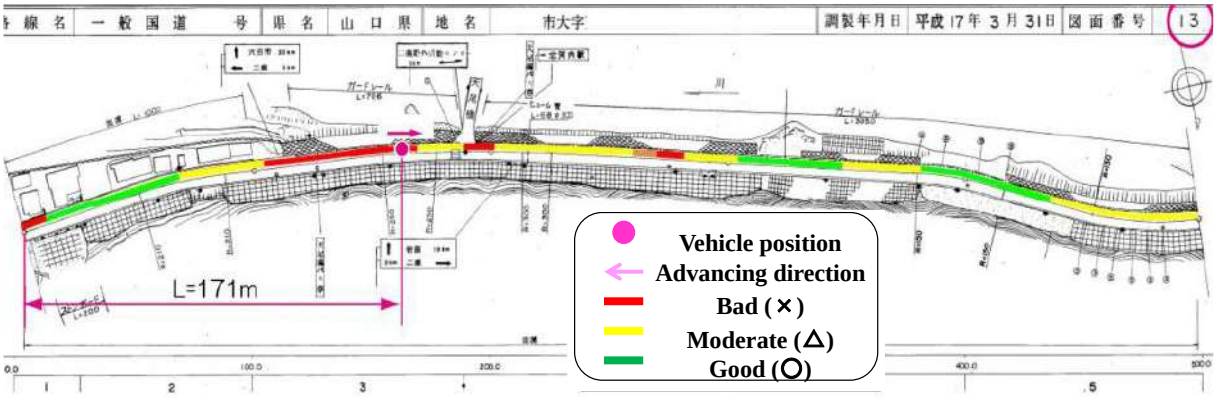

(b)

Fig. 6. a) Example of evaluation results using video file with subtitles; and b) Example of evaluation results using web map file

Furthermore, because of the different conditions of the road surfaces between the two countries, we chose a trial threshold of 0.7 to 1.2 for application to the Timor-Leste road networks. Then we tried to analyze the data that was eventually used to compare the evaluation results for both the Japanese and Timor-Leste thresholds (see Figure 7). Table 2 shows how the threshold for Timor-Leste was determined. In this measurement, we obtained 1,377 items of data: 182 for the "GOOD" condition, 452 for the "MODERATE" condition, and 743 data for the "BAD" condition. Red is clearly the dominant color, implying that the condition of the road is poor. On the other hand, for the evaluation using the trial threshold (0.7 to 1.2), the number of items for the "GOOD" condition increased to 781, the number of items for the "MODERATE" condition increased to 490, and the number of items for the "BAD" condition decreased significantly to 106. In this case, green is the dominant color, implying that the condition of the road is "GOOD". As result, the threshold for Timor-Leste was decided by defining 0 to 0.7 as the "GOOD" condition, 0.7 to 1.2 as the "MODERATE" condition, and more than 1.2 as the "BAD" condition, as shown in Figure 7.

Table 2. Evaluation results obtained with Ippo-Campo system using different thresholds

// Start Time: 13/05/2015 - 00:38:34			ルール適用: 無し						Japanese thresholds (0.4~0.6)			Trial Threshold (0.7~1.2)	
// Sample rate: 100.0Hz			音声判定付加: 無し										
// Scenario: 2.7			センサファイル名: MT 02500197 000-000.txt										
// Firmware Version: 2.6.1			ビデオファイル名: 20150513093841.m2ts										
音声周波数帯域: 150 - 250			SRTファイル名: 20150513093841.m2ts.srt						good	182	max	4.826305094	781
音声閾値: 0.05			計測時刻補正値: 0(s)						moderate	452	ave	0.732784209	490
加速度閾値(x): 0.42 < x < 0.63			センサ補正角度: 2.5(度)						bad	743	min	0.248342478	106
電子国土ポータル:	Dili-Erm_20150513.htr		速度補正: 有効							1377			1377
JST	Latitude	Longitude	X座標	Y座標	地図	点間距離	累加距離	縦断勾配(%)	判定		Acc_Z	Z軸加速度標準偏差	
2015/5/13 9:38:41	-8.55652	125.579	-4937488	-726698	地図	1.8E-10	1.08E-09	-12.8311501	○		9.76084	0.383642075	○
2015/5/13 9:38:42	-8.55652	125.579	-4937488	-726698	地図	1.8E-10	1.26E-09	-12.78674537	○		9.766366	0.349702399	○
2015/5/13 9:38:43	-8.55652	125.579	-4937488	-726698	地図	1.8E-10	1.44E-09	-12.69275586	×		9.756204	0.642628799	○
2015/5/13 9:38:44	-8.55652	125.579	-4937488	-726698	地図	1.8E-10	1.62E-09	-12.66133336	○		9.774447	0.357976721	○
2015/5/13 9:38:45	-8.55652	125.579	-4937488	-726698	地図	1.8E-10	1.8E-09	-12.60151351	○		9.780256	0.349523589	○
2015/5/13 9:38:46	-8.55652	125.579	-4937488	-726699	地図	0.845386	0.845386	-12.21586745	△		9.804959	0.493905926	○
2015/5/13 9:38:47	-8.55652	125.579	-4937488	-726699	地図	0.106191	0.951577	-11.53450111	×		9.821707	0.643425627	○
2015/5/13 9:38:48	-8.55653	125.579	-4937488	-726700	地図	0.871521	1.823098	-11.41005554	×		9.811538	0.731937321	△
2015/5/13 9:38:49	-8.55653	125.5789	-4937488	-726702	地図	2.544805	4.367903	-11.57819365	×		9.798709	0.87266775	△
2015/5/13 9:38:50	-8.55653	125.5789	-4937488	-726705	地図	2.544925	6.912827	-11.59939091	×		9.806535	0.815876303	△
2015/5/13 9:38:51	-8.55653	125.5789	-4937489	-726707	地図	2.555854	9.468681	-11.61403045	×		9.790099	0.724866878	△
2015/5/13 9:38:52	-8.55654	125.5789	-4937489	-726711	地図	3.396176	12.86486	-11.81704374	△		9.789932	0.566167683	○
2015/5/13 9:38:53	-8.55654	125.5788	-4937490	-726715	地図	4.238579	17.10344	-12.07585332	△		9.781413	0.554497024	○
2015/5/13 9:38:54	-8.55654	125.5788	-4937490	-726719	地図	4.238579	21.34202	-12.18002829	×		9.844116	0.652649982	○
2015/5/13 9:38:55	-8.55654	125.5788	-4937490	-726724	地図	5.081973	26.42399	-12.10744228	×		9.767702	1.062019582	△
2015/5/13 9:38:56	-8.55655	125.5787	-4937491	-726730	地図	5.925714	32.3497	-12.50891841	△		9.882396	0.502547031	○
2015/5/13 9:38:57	-8.55655	125.5786	-4937491	-726736	地図	5.925825	38.27553	-11.95982021	×		9.790152	0.700601242	△
2015/5/13 9:38:58	-8.55655	125.5786	-4937492	-726743	地図	6.775858	45.05138	-11.9595101	△		9.831685	0.555440249	○
2015/5/13 9:38:59	-8.55656	125.5785	-4937492	-726750	地図	7.626415	52.6778	-11.97283511	×		9.80172	0.650536003	○
2015/5/13 9:39:00	-8.55657	125.5784	-4937493	-726759	地図	8.485803	61.1636	-11.86189786	×		9.739823	0.914276356	△
2015/5/13 9:39:01	-8.55657	125.5784	-4937494	-726766	地図	7.681509	68.84511	-12.14703612	×		9.79478	0.921112067	△
2015/5/13 9:39:02	-8.55659	125.5783	-4937496	-726776	地図	9.371631	78.21674	-12.33087979	×		9.786565	0.655448561	○
2015/5/13 9:39:03	-8.5566	125.5782	-4937497	-726784	地図	8.565114	86.78186	-12.55208111	△		9.80505	0.562006388	○
2015/5/13 9:39:04	-8.55661	125.5781	-4937499	-726793	地図	9.416492	96.19835	-12.33565631	△		9.754033	0.5077247	○
2015/5/13 9:39:05	-8.55662	125.578	-4937501	-726802	地図	8.582866	104.7812	-12.52860175	△		9.755717	0.563241303	○
2015/5/13 9:39:06	-8.55664	125.578	-4937502	-726811	地図	9.433836	114.2151	-12.47858504	×		9.774732	0.655902668	○
2015/5/13 9:39:07	-8.55665	125.5779	-4937504	-726820	地図	9.416605	123.6317	-12.4889252	△		9.765231	0.589245	○
2015/5/13 9:39:08	-8.55667	125.5778	-4937506	-726830	地図	9.416515	133.0482	-12.15836094	△		9.798956	0.543859687	○
2015/5/13 9:39:09	-8.55668	125.5777	-4937507	-726838	地図	8.548653	141.5968	-12.3214707	○		9.694976	0.397876912	○
2015/5/13 9:39:10	-8.55669	125.5776	-4937509	-726846	地図	8.565104	150.1619	-12.62738381	△		9.738771	0.450777043	○
2015/5/13 9:39:11	-8.5567	125.5776	-4937510	-726856	地図	9.371532	159.5335	-12.77876843	×		9.750595	0.63757966	○
2015/5/13 9:39:12	-8.55671	125.5775	-4937511	-726863	地図	7.681645	167.2151	-12.74237816	△		9.725966	0.55213003	○

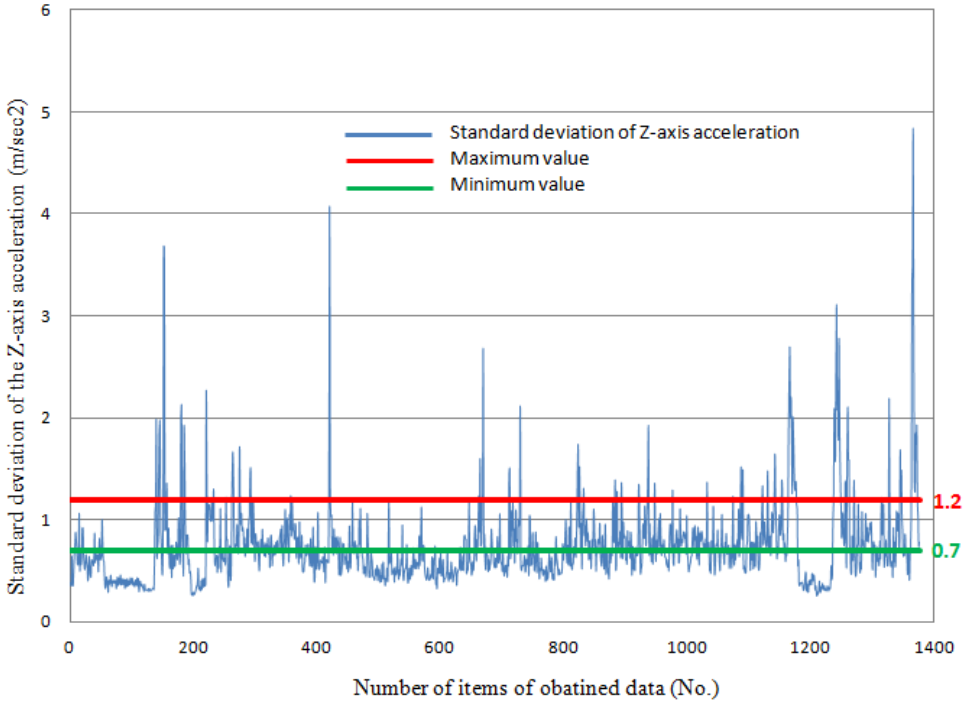

Fig. 7. Thresholds assumed for Timor-Leste

3.4. Determination of Evaluation Signal Using a Motion Sensor

The determination of the evaluation signal was made by choosing a target route and conducting measurements to understand the degree of change in the sensor data before and after pavement repair work. The measurement was performed four times. Two measurements were performed in April and May 2010 to determine the road condition before the pavement repair, and the other two were conducted in August 2010 and January 2011 to determine the condition after the pavement repair.

The evaluation signal consists of two standard deviations, sound data, and acceleration data. It is obtained by analyzing the relationship between the standard deviation and the sound data for the road surface. The sound data was obtained by running a sound test in the test car. The movement of the car along the road resulted in road noise in a frequency band of 20 to 20,000 Hz. The frequency band of the road noise produced when traveling over a road surface with irregular roughness was around 10 to 1000 Hz. Therefore, to analyze the frequency band representing the condition of the road surface, the sound data at 10,000 Hz was divided using a sound band-pass filter (BPF). Figure 8 shows how the band was partitioned into three ranges: 50 to 150 Hz, 150 to 250 Hz, and 200 to 300 Hz. The data in the 50 to 150 Hz and 200 to 300 Hz bands are not suitable for use as sound evaluation signals (Miyamoto et al., 2013). However, the sound data for the 150 to 250 Hz band is suitable for use as an evaluation signal because it is clearly discernible, despite having different values before and after the pavement repair work (Hugo et al., 2014).

Meanwhile, the evaluation signal for the acceleration data was also obtained. Figure 9 shows the standard deviation of the acceleration using three-axis vehicle vibration data. It illustrates that the X and Y-axis accelerations are not suitable for use as an evaluation signal. However, the Z-axis acceleration is suitable for use as an evaluation signal because it is clearly discernible despite having different values before and after the pavement repair work.

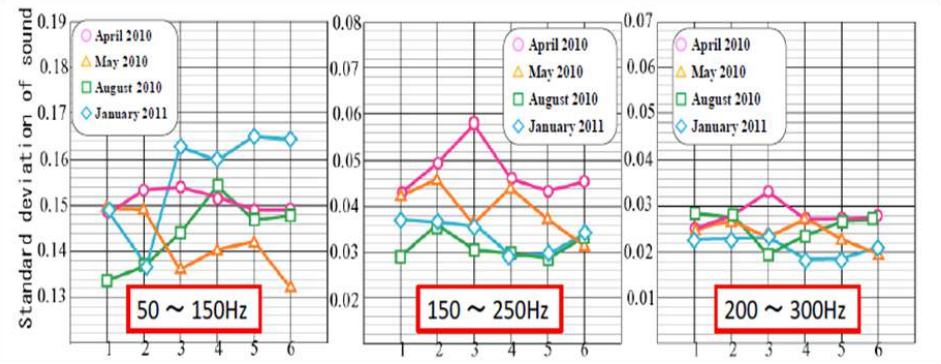

Fig. 8. Standard deviation of sound of running vehicle for various frequencies

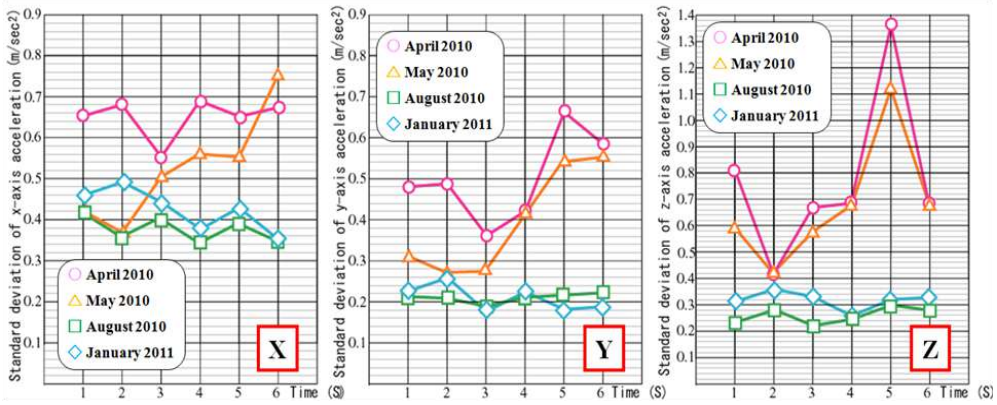

Fig. 9. Standard deviation of the acceleration obtained from vehicle vibration data

3.5. Determination of Dependent Velocity of the System

The dependent velocity of the system was determined by evaluating the velocity change of a vehicle while in motion to determine the influence on the evaluation signal. The study was conducted on a public road by using a vehicle to drive over concrete blocks placed in front of both front wheels, as shown in Figure 10. This examination was performed to obtain the data for the pavement surface by changing the velocity of the vehicle. Starting with a velocity of 5 km/h, the velocity range for the examination was 20 to 50 km/h over a distance of 30 m (Hugo et al., 2014). Figure 11 shows the result of the examination; it shows the relationship between the velocity and the standard deviation of the Z-axis acceleration in the evaluation signal. The data illustrates that the standard deviation increases with the velocity of the vehicle. Therefore, the regression equation and correlation coefficient were derived from the relationship between the evaluation signal and the velocity, defined as follows (Miyamoto et al., 2013).

$$y = 0.0061x + 0.00937 \quad (1)$$

where y: is the standard deviation of the Z-axis acceleration (m/s^2), and x: is the vehicle velocity (km/h). Eq. (1) is used as a speed correlation formula for outputting the evaluation result of a road pavement surface.

Fig. 10. Set-up in measurement vehicle

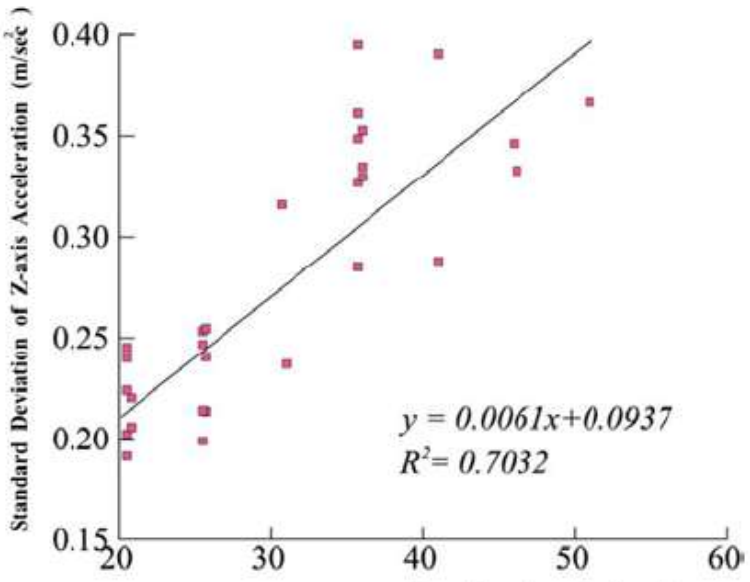

Fig. 11. Relationship between velocity and standard deviation of Z-axis acceleration

4. Practical Application of System to Road Networks

4.1. Road Conditions in Timor-Leste

Timor-Leste is one of the least developed countries in Southeast Asia. Its nonoil economy is characterized by slow and unstable growth, even though there has recently been recent strong growth in urban centers, particularly in the capital city. The economy is essentially agriculture-based, with about 72% of the total population of 1.1 million living in rural areas. Subsistence farming is the main livelihood of a large majority of the rural people, with limited production of agricultural products, mostly coffee, for cash income. The Asian Development Bank (ADB) has announced that agricultural productivity in Timor-Leste is low compared with other countries in the region (ADB Timor-Leste, 2013).

Roads constitute the primary mode of transport in Timor-Leste, carrying 70% of all freight and 90% of passengers. The road network was constructed to the Indonesian pavement standard of 4.5 m wide, with a lined masonry drain. The road networks also consist of a national road that links the districts together, district roads that link the district centers to the sub districts, and rural roads that provide access to the villages and the more remote areas. Overall, however, the road networks are in a poor condition due to the limited budget and resulting lack of maintenance. The ADB study affirmed that, due to the poor condition of the rural roads, rural people face increased travel times and transportation costs and are isolated in terms of access to social and economic facilities and services, such as local markets, schools, health facilities, job opportunities, government services, and banking services (ADB of Timor-Leste, 2013).

4.2. Application of Road Condition Assessment System to Road Networks in Japan and Timor-Leste

The Ippo-Campo system was designed for application to road surface pavement maintenance. The system was designed for Japan's roads, where it has established itself as a capable IT-based system. The use of an IT-based system makes it easier to obtain output results effectively and efficiently within the limited budget for the present condition of a road. Therefore, it was assumed that the system can be applied in other countries as well, especially developing countries. In this study, we applied the system to a few actual road networks for evaluating the effectiveness and workability of the system. To that end, we conducted measurements in two countries, namely, Japan and Timor-Leste. In Japan, the assessment of the road pavement was conducted for the road networks of Mine City in Yamaguchi Prefecture, as shown in Figure 12a (Miyamoto, 2019).

4.2.1. Target Road Route in Mine-City, Japan and Application of the System

The assessment of the road pavement condition was conducted in the road network in the Mine City (Yamaguchi Pref., Japan) jurisdiction, under the responsibility of the "Ube Civil Engineering Mine branch office". As shown in Figure 12b, the target roads are also located in Mine City, and the total distance of the measured road is 8,050 m. Table 3 lists the details of the road (line) names, types of road and the distance of each target road route. The reason for conducting the field test in Mine City is that the Yamaguchi Prefectural Government was carrying out repair work on the road pavement in this location. The measurement was performed in two ways. First, the "Ube Civil Engineering Mine branch office" conducted a road evaluation by using a patrol car. The objective was to collect information on the depth of ruts with a maximum volume of more than 40 mm^3. Second, measurements were conducted by using Ippo-Campo.

4.2.2. Measurement Details

In this study, the road measurement data was obtained using a sedan-type car. The

car was driven at a speed of 50-60 km/h, and the Mti-G configuration sampling rate was 100 Hz. The measurement was done with two recording methods: from the start point to the end point, and overturn. Measurements were taken before and after repairs to the road pavement. The objective of the measurement was to compare the results obtained under both conditions and to confirm the efficiency of the system. The confirmation evaluation result of the output data used GPS data, movie data and road register data. Measurements were taken at one-second intervals. As shown in Table 4, the system recorded the condition of the road every second and recorded the time (Japan System Time (JST)). In this practical application, there are some important matters that must be excluded to prevent a decrease in efficiency of data measurement, such as a small sample number (less than 4 points), expansion joints on bridges, railways, tunnels and traffic jams, because these would cause incorrect evaluation.

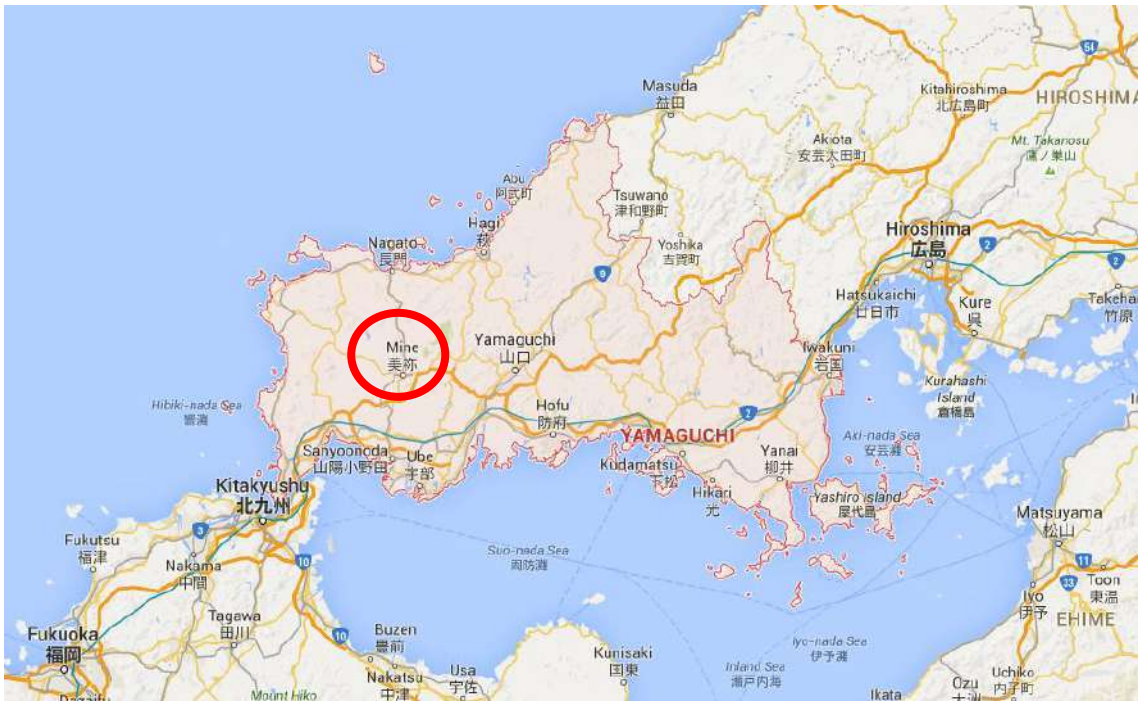

(a)

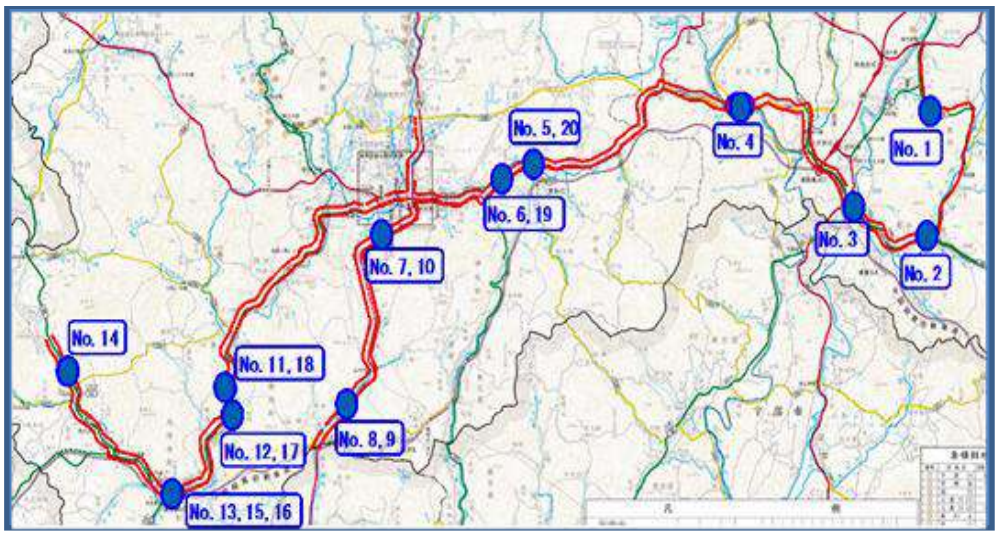

(b)

Fig. 12. a) Location of Mine City, Yamaguchi Prefecture, Japan; and b) Detailed map information and numbering of the target road route

Table 3. Detailed information about the target road route

No.	Type of road	Road (line) No.	Road (line) name	Length (m)
1	Prefecture road	28	Ogouri Misumi line	350
2	Prefecture road	31	Mito line	400
3	Prefecture road	31	Mito line	550
4	Prefecture road	240	Yunoguchi Mine line	700
5	National road	435	435 line	600
6	National road	435	435 line	200
7	National road	316	316 line	650
8	National road	316	317 line	350
9	National road	316	318 line	350
10	National road	316	319 line	650
11	Prefecture road	33	Shimonoseki Mine line	300
12	Prefecture road	33	Shimonoseki Mine line	350
13	Prefecture road	33	Shimonoseki Mine line	400
14	Prefecture road	65	Sanyou Toyota line	200
15	Prefecture road	33	Shimonoseki Mine line	400
16	Prefecture road	33	Shimonoseki Mine line	150
17	Prefecture road	33	Shimonoseki Mine line	350
18	Prefecture road	33	Shimonoseki Mine line	300
19	National road	435	435 line	200
20	National road	435	435 line	600

4.2.3. Results and Discussion

The data verification results in Table 4 show an example of a road repair point. The highlighted sign indicates the repair interval and the output result obtained by using Ippo-Campo. It also illustrates the condition before and after repair. The upper part of the table shows how bad the road condition was before repair, which is dominated by × symbols. However, the bottom part of the table shows the road condition after repair, which is dominated by ○ symbols, signifying that the road was in good condition. The total number of road pavement repair points was 57, which excluded 23 points where the number of samples was less than 4. Two data processing methods were used: calculating the standard deviation of the Z-axis acceleration, and combining the Z-axis acceleration with the sound data.

Table 5 shows the remaining samples that had more than 4 samples and the result of comparing the road pavement conditions before and after repairs. The results show that the comparison percentage between the number of bad points and the total number of samples for the condition before repair is considerably higher than the percentage after repair. It was also found that there are five missing samples (sample No. 4, 8, 9, 24 and 32) where the percentage of bad points did not change because the rut depth was bigger than the width of the wheel path.

4.2.4. Application to Timor-Leste Road Networks

First, the measurements described above were conducted in Mine City road networks because the Yamaguchi Prefectural authorities repaired the road pavement. It was thought that this road network would be representative of the road network of a developed country. On the other hand, the road network in Timor-Leste was assumed to be representative of a road network of a developing country. The roads in Timor-Leste are not in a good condition; therefore, the road used for comparison was divided into only two categories, namely, “VERY GOOD” and “VERY BAD”. The purpose of this activity was to identify differences in the road conditions for different levels of service in both countries by comparing road condition data obtained using the Ippo-Campo system. The research was conducted under the supervision of Yamaguchi University in cooperation with the teaching staff of the Dept. of Civil Engineering of Universidade Nasional Timor Lorosa’e (UNTL). UNTL is the only public university in Timor-Leste that partners with

the government to provide human resources for contributing to the development of the country. Therefore, the assessment process for the research, including the determination of the target routes, was decided based on the priority target line set by the government of Timor-Leste, for the development and improvement of well-connected and coherent road networks and other key infrastructures (Government of Timor-Leste, 2011).

Table 4. Verification results of pavement condition before and after repairs

JST	Cumulative distance	Repair interval	Z-axis acc.	Velocity of the car	Judgement using Z-axis acc.	Judgement using Z-axis acc. and sound data
Before repair						
2013/2/23 9.26.03					×	×
2013/2/23 9.26.04					×	×
2013/2/23 9.26.05	0.0		0.343	52.8	×	×
2013/2/23 9.26.06	14.7		1.222	52.8	×	×
2013/2/23 9.26.07	29.3		0.203	52.8	×	×
2013/2/23 9.26.08	43.8		0.362	52.8	×	×
2013/2/23 9.26.09	58.4		0.972	52.8	×	×
2013/2/23 9.26.10	73.1		0.347	52.8	○	×
2013/2/23 9.26.11	87.8		0.376	52.0	○	○
2013/2/23 9.26.12	102.2		0.266	51.8	○	○
2013/2/23 9.26.13	116.6	1	0.243	51.8	○	○
2013/2/23 9.26.14	131.0		0.306	54.3	○	○
2013/2/23 9.26.15	146.6		0.246	52.0	○	○
2013/2/23 9.26.16	160.5		0.223	53.6	○	○
2013/2/23 9.26.17	175.4		0.239	52.8	○	○
2013/2/23 9.26.18	190.0		0.285	53.6	○	○
2013/2/23 9.26.19	204.9		0.247	52.0	○	×
2013/2/23 9.26.20	219.4		0.204	53.3	○	☆
2013/2/23 9.26.21	234.2		0.202	53.6	○	☆
2013/2/23 9.26.22					△	△
2013/2/23 9.26.23					○	○
After repair						
2013/11/16 10.20.23					○	○
2013/11/16 10.20.24					○	○
2013/11/16 10.20.25	0.0		0.267	32.1	○	○
2013/11/16 10.20.26	8.9		0.267	32.1	○	○
2013/11/16 10.20.27	17.8		0.250	32.4	○	○
2013/11/16 10.20.28	26.8		0.324	37.9	○	○
2013/11/16 10.20.29	37.4		0.210	36.9	○	○
2013/11/16 10.20.30	47.6		0.308	40.9	○	○
2013/11/16 10.20.31	59.0		0.231	39.9	○	○
2013/11/16 10.20.32	70.1		0.243	43	○	○
2013/11/16 10.20.33	82.0	1	0.224	41.4	○	○
2013/11/16 10.20.34	93.5		0.208	43	○	○
2013/11/16 10.20.35	105.4		0.224	44.5	○	○
2013/11/16 10.20.36	117.8		0.283	44.5	○	○
2013/11/16 10.20.37	130.1		0.215	46	○	○
2013/11/16 10.20.38	142.9		0.200	46	○	○
2013/11/16 10.20.39	155.7		0.207	48.3	○	○
2013/11/16 10.20.40	169.1		0.206	46	○	○
2013/11/16 10.20.41	181.9		0.200	47.5	○	○
2013/11/16 10.20.42	195.1		0.193	48.7	○	○
2013/11/16 10.20.43	208.6		0.204	45.7	○	○
2013/11/16 10.20.44					△	△
2013/11/16 10.20.45					×	×

Table 5. Comparison between before and after pavement repair using acceleration and wheel sound

No	Type of road	Line No.	Line name	Length	Before repair				After repair			Validity
					number of sample (S)	X ☆△ (B)	B/S (%)	B/S < 50%	number of sample (S)	X ☆△ (B)	B/S(%)	
1				200	17	9	53		19	0	0	
2	Prefecture	28	Ogouri misumi line	310	23	16	70		25	4	16	
3	Prefecture	31	Mito line	480	39	32	82		36	3	8	
4	Prefecture	31	Mito line	450	31	4	13	!	32	2	6	
5	National	435	435 line	270	21	16	76		20	0	0	
6	National	316	316 line	580	41	39	95		41	2	5	
7	National	316	316 line	420	27	23	85		28	4	14	
8				170	16	7	44	!	14	0	0	
9				80	7	2	29	!	6	1	17	
10	National	316	316 line	270	17	17	100		21	1	5	
11	National	316	316 line	600	37	37	100		31	2	6	
12	Prefecture	33	Shimonoseki Mine line	320	23	16	70		23	5	22	
13	Prefecture	33	Shimonoseki Mine line	200	14	14	100		12	3	25	
14				150	11	11	100		11	0	0	
15	Prefecture			150	10	6	60		11	2	18	
16		65	Sanyou Toyota line	440	30	19	63		26	4	15	
17				420	29	20	69		25	8	32	
18				140	11	9	82		9	1	11	
19				120	10	8	80		9	2	22	
20	Prefecture	33	Shimonoseki Mine line	100	7	7	100		8	1	13	
21	Prefecture	33	Shimonoseki Mine line	170	10	10	100		12	2	17	
22	Prefecture	33	Shimonoseki Mine line	180	13	7	54		12	5	42	
23	Prefecture	33	Shimonoseki Mine line	320	22	12	55		21	3	14	
24	Prefecture	33	Shimonoseki Mine line	80	9	4	44	!	5	1	20	
25				160	12	6	50		12	1	8	
26				150	10	10	100		11	3	27	
27				160	12	12	100		12	5	42	
28				230	15	11	73		15	6	40	
29	National	435	435 line	290	21	19	90		20	7	35	
30	National	435	435 line	520	38	38	100		45	18	40	
31				590	37	37	100		37	8	22	
32				250	17	5	29	!	16	3	19	
33				230	15	10	67		16	2	13	
34				250	15	9	60		61	6	10	

Figure 13 shows the target routes for the research. Table 6 lists the road routes and the corresponding distances, which together give a total distance of 740.3 km, and which are regarded as national priority roads connecting the capital city to the district cities of Timor-Leste.

Table 7 summarizes the results of evaluating the road conditions of the "GOOD" condition roads. The comparison used the Japanese and Timor-Leste thresholds as shown in Figures 5 and 7 (Miyamoto et al., 2013; Hugo et al., 2014). The length of the selected road for both conditions was 16 km. The result of the comparison clearly produced a different analysis result when using the proposed system. It can be seen that the use of the Japanese threshold for the selected road resulted in 12.02% being judged as being "GOOD", 34.05% as being "MODERATE", and 53.93% as being "BAD". On the other hand, the results of the evaluation changed significantly after applying the Timor-Leste threshold. This resulted in 55.95% being judged as being "GOOD" and 26.71% being "MODERATE", while the ratio of "BAD"

fell to 17.35%.

The road conditions for a "BAD" condition road in Timor-Leste where evaluated, as shown in Table 8. When using the Japanese thresholds, the results show that the road was in a very bad condition. Only 0.08% of the road surface was found to be in "GOOD" condition, 4.10% was in "MODERATE" condition, and 95.82% was in "BAD" condition. At the same time, the evaluation result did not change even when the Timor-Leste threshold was used. A "GOOD" result was obtained for only 6.84% of the roads, while "MODERATE" was assigned to 41.35% and "BAD to 51.81%.

Figure 14 shows the results of evaluating a "GOOD" road in Timor-Leste. It can be seen that the use of both thresholds gives detailed information on the actual condition of this road. The threshold values play an important role in defining the standard deviation of the Z-axis evaluation (see Figures 1 and 2). This figure is just a small part of the road section. The selection of the interval uses a critical value obtained by calculating the statistical regression every second. For Japanese thresholds, this indicates that the condition is overwhelmingly" MODERATE".

Table 6. Comprehensive evaluation of road attributes for Timor-Leste road networks

	Strength	Durability	Safety	Workability	Maintenance	Comprehensive evaluation
Retaining wall	0.4814	0.4034	0.1348	0.5338	0.3428	0.3831
Drainage	0.1207	0.3512	0.0857	0.2381	0.3305	0.2179
Culverts	0.0663	0.1243	0.0509	0.1224	0.1424	0.0987
Debris and land slide removal	0.0983	0.0729	0.2818	0.0614	0.1105	0.1103
Tree and grass cutting	0.2334	0.0481	0.4467	0.0443	0.0738	0.1666
Sum	1.0	1.0	1.0	1.0	1.0	1.0

Fig. 13. Timor-Leste road network and routes targeted by the study

Table 7. Evaluation results for GOOD condition road in Timor-Leste using both thresholds

Thresholds	Evaluation results (%)			
	GOOD	MODERATE	BAD	Total
Japanese	12.02	34.05	53.93	100
Timor-Leste	55.95	26.71	17.35	100

Table 8. Evaluation results for BAD condition road in Timor-Leste using both thresholds

Thresholds	Evaluation results (%)			
	GOOD	MODERATE	BAD	Total
Japanese	0.08	4.1	95.82	100
Timor-Leste	6.84	41.35	51.81	100

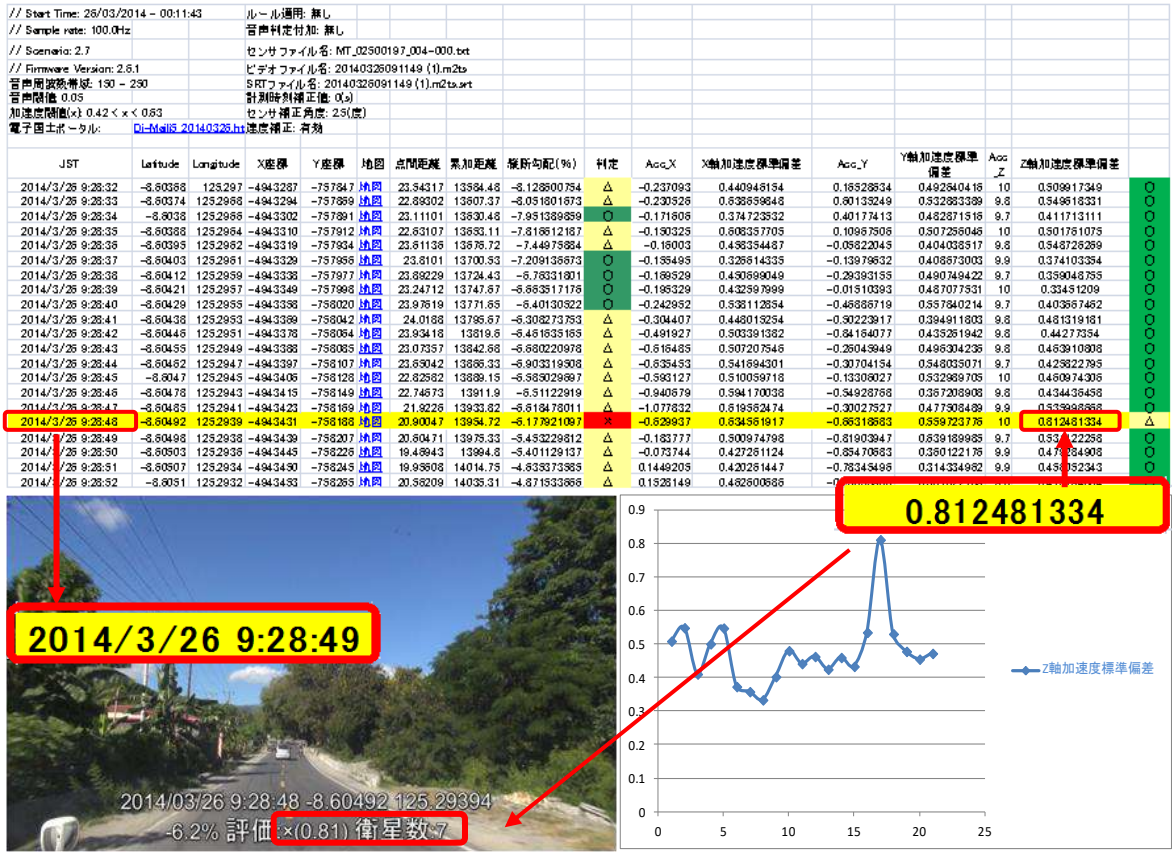

Fig. 14. Evaluation result for GOOD Timor-Leste road, obtained using Ippo-Campo

Only a few items of data indicate the "GOOD" condition, and only one item of data corresponds to the "BAD" condition. However, this condition changes significantly after using the Timor-Leste threshold. Most condition changes are from "MODERATE" to "GOOD". It can be seen that the maximum value of the Z-axis acceleration occurs at 0.812. The evaluation results can also be seen in the video data and Excel data, together with the time information and the status of the condition of the road.

Figure 15 shows an example of an evaluation result for a "BAD" condition road. It can be seen that the use of thresholds plays an important role in making a judgment as to the actual condition of the road.

Using the Japanese threshold, the result shows that the road is in a very bad condition, relative to a rural road in Japan. Only two items of data indicate the "MODERATE" condition and none indicate that the road is in the "GOOD" condition. However, the condition changes slightly after using the Timor-Leste threshold, even if the condition is still dominated by the red color of the bad condition. It can be seen that the critical value reaches a maximum at 5.111, as shown in the Excel data and the video data.

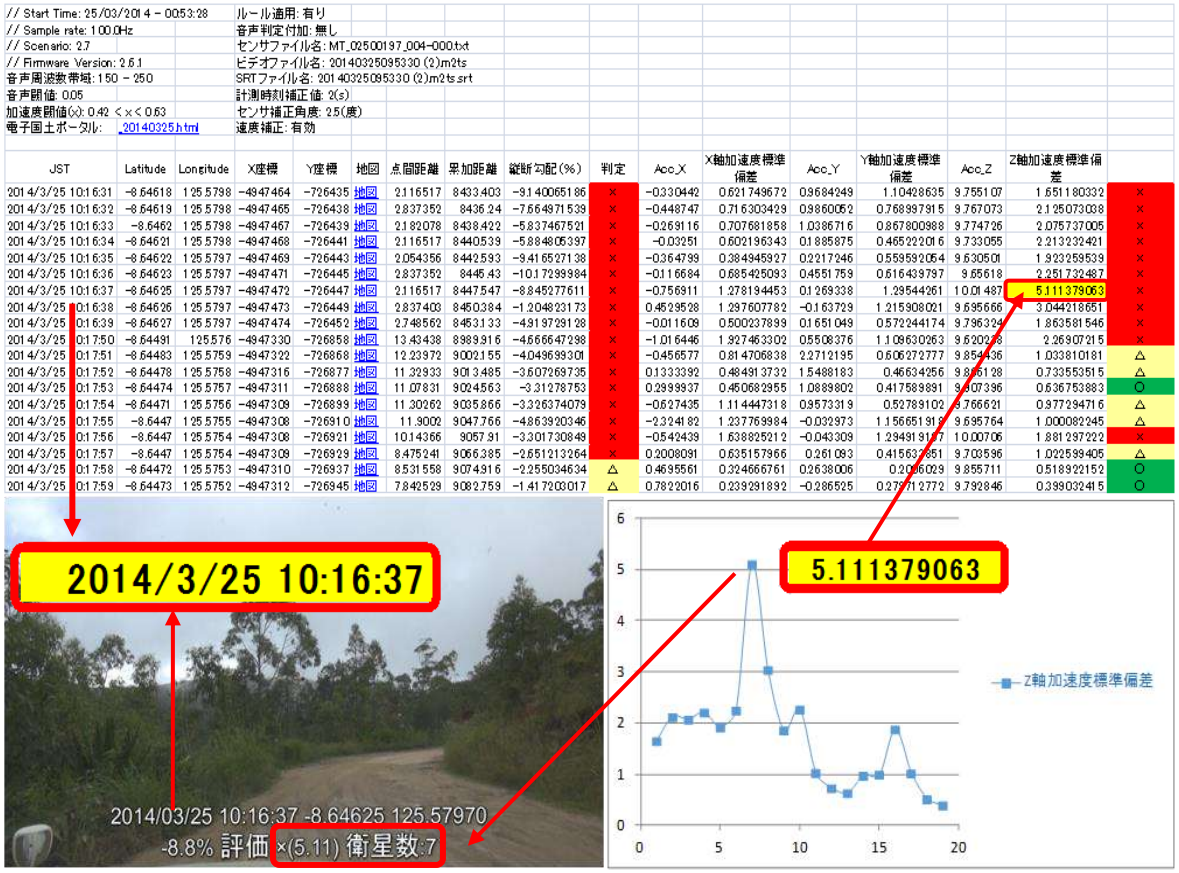

Fig. 15. Evaluation result for BAD Timor-Leste road, obtained using Ippo-Campo

The results of the pavement evaluation conditions in Timor-Leste for both the "GOOD" and "BAD" conditions can be summarized as follows: For the "GOOD" condition roads, the state of the pavement is regarded as being in a "GOOD" condition, as no serious damage is identified. The rate of cracking, the rut depth, and the smoothness are all less than certain values. However, dissimilar results for the evaluation of the "BAD" roads were obtained. It was shown that the road conditions are very poor and actually dangerous, requiring immediate repair work. The damage to this road is not only on the pavement surface, but to the actual road structure also. This situation tends to arise in all Timor-Leste road networks because no rational maintenance work had been carried out. Water overflows and forms puddles on the surface, given the bad state of the road. This applies not only to the surface of the road but also to its entire structure, including the road facilities, such as drainage and walls.

In addition, the condition of the roads in Japan is very different from that existing in Timor-Leste; this can be seen in Figure 16. It can clearly be seen from the results of the evaluation done using Ippo-Campo that 69.4% of the roads are in "GOOD" condition, 22.3% are in "MODERATE" condition, and only 8.3% are in "BAD" condition. It is notable that the maximum value of the standard deviation of the Z-axis acceleration is 0.971.

Therefore, the results of the analysis imply that even roads in Japan's rural areas are of better quality and are better maintained then the main roads in Timor-Leste, as the road construction and maintenance system in Japan involves highly advanced technology and a well-organized association of road managers. Furthermore, the cooperation between the government and university researchers in order to develop maintenance systems for evaluating the condition of the road pavement is well organized.

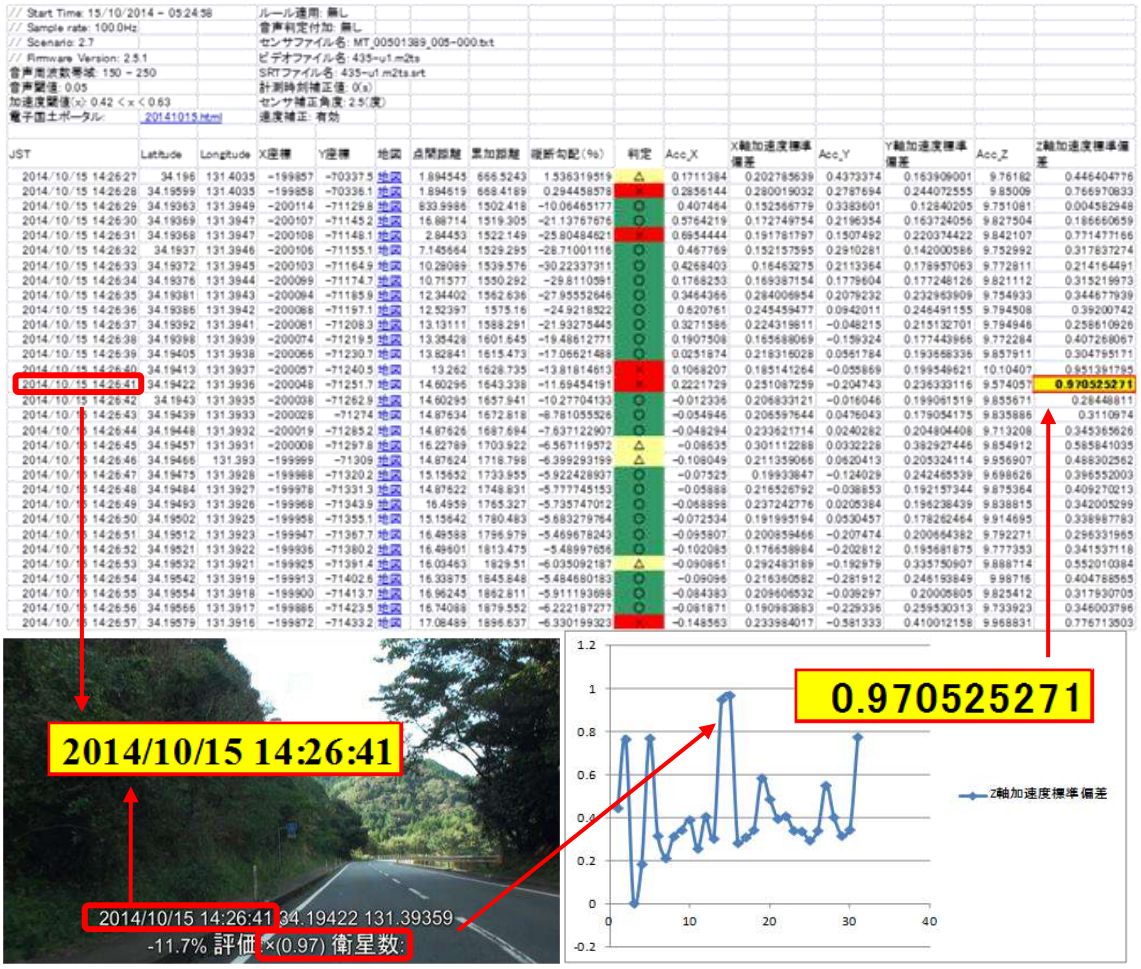

Fig. 16. Japanese road condition evaluation using Ippo-Campo system

4.3. Use of the System to Analyze Road Pavement Conditions in Timor-Leste

The analysis of the road pavement conditions in Timor-Leste was based on data obtained by the measurements at the location shown in Figure 13. The measurement was divided into four sessions due to the limited budget, as shown in Table 9. The first measurement was conducted from March 25 to 27, 2014 and covered three routes, named route I (No. 1), route II (No. 2) and route III (No. 3). The only route examined in the second measurement was called route IV (No. 4), and was conducted from July 3 to 4, 2014. The third measurement was conducted from March 18 to 20, 2015, and covered two routes, named route V (No. 5) and route VI (No.6). Lastly, the fifth measurement was conducted from May 13 to 17, 2015, and covered three routes, named route VII (No. 7), route VIII (No. 8) and route IX (No. 9).

Table 10 compares the application of both thresholds to all the routes of the Timor-Leste road network. Table 11 lists the results of evaluating the road conditions in Timor-Leste when using the Ippo-Campo system. The measurement produced different data for each route. Route I (No. 1) obtained data for a total of 17,151 points. By using the Japanese threshold, only 0.28% or 48 points were classed as being "GOOD", 5.14% or 881 points were classed as "MODERATE", and most of them, at 94.58% or 16,222 points, were "BAD". This data confirmed that the road pavement is in a very poor condition. Conversely, the results obtained using the Timor-Leste threshold change slightly to 1,563 points, or 9.11%, for the "GOOD" condition while there is a slight increase to 7,021 points, or 40.94%, for the "MODERATE" condition but a significant decrease to 8,567 points, or 49.95%, for the "BAD" condition. As a

result, the comparative changes using both thresholds increase considerably to 8.83% for the "GOOD" condition, along with a notable increase for the "MODERATE" condition to 35.80%, while 44.63% represents the greatly decreased "BAD" condition.

The results obtained for Route II (No. 2) show that the road pavement is in a poor condition. From the total of 23,422 items of obtained data, the results using the Japanese threshold shows that 635 points, or 2.71%, are in "GOOD" condition, 3,802, or 16.23%, are in the "MODERATE" condition and 18,985 points, or 81.06%, are in the "BAD" condition. On the other hand, the data using the Timor-Leste threshold changes significantly for each condition. This shows that the "GOOD" condition increased slightly to 5,923 points, or 25.29%, the "MODERATE" condition increased considerably to 6,507 points, or 27.78%, and the "BAD" condition fell significantly to 10,992 points, or 49.95%. As a result, the comparative changes using both thresholds increase noticeably to 22.58% for the "GOOD" condition, and to 11.55% for the "MODERATE" condition, while the "BAD" condition is significantly reduced to 34.13%.

Table 9. MTi-G files and video files for all routes

No	Route number	MTi-G file name (MT_02500197_)	Video file's name	Roundtrip distance (km)
1	I	000-000.txt~015-000.txt	20140325085139.m2ts~20140325152336.m2ts	70×2
2	II	000-000.txt~028-000.txt	20140326081818.m2ts~20140326180224.m2ts	149×2
3	III	000-000.txt~018-000.txt	20140327080907.m2ts~20140327161637.m2ts	122×2
4	IV	017-000.txt~038-000.txt	20140704074541.m2ts~20140704171233.m2ts	67×2
5	V	000-000.txt~020-000.txt	20150318131917.m2ts~20150318202142.m2ts	81×2
6	VI	000-000.txt~009-000.txt	20150319103258.m2ts~20150320094041.m2ts	60.7×2
7	VII	000-000.txt~010-000.txt	20150513093841.m2ts~20150513143347.m2ts	59.6×2
8	VIII	000-000.txt~010-000.txt	20150514101000.m2ts~20150514145816.m2ts	42.5×2
9	IX	011-000.txt~040-000.txt	20150515080826.m2ts~20150516090539.m2ts	88.5×2

Table 10. Comparison using both thresholds for all routes

Route No.	Evaluation results							
	Japanese thresholds				Timor-Leste thresholds			
	GOOD	MODERATE	BAD	Total	GOOD	MODERATE	BAD	Total
I	48	881	16,222	17,151	1,563	7,021	8,567	17,151
II	635	3,802	18,985	23,422	5,923	6,507	10,992	23,422
III	94	1,955	16,743	18,792	3,533	9,324	5,935	18,792
IV	132	2,849	9,384	12,365	4,189	4,664	3,512	12,365
V	1,052	2,372	15,383	18,807	5,130	5,204	8,473	18,807
VI	154	459	12,574	13,187	973	2,705	9,509	13,187
VII	388	1,714	12,785	14,887	2,766	2,679	9,442	14,887
VIII	233	540	11,351	12,124	1,156	2,727	8,241	12,124
IX	394	426	18,846	19,666	1,221	3,611	14,834	19,666

Table 11. Evaluation result of road condition in Timor-Leste using Ippo-Campo system

Route No.	Percentages of each conditions (%) (Japanese thresholds)				Percentages of each conditions (%) (Timor-Leste thresholds)				Comparative changes using both thresholds (%)		
	GOOD	MODERATE	BAD	Total	GOOD	MODERATE	BAD	Total	GOOD	MODERATE	BAD
I	0.28	5.14	94.58	100	9.11	40.94	49.95	100	8.83	35.80	-44.63
II	2.71	16.23	81.06	100	25.29	27.78	46.93	100	22.58	11.55	-34.13
III	0.50	10.40	89.10	100	18.80	49.62	31.58	100	18.30	39.21	-57.51
IV	1.07	23.04	75.89	100	33.88	37.72	28.40	100	32.81	14.68	-47.49
V	5.59	12.61	81.79	100	27.28	27.67	45.05	100	21.68	15.06	-36.74
VI	1.17	3.48	95.35	100	7.38	20.51	72.11	100	6.21	17.03	-23.24
VII	2.61	11.51	85.88	100	18.58	18.00	63.42	100	15.97	6.48	-22.46
VIII	1.92	4.45	93.62	100	9.53	22.49	67.97	100	7.61	18.04	-25.65
IX	2.00	2.17	95.83	100	6.21	18.36	75.43	100	4.20	16.20	-20.40

For route III (No. 3), the result obtained using the Japanese thresholds shows that the road pavement surface is in a BAD condition. This was confirmed by the total evaluation result for the total obtained data. The obtained consisted of a total of 18,792 points divided into three conditions, specifically, 94 points, or 0.50%, corresponding to the "GOOD" condition, 1,955 points, or 10.40%, corresponding to the "MODERATE" condition, and about 16,743 points, or 89.10%, corresponding to the "BAD" condition. Conversely, the result using the Timor-Leste threshold exhibits a significantly high value for each condition. In particular, the "GOOD" condition increased to 3,533 points, or 18.30%, the "MODERATE" condition increased to 9,324 points, or 49.62%, while the "BAD" condition fell to 31.58%.

As a result, the comparative changes using both thresholds increased noticeably to 18.30% for the "GOOD" condition, and to 39.21% for "MODERATE" condition, but fell significantly to 57.51% for the "BAD" condition.

For route IV (No. 4), the result obtained using the Japanese threshold shows that the road pavement surface corresponds to the "BAD" condition. This measurement obtained a total of 12,236 data points: 132 points, or 1.07%, for the "GOOD" condition, 2,849 points, or 23.04%, for the "MODERATE" condition and 9,384 points, or 75.89%, for the "BAD" condition. However, the results obtained using the Timor-Leste threshold resulted in a significant value for each condition: 4,189 points, or 33.88% for the "GOOD" condition and 4,664 points, or 37.72%, for the "MODERATE" condition, while the "BAD" condition fell to 3,512 points, or 28.40%. As a result, comparative changes using both thresholds increase considerably to 32.81%, with the "MODERATE" condition increasing considerably to 14.68%, while there is a significant drop to 47.49% for the "BAD" condition.

For route V (No. 5), the result obtained using the Japanese threshold shows that the road pavement surface is in a poor condition. This measurement obtained a total of 18,807 data points: 1,052 points, or 5.59%, for the "GOOD" condition, 2,372 points, or 12.61%, for the "MODERATE" condition and 15,383 points, or 81.89%, for the "BAD" condition. However, the result obtained using the Timor-Leste threshold exhibited a significantly high value for each condition: 5,130 points or 27.28% of this road can be classed as "GOOD", and 5,204 points, or 27.62%, as "MODERATE", while those which can be classed as "BAD" fell to 8,473 points, or 45.05%. As a result, the comparative changes using both thresholds increased considerably to 21.68% for the "GOOD" condition, the "MODERATE" condition increases notably to 15.06%, while the "BAD" condition falls significantly to 36.74%.

For route VI (No. 6), the result obtained using the Japanese threshold shows that the road pavement surface is in a BAD condition. This measurement obtained a total of 13,187 data points: 154 points, or 1.17%, for the "GOOD" condition, 459 points, or 3.48%, for the "MODERATE" condition, and 12,574 points, or 95.35%, for the "BAD" condition. Conversely, the results obtained using the Timor-Leste threshold resulted in a significantly high value for each condition: the results showed that 973 points, or 7.38%, for this road are "GOOD", 2,705 points, or 20.51%, are "MODERATE", while the number of "BAD" points falls to 9,509 points, or 72.11%. As a result, the comparative changes using both thresholds increase slightly to 6.21% for the "GOOD" condition, the "MODERATE" condition increases considerably to 17.03%, while the "BAD" condition falls significantly to 23.24%.

For route VII (No. 7), the result obtained using the Japanese threshold shows that the road pavement surface is in a poor condition. This measurement produced a total of 14,887 data points: 388 points, or 2.61%, for the "GOOD" condition, 1,714 points, or 11.51%, for the "MODERATE"

condition, and 12,785 points, or 85.88%, for the "BAD" condition. Conversely, the result obtained using the Timor-Leste threshold resulted in a significant value for each condition. It showed a considerable increase to 2,766 points, or 18.58%, for the "GOOD" condition and 2,705 points, or 18%, for the "MODERATE" condition, while the number of points corresponding to the "BAD" fell to 9,509 points, or 63.42%. As a result, the comparative changes using both thresholds increased noticeably to 15.97% for the "GOOD" condition, the "MODERATE" condition increased slightly to 6.48% while the "BAD" condition fell considerably to 22.46%.

For route VIII (No. 8), the result obtained using the Japanese threshold shows that the road pavement surface is in a BAD condition. This measurement obtained a total of 12,124 data points: 233 points, or 1.92%, for the "GOOD" condition, 540 points, or 4.45%, for the "MODERATE" condition and 11,351 points, or 93.62%, for the "BAD" condition. However, the results obtained using the Timor-Leste threshold exhibited a significantly high value for each condition: 1,156 points, or 9.53%, on this road are "GOOD", 2,727 points, or 22.49%, are "MODERATE", while the "BAD" condition fell to 8,241 points, or 67.97%. As a result, the comparative changes using both thresholds increase slightly to 7.61% for the "GOOD" condition, while the "MODERATE" condition increased noticeably to 18.04%, and fell significantly to 25.65% for the "BAD" condition.

For route IX (No. 9), the result obtained using the Japanese threshold shows that the road pavement surface is in a poor condition. This measurement produced a total of 19,666 data points: 394 points, or 2%, for the "GOOD" condition, 426 points, or 2.17%, for the "MODERATE" condition and 18,846 points, or 95.83%, for the "BAD" condition. Conversely, the result obtained using the Timor-Leste threshold resulted in a significant value for each condition. In this case, there was a slight increase to 1,221 points, or 6.21%, that were "GOOD" and 3,611 points, or 18.36%, that were "MODERATE", while the "BAD" condition fell to 14,834 points, or 75.43%. As a result, the comparative changes using both thresholds increased slightly to 4.2% for the "GOOD" condition, while the "MODERATE" condition increased considerably to 16.20%, and the "BAD" condition fell noticeably to 20.40%.

5. Road Maintenance Decision-Making Based on Comprehensive Evaluation by AHP Model

5.1. Application of AHP to Video Data from Timor-Leste Road Networks

The analytic hierarchy process (AHP) is an effective tool for dealing with complex decision-making, and may help the decision maker to set priorities and make the best decision (Saaty, 1980; Behbahani et al., 2014). The AHP method is used to derive a ratio scale from paired comparisons. It also allows for some small inconsistencies in judgments.

The government of the Democratic Republic of Timor-Leste intends to rehabilitate or upgrade the national road networks in accordance with the development priorities of the National Strategic Development Plan. However, there are some problems due to budget limitations, the lack of well-organized engineers etc. Therefore, there is a need for an effective means of prioritization (Taherkhani and Tajdini, 2020). Figure 17 shows the comprehensive evaluation of video files from the Ippo-Campo system using the AHP to prioritize the attributes of roads in need of maintenance and improve the Timor-Leste road networks.

The goal is to prioritize the road attributes for maintenance and improvement work on Timor-Leste road networks. The selected criteria are strength, durability, safety, workability and maintenance, as shown in Figure 17. The alternatives are retaining walls, drainage, culverts, debris and landslide removal, and

tree and grass cutting (see Figure 17). In addition, these criteria and alternatives are used to form a comparison matrix for computing the normalized principal eigenvector, as shown in Table 12. The results can be seen in the following tables.

Table 12 shows the pairwise comparisons of the criteria. The scale ranged from 7 to 1/7 and was composed of criteria and five comparisons. The consistency ratio was smaller than 10%. Therefore, the given comparison numbers are acceptable. The weights for each criterion were found to be: strength 43.63%, durability 13.52%, safety 7.59%, workability 5.69% and maintenance 29.57%. Consequently, it can be assumed that the most important criterion as identified by the pairwise comparison of the criteria is strength, followed by maintenance, durability, safety and workability, as shown in Figure 18.

Tables 13-17 summarize the results of the pairwise comparison of the alternatives for each criteria. The comparison used a scale ranging from 9 to 1/9. The comparisons were computed by arranging the judgment values in the matrix. In this case, five comparisons were needed based on the number of criteria. The weighting values for each criterion were labelled strength, durability, safety, workability and maintenance. Based on the results, the alternatives were dominated by retaining wall followed by drainage, tree and grass cutting, debris and landslide removal, and culverts, as shown in Figure 19.

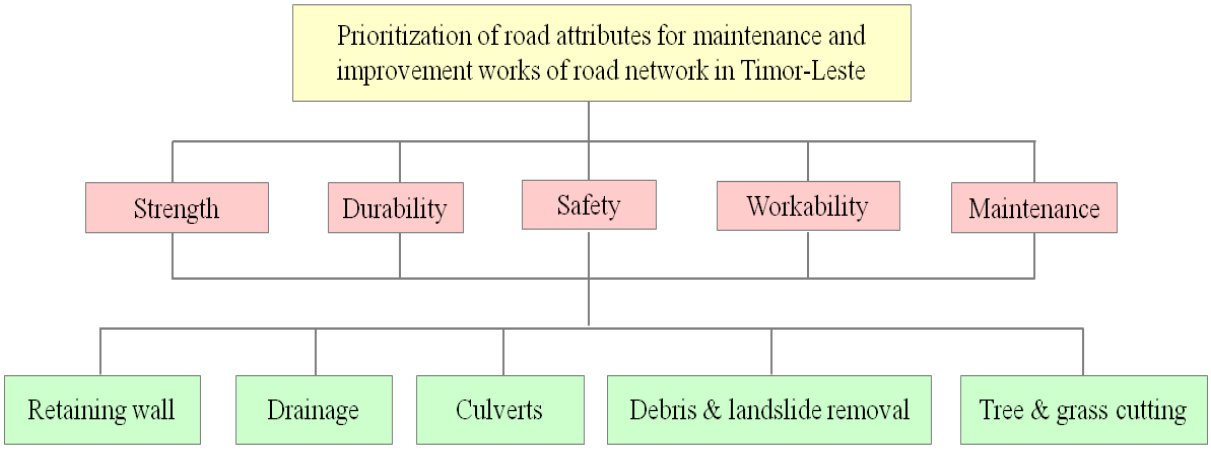

Fig. 17. AHP of Timor-Leste road networks

Table 12. Pairwise comparisons among criteria

L29D17:L28D17:L26	Strength	Durability	Safety	Workability	Maintenance	Geometric mean	Normalized	Weight
Strength	1	3	5	7	2	2.914	0.4363	0.4363
Durability	1/3	1	3	3	1/5	0.903	0.1352	0.1352
Safety	1/5	1/3	1	2	1/4	0.506	0.0759	0.0759
Workability	1/7	1/3	1/2	1	1/3	0.380	0.0569	0.0569
Maintenance	1/2	5	4	3	1	1.974	0.2957	0.2957
Sum	**2.18**	**9.67**	**13.50**	**16.00**	**3.78**	**6.68**	**1.00**	**1.00**
						Lambda (λ)-max	5.3100	
						CI	0.0775	
						CR	0.0692	< 10%

Table 13. Pairwise comparison of alternatives (strength)

	Retaining wall	**Drainage**	**Culverts**	**Debris and land slide removal**	**Tree and grass cutting**	**Geometric mean**	**Normalized**	**Weight**
Retaining wall	1	2	3	7	4	2.787	0.4814	0.4814
Drainage	1/2	1	4	1/4	1/3	0.699	0.1207	0.1207
Culverts	1/3	1/4	1	1/5	1/2	0.384	0.0663	0.0663
Debris and land slide removal	1/7	1/4	5	1	1/3	0.569	0.0983	0.0983
Tree and grass cutting	1/4	3	2	3	1	1.351	0.2334	0.2334
Sum	**2.23**	**6.50**	**15.00**	**11.45**	**6.17**	**5.79**	**1.00**	**1.00**
						Lambda(λ)-max	5.4150	
						CI	0.1037	
						CR	0.0926	< 10%

Table 14. Pairwise comparison of alternatives (durability)

	Retaining wall	**Drainage**	**Culverts**	**Debris and land slide removal**	**Tree and grass cutting**	**Geometric mean**	**Normalized**	**Weight**
Retaining wall	1	2	3	6	4	2.702	0.4034	0.4034
Drainage	1/3	1	6	6	6	2.352	0.3512	0.3512
Culverts	1/5	1/6	1	3	4	0.833	0.1243	0.1243
Debris and land slide removal	1/6	1/6	1/3	1	3	0.488	0.0729	0.0729
Tree and grass cutting	1/4	1/6	1/4	1/3	1	0.322	0.0481	0.0481
Sum	**1.95**	**3.50**	**10.58**	**16.33**	**18.00**	**6.70**	**1.00**	**1.00**
						Lambda (λ)-max	5.3886	
						CI	0.0972	
						CR	0.0867	< 10%

Table 15. Pairwise comparison of alternatives (safety)

	Retaining wall	**Drainage**	**Culverts**	**Debris and land slide removal**	**Tree and grass cutting**	**Geometric mean**	**Normalized**	**Weight**
Retaining wall	1	2	3	1/2	1/5	0.903	0.1348	0.1348
Drainage	1/2	1	2	1/4	1/4	0.574	0.0857	0.0857
Culverts	1/3	1/2	1	1/6	1/6	0.341	0.0509	0.0509
Debris and land slide removal	2	4	6	1	1/2	1.888	0.2818	0.2818
Tree and grass cutting	5	4	6	2	1	2.993	0.4467	0.4467
Sum	**8.83**	**11.50**	**18.00**	**3.92**	**2.12**	**6.70**	**1.00**	**1.00**
						Lambda (λ)-max	5.1428	
						CI	0.0357	
						CR	0.0319	< 10%

Table 16. Pairwise comparison of alternatives (workability)

	Retaining wall	Drainage	Culverts	Debris and land slide removal	Tree and grass cutting	Geometric mean	Normalized	Weight
Retaining wall	1	3	5	7	9	3.936	0.5338	0.5338
Drainage	1/3	1	2	5	5	1.755	0.2381	0.2381
Culverts	1/5	1/3	1	3	3	0.903	0.1224	0.1224
Debris and land slide removal	1/7	1/5	1/3	1	2	0.453	0.0614	0.0614
Tree and grass cutting	1/9	1/5	1/3	1/2	1	0.326	0.0443	0.0443
Sum	**1.79**	**4.73**	**8.67**	**16.50**	**20.00**	**7.37**	**1.00**	**1.00**
						Lambda (λ)-max	5.0407	
						CI	0.0102	
						CR	0.0091	< 10%

Table 17. Pairwise comparison of alternatives (maintenance)

	Retaining wall	Drainage	Culverts	Debris and land slide removal	Tree and grass cutting	Geometric mean	Normalized	Weight
Retaining wall	1	2	3	2	3	2.048	0.3428	0.3428
Drainage	1/2	1	3	4	5	1.974	0.3305	0.3305
Culverts	1/3	1/3	1	2	2	0.850	0.1424	0.1424
Debris and land slide removal	1/3	1/4	1/2	1	3	0.660	0.1105	0.1105
Tree and grass cutting	1/2	1/5	1/2	1/3	1	0.441	0.0738	0.0738
Sum	**2.67**	**3.78**	**8.00**	**9.33**	**14.00**	**5.97**	**1.00**	**1.00**
						Lambda (λ)-max	5.3680	
						CI	0.0920	
						CR	0.0821	< 10%

5.3. Analysis of Results and Discussions

The application of AHP to Timor-Leste road networks was conducted to study multi-criteria decision-making, particularly the prioritization of work with a limited budget. The comprehensive evaluation of Timor-Leste road network used five criteria: strength, durability, safety, workability and maintenance. However, the alternatives included retaining walls, drainage, culverts, debris and landslide removal and tree and grass cutting. The results of the comparisons were arranged in a matrix using the comparison ranging scale. The weighting percentages were obtained by computing the normalized principal eigenvector. The consistency ratio was checked in order to confirm that the complete results were consistent (CR < 10%). For example, in this case, the subjective evaluation for the Timor-Leste road networks was consistent. Therefore, the analysis of the road attributes in need of maintenance and improvement work resulted in the most preferred alternative of retaining wall with a 38.31% weighting, followed by drainage at 21.79%, tree and grass cutting at 16.66%, debris and landslide removal at 11.03%, and culverts at 9.87%, as shown in both Table 18 and Figure 20. According to these results, the application of the AHP method using the video file obtained from Ippo-Campo will help road administrators to establish

rational strategies for both maintenance and improvement of the road networks in Timor-Leste. In this study, the preferred target routes were defined by comparing the pairwise comparison among alternatives for each route. As a result, the most important route that gives an economic improvement to the development of Timor-Leste was identified as route III (No. 3), followed by route II (No. 2), route I (No. 1), route VII (No. 7), route V (No. 5), route IX (No. 9), route VI (No. 6), route IV (No. 4) and finally route VIII (No. 8).

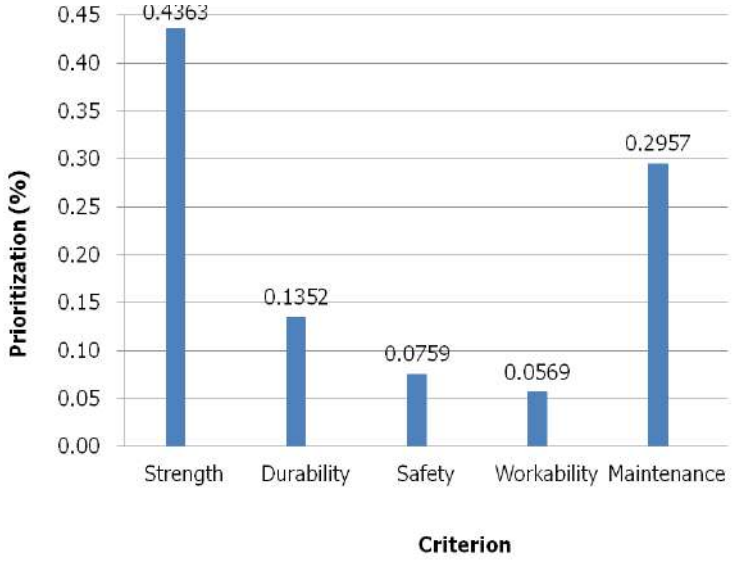

Fig. 18. Pairwise comparison of criteria

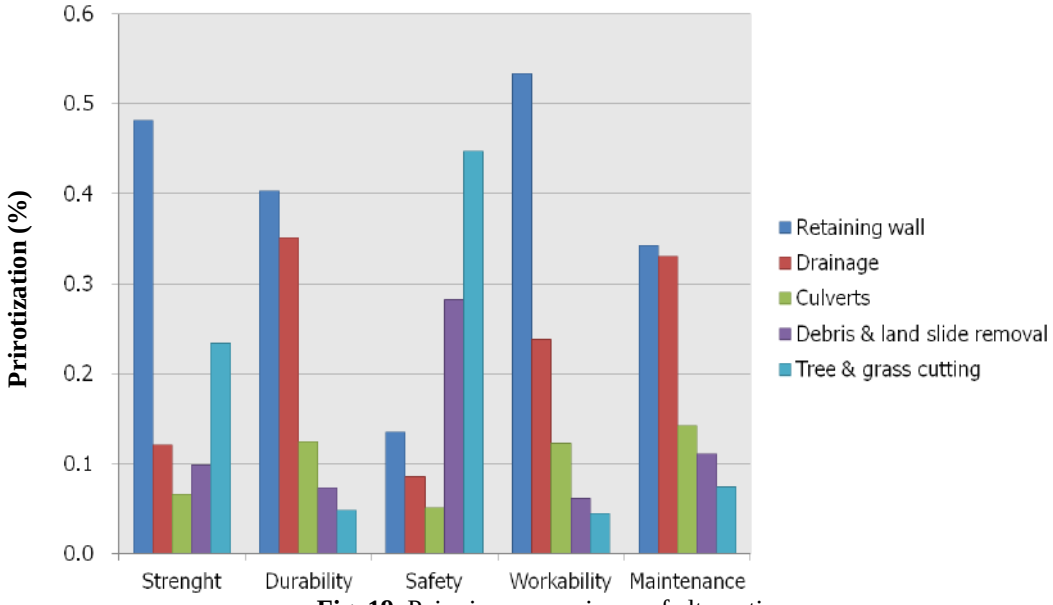

Fig. 19. Pairwise comparisons of alternatives

Table 18. Comprehensive evaluation of road attributes for Timor-Leste road networks

	Strength	**Durability**	**Safety**	**Workability**	**Maintenance**	**Comprehensive evaluation**
Retaining wall	0.4814	0.4034	0.1348	0.5338	0.3428	0.3831
Drainage	0.1207	0.3512	0.0857	0.2381	0.3305	0.2179
Culverts	0.0663	0.1243	0.0509	0.1224	0.1424	0.0987
Debris and land slide removal	0.0983	0.0729	0.2818	0.0614	0.1105	0.1103
Tree and grass cutting	0.2334	0.0481	0.4467	0.0443	0.0738	0.1666
Sum	**1.0**	**1.0**	**1.0**	**1.0**	**1.0**	**1.0**

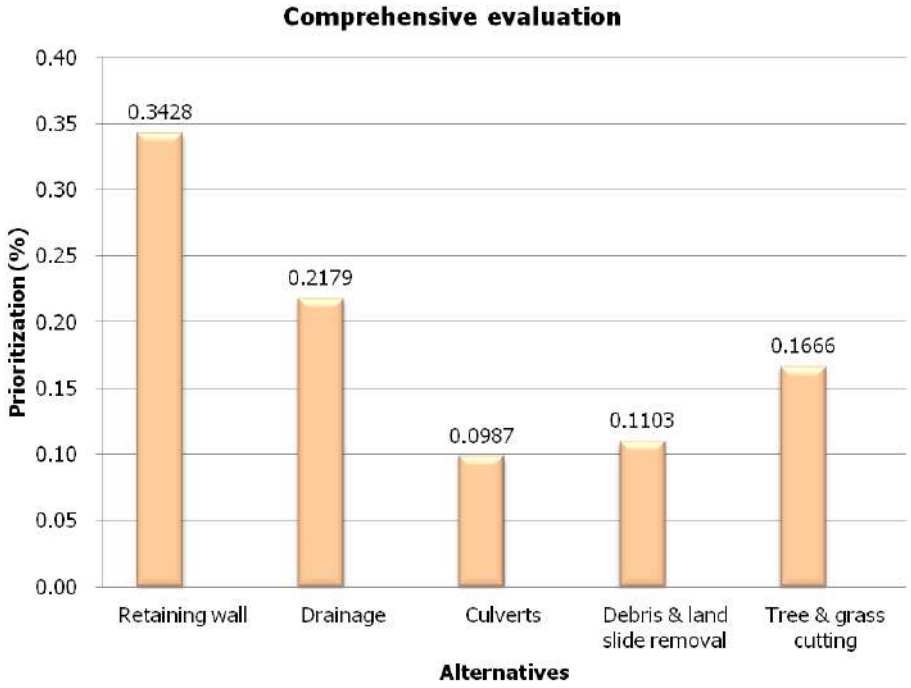

Fig. 20. Analysis result of comprehensive evaluation of road attributes

6. Conclusions

The Ippo-Campo system is a low-cost IT-based road condition assessment system that has been developed based on digital video, vehicle vibrations, audio and GPS data. Initially, this system was designed for Japan's roads, where it has become established as a suitable IT-based system. Because the system is IT-based, it can easily obtain output data in various formats that are both effective and efficient. In addition, the AHP method for multi-decision-making can be considered to prioritize a decision related to the required work according to the urgency of the need. Therefore, both the Ippo-Campo system and the AHP method can be applied in other countries. In developing countries, there are some problems related to road maintenance because there are budget limitations for maintaining the road networks. This issue results in many roads remaining damaged, and is affected by the economic status of the country. Hence, the use of this system in a developing country is advantageous because it is a relatively low-cost system. The application of the system and the AHP method to a road network in Timor-Leste confirmed the effectiveness and workability of the system.

The main conclusions obtained in this study can be summarized as follows:

- A low-cost IT-based road condition assessment system ("Ippo-Campo") developed based on digital video, vehicle vibrations, audio and GPS data can be applied to Timor-Leste's road network with a different threshold.
- The proposed system was applied to actual road networks (target routes) in both Mine City in Yamaguchi Pref., Japan and Timor-Leste to evaluate its effectiveness. As a result, the system will allow a rational maintenance strategy for repairs works to be established based on the condition assessment.
- Timor-Leste, as a developing country, needs a simple and rational system to assess the condition of its roads and prioritize their maintenance. Therefore, the Ippo-Campo system and the AHP method can contribute to make a maintenance strategy for Timor-Leste's road network in the future.
- The application of the AHP method to the Timor-Leste road maintenance strategy will effectively support

decision-making with regard to complex sustainability issues and can help to recognize and define problems in detail.
- The AHP helps to capture subjective and objective evaluation measures in the Timor-Leste road maintenance strategy, while providing a useful mechanism for checking the consistency of the evaluation measures and alternatives and thus reduce bias in decision-making.

7. Acknowledgment

The authors would like to thank the staff of the JICA CADEFEST Project in Timor-Leste for their great support and special thanks to Mr. Jose Maria C.B. Ximenes and Mr. Alfredo da Costa Sarmento for their great help and advice.

8. References

American Association of State Highway and Transportation Officials (AASHTO). (1993). *AASHTO guide for design of pavement structures*, American Association of State Highway and Transportation Officials, Washington, D.C.

Asian Development Bank (ADB) of Timor-Leste. (2013). "Democratic Republic of Timor-Leste: Road network upgrading project", *ADB LOAN* No. 2857-TIM, Dili, Timor-Leste.

Behbahani, H., Rezaei, S. and Nafar, H. (2014). "Prioritizing roads safety based on the quasi-induced exposure method and utilization of the Analytical Hierarchy Process", *Civil Engineering Infrastructures Journal*, 47(1), 43-58.

Committee on Earth Structures and Foundations of Japan (CESFJ), Subcommittee on Evaluation of Pavement Performance. (1993). "Present state and future of pavement performance evaluation technology", *Proceedings of the Japan Society of Civil Engineers*, 472(V-20), 13-28.

Government of Timor-Leste. (2011). "Timor-Leste strategic development plan 2011-2030", Dili, Timor-Leste.

Government of Japan. (2008). "Recommendations on preventive maintenance of road bridges", Ministry of Land, Infrastructure, Transport and Tourism, Advisory Council on Preventive Maintenance of Road Bridges, (in Japanese).

Hugo da C.X., Emoto, H., Miyamoto, A. and Sarmento, A. (2014). "Practical application of road condition assessment system to road networks in Timor-Leste", *Proceedings of the Asia-Pacific Computer Science and Application Conference*, 1-21, ISBN: 978-1-135-68498-7.

Miyamoto, A., Nakano, T. and Yoshitake, T. (2013). "Development of a road condition assessment system using digital movies, vehicle vibration and sound", *Proceedings of the Fourteenth International Conference on Civil, Structural and Environmental Engineering Computing*, Civil-Comp Press, Paper No.195, 1-22.

Miyamoto, A. and Yoshitake, T. (2009). "Development of a remote condition assessment system for road infrastructure", *International ECCE Conference, EUROINFRA 2009, Current State and Challenges for Sustainable Development of Infrastructure*, Symposium 1, Helsinki, Finland, 21-22, (USB Memory: 109-124).

Miyamoto, A. (2019). "Remote monitoring system for road condition assessment and its application", *Proceedings of the Fifth Conference on Smart Monitoring, Assessment and Rehabilitation of Civil Structures* (SMAR 2019), 1-10.

Modarres, A. and Shabani, H. (2015) "Investigating the effect of aircraft impact loading on the longitudinal top-down crack propagation parameters in asphalt runway pavement using fracture mechanics", *Engineering Fracture Mechanics*, 150, 28-46.

Road for Development (R4D). (2011). "Building a sustainable rural road network in Timor-Leste", AusAID Timor-Leste, Dili, Timor-Leste.

Saaty, T.L. (1980). *The Analytic Hierarchy Process*, McGraw-Hill, New York.

Sayers, M.W., Gillespie, T.D. and Paterson, W.D.O. (1985). "The international road roughness experiment", World Bank Technical Report, 45.

Taherkhani, H. and Tajdini, M. (2020). "Investigating the performance of cracked asphalt pavement using Finite Elements Analysis", *Civil Engineering Infrastructures Journal*, 53(1), 33-51.

Zhao, Y., Alae, M. and Fu, G. (2018). "Investigation of mechanisms of top-down fatigue cracking of asphalt pavement", *Road Materials and Pavement Design*, 19(6), 1436-1447.

Civil Engineering Infrastructures Journal 2021, 54(2): 253-266
DOI: 10.22059/CEIJ.2020.294512.1644

RESEARCH PAPER

Damage Detection in Double Layer Grids with Modal Strain Energy Method and Dempster-Shafer Theory

Teimouri, H.[1], Davoodi, M.R.[2], Mostafavian, S.A.[3]* and Khanmohammadi, L.[3]

[1] Ph.D. of Structural Engineering, Babol Noshirvani University of Technology, Babol, Iran.
[2] Associate Professor, Faculty of Civil Engineering, Babol Noshirvani University of Technology, Babol, Iran.
[3] Assistant Professor, Department of Civil Engineering, Payame Noor University (PNU), Tehran, Iran.

Received: 23 Dec. 2019; Revised: 01 Jun. 2020; Accepted: 09 Aug. 2020

ABSTRACT: Change in modal strain energy is one of the indicators used to detect damage in structures. However, in structures with high degrees of freedom, such as double-layer grids, this method requires a relatively large number of mode shapes which in practice is difficult to determine. Therefore, it is necessary to reduce the number of required mode shapes. In this study, a damage detection technique based on modal strain energy and Dempster-Shafer evidence theory is presented for locating damage in double layer grids using only a few number of mode shapes. First, by calculating mode shapes of the grid in undamaged and damaged states, the modal strain energy based index for each mode shape is determined. Then, the results obtained from separate mode shapes are combined using Dempster-Shafer theory to achieve better results. In order to investigate the effect of noise on damage detection, 3% random noise is added to mode shapes. To demonstrate the performance of the proposed method, different single and multiple damage cases with different damage intensities are considered. Numerical results show that using 5 mode shapes, the presented technique can detect up to 3 damaged elements with different damage intensities in different parts of the grid with good accuracy (probability of 92.3%). Considering the fact that the classical modal strain energy method fails to distinguish even 1 damaged element in the double layer grid, the result shows significant improvement.

Keywords: Damage Detection, Dempster-Shafer Theory, Double Layer Grids, Modal Strain Energy.

1. Introduction

Double layer grids constitute a significant part of the space structure's family and are utilized for covering large spans without internal supports or with a few of them (Arekar et al., 2016). Elements in double layer grids are dominated by axial forces and these structures usually are treated like space trusses. Double layer grids, like every other type of structure, may encounter damage due to natural or artificial reasons

* Corresponding author E-mail: amin.mostafavian@gmail.com

during their service life. Early damage detection for these structures is important since it can prevent progressive or overall collapse of the structure.

Damage in a structure changes physical properties (stiffness, mass and damping) of structure. Since the physical properties of a structure are equivalent to its dynamic properties (natural frequencies, mode shapes and damping ratios), usually changes in dynamics properties are used to detect damage in structures. These dynamic properties can be determined in practice by experimental modal analysis (Mahdavi et al., 2012; Davoodi et al., 2012; Mostafavian et al., 2012). Many damage detection techniques based on dynamic properties have been developed in recent decades (Dawari and Vesmawala, 2016; Ding et al., 2017; Wei et al., 2017; Rezaifar and Doost mohammadi, 2016; Yasi and Mohammadizadeh, 2018). One of these methods which uses dynamic properties to identify damage is modal strain energy technique. Damage location in this method can be detected by comparison of modal strain energy of elements in undamaged and damaged states.

Carrasco et al. (1997) used modal strain energy method to detect damage in a space truss structure with 300 elements. They were able to detect damaged elements when one or two elements were at least 50% damaged. Shi et al. (1998) used modal strain energy methods to detect damage in structures. They found that modal strain energy change index is at its highest in the damaged element and that the value becomes much smaller at elements far from the damaged elements. But, elements located at nodal points of the mode shape do not follow this rule and have unusually small or large values, at times leading to wrong detection of damage location. To overcome this problem, they proposed using multiple modes in calculating modal strain energy. Srinivas et al. (2011) used a method based on modal strain energy to detect damage in a 2D truss structure. In the damage localization stage they observed that even though the damage index has its largest value at the damaged element, the value is sometimes too close to that of adjacent elements.

Ma et al. (2014) used modal strain energy method to detect damage in a seven story frame structure. Since damage index for some of the healthy elements was considerable, they proposed to use a threshold level to separate damaged and healthy elements, which means that only elements with damage index greater than threshold level were considered as damaged elements. Seyedpoor (2012) proposed a two-step damage detection technique on the basis of modal strain energy to find damage in structures. He used this method to identify damage in a 2D truss with 25 degrees of freedom. Despite using five mode shapes in damage detection procedure, still some healthy elements had considerable damage index; therefore he used a threshold level of 0.05 to separate damaged and healthy elements.

Wei et al. (2016) used modal strain energy technique to identify damage in plate like structures. At first, damage was localized by means of modal strain energy change ratio. Then a method was suggested to reduce the number of suspicious damaged elements entailed by the 'Vicinity Effect', in order to better results. Torkzadeh et al. (2013) presented a two-step damage detection technique on the basis of modal strain energy to indicate damage in double layer grids. They needed a relatively high number of mode shapes to detect damage. In practice determining many mode shapes is unfeasible and thus solution requiring fewer number of mode shapes is urged.

Data fusion is a technique that combines data from different information sources to achieve better results. Recently, data fusion has appealed increasing consideration in structural health monitoring due to its abilities in taking out information from various sources and merging them into a consistent, precise and apprehensible data set (Zhao et al., 2014). Guo (2006) used three fusion approaches, including

Dempster-Shafer evidence theory, Bayesian fusion and fuzzy fusion method to detect the damage in a two dimensional truss structure. The numerical results showed that the Dempster-Shafer evidence theory is the most efficient fusion method between the three. Guo and Li (2011) used the Dempster-Shafer evidence theory to detect damage in 2D and 3D truss structures. Grande and Imbimbo (2014) used Dempster-Shafer evidence theory to amalgamate information which was acquired from different mode shapes in modal strain energy method to detect damage location in a fixed end beam. Grande and Imbimbo (2016) proposed a technique based on flexibility method and Dempster-Shafer theory to detect damage in structures. The efficacy of this technique has been shown with reference to a fixed end beam and a 3D structure. Guo et al. (2019) used an enhanced Dempster-Shafer theory and a model in time domain to locate nonlinear damages in structures. They indicate that the enhanced Dempster-Shafer theory has great recognition accuracy and decent performance. Cheng et al. (2019) proposed a new damage detection technique based on the flexibility identification principle and Dempster-Shafer theory. They showed that the proposed method is more suitable to detect damage in beam structure in noisy environments in comparison to traditional methods. Ding et al. (2019) used an improved Dempster-Shafer data fusion algorithm to detect damages in a spatial truss structure.

As mentioned above, the results obtained solely from classic modal strain energy methods cannot clearly distinguish damaged elements from healthy ones and therefore demand further enhancement. This problem is exacerbated in high degrees of freedom structures which require many mode shapes for reliable damage detection. In this study, modal strain energy method and Dempster-Shafer evidence theory are used to detect damage location in a double layer grid. By performing modal analysis and calculating vibration mode shapes of the grid in undamaged and damaged states, the modal strain energy based index for each mode shape is determined. The indices are then combined with Dempster-Shafer evidence theory to improve the results. In practice, measurements are corrupted by noise and therefore we added random noise to mode shapes. A set of 1000 damage detection runs is performed for each damage case and the mean of results is considered. The complete process of damage detection has been implemented in MATLAB.

2. Modal Strain Energy Based Damage Localization

The modal characteristics of an undamaged structure are described by the eigenvalue equations (Ren and Roeck, 2002):

$$K\varphi_i = {\omega_i}^2 M\varphi_i, \qquad i = 1, \dots, n \tag{1}$$

where K and M: are stiffness and mass matrices, respectively; ω_i and φ_i: are the ith natural frequency and mode shape of the structure, respectively.

The Modal Strain Energy of element j in mode i before damage and after that is denoted as (Shi et al., 1998):

$$\begin{aligned} MSE_{ij}^{u} &= {\varphi_i^u}^T K_j \varphi_i^u \\ MSE_{ij}^{d} &= {\varphi_i^d}^T K_j \varphi_i^d \end{aligned} \tag{2}$$

where MSE_{ij}^{u} and MSE_{ij}^{d}: are the undamaged and damaged modal strain energy of the jth element in ith mode respectively; φ_i^u and φ_i^d: are the partial mode shape vectors before and after damage respectively, containing the ith mode shape elements related to the degrees of freedom of jth element. As the damage locations are unknown, the undamaged elemental stiffness matrix K_j is used for estimating MSE_{ij}^{d} (Shi et al., 2000).

The whole modal strain energy of ith mode of the structure is calculated by the summation of modal strain energy of all structural elements as follows:

$$MSE_i = \sum_{j=1}^{ne} MSE_{ij} \quad (3)$$

where MSE_i: is the total MSE of the structure in mode i and ne: is the total number of elements. The normalized modal strain energy of jth element for mode i will be determined by dividing MSE_{ij} by MSE_i as:

$$NMSE_{ij} = \frac{MSE_{ij}}{MSE_i} \quad (4)$$

where $NMSE_{ij}$: is the normalized modal strain energy of jth element in mode i. Since damage changes the dynamic properties of the structure, normalized MSE of an element in each mode will change after damage occurs. Modal Strain Energy Based Index (MSEBI) is an efficient indicator for damage localization which can be determined as:

$$MSEBI_{ij} = max\left[0, \frac{NMSE_{ij}^{d} - NMSE_{ij}^{u}}{NMSE_{ij}^{u}}\right] \quad (5)$$

where $NMSE_{ij}^{u}$ and $NMSE_{ij}^{d}$: are the undamaged and damaged normalized modal strain energy of jth element in ith mode, respectively. $MSEBI_{ij}$: is the modal strain energy based index of jth element in ith mode. $MSEBI_{ij}$ will be zero for undamaged elements and greater than zero for damaged ones. Elements with higher $MSEBI$ are thus more likely to be the damaged ones.

$MSEBI$ for an element can be evaluated with several first mode shapes as follows:

$$MSEBI_j = max\left[0, \frac{\sum_{i=1}^{nm} NMSE_{ij}^{d} - \sum_{i=1}^{nm} NMSE_{ij}^{u}}{\sum_{i=1}^{nm} NMSE_{ij}^{u}}\right] \quad (6)$$

where $MSEBI_j$: is the modal strain energy based index of jth element evaluated by considering nm first mode shapes.

3. Dempster-Shafer Evidence Theory

Information fusion methods can incorporate data from numerous information sources and corresponding information from dependent databases, to attain better accuracies and more particular deductions than could be attained by using only one source (Guo, 2006). Dempster-Shafer evidence theory is a data fusion technique based on mathematical theory first suggested by Dempster (1967) and then developed by Shafer (1976).

Considering a finite set θ of mutually exclusive and exhaustive proportions, the power set 2^{θ} is the set of all the subsets of θ containing itself and an empty set $\emptyset$. For instance, if $\theta = \{a, b, c\}$, then $2^{\theta} = \{\emptyset, \{a\}, \{b\}, \{c\}, \{a, b\}, \{a, c\}, \{b, c\}, \{a, b, c\}\}$. Dempster-Shafer theory is based on probability and allocates a Basic Probability Assignment (BPA) function to any subset of 2^{θ}. m which represents the BPA, describes a map of the power set to the range [0, 1], so that BPA of the empty set is equal to 0 and BPAs of all the subsets of the power set have a total of 1. This can be mathematically represented by:

$$\begin{aligned} &m: 2^{\theta} \rightarrow [0,1] \\ &m(\phi) = 0 \\ &\sum_{x \subset 2^{\theta}} m(x) = 1 \end{aligned} \quad (7)$$

Since the subset X has 2 data sources, s_1 and s_2, let $m_1(s_1)$ and $m_2(s_2)$ be BPAs given by the sources s_1 and s_2, respectively. The composition, namely the joint m_{12} is computed by the orthogonal sum of 2 BPAs $m_1(s_1)$ and $m_2(s_2)$:

$$\begin{aligned} &m_{12}(\phi) = 0 \\ &m_{12}(X) = \frac{\sum_{s_1 \cap s_2 = X} m_1(s_1).m_2(s_2)}{1 - K'} \\ &K' = \sum_{s_1 \cap s_2 = \emptyset} m_1(s_1).m_2(s_2) \\ &when \quad X \neq \emptyset \end{aligned} \quad (8)$$

where K': is a basic probability mass related

to conflicts which is evaluated by summing the products of the BPAs of all the sets in which the intersection is null (Chen and Xia, 2011).

4. Application of Modal Strain Energy Method and Dempster-Shafer Theory in Damage Localization

Dempster-Shafer theory and modal strain energy method can be used to detect damage in structures. Let $\theta = \{D_1, D_2, \dots, D_{ne}\}$ be a set which shows damage condition of a structure with ne elements. The power set 2^θ can be shown as follows:

$$2^\theta = \{\emptyset, \{D_1\}, \{D_2\}, \{D_3\}, \dots, \{D_n\}, \dots, \{D_1, D_2\}, \{D_1, D_3\}, \dots\} \quad (9)$$

Since modal strain energy method gives only damage index of each element, only n members of 2^θ which have one element e.g. $(\{D_1\}, \{D_2\}, \{D_3\}, \dots, \{D_n\})$ are considered.

Let $s_1$and $s_2$be two information sources which containing MSEBI evaluated by considering mode shapes 1 and 2, respectively.

$$s_1 = \{MSEBI_{11}, MSEBI_{12}, \dots, MSEBI_{1j}\}$$
$$s_2 = \{MSEBI_{21}, MSEBI_{22}, \dots, MSEBI_{2j}\}' \quad (10)$$
$$j = 1, \dots, ne$$

BPA can be determined by dividing MSEBI of each element in ith mode by the summation of the MSEBI of all elements in that mode.

$$m_1(s_1) = \left\{\frac{MSEBI_{11}}{\sum_{i=1}^{n} MSEBI_{1i}}, \frac{MSEBI_{12}}{\sum_{i=1}^{n} MSEBI_{1i}}, \dots, \frac{MSEBI_{1j}}{\sum_{i=1}^{n} MSEBI_{1i}}\right\}$$
$$m_2(s_2) = \left\{\frac{MSEBI_{21}}{\sum_{i=1}^{n} MSEBI_{2i}}, \frac{MSEBI_{22}}{\sum_{i=1}^{n} MSEBI_{2i}}, \dots, \frac{MSEBI_{2j}}{\sum_{i=1}^{n} MSEBI_{2i}}\right\}, \quad j = 1, \dots, ne \quad (11)$$

Each member of $m_1(s_1)$ and $m_2(s_2)$ shows damage probability of elements determined from modes 1 and 2, respectively. s_1 and s_2 can be merged with Dempster's combination rule as follows:

$$m_{12}(s_{12}) = \frac{\sum_{s_1 \cap s_2 = s_{12}} m_1(s_1).m_2(s_2)}{1 - \sum_{s_1 \cap s_2 = \emptyset} m_1(s_1).m_2(s_2)} \quad when \quad s_{12} \neq \emptyset \quad (12)$$

where $m_{12}(s_{12})$: is the combination of $m_1(s_1)$ and $m_2(s_2)$. To improve the results, $m_{12}(s_{12})$ can be combined with damage probability of elements obtained from mode 3, represented by $m_3(s_3)$, as follows:

$$m_{12}(s_{123}) = \frac{\sum_{s_{12} \cap s_3 = s_{123}} m_{12}(s_{12}).m_3(s_3)}{1 - \sum_{s_{12} \cap s_3 = \emptyset} m_{12}(s_{12}).m_3(s_3)} \quad when \quad s_{123} \neq \emptyset \quad (13)$$

where $m_{12}(s_{123})$: is the combination of $m_1(s_1)$, $m_2(s_2)$ and $m_3(s_3)$ which are first, second and third information sources, respectively. Data fusion can be continued until reaching desirable results.

5. Damage Detection in a Double Layer Grid

The feasibility of the Dempster-Shafer theory and modal strain energy method in damage detection is demonstrated by detecting damage in a double layer grid. The model chosen for this study is a double layer grid with 32 nodes and 96 elements as shown in Figure 1.

Width, length and height of grid are 7.5 m, 10 m and 1.77 m, respectively. Each element is 2.5 m long with 0.004 m^2 cross section. In the grid, the Young's modulus is 200 GPa and mass density of each element is 7850 kg/m^3, respectively. In Figure 1 the top, bottom and middle elements are shown with thick, thin and dash lines, respectively and the grid has 4 supports.

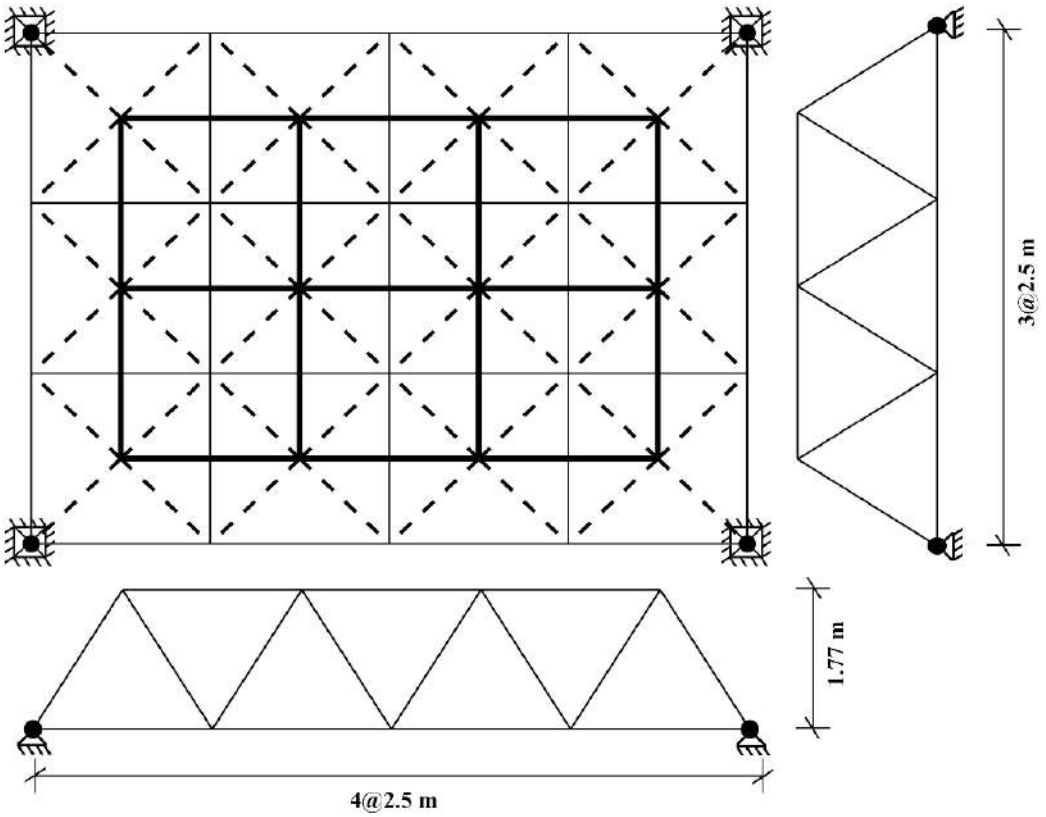

Fig. 1. Double layer grid chosen for study

To simulate a damaged grid, Young's modulus of material is decreased as follows:

$$E_j^d = (1 - \alpha_j)E_j^u \quad (14)$$

where E_j^u and E_j^d: are the undamaged and damaged Young's modulus of jth element, respectively; and α_j: is the damage percentage of jth element.

To study the effect of noise on the efficiency of the suggested damage detection technique, 3% random noise (Messina et al., 1998) is added to mode shape as follows:

$$\overline{input} = input(1 + 0.03 * rand) \quad (15)$$

where $rand$: is a random number which is normally distributed with mean 0, variance $\sigma^2 = 1$, and standard deviation $\sigma = 1$. $input$: is each component of mode shape matrices and $\overline{input}$: is the noise polluted input. Due to the random characteristics of noise, a set of 1000 damage detection runs is performed for each damage case and the average is considered.

Three single and four multiple damage cases shown in Table 1 are considered. For all cases, damage simulation is done by reducing the Young's modulus of damaged elements. Damaged elements are shown in Figure 2 with thick lines. For all damage cases 3% random noise is added to mode shapes and a set of 1000 damage detection runs is performed.

Table 1. Damage cases

Case	Damage type	Damaged element and intensity (%)
D1	Single	Element 16 with 40%
D2	Single	Element 48 with 40%
D3	Single	Element 81 with 40%
D4	Multiple	Element 16 with 50% and Element 48 with 40%
D5	Multiple	Element 48 with 50% and Element 81 with 40%
D6	Multiple	Element 16 with 50% and Element 81 with 40%
D7	Multiple	Element 16 with 50% and Element 48 with 40% and Element 81 with 50%

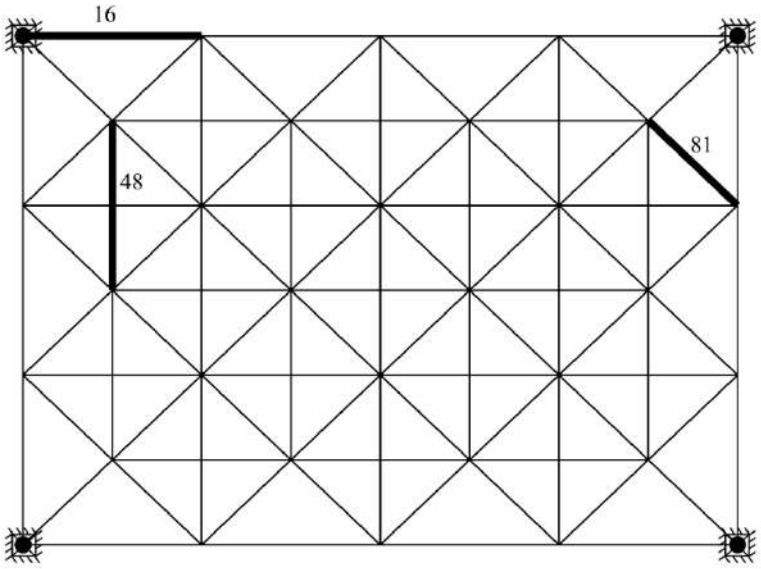

Fig. 2. Damaged elements

In the first damage case D1, damage occurs at element 16 from the bottom layer. The value of MSEBI is evaluated by considering only the first mode shape. Figure 3a shows the mean value of MSEBI for a set of 1000 runs evaluated by considering first mode shape. As it is shown, by considering only first mode shape, a lot of healthy elements have high value of MSEBI which leads to misdiagnosis in damage detection procedure. The value of MSEBI can also be evaluated by considering other mode shapes. Figure 3b-3e show the mean value of MSEBI for a set of 1000 runs when mode shapes 2-5 are considered, respectively. According to Figure 3a-3e, by considering only one mode shape to evaluate the value of MSEBI, a lot of healthy elements are introduced as potentially damaged elements. The figure clearly shows that MSEBI for the damaged element depends on the mode shape used; MSEBI for the damaged element is highest using mode 5 and lowest using mode 4. The result also depends on the location of the damaged element in the double layer grid. Moreover, the value and distribution of MSEBI for healthy elements are different among mode shapes; some mode shapes yield higher MSEBI values for fewer elements (Figure 3e), and other mode shapes give lower MSEBI value for more elements (Figure 3a).

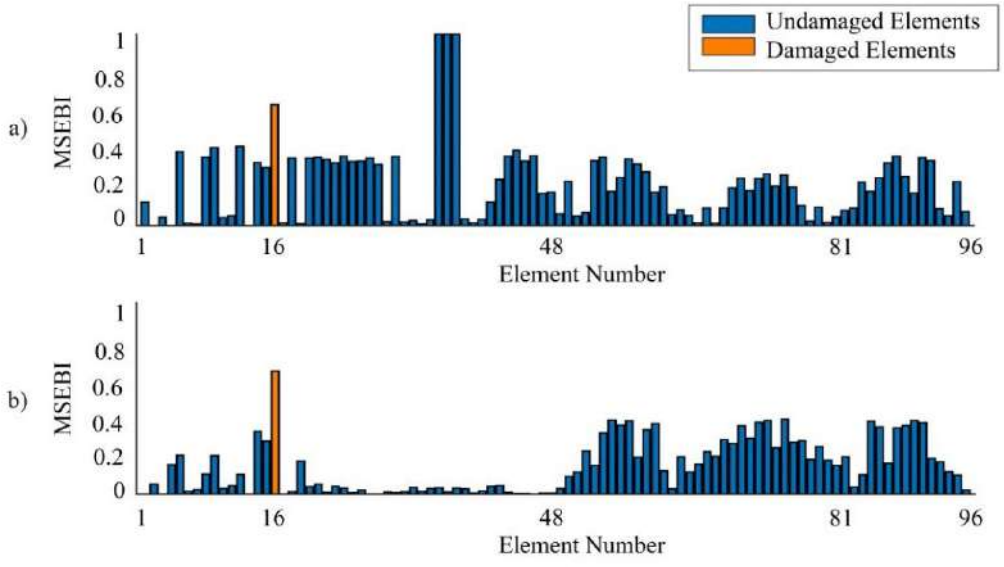

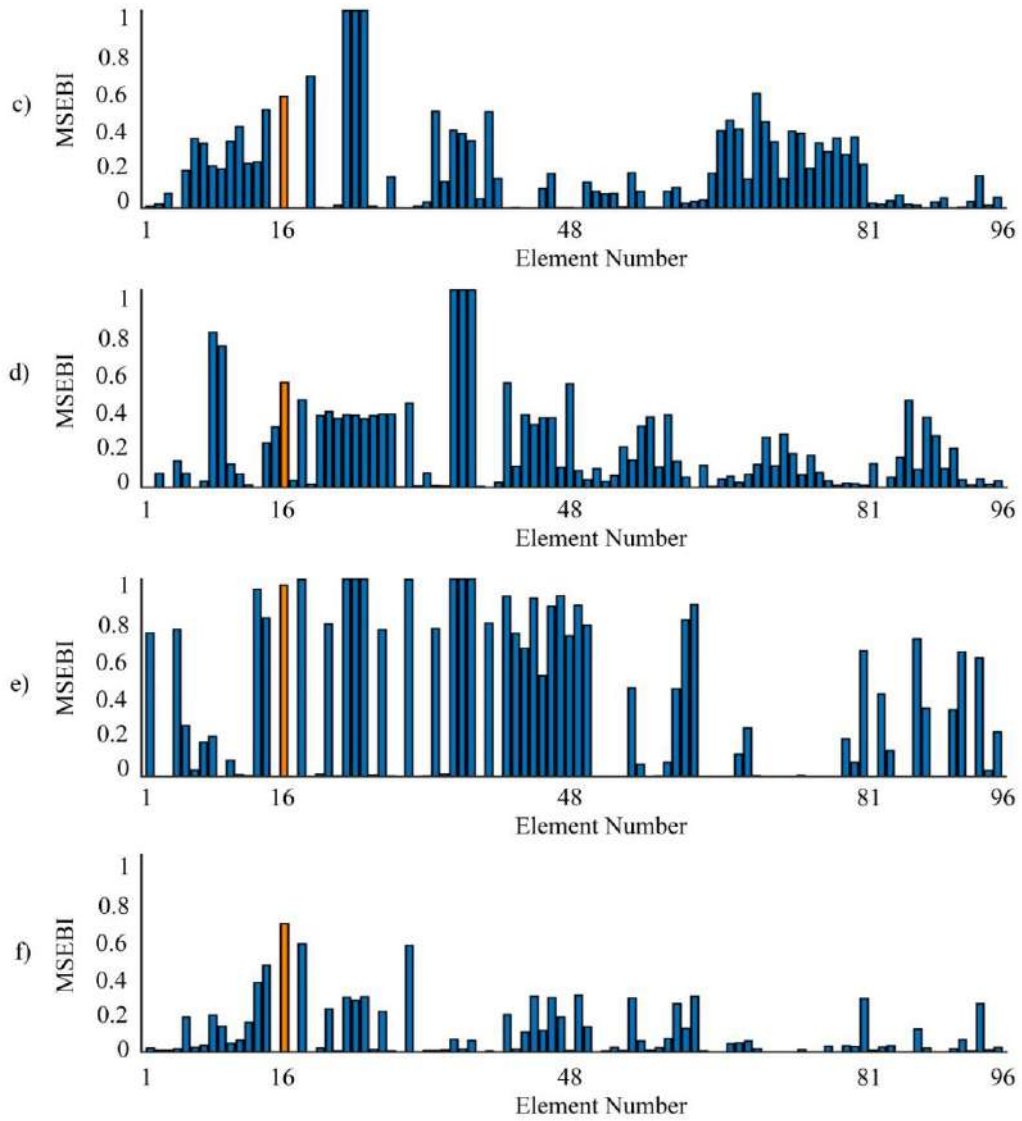

Fig. 3. MSEBI values for damage case D1 considering: a) Mode1; b) Mode 2; c) Mode 3; d) Mode 4; e) Mode 5; and f) Modes 1 to 5

The MSEBI value can also be evaluated by considering several first mode shapes according to Eq. (6). Figure 3f shows the mean value of MSEBI for a set of 1000 runs evaluated by considering five first mode shapes. As shown in Figure 3f, considering the first five mode shapes to evaluate the MSEBI gives better results, however still some healthy elements have considerable MSEBI which may lead to misdiagnosis in damage localization.

Dempster-Shafer theory is used to improve damage identification results. In the first stage, the value of MSEBI evaluated by mode shapes 1 and 2 are combined by Eq. (12). The result of the combination is damage probability and is shown in Figure 4a. As can be seen in thid figure, damage probability for element 16 is 18.61% and summation of the damage probability of other 95 elements is 81.39%. In this case, the damage probability of element 16 is not sufficiently high to be considered as a damaged element. The value of MSEBI evaluated by mode shapes 1 and 2 are combined with the value of MSEBI evaluated by mode shape 3 and the result is shown in Figure 4b. Combining the MSEBI evaluated by mode shapes 1-4 using Dempster-Shafer theory leads to better results, as shown in Figure 4c. Finally, Figure 4d shows damage probability obtained from combining the MSEBI evaluated from mode shapes 1-5.

Comparing Figures 4a-4d show that as the number of used mode shapes increases, the damage probability of the damaged element increases and the number of healthy elements with a damage probability decreases. As shown in Figure 4d the damaged element is distinct and no more elements have considerable damage probability, therefore no more data combination is needed. Here, damage probability of element 16 is 77.19% and summation of the damage probability of other 95 elements is 22.81% which is not a considerable value.

Element 48 from the top layer is considered as the second damage case D2. The mean value of MSEBI for a set of 1000 runs by considering first five mode shapes is evaluated and is shown in Figure 5a. It can be seen that, damaged element is detected but still some healthy elements have considerable value. The damage probability obtained from combining the MSEBI evaluated from mode shapes 1-5 is shown in Figure 5b. As can be seen in this figure, damage probability of element 48 is 81.54% and the summation of the damage probability of other 95 elements is 18.46% which is not a considerable value.

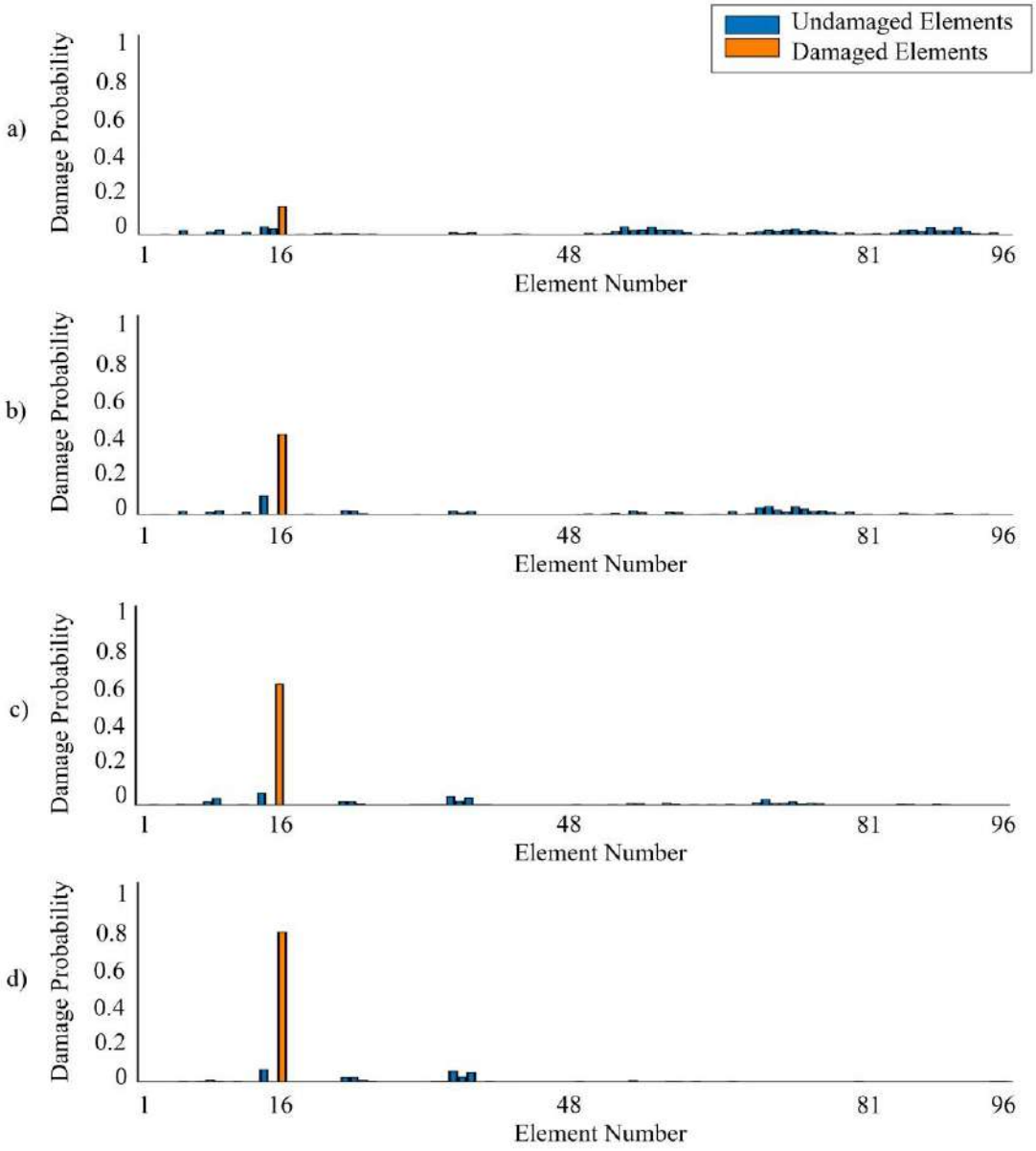

Fig. 4. Dempster-Shafer theory damage probabilities for damage case D1 considering: a) Modes 1 and 2; b) Modes 1 to 3; c) Modes 1 to 4; and d) Modes 1 to 5

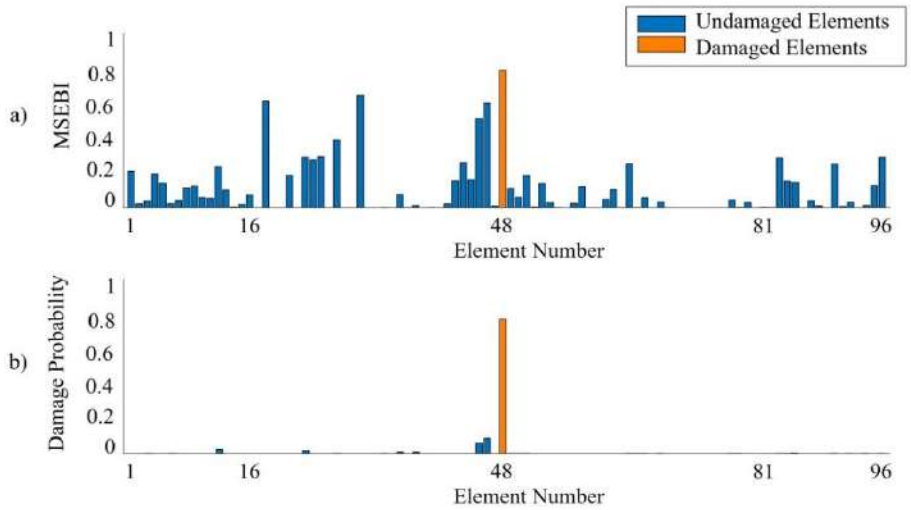

Fig. 5. Damage case D2 considering modes 1 to 5: a) MSEBI values; and b) Dempster-Shafer theory damage probabilities

In damage case D3, element 81 from the middle layer is considered as a damaged element. The mean value of MSEBI for a set of 1000 runs is shown in Figure 6a and damage probability obtained from Dempster-Shafer theory is shown in Figure 6b. First five mode shapes are considered in both MSEBI evaluation and Dempster-Shafer combination. As shown in Figures 6a-6b, by using Dempster-Shafer theory, the results are improved compared to the classical modal strain energy method. Damage probability of element 81 is 84.77% and the summation of the damage probability of other 95 elements is 15.23% which is not a considerable value.

Comparing the damage probability obtained for the damaged element in damage cases D1, D2 and D3 (respectively 77.19%, 81.54% and 84.77%) shows that the technique is relatively insensitive to the location of damaged element in the double layer grid and can find the damaged element anywhere in the grid with a sufficiently high damage probability.

D4, D5 and D6 are multiple damage cases where two elements are damaged. Figures 7a-7b, 8a-8b and 9a-9b show the mean value of MSEBI and damage probability obtained from Dempster-Shafer combination for damage cases D4, D5 and D6, respectively. Similar to the other damage cases, a set of 1000 damage detection runs and first five mode shapes are considered in both MSEBI evaluation and Dempster-Shafer combination.

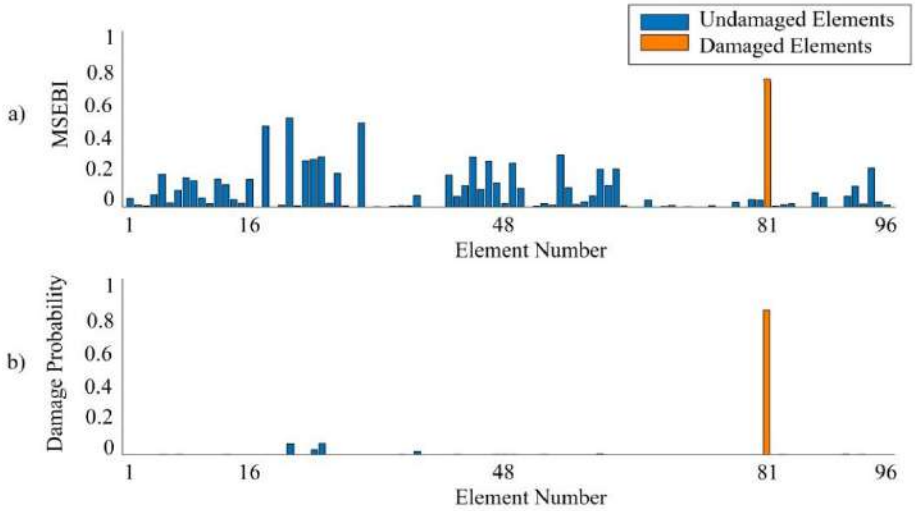

Fig. 6. Damage case D3 considering modes 1 to 5: a) MSEBI values; and b) Dempster-Shafer theory damage probabilities

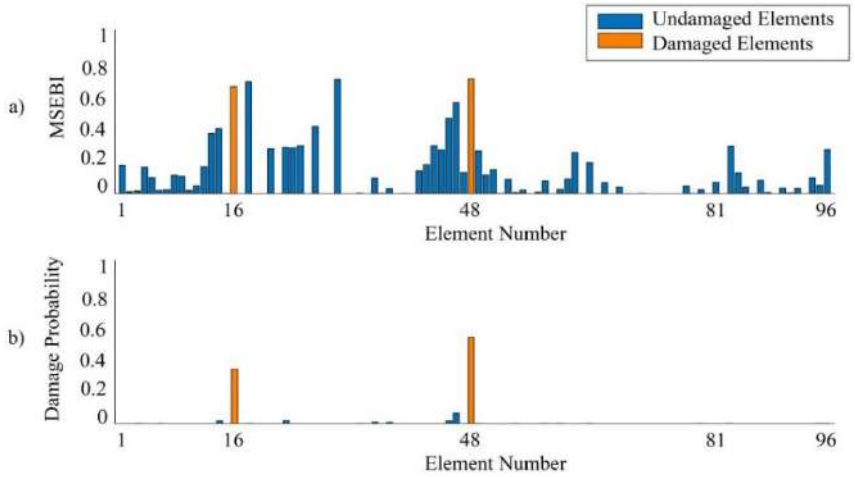

Fig. 7. Damage case D4 considering modes 1 to 5: a) MSEBI values; and b) Dempster-Shafer theory damage probabilities

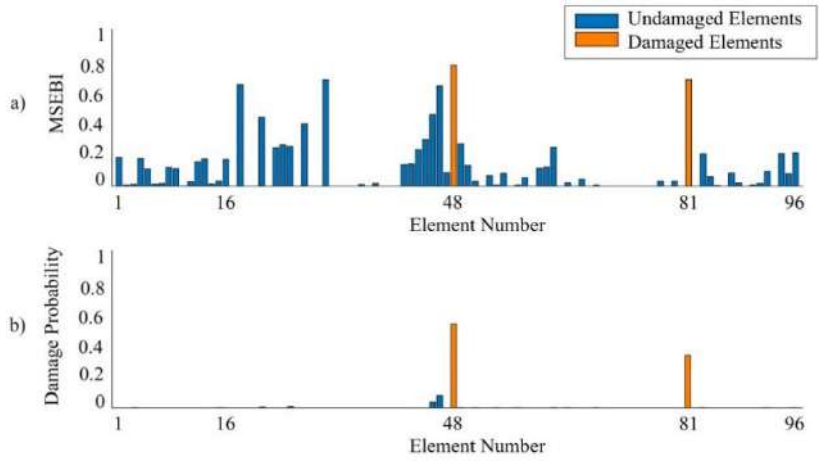

Fig. 8. Damage case D5 considering modes 1 to 5: a) MSEBI values; and b) Dempster-Shafer theory damage probabilities

As can be seen in Figures 7-9, the MSEBI value of some of the healthy elements is near that of the two damaged elements and therefore it is not possible to identify damaged elements only based on the MSEBI values. However, Dempster-Shafer damage probabilities clearly distinguished damaged elements from other healthy elements. In these two damaged elements cases, the probability of damaged elements are not related to the values of damage intensity. Sum of the probability of damaged elements are 88.11%, 89.57% and 90.23% for cases D4, D5 and D6 respectively, which indicate a high probability of damage has been obtained for damaged elements. These values are higher than the values obtained for single damage cases.

Damage case D7 is a multiple damage case where elements 16, 48 and 81 have 50%, 40% and 50% stiffness reduction, respectively. Figures 10a-10b show the mean value of MSEBI and Dempster-Shafer combination results for a set of 1000 damage detection runs. First five mode shapes are considered in both MSEBI evaluation and Dempster-Shafer combination. As shown in Figure 10a, separating damaged and healthy elements is not possible, because MSEBI values for some of the healthy elements is at the same level as the damaged elements. Figure 10b shows that by using Dempster-Shafer combination, the summation of the damage probability of damaged elements is 92.31% and the summation of the damage probability of other 93 elements is 7.69%, which means the combination was able to detect three simultaneously damaged elements with different damage intensities with good accuracy.

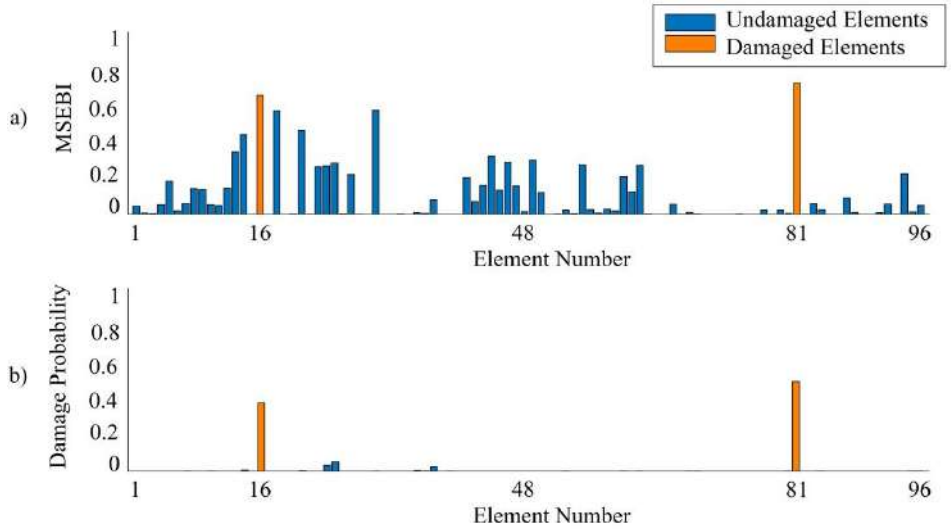

Fig. 9. Damage case D6 considering modes 1 to 5: a) MSEBI values; and b) Dempster-Shafer theory damage probabilities

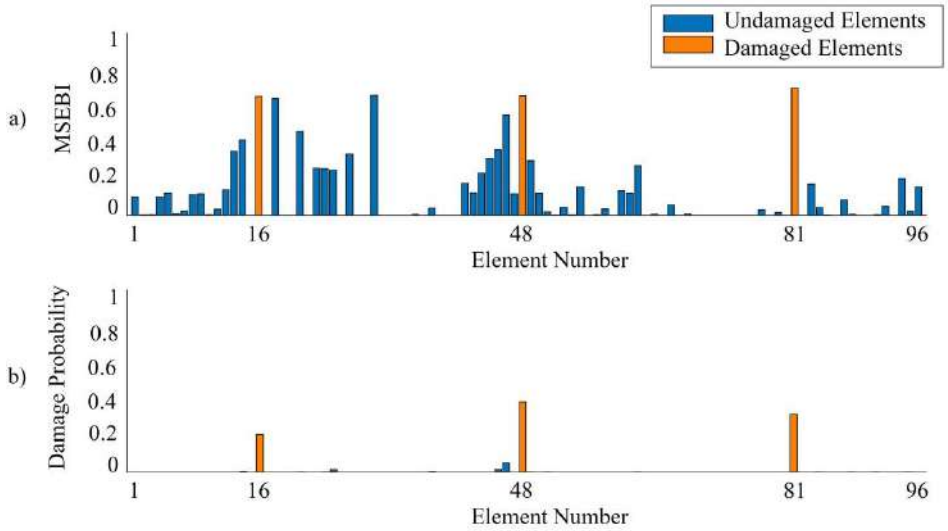

Fig. 10. Damage case D7 considering modes 1 to 5: a) MSEBI values; and b) Dempster-Shafer theory damage probabilities

6. Conclusions

Damage detection methods for structures with high degrees of freedom, usually requires a large number of mode shapes to locate damage. In practice, however, only a few first mode shapes of structures can be measured. In this paper, a damage detection technique based on modal strain energy and Dempster-Shafer theory has been presented for detecting damage in double layer grids using only a few number of mode shapes. To study the effect of noise on the efficiency of the suggested damage detection technique, 3% random noise was considered. The modal strain energy based index was calculated for each mode shape. Then, Dempster-Shafer theory was used to combine the value of indices obtained from each mode. Three single and four multiple damage cases were considered with different damage intensities in different elements of the grid. Using the first five mode shapes of the grid, the modal strain energy based index could not distinguish the damaged element(s) in any of the damage cases. This was mainly because in addition to the damaged element(s), many of the other healthy elements showed a considerable index value. However, combining the value of the indices with Dempster-Shafer theory and calculating damage probabilities of the elements, gave far better results compared to the classical

modal strain energy method. In the cases with one damaged element, damage probability of 77.19%, 81.54% and 84.77% was obtained for the damaged element. In the cases with two damaged elements, the sums of the damage probabilities were 88.11%, 89.57% and 90.23%. In the case with three damaged elements, the sum was 92.31%. From this point of view, the Dempster-Shafer combination performed better with a larger number of damaged elements. Unlike classical modal strain energy methods, damaged elements were distinct and none of healthy elements had considerable damage probability. The presented damage detection technique performed very well for a relatively high degree of freedom structure with multiple damaged elements using a limited number of noise contaminated vibration mode shapes.

7. References

Arekar, V.A., Patil, Y.D. and Patil, H.S. (2016). "Development of a new connector for double layer space grids", *Perspectives in Science*, 8, 525-528.

Carrasco, C.J., Osegueda, R.A., Ferregut, C.M. and Grygier, M. (1997). "Damage localization in a space truss model using modal strain energy", In: *Proceedings-SPIE the International Society for Optical Engineering*, Orlando, Florida, USA, pp. 1786-1792.

Chen, M. and Xia, X. (2011). "A new combination rule of DS theory", *IEEE International Conference on Computer Science and Automation Engineering*, 3, 202-205.

Cheng, Y.Y., Zhao, C.Y. and Zhang, J. (2019). "A novel damage detection method based on flexibility identification theory and data fusion technique", *Scientia Iranica A*, 26(4), 2286-2298.

Davoodi, M.R., Mahdavi, M. and Mostafavian, S.A. (2012). "Experimental and analytical determination of dynamic properties of a steel frame with bolted flange joints", *Proceedings of International Conference on Engineering and Information Technology (ICEIT2012)*, Toronto, Canada.

Dawari, V.B. and Vesmawala, G.R. (2016). "Structural damage identification of beam structures using two stage method based on modal strain energy indicators and artificial neural networks", *Journal of Vibroengineering*, 18(1), 119-128.

Dempster, A.P. (1967). "Upper and lower probabilities induced by a multivalued mapping", *The Annals of Mathematical Statistics*, 38(2), 325-339.

Ding, Z.H., Yao, R.Z., Huang, J.L., Huang, M. and Lu, Z.R. (2017). "Structural damage detection based on residual force vector and imperialist competitive algorithm", *Structural Engineering and Mechanics*, 62(6), 709-717.

Ding, Y., Yao, X., Wang, S. and Zhao, X. (2019). "Structural damage assessment using improved Dempster-Shafer data fusion algorithm". *Earthquake Engineering and Engineering Vibration*, 18(2), 395-408.

Grande, E. and Imbimbo, M. (2014). "A multi-stage data-fusion procedure for damage detection of linear systems based on modal strain energy", *Journal of Civil Structural Health Monitoring*, 4(2), 107-118.

Grande, E. and Imbimbo, M. (2016). "A multi-stage approach for damage detection in structural systems based on flexibility", *Mechanical Systems and Signal Processing*, 76, 455-475.

Guo, H.Y. (2006). "Structural damage detection using information fusion technique", *Mechanical Systems and Signal Processing*, 20(5), 1173-1188.

Guo, H.Y. and Li, Z.L. (2011). "Two-stage multi-damage detection method based on energy balance equation", *Journal of Nondestructive Evaluation*, 30(3), 186-200.

Guo, H., Zhou, R. and Zhang, F. (2019). "Structural nonlinear damage detection using improved Dempster-Shafer theory and time domain model", *Journal of Vibroengineering*, 21(6), 1679-1693.

Ma, S.L., Jiang, S.F. and Weng, L.Q. (2014). "Two-stage damage identification based on modal strain energy and revised particle swarm optimization", *International Journal of Structural Stability and Dynamics*, 14(5), 1440005.

Mahdavi, M., Davoodi, M.R. and Mostafavian, A. (2012). "Determination of joint stiffness of a three story steel frame by finite element model updating", *Proceedings of the 15th World Conference on Earthquake Engineering, Lisbon, Portugal.*

Messina, A., Williams, E.J. and Contursi, T. (1998). "Structural damage detection by a sensitivity and statistical-based method", *Journal of Sound and Vibration*, 216(5), 791-808.

Mostafavian, S.A., Davoodi, M.R. and Vaseghi Amiri, J. (2012). "Ball joint behavior in a double layer grid by dynamic model updating", *Journal of Constructional Steel Research*, 76, 28-38.

Ren, W.-X. and De Roeck, G. (2002). "Structural damage identification using modal data, I: Simulation verification", *Journal of Structural Engineering*, 128(1), 87-95.

Rezaifar, O. and Doost Mohammadi, M.R. (2016). "Damage detection of axially loaded beam: A frequency-based method", *Civil Engineering Infrastructures Journal*, 49(1), 165-172.

Seyedpoor, S.M. (2012). "A two stage method for structural damage detection using a modal strain energy based index and particle swarm optimization", *International Journal of Non-Linear Mechanics*, 47(1), 1-8.

Shafere, G. (1976). *A mathematical theory of evidence*, Princeton University Press.

Shi, Z., Law, S.S. and Zhang, L. (2000). "Structural damage detection from modal strain energy change", *Journal of Engineering Mechanics*, 126(12), 1216-1223.

Shi, Z.Y., Law, S.S. and Zhang, L.M. (1998). "Structural damage localization from modal strain energy change", *Journal of Sound and Vibration*, 218(5), 825-844.

Srinivas, V., Ramanjaneyulu, K. and Jeyasehar, C.A. (2011). "Multi-stage approach for structural damage identification using modal strain energy and evolutionary optimization techniques", *Structural Health Monitoring*, 10(2), 219-230.

Torkzadeh, P., Goodarzi, Y. and Salajegheh, E. (2013). "A two-stage damage detection method for large-scale structures by kinetic and modal strain energies using heuristic particle swarm optimization", *International Journal of Optimization in Civil Engineering*, 3(3), 465-482.

Wei, Z., Liu, J. and Lu, Z. (2017). "Structural damage detection using improved particle swarm optimization", *Inverse Problems in Science and Engineering*, 26(6), 792-810.

Wei, Z.T., Liu, J.K. and Lu, Z.R. (2016). "Damage identification in plates based on the ratio of modal strain energy change and sensitivity analysis", *Inverse Problems in Science and Engineering*, 24(2), 265-283.

Yasi, B. and Mohammadizadeh, M.R. (2018). "Identification of structural defects using computer algorithms", *Civil Engineering Infrastructures Journal*, 51(1), 55-86.

Zhao, X.K., Wang, R.L., Gu, H.C., Song, G.B. and Mo, Y.L. (2014). "Innovative data fusion enabled structural health monitoring approach", *Mathematical Problems in Engineering*, Vol. 2014, Article ID. 369540, 10 p.

Civil Engineering Infrastructures Journal 2021, 54(2): 267-280
DOI: 10.22059/CEIJ.2020.295339.1647

RESEARCH PAPER

Prediction of Q-Value by Multi-Variable Regression and Novel Genetic Algorithm Based on the Most Influential Parameters

Taban, M.H.[1], Hajiazizi, M.[2*] and Ghobadian, R.[3]

[1] M.Sc. Student, Department of Geotechnical Engineering, Razi University, Kermanshah, Iran.
[2] Associate Professor, Department of Geotechnical Engineering, Razi University, Kermanshah, Iran.
[3] Associate Professor, Department of Water Engineering, Razi University, Kermanshah, Iran.

Received: 05 Jan. 2020; Revised: 17 Apr. 2020; Accepted: 28 May 2020

ABSTRACT: Determination of tunnel support, required for tunnel stability and safety, is an important debate in tunnel engineering field. Q-system classification is a technique used to determine the support system of a tunnel in rock. The problem is that all the required parameters of support system are not accessible. On the other hand, such accesses are very costly and time consuming. Therefore, it is impossible to determine the Q-value in all cases. This paper identifies the most influential parameters of Q-system using SPSS program. Then, it adopts multi-variable regression (MVR) and genetic algorithm (GA) methods to propose a relation for predicting the Q-value using three influential parameters. To this end, 140 experimental data are used. To assess the obtained models, 34 new experimental data, which are not in the primary dataset, are used. The innovation of this paper is that instead of six parameters, the Q-value is determined using three parameters with the highest impact on it instead of six parameters. In this study, the MVR model, with RMSE = 2.68 and correlation coefficient = 0.81 for train data and RMSE = 2.55 and correlation coefficient = 0.80 for test data, showed better performance than GA model, with RMSE = 2.90 and correlation coefficient = 0.82 for train data and RMSE = 2.61 and correlation coefficient = 0.84 for test data.

Keywords: Genetic Algorithm, Influential Parameters, Multi-Variable Regression, Q-System, Tunnel Support.

1. Introduction

Today, underground spaces are increasingly used in developed and developing countries. Limitation on surface spaces, constructing nuclear power plants, and constructing ammunition and weapon depots make it inevitable to use underground spaces and to design tunnels. Different classification systems have been proposed for tunnel design from the past till now. Some researches proposed the empirical methods for designing tunnel supports (Terzaghi, 1946); Wickham et al., 1972; Bieniawki, 1973; Barton et al., 1974). Liu et al. (2004) predicted required tunnel support using Support Vector Regression (SVR) technique. They showed that SVR

* Corresponding author E-mail: mhazizi@razi.ac.ir

can yield acceptable results. Tzamos and Sofianos (2006) used fuzzy logic and predicted tunnel support in Q-system. They used collected data and concluded that fuzzy system shows higher accuracy in predicting tunnel support. Chun et al. (2009) used multinomial regression analysis and multiple regression method to predict the deformation modulus of a rock mass using RMR-system. They showed that the results of both methods almost agree with each other. Majdi and Beiki (2010) used neural network to optimize the estimation of the deformation modulus of rock. They optimized the number of neurons of each layer, the momentum coefficient and the learning rate of hidden and output layers using GA. They showed that the GA method optimizes results and yields better results than neural networks.

Jalalifar et al. (2011) used the fuzzy-neural inference system and predicted RMR-value. They used three types of fuzzy-neural networks and showed that the subtractive clustering method is more efficient in predicting RMR-value. Ding et al. (2013) used hybrid encoding method to propose an algorithm for optimizing the RBF neural network learning based on GA. Jang and Topal (2013) used MVR model and neural network to predict the load-failure curve. They compared the performance of linear MVR, non-linear MVR and neural network in predicting load-failure curve and showed that neural network yields more accurate results than MVR models.

Beiki et al. (2013) used genetic programming method to predict the uniaxial compressive strength and the elastic modulus of carbonated rocks. They used collected data and offered relations based on regression and genetic programming models. They showed that genetic programing yields better results than regression models. Jalalifar et al. (2014) predicted RMR-value using MVR model and fuzzy inference system. They resulted that the latter shows higher accuracy than the former in predicting RMR.

Park et al. (2015) used GA to predict the settlement of thick clay layers and showed that GA could better predict settlement than graphical methods and could serve as a useful tool for reducing calculation time. Miyamoto and Motoshita (2015) attempted to develop a decision support system for rehabilitation strategies of existing concrete bridges, based on the life cycle analysis. They presented a new bridge management system that can be used to evaluate the serviceability of existing concrete bridges. GA technique was used to search for an approximation of the optimal maintenance plan. They showed that this system can accurately predict optimal maintenance planning, as well as bridge rating. Karimaee Tabarestani and Zarrati (2015) was studied the stability of riprap stones around circular as well as aligned and skewed round-nose and tail rectangular bridge piers based on a large amount of experimental data. Alemdag et al. (2016) studied experimental and numerical simulation results to estimate the deformation modulus of stratified rock masses. They used neural networks, fuzzy-neural network and genetic programming. They resulted that genetic programming has higher accuracy than other methods. However, both the neural network and fuzzy-neural network methods show a satisfactory performance.

Erdik and Pektas (2019) for predicting the damage level of armor blocks of breakwaters used the Multivariate Adaptive Regression Splines (MARS) approach. This technique presents a flexible regression by the use of separate regression slopes in distinct intervals of the independent variable. Abdollahzadeh et al. (2017) used two models based on Gene Expression Programming to predict compressive strength of high strength concrete. They used experimental results from a widely spread database that have been used for developing the models. They showed that the suggested GEP models can predict the compressive strength amounts of high strength concrete for each of the training and testing phases according to the

statistical parameters.

Dastorani et al. (2018) used a number of machine learning and data mining methods including support vector machine, regression trees, model trees and artificial neural networks to simulate rainfall-runoff process in Zayandeh Rood dam basin in Iran. Yagiz et al. (2018) developed predictive models for estimating the rock brittleness using two techniques, genetic algorithm, and particle swarm optimization. They developed four different models including linear and non-linear using GA and particle swarm optimization techniques. Hassan (2019) used a GA technique, integrated with the FEM to compute the optimal cut-off location and angle of inclination for barrages constructed on homogenous anisotropic soil foundations. Bhandary et al. (2019) proposed a procedure to determine the safety factor (SF) using the FEM in conjunction with GA. They concluded that the elastic parameters have impact on the value of SF in non-homogenous slope's stability analysis using FEM.

This study implements GA and MVR models to predict the value of Q using the most influential three parameters. Then the results are compared with each other. In this way, Q is calculated by fewer parameters to save costs and time for tunnel design.

2. Q-System

There are different analytical, empirical and numerical approaches to determining tunnel supports. The use of analytical methods depends on the continuum assumption of the domain. In the other hand, numerical methods demand initial data sets which are not easily determinable. In majority of cases, therefore, empirical methods are used to determine tunnel supports. However, the combinations of empirical and numerical methods yield better results. Proposed by Barton et al. (1974), Q-system is the most reputable empirical method with six parameters shown in Eq. (1).

$$\mathrm{Q} = \frac{RQD}{J_n}\frac{J_r}{J_a}\frac{J_w}{SRF} \quad (1)$$

where *RQD*: is the rock quality designation, J_n: is the joint set number, J_r: is the joint roughness number, J_a: is the joint alteration number, J_w: is the joint water reduction factor and *SRF*: is the stress reduction factor. The numerical value of the index *Q* varies on a logarithmic scale from 0.001 to a maximum of 1000.

3. Materials and Methods

3.1. Used Data

The data used in this study were collected from valid references (Goel et al., 1996; Barton, 2002; Anbalagana et al., 2003; Makurat et al., 2006; Dadkhah et al., 2010; Dadkhah and Hoseeinmirzaee, 2014). Totally, 140 data were used in this study. Table 1 shows the range of data used by each reference for modeling purposes. For each data, the values of *RQD, Jn, Jr, Ja, Jw and SRF* were measured. In addition, 34 test data (Schwingenschloegl and Lehmann, 2009; Barton and Gammelsaeter, 2010; Barton and Grimstad, 2014; Barton and Grimstad, 2014; Fereidooni et al., 2015) were used to assess results.

3.2. Multi-Variable Regression (MVR)

In statistical models, regression analysis is a statistical process used to estimate the relationship between variables. It aims to estimate a function from independent variables which are called regression function. Dozens of techniques have been developed for regression analysis. Pearson correlation coefficient is a parametrical method used for data with a normal distribution (Mardia et al., 1979). Pearson correlation analysis was used to determine the effect of all six parameters on Q-system. Table 2 shows the results of Pearson correlation analysis conducted on the parameters of Eq. (1). According to Table 2, the relationship between each parameter and itself is equal to one where Pearson correlation for *Q* is 1 for example. This means that there is a direct and complete

relationship between any parameter with itself. In the process of assessing the correlation of the mentioned 6 parameters with *Q*, if the obtained value is positive, the relationship will be a direct relationship; otherwise, it will be an inverse relationship. Moreover, the closer positive numbers to 1, and the closer negative numbers to -1, the higher is the relationship of that parameter with *Q*. According to Table 2, *RQD, Jn, Jr* and *Ja* have the highest impact on Q. Therefore, the impact of three parameters is first studied, and then the impact of the 4 parameters is evaluated.

The most influential parameters are *RQD*, J_n, J_r and J_a. Therefore, three possible combinations are considered as follows: 1) *RQD*, J_n, J_r, 2) *RQD*, J_n, J_a; and 3) *RQD*, J_n, J_r, J_a (Table 3). It should be mentioned that the obtained results and relationships are valid only in the scope of this study.

3.3. Genetic Algorithm (GA)

As a comprehensive probabilistic search method, GA was introduced by Holland (1975). GA is a programming technique that uses genetic evolution as a problem-solving model. It is an iteration-based algorithm the majority parts of which are selected randomly (Rezae and Rangbaran, 2012). Figure 1 shows the flowchart of the genetic algorithm (Safarzadeh et al., 2017). Visual Basic was used to develop codes for GA model. Table 4 shows the range of parameters used for developing codes for GA. The best model was obtained using these parameters as well as try and error technique. The number of iterations was selected to be 500.

3.4. Accuracy of Assessment

In this study, some statistical parameters including root mean squared error (RMSE), mean squared error (MSE), mean absolute error (MAE) and average absolute deviation (δ) and Nash number were used to assess the accuracy of the obtained models.

Table 1. Variation of collected data for parameter in present study

	Test data				Train data			
Parameters	**STD**	**Mean**	**Maximum**	**Minimum**	**STD**	**Mean**	**Maximum**	**Minimum**
Q	6.53	9.21	19.35	0.006	6.75	9.84	25	0.008
RQD	28.86	78.42	100	10	23.49	79.45	100	10
Jn	4.63	7.64	20	2.5	3.22	6.66	20	3
Jr	0.80	2.25	4	1	0.72	2.39	3.1	1
Ja	2.31	2.65	13	1	1.10	2.26	8	0.75
Jw	0.17	0.90	1	0.5	0.11	0.95	1	0.5
SRF	0.92	2	5	1	0.87	2.15	10	1

Table 2. Result of Pearson correlation analysis

Parameters	***Q***	***RQD***	J_n	J_r	J_a	J_w	***SRF***
Q	1	0.69	-0.64	0.56	-0.53	0.36	-0.23
RQD	0.69	1	-0.67	0.36	-0.56	0.32	-0.40
J_n	-0.64	-0.67	1	-0.47	0.58	-0.25	0.28
J_r	0.56	0.39	-0.47	1	-0.40	0.18	-0.14
J_a	-0.53	-0.56	0.58	-0.40	1	-0.30	0.38
J_w	0.36	0.32	-0.25	0.18	-0.30	1	-0.23
SRF	-0.23	-0.40	0.28	-0.14	0.38	-0.23	1

Table 3. Three types of possible combination of effective parameters on Q value

Models	**Parameters**
Combination 1	*RQD – Jn – Jr*
Combination 2	*RQD – Jn – Ja*
Combination 3	*RQD – Jn – Jr – Ja*

Table 4. Variation of GA parameters

Parameters	**Value**
Population size	100 - 400
Mutaion rate	0.01 – 0.99
Repeat Number	500
Intersection	0.01 – 0.99

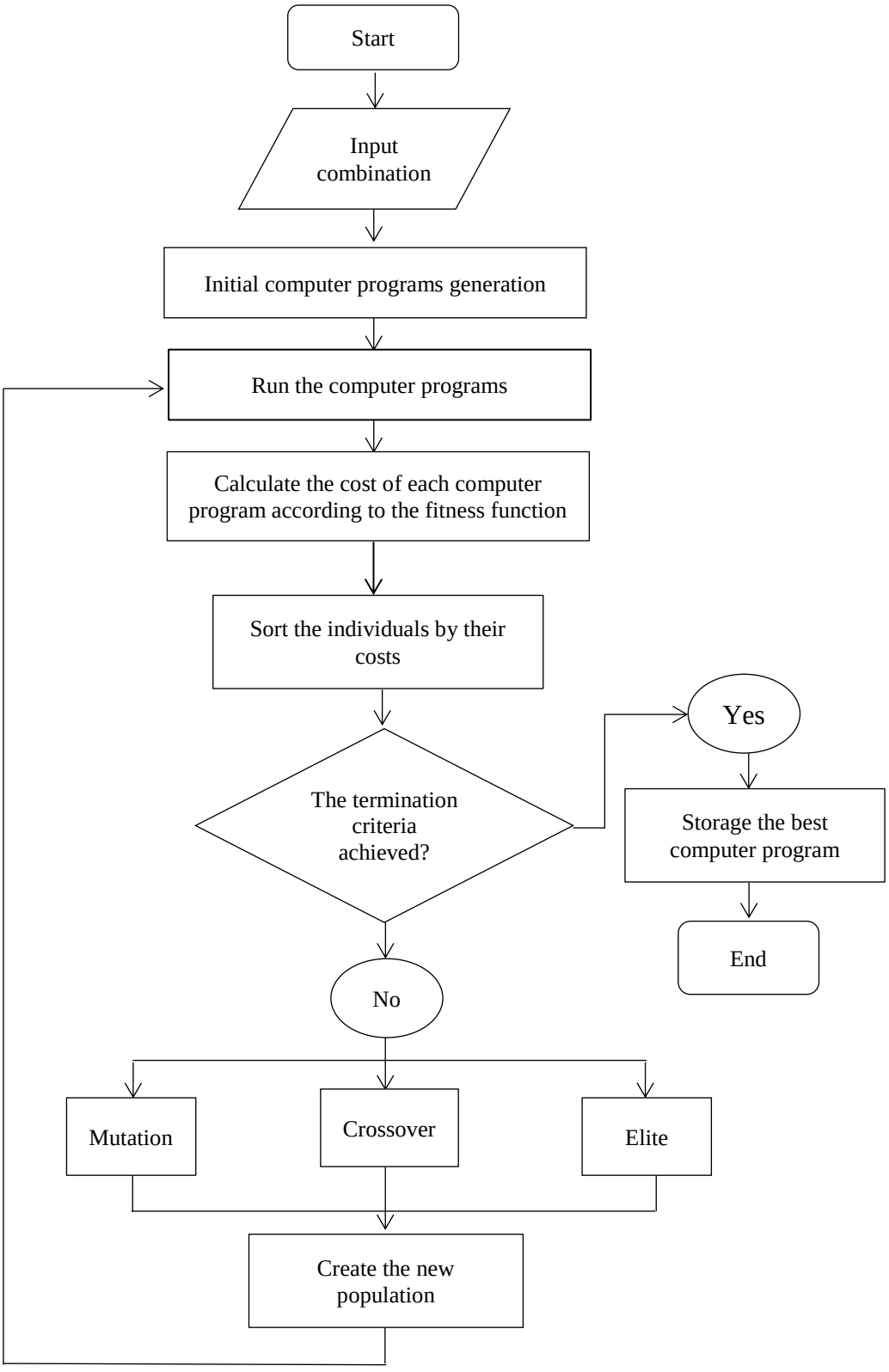

Fig. 1. GA flowchart

The mentioned functions show the difference of predicted deviations and real deviations. The lower values of the functions imply the higher performance of the model. The used statistical parameters are shown in the following:

$$MSE = \frac{\sum_{i=1}^{n}(Y_{p-}Y_m)^2}{n} \quad (2)$$

$$MAE = \frac{1}{\mathrm{n}}\sum_{\mathrm{i=1}}^{\mathrm{n}} |(\mathrm{Y_{p-}Y_m})| \quad (3)$$

$$RMSE = \sqrt{\frac{\sum_{i=1}^{n}(Y_p - Y_m)^2}{n}} \quad (4)$$

$$\delta = \frac{\sum_{i=1}^{n}|(Y_p - Y_m)|}{\sum_{i=1}^{n} Y_p} \times 100 \quad (5)$$

$$R^2 = \left[\sum_{i=1}^{n} \frac{(y_m - \bar{y}_m)(y_p - \bar{y}_p)}{\sqrt{\sum_{i=1}^{n}(y_m - \bar{y}_m)^2 \sum_{i=1}^{n}(y_p - \bar{y}_p)^2}}\right]^2 \quad (6)$$

$$NASH = 1 - \frac{\sum_{i=1}^{n}(Y_p - Y_m)^2}{\sum_{i=1}^{n}(Y_m - \bar{Y}_m)^2} \quad (7)$$

where Y_m, Y_p: are the observed and calculated values for Q, and $\bar{y}_m$, $\bar{y}_p$ and n: are the mean observed value, mean calculated value and number of data, respectively.

4. Results

4.1. Determination of Optimal Models for MVR and GA

In MVR and GA-based modeling, optimal values are proposed by a number of fit functions. Table 5 shows conventional MVR models used in this study for predicting Q-value (Beiki et al., 2013). According to Table 5, the Power equation yields the best result in all models. Figure 2 shows the MVR results of the Power model for all combinations.

In the GA model, the optimum value of parameters was defined after 27 tries and errors. Then, a fitness function was obtained for the optimum values. Table 6 shows the optimum values of GA parameters. RMSE, MAE and Nash function were assessed to select a suitable fitness function for the GA model. Table 7 compares three different fitness functions by statistical parameters. According to Table 7, fitness functions show almost close performances in all models but Nash function yields better results. Figure 3 shows the results of different combinations for Nash fitness function.

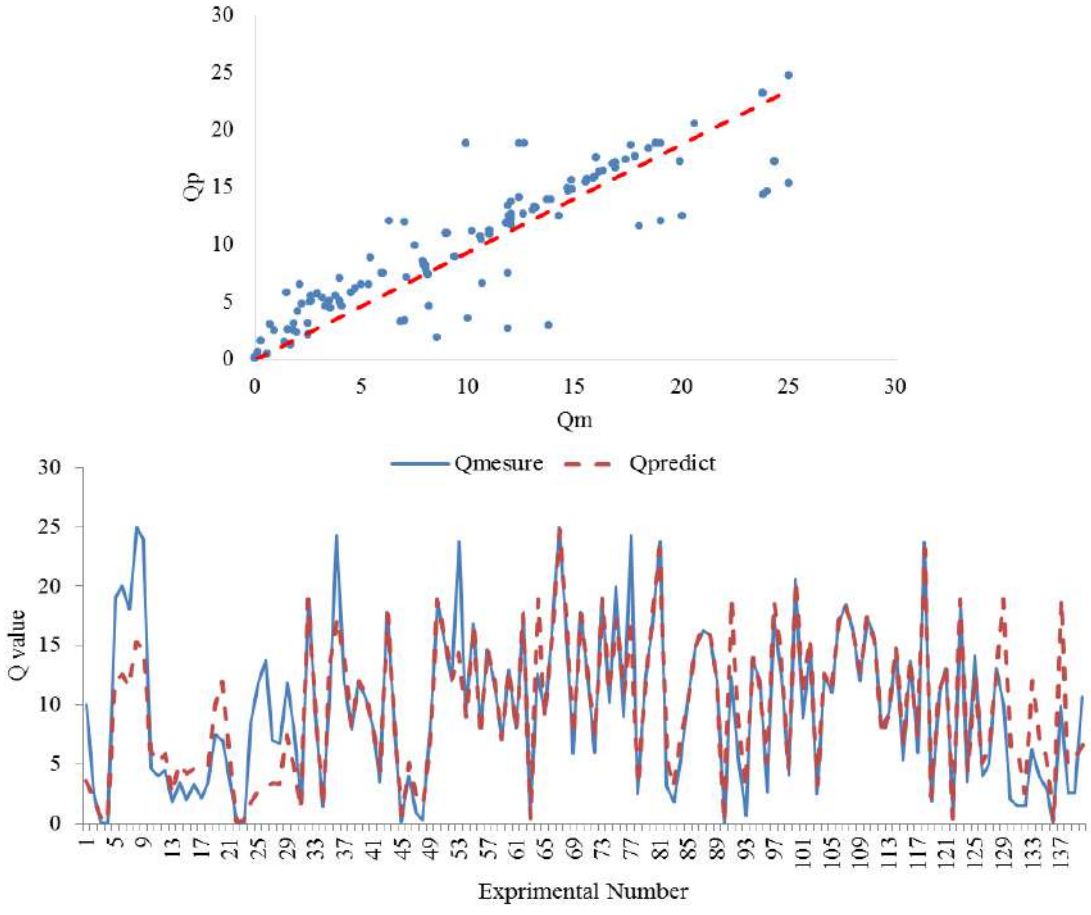

(a)

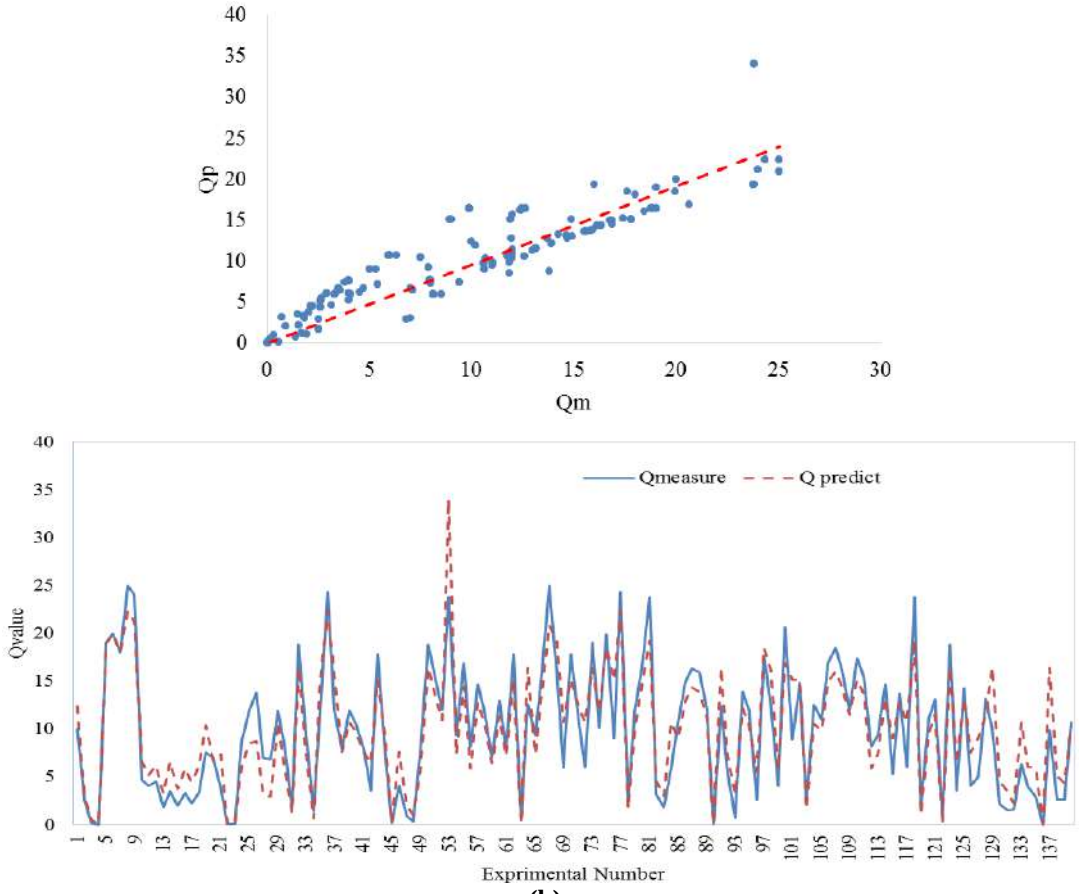

(b)

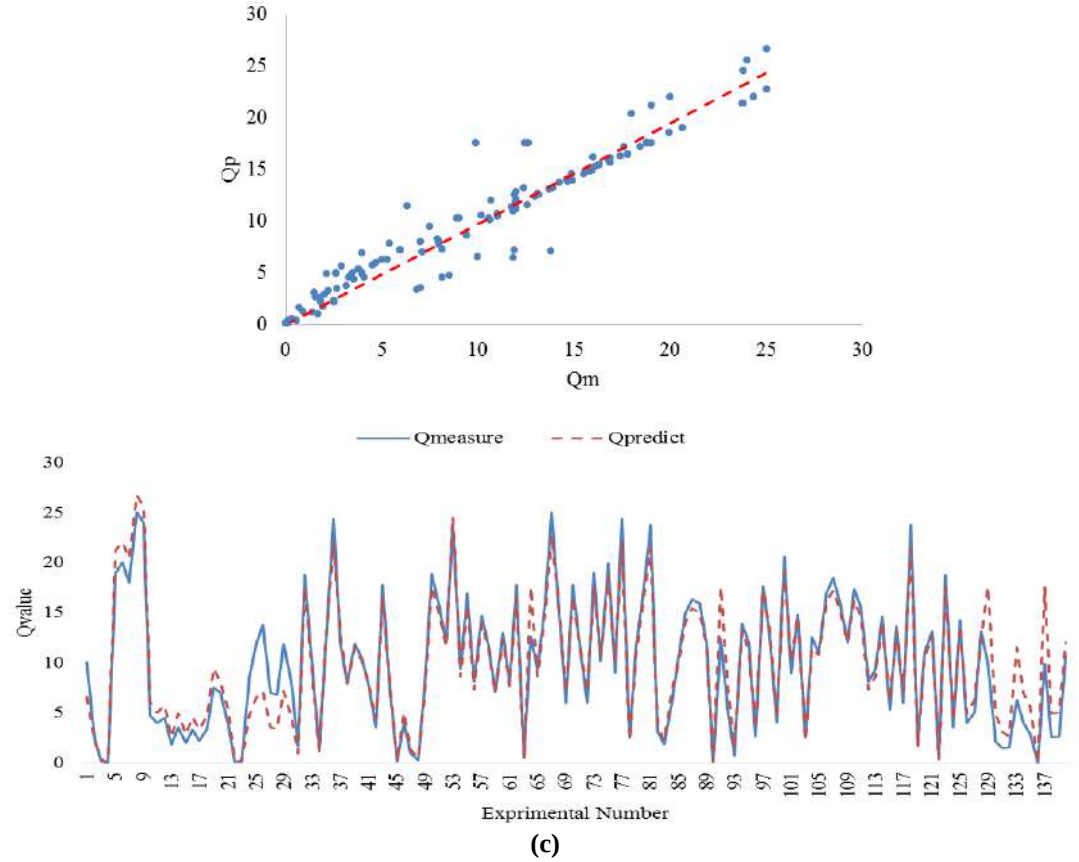

(c)

Fig. 2. Measured against predicted value of *Q* by power model for: a) Combination 1; b) Combination 2; and c) Combination 3 of effective parameters (Table 3)

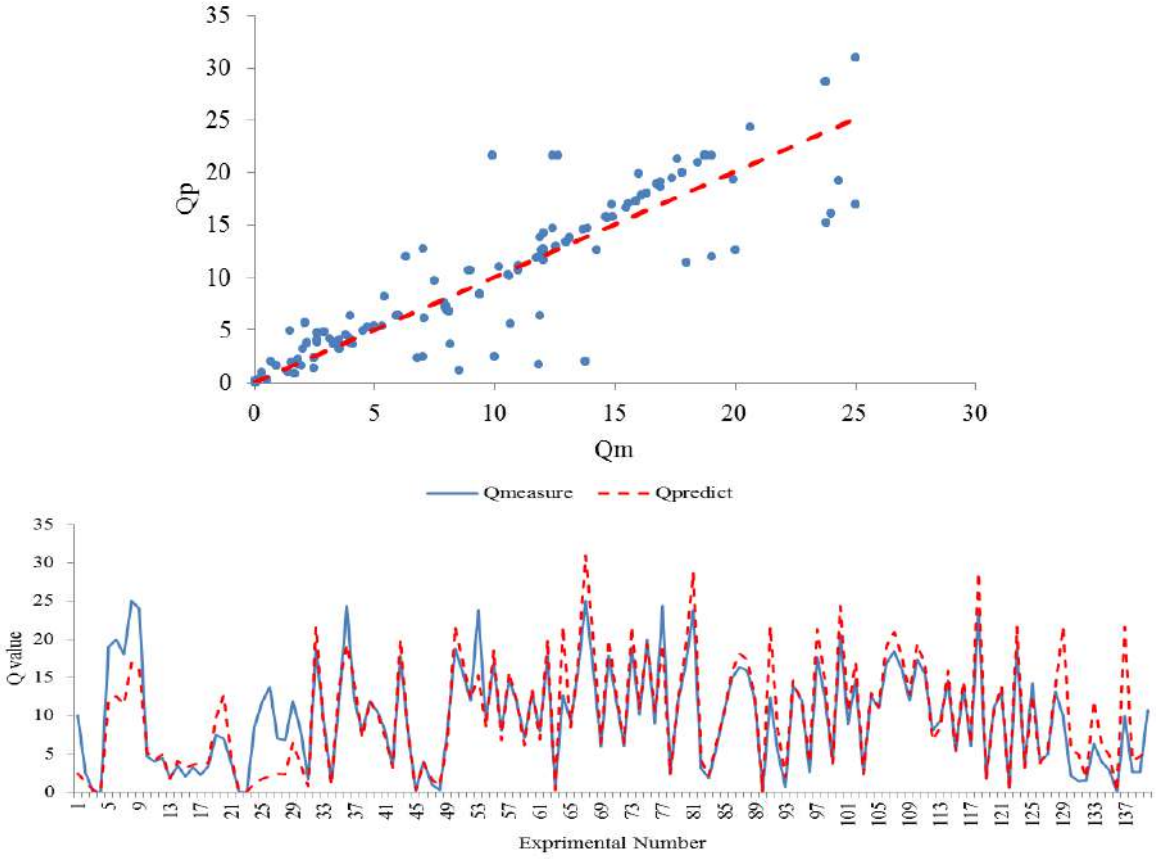
Qp
Qm
Qmeasure
Qpredict
Q value
Exprimental Number

(a)

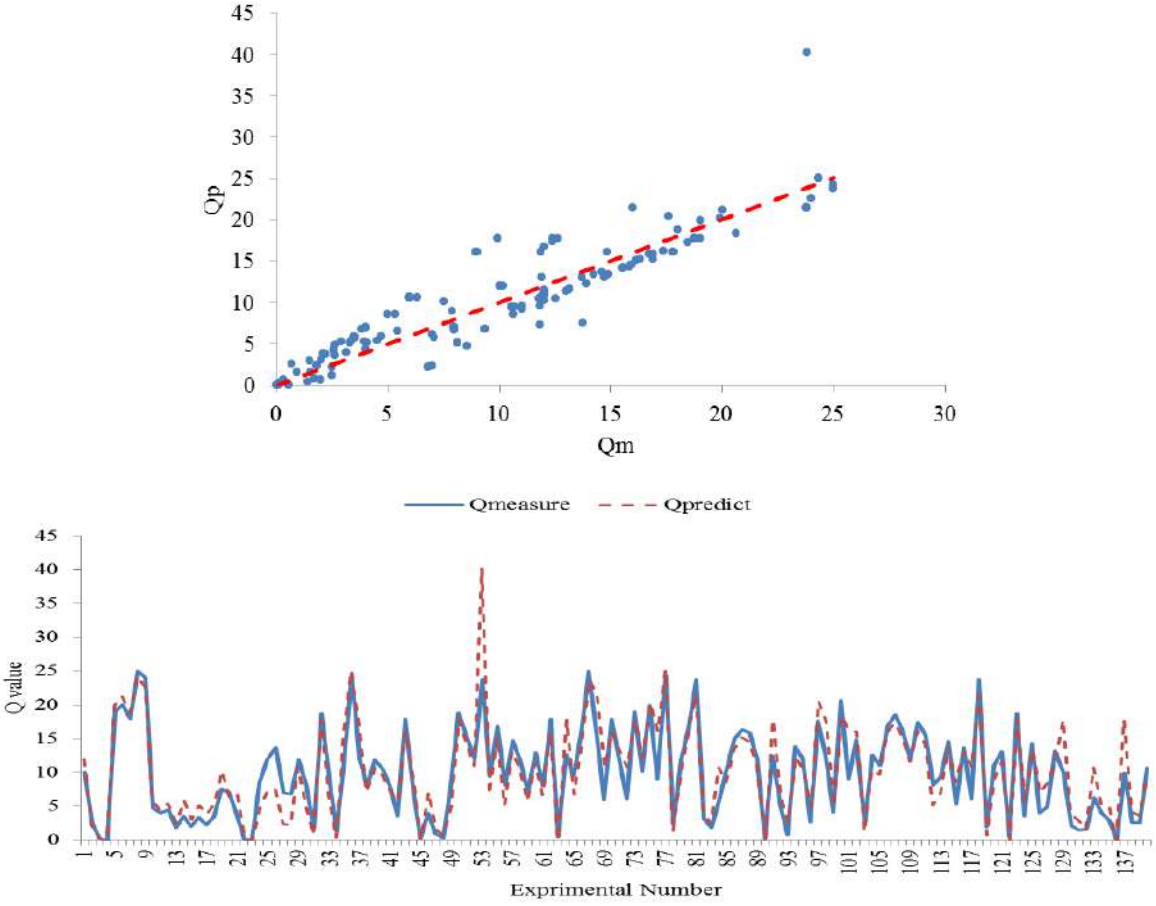
Qp
Qm
Qmeasure
Qpredict
Q value
Exprimental Number

(b)

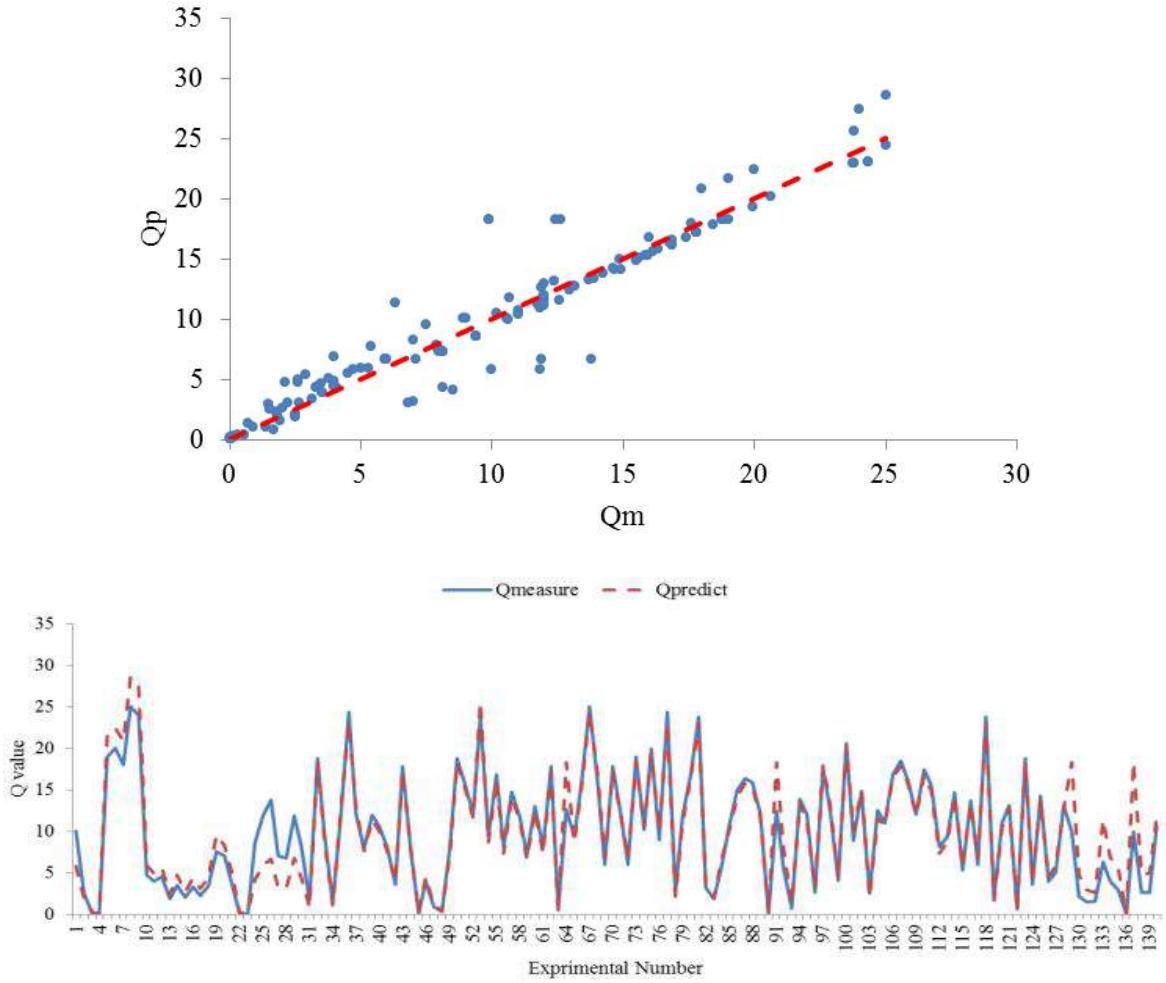

(c)

Fig. 3. Measured against predicted value of *Q* by GA model when using Nash fitness function for: a) Combination 1; b) Combination 2; and c) Combination 3 of effective parameters (Table 3)

Table 5. Statistical parameters for different regression model in prediction of Q values

Regression model	Eqution	Model		Model		Model	
		R	RMSE	R	RMSE	R	RMSE
Linear	$y = \sum_{i=1}^{n} a_i x_i + b$	0.39	4.25	0.27	4.55	0.42	4.23
Inverse	$y = \sum_{i=1}^{n} \frac{a_i}{x_i} + b$	0.35	3.92	0.69	3.36	0.74	3.13
Logarithmic	$y = \sum_{i=1}^{n} a_i \ln(x_i) + b$	0.41	4.19	0.50	4.04	0.56	3.85
Growth	$y = \sum_{i=1}^{n} \exp(a_i)^2 + b$	0.68	4.06	0.33	4.44	0.50	4.01
Power	$y = b \prod_{i=1}^{n} x_i^{a_i}$	0.74	3.12	0.81	2.68	0.91	1.94

Table 6. Optimum values of GA parameters

Parameters	Value
Population size	400
Mutaion rate	0.05
Repeat number	500
Intersection	0

Table 7. Statistical parameters for different fitness function for each model

Models	Fitness function	%δ	GA		
			MAE	RMSE	R
Model 1	RMSE	18.84	1.86	3.13	0.73
	MAE	18.41	1.64	3.19	0.75
	Nash	21.40	2.21	3.47	0.77
Model 2	RMSE	22.94	2.25	2.72	0.81
	MAE	18.53	2	3.03	0.82
	Nash	20.45	2.07	2.90	0.82
Model 3	RMSE	13.86	1.36	1.95	0.91
	MAE	10.10	1.05	2.13	0.90
	Nash	12.03	1.22	2	0.91

4.2. Comparison of Finalized Models

This section compares MVR and GA models in order to determine that which model shows a better performance in predicting the Q-value. Table 8 shows the comparison results. According to this table, train data are very close to each other in all combinations and both models have almost the same performance. Therefore, 34 test data were used to compare results. Table 9 shows the results derived from GA and MVR models for test data. This table reveals that GA and MVR models show close performances in all models where the performance of MVR model is slightly better. Figure 4 compares the results of MVR and GA models for test data where both models show almost the same performance in predicting Q-value by test data. However, the results of MVR model are slightly better than those of GA.

Despite the fact that GA and MVR models yield almost close results, the output results indicate that MVR model yields better results in all models. According to Tables 8-9, both GA and MVR models well assess all types of data. In addition, the Q-value predicted by the proposed models agrees with empirical data. Table 10 shows the coefficients of the equation proposed for the best MVR and GA models. Amongst the three combinations, the second one is proposed due to having fewer parameters with a correlation coefficient of 0.81 and 0.80 for train and test data, respectively. Furthermore, RMSE of train and test data is 2.68 and 2.55, respectively in this combination. In other words, given *RDQ*, J_n and J_a parameters, the Q-value can be obtained with an acceptable approximation.

Table 8. Statistical comparison of GA and MVR models for training data

Statistical parameters	Regression			GA		
	Model 1	Model 2	Model 3	Model 1	Model 2	Model 3
R^2	0.74	0.81	0.91	0.77	0.82	0.91
RMSE	3.12	2.68	1.94	3.47	2.90	2

Table 9. Statistical comparison of GA and MVR models for test data

Statistical parameters	Regression			GA		
	Model 1	Model 2	Model 3	Model 1	Model 2	Model 3
R^2	0.83	0.80	0.93	0.83	0.84	0.93
RMSE	2.55	2.55	1.55	3.13	2.71	1.66

Table 10. Best derived equations for each combination of effective parameters

Models	Proposed equation	a	b	c	d	e	f
Model	$Q = a * \left(\frac{RQD^b}{J_n^c}\right) * \left(\frac{J_r^d}{1}\right) + e$	0.094	1.272	0.944	0.686	0	-
Model	$Q = a * \left(\frac{RQD^b}{J_n^c}\right) * \left(\frac{1}{J_a^d}\right) + e$	0.063	1.585	0.843	0.822	0	-
Model	$Q = a * \left(\frac{RQD^b}{J_n^c}\right) * \left(\frac{J_r^d}{J_a^e}\right) + f$	0.214	1.197	0.895	0.683	0.886	0

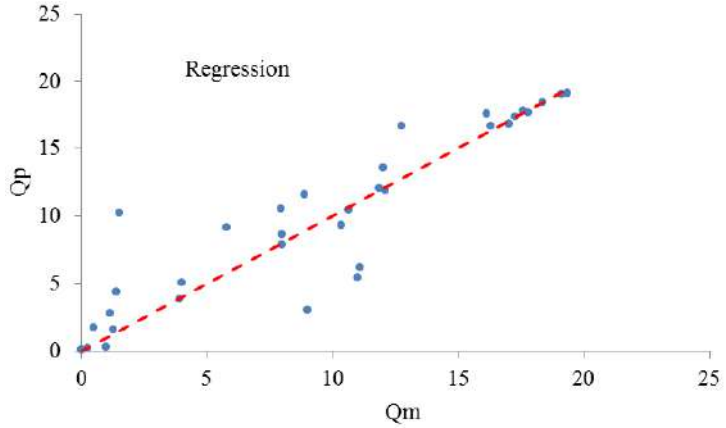
Regression
Qp
Qm
0
5
10
15
20
25

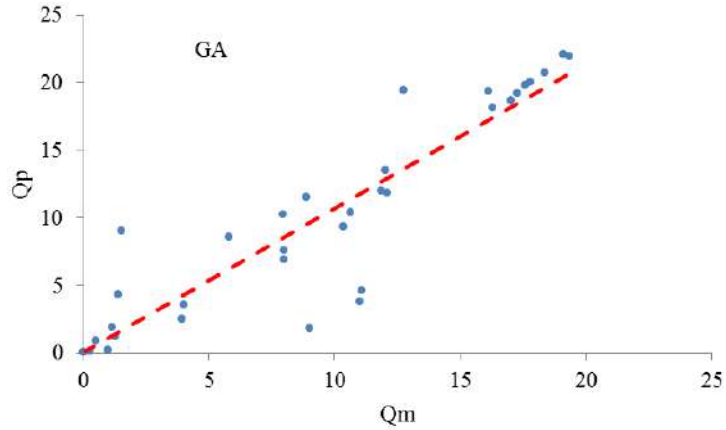
GA
Qp
Qm
0
5
10
15
20
25

(a)

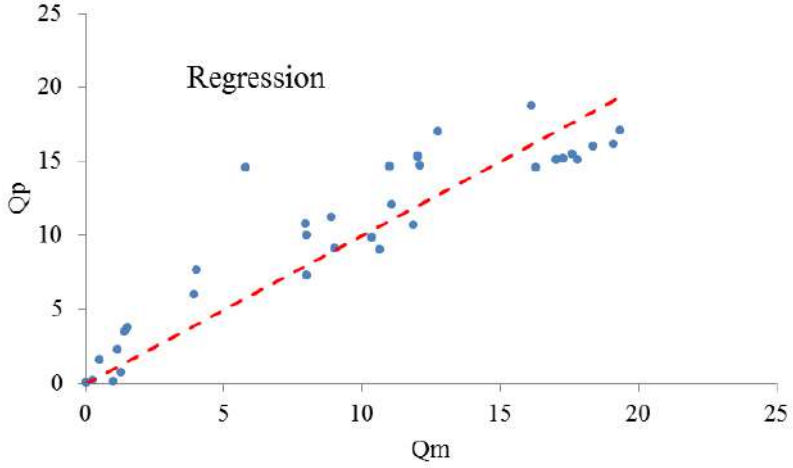
Regression
Qp
Qm
0
5
10
15
20
25

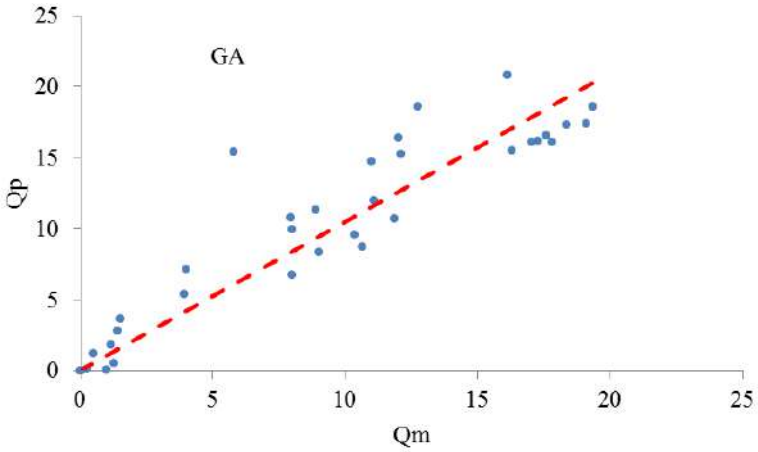
GA
Qp
Qm
0
5
10
15
20
25

(b)

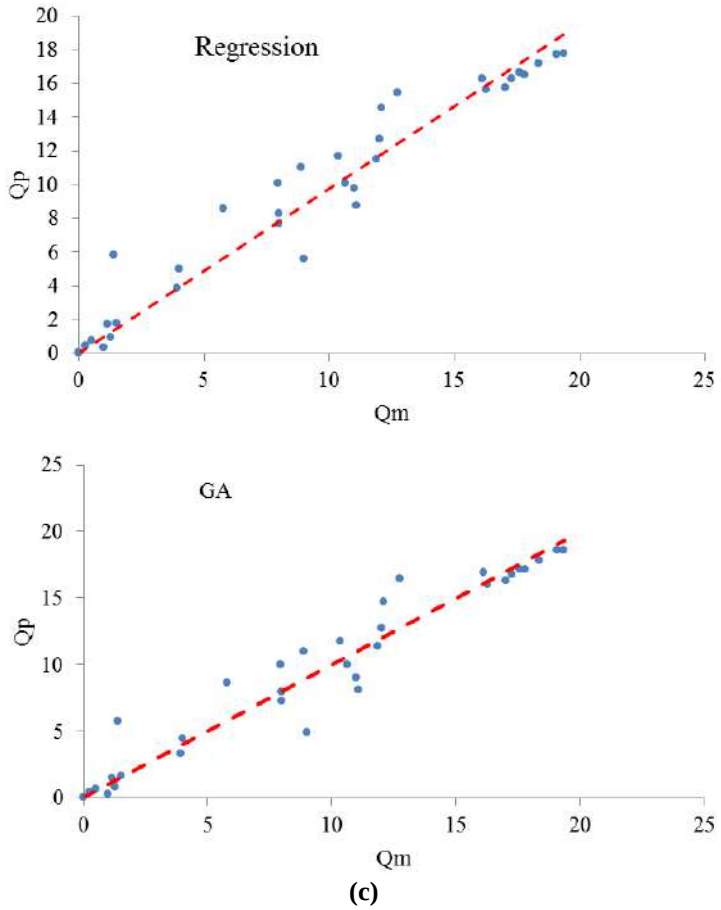

(c)

Fig. 4. . Measured against predicted value of *Q* by GA model when using Nash fitness function for: a) Combination 1; b) Combination 2; and c) Combination 3 of effective parameters (Table 3)

5. Summary and Conclusions

This study evaluated the capabilities of MVR and GA techniques in estimating the Q-value. To this end, 140 experimental data, collected from different tunnels, were used. In addition, three combinations with the highest impact on Q were applied on the models. The effect of each parameter on Q was obtained using Pearson analysis. In MVR model, frequently-used equations were adopted to obtain the best model. In the GA model, however, different fitness functions were used, after obtaining optimal parameters, to obtain the best model. In the MVR and GA models, Power equation and Nash function yielded the best results, respectively. The extracted models, then, were compared with each other. According to the obtained results, both models show an acceptable performance. However, MVR model works slightly better. In addition, the results of both models were assessed by 34 test data which were not among the primary data set.

Finally, the second combination of MVR model with RMSE=2.68 and 2.55 for train and test data, respectively, was elected as the best combination due to showing more acceptable performance and having fewer parameters. The determination of all parameters of Q is a costly and time-consuming process which is not always accessible. However, the results of this study indicated that the Q-value could be calculated only by three parameters by which acceptable results could be obtained.

6. References

Abdollahzadeh, G.R., Jahani, E. and Kashir, Z. (2017). "Genetic Programming based formulation to predict compressive strength of high strength concrete", *Civil Engineering Infrastructures Journal*, 50(2), 207-219.

Alemdag, S., Gurocak, Z., Cevik, A., Cabalar, A.F. and Gokceoglu, C. (2016). "Modeling deformation modulus of a stratified sedimentary

rock mass using Neural Network, Fuzzy Inference and Genetic Programming", *Engineering Geology*, 203, 70-82.

Anbalagana, R., Singhb, B. and Bhargavab, P. (2003). "Half tunnels along hill roads of Himalaya, An innovative approach", *Tunnelling and Underground Space Technology*, 18, 411-419.

Barton, N. (2002). "Some new Q-value correlations to assist in site characterization and tunnel design", *International Journal of Rock Mechanics and Mining Sciences*, 39, 185-216.

Barton, N. and Gammelsaeter, B. (2010). "Application of the Q-system and QTBM prognosis to predict TBM tunnelling potential for the planned Oslo-Ski Rail tunnels", *Nordic Rock Mechanics Conference*, Kongsberg, Norway.

Barton, N. and Grimstad, E. (2014). "Forty years with the Q-system in Norway and Abroad", *FJELLSPRENGNINGSTEKNIKK*, NFF, Oslo, 4.1-4.25.

Barton, N. and Grimstad, E. (2014). "Q-system, An illustrated guide following Forty years in tunnelling", Technical Report, www.nickbarton.com.

Barton, N.R., Lien, R. and Lunde, J. (1974). "Engineering classification of rock masses for the design of tunnel support", *Rock Mechanics*, 6(4), 189-239.

Beiki, M., Majdi, A. and Givshad, A. (2013). "Application of genetic programming to predict the uniaxial compressive strength and elastic modulus of carbonate rocks", *International Journal of Rock Mechanics and Mining Sciences*, 63, 159-169.

Bhandary, R.P., Krishnamoorthy, A. and Rao, A.U. (2019). "Stability analysis of slopes using Finite Element method and Genetic Algorithm", *Geotechnical and Geological Engineering*, 37, 1877-1889.

Bieniawski, Z.T. (1973). "Engineering classification of jointed rock masses", *Transaction of the South African Institution of Civil Engineers*, 15, 335-344.

Chun, B.S., Ryu, W., Sagong, M. and Nam Do, J. (2009). "Indirect estimation of the rock deformation modulus based on polynomial and multiple regression analyses of the RMR system", *International Journal of Rock Mechanics and Mining Sciences*, 46, 649-658.

Dadkhah, R., Ajalloeian, R. and Hoseeinmizaei, Z. (2010). "Investigation of engineering geology characterization of Khersan 3 dam site", *The 1st International Applied Geological Congress*, Tabriz, Iran.

Dadkhah, R. and Hoseeinmirzaee, Z. (2014). "Determination strength parameters rock masses Jajarm tunnel based on geotechnical study", *Journal of Biodiversity and Environmental Sciences*, 4(6), 495- 502.

Dastorani, M.T., Mahjoobi, J., Talebi, A. and Fakhr, F., (2018). "Application of machine learning Aapproaches in rainfall-runoff modelling (Case study: Zayabdeh Rood basin in Iran)", *Civil Engineering Infrastructures Journal*, 51(2), 293-310.

Ding, S., Xu, L., Su, C. and Jin, F. (2013). "An optimizing method of RBF Neural Network based on Genetic Algorithm", *Neural Computing and Applications*, 21(2), 333-336.

Erdik, T. and Pektas, A.O. (2019). "Rock slope damage level prediction by using multivariate adaptive regression splines (MARS)", *Neural Computing and Applications*, 31, 2269-2278.

Fereidooni, D., Khanlari, Gh. and Heidari, M. (2015). "Assessment of a modified rock mass classification system for rock slop stability analysis in the Q-system", *Earth Sciences Research Journal*, 19(2), 147-152.

Goel, R.K., Jethwa, J.L. and Paithankar, A.G. (1996). "Correlation between Barton's Q and Bieniawski's RMR, A new approach", *International Journal of Rock Mechanics and Mining Sciences*, 33(2), 179-181.

Hassan, W.H. (2019). "Application of a Genetic Algorithm for the optimization of a location and inclination angle of a cut-off wall for anisotropic foundations under hydraulic structures", *Geotechnical and Geological Engineering*, 37, 883-895.

Holland, J. H. (1975). *Adaptation in natural and artificial systems*, University of Michigan Press, Ann Arbor.

Jalalifar, H., Mojedifar, S., Sahebi, A.A. and Nezamabadipour, H. (2011). "Application of the adaptive neuro-fuzzy inference system for prediction of a rock engineering classification system", *Computers and Geotechnics*, 38, 783-790.

Jalalifar, H., Mojedifar, S. and Sahebi, A.A. (2014). "Prediction of rock mass rating using fuzzy logic and multi-variable RMR regression model", *International Journal of Mining Science and Technology*, 24, 237-244.

Jang, H. and Topal, E. (2013). "Optimizing overbreak prediction based on geological parameters comparing multiple regression analysis and Artificial Neural Network", *Tunnelling and Underground Space Technology*, 38, 161-169.

Karimaee Tabarestani, M. and Zarrati, A.R. (2015). "Design of riprap stone around bridge piers using Empircal and Neural Network method", *Civil Engineering Infrastructures Journal*, 48(1), 1755-188.

Liu, K.Y., Qiao, C.S. and Tian, S.F. (2004). "Design of tunnel shotcrete-bolting support based on a Support Vector Machine", *International Journal of rock Mechanics and Mining Sciences*, 41(3),

3-9.
Majdi, A. and Beiki, M. (2010). "Evolving neural network using a genetic algorithm for predicting the deformation modulus of rock masses", *International Journal of Rock Mechanics and Mining Sciences*, 47, 246-253.
Mardia, K.V., Kent. J.T. and Bibby. J.M. (1979). *Multivariate analysis*, Academic Press, ISBN 0-12-471252-5.
Makurat, A., Loset, F., Wold Hagen, A., Tunbridge, L., Kveldsvik, V. and Grimstad, E. (2006). "A descriptive rock mechanics model for the 380-500 m level", Norwegian Geotechnical Institute, Report No. R-02-11, ISSN 1402-3091.
Miyamoto, A. and Motoshita, M. (2015). "Development and practical application of a bridge management System (J-BMS) in Japan", *Civil Engineering Infrastructures Journal*, 48(1), 189-216.
Park, H., Kim, K. and Kimb, Y. (2015). "Field performance of a genetic algorithm in the settlement prediction of a thick soft clay deposit in the southern part of the Korean peninsula", *Engineering Geology*, 196, 150-157.
Rezae, A. and Rangbaran, S. (2012). *Practical training Genetic Algorithm and Fuzzy Logic in Matlab*, Padideh Publication.
Safarzadeh, A., Zaji, A.M. and Bonakdari, H. (2017). "Comparative assessment of the Hybrid Genetic Algorithm, Artificial Neural Network and Genetic Programming methods for the prediction of longitudinal velocity field around a single straight groyne", *Applied Soft Computing*, 60, 213-228.
Schwingenschloegl, R. and Lehmann, Ch. (2009). "Swelling rock behaviour in a tunnel: NATM-support vs. Q-support, A comparison", *Tunnelling and Underground Space Technology*, 24, 356-362.
Terzaghi, K. (1946). "Rock defects and loads on tunnel supports in rock tunneling with steel supports", *Commercial Shearing and Stamping Company*, 1, 17-99.
Tzamos, S. and Sofianos, A.I. (2006). "Extending the Q system prediction of support in tunnels employing fuzzy logic and extra parameters", *International Journal of rock Mechanics and Mining Sciences*, 43, 938- 949.
Wickham, G.E., Tiedemann, H.R. and Skinner, E.H. (1972). "Support determination based on geologic predictions", *North American Rapid Excavation Tunneling Conference*, Chicago, pp. 43-64.
Yagiz, S., Ghasemi, E. and Adoko, A.C. (2018). "Prediction of rock brittleness using Genetic Algorithm and Particle Swarm Optimization techniques", *Geotechnical and Geological Engineering*, 36, 3767-3777.

Civil Engineering Infrastructures Journal 2021, 54(2): 281-299
DOI: 10.22059/CEIJ.2020.295522.1649

RESEARCH PAPER

Building Information Modeling Deployment in Oil, Gas and Petrochemical Industry: An Adoption Roadmap

Fakhimi, A.[1], Majrouhi Sardroud, J.[2*], Mazroi, A.[3], Goreishi, S.R.[4] and Azhar, S.[5]

[1] Ph.D. Candidate, Department of Civil Engineering, Central Tehran Branch, Islamic Azad University, Tehran, Iran.
[2] Associate Professor, Department of Civil Engineering, Central Tehran Branch, Islamic Azad University, Tehran, Iran.
[3] Assistant Professor, Department of Civil Engineering, Central Tehran Branch, Islamic Azad University, Tehran, Iran.
[4] Ph.D., Principal Engineer in the DNV GL - Oil and Gas, Det Norske Veritas, Denmark A/S.
[5] Associate Professor, Mc Whorter School of Building Science, College of Architecture, Design and Construction, Auburn University, AL, USA.

Received: 15 Jan. 2020; Revised: 17 Sep. 2020; Accepted: 28 Sep. 2020

ABSTRACT: The implementation of Building Information Modeling (BIM) in the Architecture, Engineering and Construction (AEC) industry is growing rapidly. The Oil, Gas and Petrochemical industry (OGPi), however, is still lagging in harnessing the BIM capabilities. Therefore, the main question of this research is: How and what actions should be adopted for deploying BIM in the OGPi? The research is divided into three parts as an action research. This study investigates the second part, namely preparation of an adoption roadmap for deploying BIM in collaboration with Integrated Project Delivery (IPD) in the OGPi. To achieve this goal, an extensive literature review including the most established roadmaps in the AEC industry and also the semi-structured interviews with the OGPi's experts are conducted. Then, an adoption roadmap is derived for OGPi via Innovation Diffusion Theory (IDT), 'Why, How, What' questions (Sink model), strategic planning and innovation roadmap as well as the iterative process in the studies and interviews. The prepared roadmap validated by triangulation through focus group meetings and oils the wheels of BIM implementation alongside with IPD in the OGPi firms to grabs BIM merits and harness its challenges. Finally, the major limitations and the required future studies are addressed.

Keywords: Adoption Roadmap, BIM, IDT, Integrated Project Delivery, OGP Industry.

1. Introduction

Oil, Gas and Petrochemical (OGP) industry has important differences with the Building (AEC) industry, such as: the high-risk atmosphere for all parties in whole lifecycle, need to high-quality material and equipment due to harsh operating environment, vast investment, long-term construction period, high complexity, high-

* Corresponding author E-mail: j.majrouhi@iauctb.ac.ir

level technical requirements, multidisciplinary team working through whole lifecycle, and many other aspects (Song, 2007). Nowadays, due to the complexity of civil and infrastructure projects including the AEC, Non-Building (NB) projects and Oil, Gas and Petrochemical Industry (OGPi), new construction management theories are needed to achieve higher performance and greater improvement (Le et al., 2018). In this regard, to overcome the big dilemmas of project complexities, the Integrated Project Delivery (IPD) and Building Information Modelling (BIM) have been emerged as the enhanced ideas for crossing the operational and technological perspectives of the project complexities (Singh et al., 2017; AIA, 2014).

Due to the differences with respect to other industries including AEC, OGPi has already moved towards the new theories of construction management to achieve the improved performance (Rui et al., 2017; Songhurst, 2014). For this purpose, OGPi has started implementing IPD methods to overcome the low efficiency and productivity issues since 1990 (O'Connor, 2009). According to AIA (American Institute of Architects), the most recent definition of IPD is defined as: A project delivery method that integrates people, systems, business structures and practices into a process that collaboratively harnesses the talents and insights of all participants to reduce waste and optimise efficiency through all phases of design, fabrication and construction (AIA, 2014). The minimum elements of IPD approach consist of six major characteristics: 1) A multi-party contract; 2) Early involvement of key partners; 3) Collaborative decision making and control during whole project lifecycle; 4) Shared risks and rewards based on project outcomes; 5) limited liability among key partners; and 6) Developing project objectives jointly (Ghassemi, 2011; AIA, 2014). These characteristics are widely distinct from the traditional project delivery characteristics (Bosch-Sijtsema, 2019) and they are referred to as IPD1 to IPD6 in this study, respectively.

Despite the fact that the OGP industry is wider and more complex than AEC industry (Wang et al., 2016), OGPi has demonstrated its incentivises and capabilities for using the digital modelling technologies to improve the cost, time, quality and efficiency which is very similar to BIM as the novel idea (Lee et al., 2016). Furthermore, projects of the oil, gas and petrochemical industry are more structured and the key partners are familiar with the concept of integrated project delivery. Considering these issues, this research aims to investigate the adoption of BIM technology in collaboration with IPD method to achieve a modern method in the OGPi firms to overcome the low productivity and efficiency. The previous study in the first part of this research clearly showed that the BIM has not yet been implemented in the oil, gas and petrochemical industry and there is still a deep gap for its deployment in this context (Fakhimi et al., 2017). Since the projects of the oil, gas and petrochemical industry have wider and larger technical, financial and executive dimensions than the AEC industry projects, many attempts are needed to alleviate the losses and wastes and improve the productivity and efficiency. This need has been further increased in the current situation, as the global oil price has fallen and the recession caused by the lack of projects has hit the industry.

The research objective is to offer an insight and provide the valid information necessary to help the study make the right decisions about BIM adoption in OGPi firms alongside IPD. For this purpose, in the first part of this research, the data is gathered through the literature review and interviews and show that BIM can be highly beneficial for OGP industry and can empower it quicker than before. The first part consists of: 1) The shortage of appropriate research; 2) The implementation of BIM in OGPi has not yet been launched systematically; and 3) The

need for an expressive strategy that can harness the challenges and offer a BIM implementation guideline for OGPi firm's projects.

The aim of this part of the research is to identify the causes that challenge the BIM adoption in OGPi firms and to derive a roadmap for an optimised and structured adoption process in the OGPi firms. In this way, it can lubricate the wheels of BIM implementation and its synergism with IPD in the OGPi firms to grabs BIM merits and harness its challenges. In the next part, what has been done in the OGP industry for BIM is stated. After that, the research method and results are presented. In the results section, the way of preparing the roadmap along with the necessary activities and actions for its implementation are presented. At the end, findings including the roadmap and conclusion are given.

2. Background

Almost a decade ago, AEC industry has introduced and implemented the Building Information Modelling (BIM) (Azhar et al., 2012). There are too many different definitions for BIM, but as a commonly appreciated definition, BIM is the digital representation of physical and functional characteristics of a facility. A BIM is a shared knowledge resource for information about a facility, forming a reliable basis for decisions during its life-cycle, defined as existing from earliest conception to demolition (NIBS, 2007).

A review of the way BIM has been launched in different countries and organisations has made it clear that they have prepared a roadmap for BIM adoption before taking any other action (Khosrowshahi, 2012; Hafizah et al., 2015; Silva et al., 2016). According to Bob Galvin, former CEO of Motorola, an all-encompassing view of the future about a specific field using collective knowledge and considering of the brightest drivers of change in that field is called the 'roadmap' (Cetindamar et al., 2013). The roadmapping approach has many cited benefits. However, the communication across functional and organisational boundaries is the most frequently cited benefit (Phaal, 2015).

Performing a relatively comprehensive review of the use of BIM has revealed the application of this technology in the OGP industry. It has shown that, with the exception of a limited number of cases that have implemented BIM in some part of life cycle (Table 1), no cases have been reported on the use of BIM in whole lifecycle of the oil, gas and petrochemical industry firms and their projects (Cheng et al., 2016). In addition, in another research on 28 BIM instructions from around the world, 83 academic papers and 101 case studies concerning the digital modelling in the OGPi showed that the overlapped applications of BIM in the AEC industry and digital modelling in the OGPi are overwhelming. The research described 36 BIM applications that were very similar to digital modelling applications and could be used in the OGPi (Lee et al., 2016). In fact, it highlighted the lack of research on the implementation of BIM in OGPi and its importance.

On the other hand, a study was previously conducted as the first part of this research to investigate the influence of BIM on the oil, gas and petrochemical industry. The way of implementing BIM and how to overcome the challenges were the main concern of the OGPI experts. The strategic level persons generally focused on the challenges that effected their organization characteristics like standard BIM contract, needed business model, main requirements of the BIM implementation (cost, time, tools, etc.) and financial benefits. At the tactical level any changes that affected the execution of the project like data exchange methods, interoperability, needed training, work processes and workflows, staff roles and responsibilities, information flow management and parties' roles and responsibilities, were placed in the center of their concern. The operational level persons

were concerned over new methods and standards, applicability of specialized software, required training, integration of information, and redefining staff roles and responsibilities. In the first part, it was shown that BIM research should be in line with the OGP industry trend and needs to providing an adoption roadmap was recommended in this regards. It was concluded that an appropriate roadmap accelerates BIM implementation alongside IPD in the OGPi firms (Fakhimi et al., 2017). Thus, given the capabilities and flexibility with which a roadmap can be used as an efficient and powerful tool for deploying strategic plans, this research conducted the BIM roadmap and accomplished related actions for the OGPi firms. To this end, this study was inspired by the long-term strategic planning of complex projects (Shadid, 2017) in AEC industry in the countries such as England (Khosrowshahi, 2012), Hong Kong (Construction Industry Council, 2014), Portugal (Silva et al., 2016), Canada (Building SMART Canada, 2014), Australia (Hafizah et al., 2015) and Singapore (Teo et al., 2016) for adopting and deploying BIM in the AEC industry where the roadmap played a pivotal role in providing the right path based on the identification of the existing situation and the related implementation challenges.

3. Research Design and Methods

3.1. Research Design

The present research is planned as an action research that uses the reflective practice method. It is divided into three parts (Figure 1). At the first part, the capabilities of BIM in OGPi, the related challenges and the most important prerequisite for deploying BIM in OGPi are addressed via the literature review and interviewing with the experts of Iranian OGPi firms. The present study (the second part of the research) focuses on deriving BIM adoption roadmap alongside IPD for the OGPi firms through the recommendations of the first part and an iterative process based on the comments from the specialists (Figure 1). The research is designed in the context of Iranian OGPi firms so as to make it possible to evaluate the results using the views of experts. Considering the scope of this study, the phases of implementing and evaluating the actual process are performed in the third part of the research. Hence, the evaluation of the results in the form of roadmap implementation in a realistic case is performed in the third part of the research.

3.2. Research Methods

The actions for adopting the roadmap for OGPi firms should be provided through considering the causes of BIM implementation challenges in AEC industry, as defined in part 1. In this sense, the roadmap focused on the processes necessary to deploy BIM alongside IPD for OGP industry, considering the main challenges and their causes identified in part 1, and did not concentrate on the costs and schedules for these activities. Therefore, the input data consists of literature review (theoretical documents, theory on the technology and BIM implementation approaches, standards and scientific practice that can assist in specifying the research perspective) and empirical practical information formulated by interviewees. As such, an initial roadmap was established which discussed with OGPi experts through semi-structured interviews. As a rule, the interviews had to be continued to reach the saturation and no new data to be provided in the interviews (Marshall et al., 2013), but contrary to the AEC industry and due to the fact that the OGP industry is wider and more complex, the key people involved in this industry were limited and therefore, the selection of the interviewees was exclusive.

Considering the fact that it was not possible to reach saturation, based on the recommendations in such cases, it is decided to select 40 key personnel for the interview (Mason, 2010). The interviewees

were selected according to their responsibilities and/or previous experiences (Table 2) from the whole key stakeholders of the OGP industry (owner/client, general contractor and consultant, operators and facility managers). They had enough knowledge in their field of expertise and were well versed in modern construction management practices. Most of the interviewees were aware of BIM and had experience in implementing new construction management practices in their firms. However, they had no experience of working in BIM environment. The total time spent on the interviews was 490 minutes for top managers (8 person), 2060 minutes for senior managers (24 person), 550 minutes for others (8 person) and 135 minutes for two separate joint meetings, with an average value of about 77 minutes per person (Table 2). Joint meetings were conducted for presenting, discussing and finalising the results of interviews with all interviewees.

In this study, the Grounded Theory (GT) was used to analyse the data collected from the literature reviews and semi-structured interviews (Khan, 2014) and to extract the final roadmap. This theory was used as the basis for the use of Innovation Diffusion Theory (IDT). IDT is one of the most behaviour-change models that used commonly over a wide area of innovation adoption (Hong et al., 2019; Akintola et al., 2019) and argues about spreading the innovation into a new area.

Rogers (2003) defines innovation as 'an idea, practice or object that is perceived as new by an individual or another unit of adoption', diffusion as 'the process by which an innovation is communicated through certain channels over time among the members of a social system' and adoption as a decision of 'full use of an innovation as the best course of action available'. The IDT has been founded on five underpinned pillars for adoption, each with its own attributes. In order to spread the BIM in OGPi, inspired by the Innovation Diffusion Theory (IDT), five phases including awareness, convincing, decision making (implementation design), implementation, and evaluation were applied.

Table 1. Research for using BIM in various sector of OGP industry

Sector	Main objective	Domain	Reference
Liquid natural gas	Productivity improvement via integrates advanced technologies including ICT, RFID, smart tag, laser scanning, BIM and AR in real LNG construction.	Construction	Lei et al. (2014)
Liquid natural gas	Construction Process controlling through AR+BIM	Construction	Wang et al. (2014)
Oil and gas facilities	Quality improvement of operating activities via involving the operator and subcontractors during the construction phase	Construction	Bezkorovayniy et al. (2018)
Offshore oil and gas platforms	Process Optimisation of multiple offshore platforms disassembly using BIM and GIS	Demolishing	Tan et al. (2018)
Offshore oil and gas platforms	Evaluation of different decommissioning options	Demolishing	Cheng et al. (2017)
Petroleum pipeline	Corrosion prediction	Operation	Tsai et al. (2019
Offshore oil and gas platforms	BIM-base process of offshore platforms disassembly	Demolishing	Tan et al. (2017)
Offshore oil and gas platforms	BIM-based 4D simulation for mitigating noise impact on maintenance workers	Operation	Tan et al. (2019)
Offshore oil and gas platforms	Evaluation of evacuation scenarios	Engineering	Cheng et al. (2018)
Liquid natural gas	Resource allocation	Construction	Zhou et al. (2015)
Oil/Gas industry	Increasing collaboration between engineering and construction in detail	Engineering	Larson (2019)
Oil/Gas industry	Suggesting appropriate integration technology for engineering company	Engineering	Xue (2015)

Table 2. Summarized results of interview

Partner	No. of interviewee	Average experience (year)	Total interview duration (Min.)	Average interview duration (Min./Per.)
Client/Owner	6	>20	375	62.5
General Contractor	28	>15	2300	82
Operator/FM	6	>20	425	71
Total	40	17.5	3100	77.5

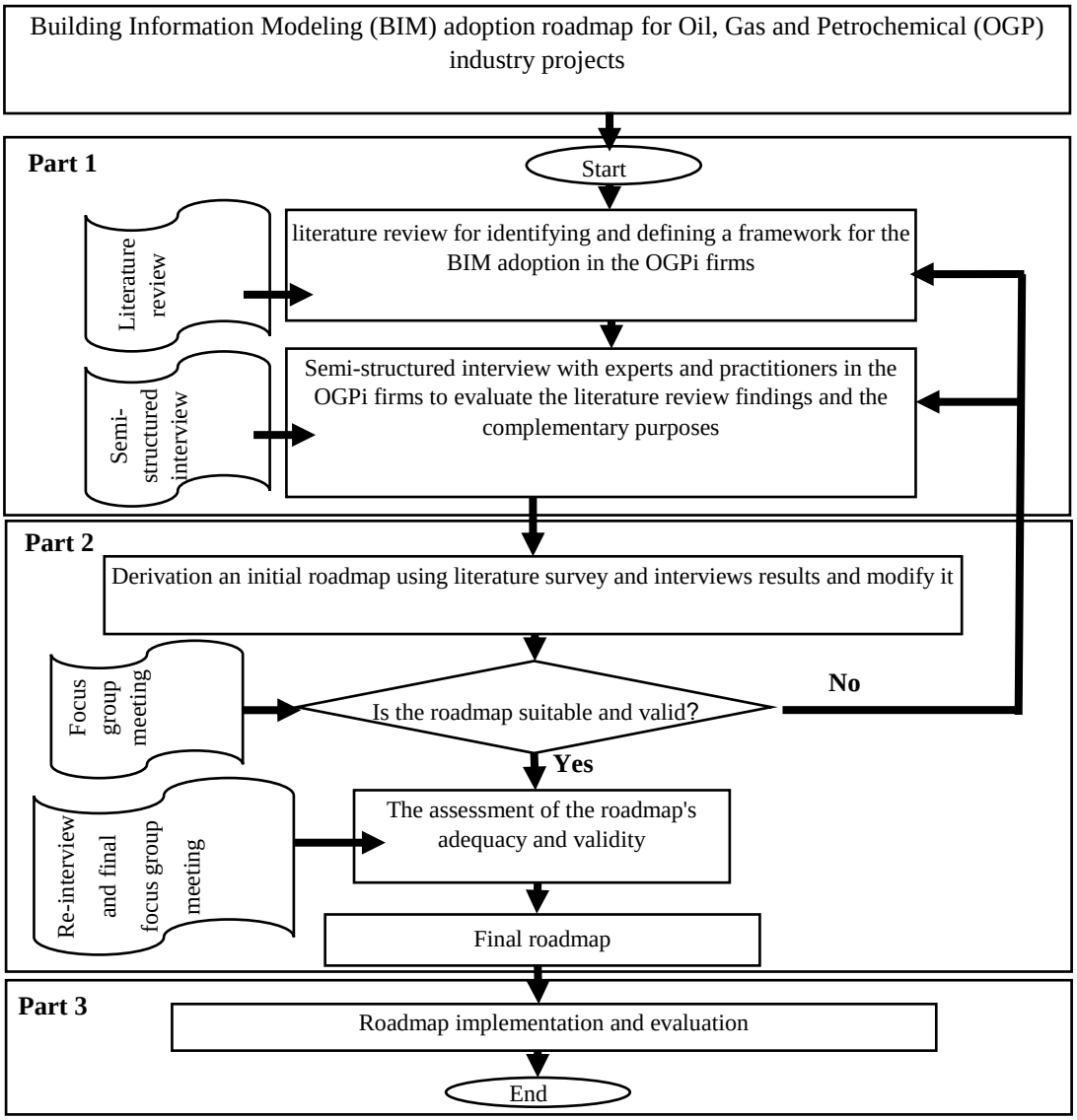

Fig. 1. Research methodology plan and process

The list of actions that should ultimately be used to overcome the challenges using Simon Sink's model, 'Why, How, What', is developed in conjunction with IDT (Sinek, 2009). The interviews, inspired by Sink's model, focused on why the challenges arise when managing complex projects, how to overcome them by adopting the necessary methods and actions, and what are the results of taking action. The research analysis was performed based on the confrontation between the practical and theoretical perspectives, as the assessment of the first one was based on the second one.

The final roadmap should fulfil the functional (organisational, legal, etc.) and structural specifications. The functional requirements refer to the conditions that the involved parties consider necessary for the adoption. The structural requirements are

the material and intangible characteristics of the roadmap, which are necessary to meet the functional requirements and from which can be deduced (Muller, 2011). According to GT, an iterative process based on the comments from the OGPi firms' experts was set up in order to verify the findings and provide feedback for refining the findings and consequently, deriving the final version of the roadmap.

To ensure the validity of the results of this study, the triangulation including interviewing experts through individual interviews and group meetings was selected. Group meeting (focus group) is a method for collecting qualitative data. In this method, individuals participate in one or more informal group discussions about the research topic. The chairman of the focus group meeting seeks to gain access to the important experiences of the participants on the research topic in the form of a systematic and structured plan. Interaction between members of the focus group is an important and fundamental feature of this research method and makes it different from group interview, which is the interaction between the interviewer and the interviewee. In the focus group, participants respond to the views of other participants based on their experiences. This method is in accordance with the roadmap preparation method described earlier and is also in full compliance with the reflective practice method. In this regard, interviews were started based on the results of library studies and their feedback was used to refine the results. The refined results, which were the result of applying the points of view of the interviewees for each section, were assessed during focus group meetings by the following measures:

All activities and related actions that could affect the results of this research were identified and categorized through library studies and interviews. Among the categorized activities and related actions; the more relevant to the research topic were selected in the focus group meeting. At this stage, 4 fixed criteria as well as internal negotiations were used for assessment. The fixes criteria were: 1) How much does this activity contribute to the success of the roadmap? 2) Does the introduced action relate with the nominated activity? 3) Does the proposed action comply to the IDT phases and category in which it is located? 4) How sufficient are the steps for the roadmap setup? In the internal negotiations, the question of: "Based on participant's experience, is there anything else that should be considered in the preparation of the roadmap?", put in the core of negotiations.

After that, based on the group member experiences and negotiations the factors that seemed to have a small effect were removed from the list through 5-point Likert scale. To this end, each participant assigned a point of 1 to 5 to each activity and its relevant actions. A point of 1 was considered for the least effect and a point of 5 for the most effect in creating value for the roadmap. At the end, the average point of all activities and actions were calculated and all those with point below 3 were omitted. Finally, 5 activities and 24 related actions were selected as the refined results.

The refined results were re-examined through re-interviews and final focus group and the final results including 5 activities and 20 related actions were extracted from them. At this stage, 4 actions (PESTG analysis, following the current government construction strategy to define the BIM strategy set up, use of the LEED concept alongside with BIM and IPD, introducing a specific set of software) that had border point (close to 3) and were not agreed upon were eliminated. The re-interview method based on previous feedback and final focus group were used to ensure the adequacy and validity of the results. In the other words, during this interaction and iterative process, the research conclusions and recommendations were drawn and validated.

4. Results

The roadmap is generally represented as a

flexible and powerful graphical display, including a multi-layer-based graph that connects different perspectives of the topic of interest in a strategic perspective view (UNIDO, 2009). A successful roadmap connects the current situation to the goals (desired situation) through the milestones, challenges and actions during a specified timeline. This study looks for the subject of BIM as incorporated in the Oil, Gas and Petrochemical industry and tries to provide an adoption roadmap for BIM deployment for OGPi firms. In the roadmap, the activities and actions are related together via the cause and effect during the desired timeline to achieve the goals.

Roadmap is a strategic and, in fact, an integrating plan which can help the planning process by considering all the important levels involved in the problem situation. The roadmap development process brings together the views of key parties. When a roadmap is developed, it can be widely used as the reference point for the communications and continuous actions (Phaal, 2015). Due to the fact that the roadmap should be defined within a timeline, the IDT phases incorporated in the roadmap were considered instead of the timeline. Therefore, to prepare a real adoption roadmap, it is sufficient to add the required time to execute each phase for the suggested final roadmap.

4.1. Current and Desired BIM Situation in OGPi Firms

Iranian oil, gas and petrochemical firms typically use a software called PDMS (Plant Design Management System) introduced by the AVEVA software company that is a 3D multi-user and multi-discipline software package for engineering, design and construction of the OGPi projects. Furthermore, few specialised software is used for the design of structure, process, piping, stress control, supports, electrical, instrument, etc., and the results are transferred to this software. Few outputs of these specialised software are interoperable with PDMS and other software outputs are manually entered into this software. Finally, the PDMS output is transmitted into the Navisworks software (Autodesk) to review the 3D model and extract possible clashes. The final PDMS model is used to prepare few procurement, fabrication and construction purpose such as drafting, material take-off, isometric drawing, spooler and so on.

According to the results of the interviews conducted in part 1, all processes among the partners' general current practices were recognised as maturity level 1 and fully or partially fragmented. The engineering practices were also recognised as maturity level 1, with trends to higher level due to the nature and required interdisciplinary checks. All the parties involved in the selected OGPi firm (owner, client, general contractor and their subsidiaries, vendors and operator) showed their interest to level up their activities. Thus, BIM level 2 was set up as the desired level.

BIM level 2 is introduced as a collaborative object-oriented model. At this level, the parties involved in the project do not necessarily work with a single unique model. Rather, they use their own three-dimensional models. The procedure of information exchange between different parties involved in the project is determined by the type of partner's cooperation, which is the critical aspect of this level. The design information is shared across the same format in the same way which enables the project organisation to combine the data of all parties in a unique 3D model and build a common BIM model. Hence, the software used by each party should be able to deliver the files to one of the common formats such as the Industry Foundation Class (IFC) format.

4.2. Milestones

Although the research does not include the implementation and evaluation phases, but it intends to generate a roadmap to enable the OGPi firms assess their organisation and projects and choose the right direction in the adoption and

implementation of BIM. The roadmap derived in this study did not include a timetable. The required timeline milestones for the roadmap derived in this study were replaced with the specified phases of the innovation diffusion theory. In other words, raising awareness, convincing, decision-making (implementation design), implementation, and evaluation phases were considered as the time phases of the roadmap and their interface was considered as the roadmap milestones. In the future, to implement the roadmap in a real case, the real time could be easily installed at these interfaces.

4.3. Identified Challenges and Related Activities and Actions

Given that the roadmap marks the pathway from the current situation to the desired situation as the goal, the identification and categorisation of the challenges and related activities and actions for overcoming the challenges are the most important issues in the roadmap preparation process. To respond to all the challenges using the Sink model, a set of activities were identified each containing several actions. Identifying the activities and related actions was done according to the model shown in Figure 2. They were based on the use of conventional methods for the strategic management along with the Sink model. The list of actions is prepared using the 'Why, How, What' questions. According to this model, in order to express the actions, the first category of information to be explained is 'why' and what is our motive. The second category of information is extracted from the 'How' question and explains the methods used to carry out the actions. Finally, the third category of information answers the 'what' question and describes the purpose and final result. Using these questions, the challenges are linked to the list of expected actions and outcomes. One of the main causes as to why organisations and people who use it can successfully find their appropriate direction is that this approach is a natural way of argumentation (Sinek, 2009). Therefore, in the current research, this approach was adopted as an effective way to describe the list of actions.

To prepare the roadmap in the described manner, the challenges of BIM implementation in the AEC industry were identified through the literature review, and were categorised into processes, people and tools which are called the golden triangle of the changes. They were ultimately finalised for the oil, gas, and petrochemical industry by interviewing OGP industry experts. By finalising the list of challenges, the challenge map (Figure 3) was drawn to provide the main focus and identify the activities and actions that should be considered in the roadmap. The challenge map in Figure 3 was drawn by grouping the challenges into four categories of 'should be described', 'should be covered', 'should be explained' and 'should be provided' to be used in deriving the roadmap. It is obvious that the challenges related to 'should be provided' are more important than the others and lead to defining the outcomes.

As the roadmap is a strategic plan in context, the list of roadmap activities to be performed in this study were customised based on the required activities for implementing the strategy plan. The feasibility study for adopting BIM in OGPi firms, BIM strategy setup, establishment of leading BIM group (task group), development of BIM business model, and development of IPD-BIM collaboration protocol are the five activities considered in this way. Hereinafter in this study, these activities are referred to as S1 to S5, respectively. The highlighted point of this roadmap, which is not included in the roadmap of the AEC industry, is to pay attention to the more structured OGP industry, familiarity of OGPi with the IPD approach and IPD-BIM collaboration. The issue of BIM and IPD collaboration highlighted in the text of all activities while activity S5 has dealt to this issue specifically. To provide a list of actions to be performed for overcoming the

challenges and removing the obstacles, the experiences of companies implementing the BIM technology in the AEC industry and also the results of the interviews were utilised. In addition, considering the context created for the execution of the projects in an integrated environment, focusing on the synergy that can be achieved by BIM-IPD collaboration shortens the list of actions.

Figure 3 depicts the challenge map and shows the finalised challenges where the IPD features can assist in overcoming them. It is necessary to emphasise that the methods of overcoming the challenges in any organisation are unique and dependent on the process assets and organisational culture and hence, they are not possible to be used directly. However, the experiences and actions that these companies have incorporated are categorised and used to extract the final list of actions for each activity. The final list of actions extracted based on 'Why, How, what' questions and the above-mentioned considerations can be reduced or increased depending on the maturity of the organisation. Table 3 shows the summarised results of this process. The list of activities and related actions consisting of 5 activities and 20 actions is presented in Table 4. All of the above processes were carried out on a repeated path by the specialists of the OGPi to make sure the results are reliable. Table 5 shows the distribution of the actions during the IDT phases. This table was used for directly preparing the roadmap.

4.4. Setting up the Roadmap

Considering the actions related to BIM challenges alongside the IDT phases including the awareness, convincing, decision making (implementation design), implementation and evaluation is the approach adopted in this research to formulate a roadmap for deploying BIM in the OGPi firms. To this end, the roadmap was planned with six interconnected steps to guarantee the BIM deployment in OGPi firms through performing the actions in response to the related challenges and activities. These six steps are as follows:

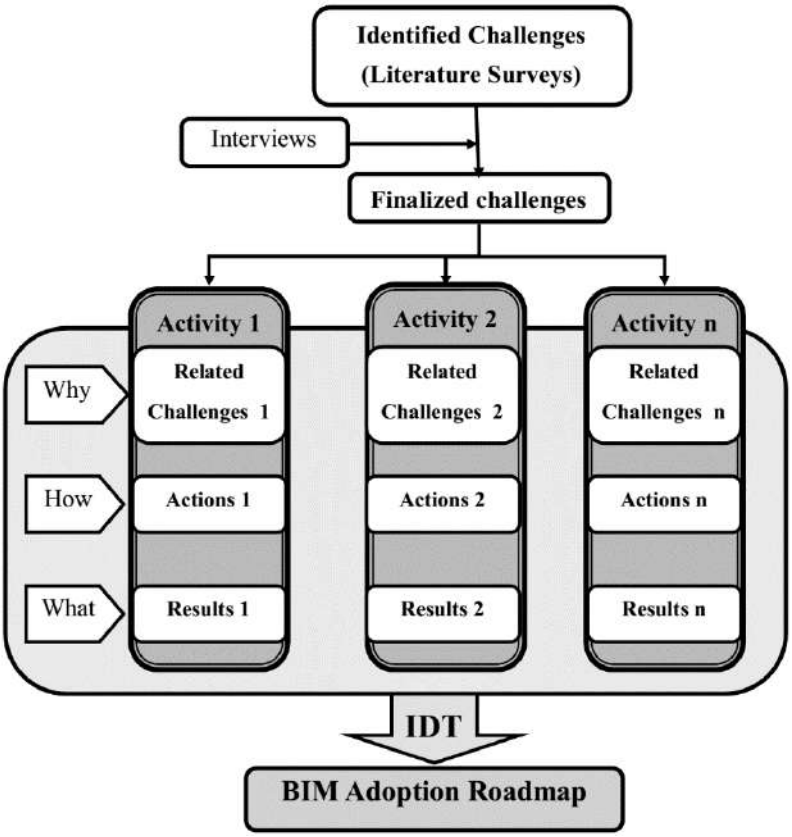

Fig. 2. Model for identification of activities and related actions

Table 3. Summarized results of identification of required actions and expected outcomes

	Why	How	What
S1	For awareness and convincing people and organization. By doing this activity, the T5, M4, P10, P5 and P1 challenges are addressed.	By analysis of the strengths, weaknesses, opportunities and threats (SOWT) of BIM implementation within the OGPi. They are achieved by actions 1 and 2.	The output of this action will be a complete and reliable analysis of the BIM capability of for successful implementation in the OGPi firms' projects.
S2	By doing this activity, in addition to achieve the intended goals including increase of cost-effectiveness of BIM implementation and creating interoperability between involved parties, theT1, M3, P10, P3, and P1 challenges are addressed.	By doing this activity, the goals of adopting BIM are established and the business strategy of the involved parties is linked to the current and future development of BIM technology. It is done by actions 3 to 5.	By setting up a BIM strategy, it is expected to achieve the following results: 1. Parties visions and missions 2. Parties strategy to achieve missions and setting goals for BIM. Principles of this strategy concerning BIM-IPD collaboration and technology interoperability.
S3	To prevent reduced motivation of members in the long term implementation of BIM process. By doing this activity, the challenges M1and P10 are addressed.	The leading BIM group is responsible for the following tasks: 1. Supervision and leadership at party-level strategy implementation 2. Ensure that the parties go in the right direction and with the right speed. 3. Defining new goals and future BIM strategy. It is done by actions 6 to 11.	1. Continuous monitoring of the BIM strategy at the parties and party level 2. Assigning resources to support creation of the required BIM structures. Support the use of BIM by all involved parties.
S4	This activity not only requires focusing on the technical and educational aspects of the process, but also should analyze to the way of integrating BIM in its business structure and how it is tailored to compete in the market. By doing this activity, the challenges T5, T2, M6, M3, M2, P12, P10, P8, P4 and P3 are addressed.	Creating a business model for implementing BIM at the level of all parties, each party will make its business model compatible with the mentioned model. It is done by actions 12 to 17.	1. Decision to adopt BIM capabilities across the entire parties and each party 2. Investing in development of the BIM skills among the key personnel in connection with the clients Creating an up-to-date business model for higher rate of market penetration.
S5	By doing this activity in addition to setting collaborative relations between and within the involved parties, the legal and contractual aspects of BIM are defined and the challenges T4, T3, T1, M5, M3, P11, P9, P7, P6, P4 and P2 are addressed.	Creating a collaborative environment in which the parties are involved at each stage of the project life cycle, the activities to be performed at each stage, and the outputs that should be attained in an integrated environment based on IPD in the context of the BIM tool has been specified. It is done by actions 18 to 20.	Providing a structural plan for collaborative use of the BIM and IPD in projects, describing the contractual and legal issues, describing responsibilities, expected outcomes, model level of details and model ownership and management are the most important outputs of this activity.

1) The leading BIM group (BIM task group) is created. The group conducts the feasibility study to apply BIM at maturity level 2, focusing on raising awareness of adopting the new technology in oil, gas and petrochemical industries.

2) The leading group sets up the BIM strategy using the results of the feasibility study carried out in the first step and appreciates the OGPi from the BIM technology and, at the same time, convinces the top management of the OGPi firms to

adopt BIM.
3) After convincing the top management of the OGPi firms and decision making in relation to the implementation of BIM, intends to develop the relevant business plan.
4) Considering the characteristics of the business plan, the BIM implementation plan including the collaborative procedures and cooperation processes are prepared. The contractual framework and the specifications of the implemented software are planned among the parties and within their organisations. In this step, the objectives of the collaboration, human resources development plan, software development plan and required resources for the support and supervision are finalised to achieve the integrity in the entire OGPi firms.
5) The BIM is implemented based on the four above steps, and
6) The BIM implementation evaluation is made based on the received feedback and necessary corrective actions.

The results of this research using the Sink model and the steps explained for the BIM implementation lead to the derivation of the roadmap for the adoption of building information modeling in the oil, gas and petrochemical industries firms.

Table 4. List of activities and related actions

	Activity	Related actions
S1	Feasibility study for adopting BIM in OGPi firms	Action 1: SWOT analysis for use in awareness and convincing of key parties. Providing situation assessment and strategic actions matrix and determination of aggressive, conservative, defensive or competitive strategies for use in convincing and decision-making phases.
S2	BIM strategy set up	Action 2: Establishing long-term goals for use in convincing and decision-making phases. Action 3: Estimating related costs for use in awareness and convincing phases. Formulating of party's interoperability principles for use in decision-making and implementation phases.
S3	The leading BIM group (task group) establishment	Action 4: Creating a BIM task group for decision making, implementation and evaluation phases. Action 5: Forming leading teams inside the community for implementation and evaluation phases. Action 6: Set up the communication line between the party's internal and external teams in order to create integrity between all parties for the implementation and evaluation phases. Action 7: Forming monitoring and evaluation teams for implementation and evaluation phases Action 8: Supporting BIM implementation in all parties involved in the project for implementation phase. Defining new goals and future development for the evaluation phase.
S4	Development of the BIM business model	Action 9: Technical studies and the determination of technology requirements in the entire parties for the decision making phase. Action 10: Industry analysis and market studies for awareness and convincing phases. Action 11: Determining the role and responsibilities of parties for the decision making phase. Action 12: Financial and economic analysis for the decision making phase Action 13: Risk assessment for the convincing and decision making phases. Updating business plan for implementation and evaluation phases.
S5	Development of the IPD-BIM collaboration protocol	Action 14: Determining how to coordinate between and within the parties for the implementation and evaluation phases. Action 15: Set up a party's interoperability protocol for decision making, implementation and evaluation phases. Establishing a standard contract format based on the BIM-IPD collaboration model for decision making and implementation phases.

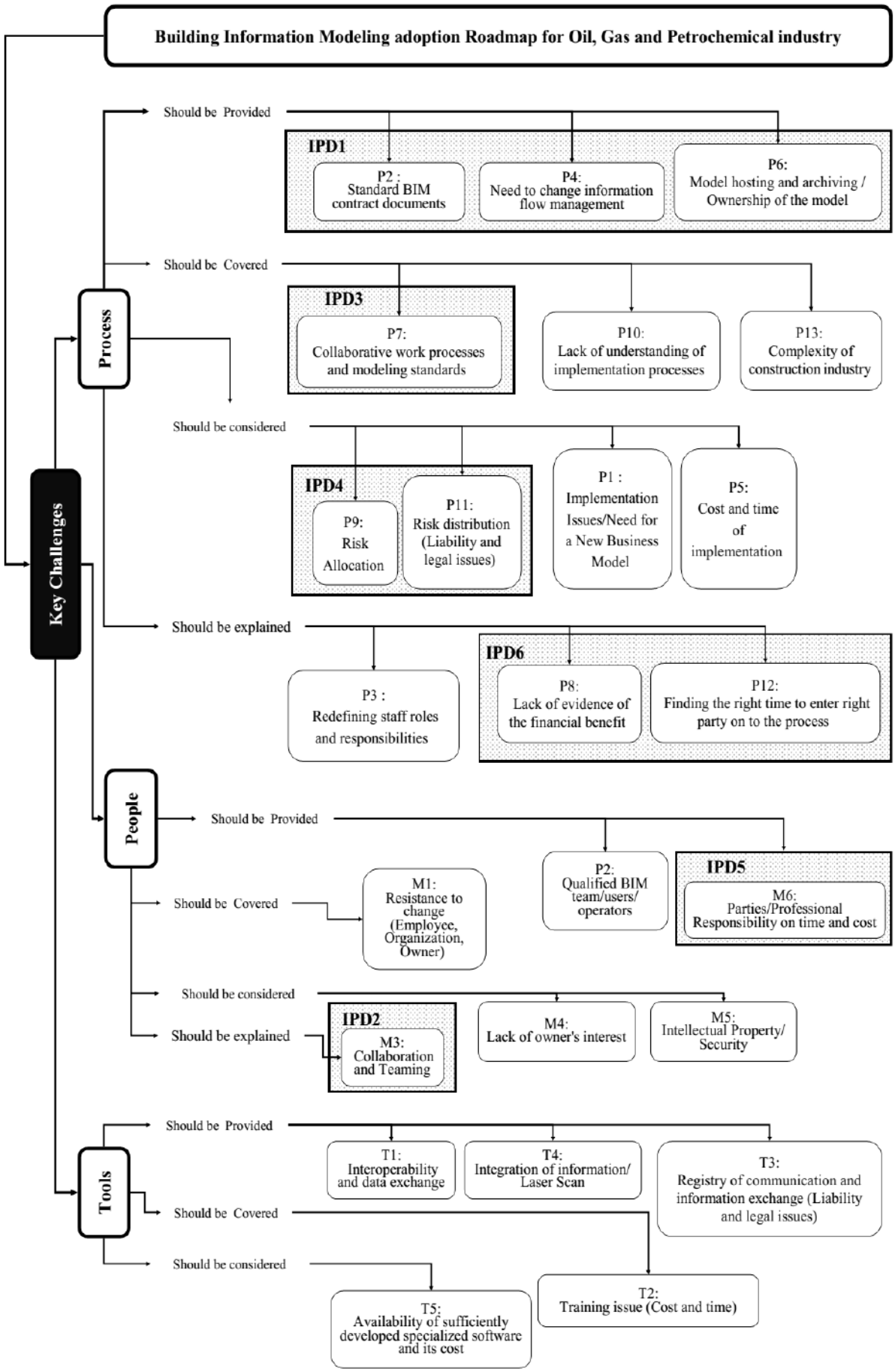

Fig. 3. Challenge map for adopting BIM in OGPi according to IPD features

Table 5. Distribution of identified challenges and related actions during IDT phases

	BIM barriers and challenges	Activity	Gu et al. (2010)	Azhar (2011)	Eastman et al. (2011)	Succar (2013)	Both et al. (2012)	Azhar et al. (2012)	Kalinichuk et al. (2013)	Ibrahim (2013)	Stanley et al. (2014)	Elmualim et al. (2014)	Risto (2015)	Actions: Awareness	Convincing	Planning	Implementation	Evaluation
Process	P1 Implementation issues	S1,S2,S3	•	•	•	•	•		•			•		1,2,3,4	1,2,3,4	5,6	5,6,7,8,9	6,7,8,9
	Need for a new business model	S4	•	•	•	•	•		•			•		13	13	12,14,15,16	17	17
	P2 Absence of sandard BIM contract documents	S5		•	•	•	•									20	20	
	P3 Redefining staff roles and responsibilities	S2,S4	•		•			•					•			5,14		
	P4 Need to change information flow management	S4,S5	•	•		•		•		•	•					19,12	19	19
	P5 Cost and time of implementation	S1,S2,S4		•				•				•		2	2,4	4,15		
	P6 Model hosting and archiving /ownership of the model	S5							•	•	•					20	18,20	18
	P7 Lack of collaborative work processes and modeling standards	S5				•		•			•					19,20	19,20	19
	P8 Lack of evidence of the financial benefit	S3,S4								•		•		13	13,16	15,16		11
	P9 Risk Allocation	S1,S5		•										1	1	15		
	P10 Lack of understanding of implementation processes	S2,S3,S4				•						•	•		3	3,5,20	5,8,10,20	8
	P11 Risk distribution (liability and legal issues)	S5								•		•				20	20	
	P12 Finding the right time to enter right party on to the process	S4		•									•			12,14		
	P13 Complexity of construction industry	S1				•					•			1,2	1,2			
People	M1 Inertia/Resistance to change (employee, organisation, owner)	S3			•	•	•		•		•					6	6,10	6
	M2 Absence of qualified BIM team/users/operators	S4						•	•	•	•	•	•			12,14		
	M3 Collaboration and teaming	S2,S4,S5		•	•	•		•							3	3,5,19	5,18,19	18,19
	M4 Absence of owner's interest	S1		•					•		•			1	1			
	M5 Intellectual property/security	S5		•				•		•						20	20	
	M6 Parties/Professional responsibility on time and cost	S4						•	•							14	17	17
Tools	T1 Interoperability and data exchange	S2		•	•	•	•			•	•		•			5	5	
	T2 Training issue (cost and time)	S2,S4				•	•	•								4,15		
	T3 Registry of communication and information exchange	S5		•				•			•					19,20	19,20	19
	Integration of information/Laser scan	S5			•			•				•				12,19	18,19	18,19
	T5 Availability of sufficiently developed specialized software and its cost	S1,S4										•	•			4	4,12	

4.4. Research Limitations

The limitations of this research are as follows:

1) The lack of real cases that have implemented the BIM in the OGPi firms mandated this research to inspire the experience of the AEC industry in this regard.

2) Normally, any roadmap should contain a timeline for its implementation. However, given the limitations, the present roadmap for adopting BIM technology in the OGPi firms was replaced with IDT phases.

5. Findings

The findings of this research are as follows:

1) The utilisation of BIM in AEC industry projects has been well developed so that today, all the developed and developing countries implement or plan to deploy BIM in their building projects.

2) The studies on the situation of the AEC industry have shown that BIM has greatly contributed to the improvement of the industry. However, it has not yet been able to fill the gap between the productivity and efficiency of this industry and the other industries.

3) The oil, gas and petrochemical industry has been utilised the integrated project delivery method to achieve the productivity and efficiency improvement. However, IPD cannot solve the problems of this industry, especially the island functions, and lack of integration in the process, people and tools. Therefore, to overcome the existing challenges, it is necessary to adopt a complementary project management approach that can correct this defect.

4) BIM and IPD have a synergistic role for each other which can correct the defects of each other. Through the creation of standard contractual formats for IPD and BIM, the AEC industry has overcome many challenges of the BIM and has proven its positive role in this respect.

5) The oil, gas and petrochemical industry has sufficient incentive to implement the BIM in collaboration with the integrated project delivery methods. However, due to the lack of any research and proven experience as well as the breadth of the industry, a roadmap for adopting BIM in the OGPi firms should be derived to avoid repeating the mistakes experienced in the AEC industry and achieve the established benefits of BIM.

6) In order to draw up an appropriate roadmap, the existing situation of an Iranian oil, gas and petrochemical industry firm was analysed and a set of necessary activities and actions were proposed hereupon. Given the more suitable situation of the OGPi firms in the developed countries, this is a conservative roadmap in these countries.

7) The roadmap was derived using the standard principles of preparing strategic plans (Figure 4). It depicted all the needed actions that should be adopted at the process, people and tool levels at different IDT phases in accordance with the given deployment steps.

8) The roadmap should be prepared with a real timeline for actions in Iran using the support of the government as the main owner of the oil, gas and petrochemical industry, and then the implementation plan for BIM in this industry could be finalised.

9) The effective and efficient BIM-IPD deployment in OGPi firms requires some incentives such as the government support, publication of BIM–IPD requirements and guidelines, growth of demand for BIM-IPD projects, development of IT infrastructure capabilities, widespread global support of the BIM-IPD and finally, mandated use of BIM.

6. Conclusions

Adopting BIM alongside IPD was investigated in this study in an effort to reduce the waste, costs, time and materials, and increase the efficiency and productivity of the OGPi projects. The results of the present research showed that despite the fact that the process, people, and tool platforms in OGPi were more established

than the AEC industry, there were no significant effects of implementing BIM in the oil, gas and petrochemical industry. The study, therefore, aimed to provide a roadmap for adopting BIM alongside with IPD for oil, gas and petrochemical firms (Figure 4) through literature review, semi-structured interview and focus group meetings. The highlighted point of this roadmap, which is not included in the roadmap of the AEC industry, is to pay attention to the more structured OGP industry, familiarity of OGPi with the IPD approach and IPD-BIM collaboration. Finally, the roadmap was derived via inspiring by a few models and approaches. The innovation diffusion theory, 'Why, How, What' questions (Sink model), strategic planning and innovation roadmap as well as the triangulation method through iterative process between literature review, interviews and focus group meetings were used to directly derive the roadmap and its key elements. Triangulation was used to ensure the validity of the final roadmap.

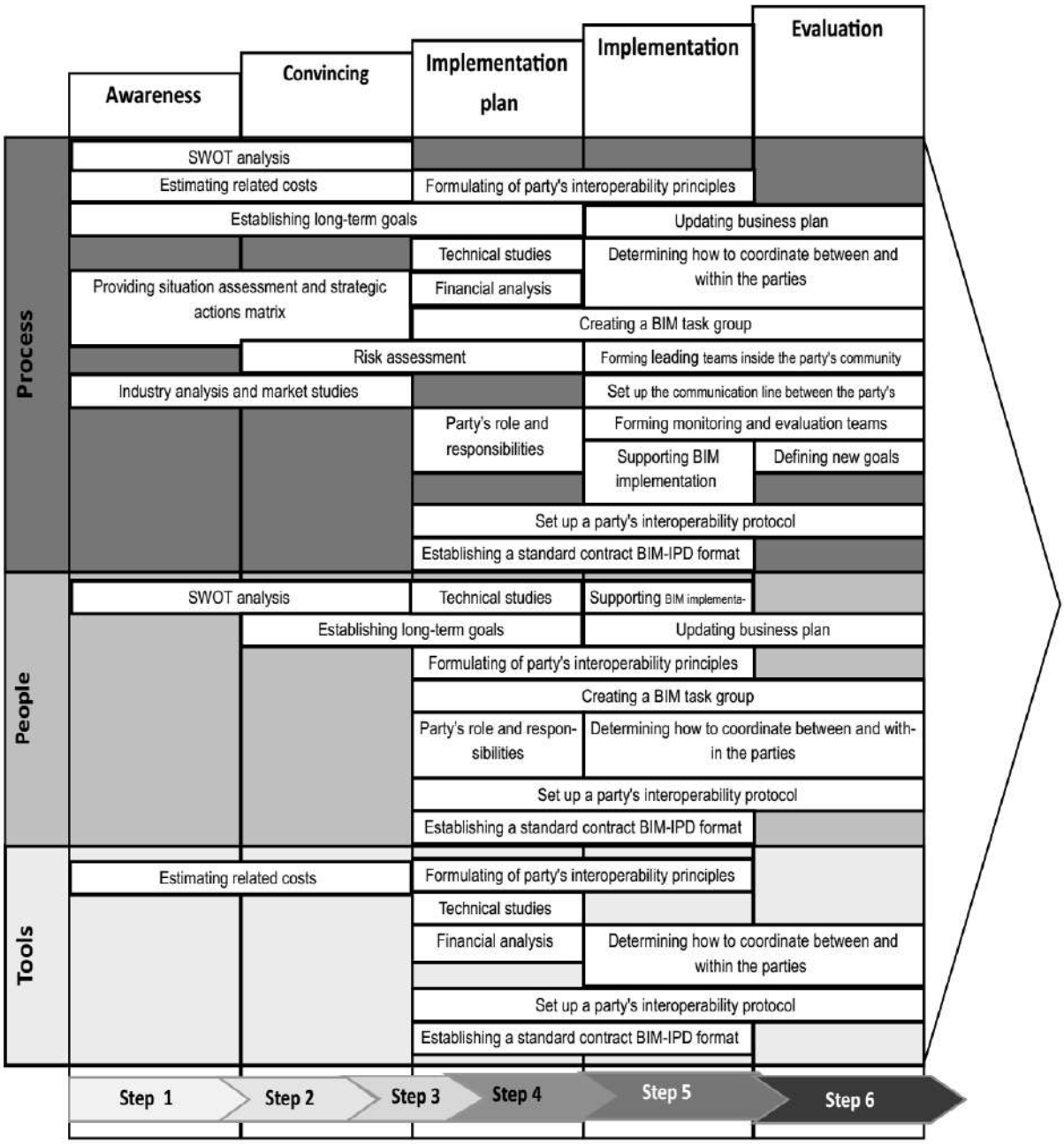

Fig. 4. BIM adoption roadmap for oil, gas and petrochemical industry

Given the time constraints and the scope defined for this part of the research, the implementation and evaluation phases of the roadmap were not considered and postponed to the future subsequent research. The activities and actions identified in this research may vary in a real case based on the OGPi firm's process assets and organizational culture. However, in the continuation of this research, the roadmap could be utilized to prepare a specific detailed roadmap for the Iranian OGPi firms or any other country that would wish to introduce the new managerial approaches to this industry. In this regard, given the compulsion of British construction companies, this country could also be among the target countries for the continuation of this research and preparation of a detailed specific implementation roadmap. Other new managerial approaches such as Lean Construction could also be merged into the roadmap.

7. Geolocation Information

This research was conducted to prepare a roadmap for BIM implementation in the oil, gas and petrochemical industry based on international experiences of BIM implementation in the architectural, engineering and construction industry. In this study, in addition to the international references, the semi-structured interviews were used. The experts selected for the interviews were chosen from Iran.

8. References

Akintola, A., Venkatachalam, S. and Root, D. (2019). "Understanding BIM's impact on professional work practices using activity theory", *Construction Management and Economics*, 37(3), 1-17.

American Institute of Architects (AIA). (2014). "Integrated project delivery - an updated working definition, Version 3", Retrieved from http://www.aiacc.org/wp-content/uploads/2014/07/AIACC_IPD.pdf.

Azhar, S. (2011). "Building information modeling (BIM): trends, benefits, risks, and challenges for the AEC industry", *Leadership and Management in Engineering*, 11(3), 241-252.

Azhar, S., Khalfan, M. and Maqsood, T. (2012). "Building information modelling (BIM): now and beyond", *Australasian Journal of Construction Economics and Building*, 12(4), 15-28.

Bezkorovayniy, V., Bayazitov, V. and Bobov, D. (2018). "Management of the design and construction of offshore oil and gas facilities with BIM Base", *IOP Conference Series: Materials Science and Engineering*, Vol. 463, Part 3, Vladivostok, Russian Federation.

Bosch-Sijtsema, P. and Gluch, P. (2019). "Challenging construction project management institutions: The role and agency of BIM actors", *International Journal of Construction Management*, 21(11), 1077-1087.

Both, P. and Kindsvater, A. (2012). "Potentials and barriers for implementing BIM in the German AEC market, Results of a current market analysis", *Proceedings of the 30th eCAADe Conference*, Vol. 2, pp. 151-158, Prague, Czech Republic.

Cetindamar, D., Daim, T.U., Beyhan,B. and Basoglu, N. (2013). *Strategic planning decisions in the high tech industry*, Springer, London.

Cheng, J.C.P., Tan, Y., Song, Y., Mei, Z., Gan, V.G.L. and Wang X. (2018). "Developing an evacuation evaluation model for offshore oil and gas platforms using BIM and agent-based model", *Automation in Construction*, 89, 214-224.

Cheng, J.C.P., Tan, Y., Song, Y., Liu, X. and Wang, X. (2017). "A semi-automated approach to generate 4D/5D BIM models for evaluating different offshore oil and gas platform decommissioning options", *Visualization in Engineering*, 5, 266-272.

Cheng, J.C.P., Lu, Q. and Deng, Y. (2016). "Analytical review and evaluation of civil information modeling", *Automation in Construction*, 67, 31-47.

Construction Industry Council. (2014). "Roadmap for BIM strategic implementation in Hong Kong's construction industry, Version 1", Retrieved from http://54.255.237.184/bim/Upload/publication/32/download_1/f0a9c1250c7d4c639b7f2865897275b9.pdf.

Eastman, C., Teicholz, P., Sacks, R. and Liston, K. (2011). *BIM Handbook: A guide to building information modellin for owners, managers, designers, engineers and contractors*, Second edition, John Wiley & Sons, New Jersey.

Elmualim, A. and Gilder, J. (2014). "BIM: innovation in design management, influence and challenges of implementation", *Architectural Engineering and Design Management*, 10(3), 183-199.

Fakhimi, A., Majrouhi Sardrood, J., Mazroi, A.,

Ghoreishi, S.R. and Azhar, S. (2017). "Influences of building information modeling (BIM) on oil, gas, and petrochemical firms", *Science and Technology for the Built Environment*, 23(6), 1063-1077.

Ghassemi, R. and Becerik-Gerber, B. (2011). "Transitioning to integrated project delivery: Potential barriers and lessons learned", *LCI Lean Construction Journal, Lean and Integrated Project Delivery Special Issue*, 32-52.

Gu, N. and London, K. (2010). "Understanding and facilitating BIM adoption in the AEC industry", *Automation in Construction*, 19(8), 988-999.

Hafizah, H.N.A., Takim, R. and Nawawi, A.H. (2015). "BIM roadmap strategic implementation plan: Lesson learnt from Australia, Singapore and Hong Kong", In: *Raidén, A.B., and Aboagye-Nimo, E. (eds.), Proceedings of the 31st Annual Association of Researchers in Construction Management (ARCOM) Conference*, pp. 611-620, Lincoln, UK.

Hong, Y., Hammad, A.W.A. and Akbarnezhad, A. (2019). " Impact of organization size and project type on BIM adoption in the Chinese construction market", *Construction Management and Economics*, 37, 675-691.

Ibrahim, N.H. (2013). " Reviewing the evidence: use of digital collaboration technologies in major building and infrastructure projects", *Journal of Information Technology in Construction*, 18, 40-63.

Kalinichuk, S. and Tomek, A. (2013). " Construction industry products diversification by implementation of BIM", *International Journal of Engineering and Technology Innovation*, 3(4), 251-258.

Khan, S. (2014). " Qualitative research method: Grounded theory", *International Journal of Business and Management*, 9(11), 224-233.

Khosrowshahi, F. and Arayici, Y. (2012). "Roadmap for implementation of BIM in the UK construction industry", *Engineering, Construction and Architectural Management*, 19(6), 610 - 635.

Larsen, M. (2019). "Use of project execution models and BIM in oil and gas projects: Searching for relevant improvements for construction", Ph.D. Thesis, Norwegian University of Science and Technology, Faculty of Architecture and Design, Department of Architecture and Planning.

Larsen, M. (2015). "Generalising via the case studies and adapting the oil and gas industry's project execution concepts to the construction industry", *Procedia Economics and Finance*, 21, 271-278.

Le, P., Elmughrabi, W., Dao, T.M. and Chaabane, A. (2018). "Present focuses and future directions of decision-making in construction supply chain management: A systematic review", *International Journal of Construction Management*, 20(5), 490-509.

Lee, C.Y., Chong, H.Y. and Wang X. (2016). "Streamlining digital modeling and building information modelling (BIM) uses for the oil and gas projects", *Archives of Computational Methods in Engineering*, 25(2), 349-396.

Lei, H., Wang, X., Wang, J. and Truijens, M. (2014). "An integration framework of advanced technologies for productivity improvement for LNG mega- projects", *Journal of Information Technology in Construction*, 19, 360-382.

Marshall, B., Cardon, P., Poddar, A. and Fontenot, R.J. (2013). "Does sample size matter in qualitative research?: A review of qualitative interviews in IS research", *Journal of Computer Information Systems*, 54(1), 11-22.

Mason, M. (2010). "Sample size and saturation in PhD studies using qualitative interviewes", *Forum: Qualitative Social Research*, 11(3), 1-13.

Muller, G. (2011). *Systems architecting: A business perspective*, CRC Press, New York.

National Institute of Building Sciences (NIBS), (2007). "United States national building information modeling standard, version 1, Part 1, overview, principles, and methodologies", Retrieved from.http://www.Nibs.org.

O'Connor, P. (2009). *Integrated project delivery: collaboration through new contract forms*, Faegre and Benson LLP, Minneapolis.

Phaal, R. (2015). *Roadmapping for strategy and innovation*, Centre for Technology Management, Institute for Manufacturing, University of Cambridge.

Building SMART Canada, (2014). "Roadmap to lifecycle building information modeling in the Canadian AECOO community", Retrieved from https://buildingsmartcanada.ca/wp-content/uploads/2019/07/ROADMAP_V1.0.pdf.

Rogers, E.M. (2003). *Diffusion of innovations*, Fifth edition, Free Press, New York.

Rui, Z., Li, C., Peng, F., Ling, K., Chen, G., Zhou, X. and Chang H. (2017). " Development of industry performance metrics for offshore oil and gas project", *Journal of Natural Gas Science and Engineering*, 39, 44-53.

Shadid, W.K. (2017). " A framework for managing organizations in complex environments", *Construction Management and Economics*, 36(4), 182-202.

Silva, M.F., Salvado, F., Couto, P. and Vale e Azevedo, Á. (2016). " Roadmap proposal for implementing building information modelling (BIM) in Portugal", *Open Journal of Civil Engineering*, 6, 475-481.

Sinek, S. (2009). *Start with Why - how great leaders inspire everyone to take action*, Penguin Publishing Group, New York.

Singh, M.V., awhney, A. and Borrmann, A. (2017). "Integrating rules of modular coordination to improve model authoring in BIM", *International*

Journal of Construction Management, 19(1), 15-31.

Song, C. (2007). "Risk analysis of international offshore oil project", Ph.D. Thesis, Tianjin University.

Songhurst, B. (2014). "LNG plant cost escalation", Oxford: Institute for Energy Studies, Retrieved from https://www.oxfordenergy.org/wpcms/wp-content/uploads/2014/02/NG-83.pdf.

Stanley, R. and Thurnell, D. (2014). " The benefits of, and barriers to, implementation of 5D BIM for quantity surveying in New Zealand", *Australasian Journal of Construction Economics and Building*, 14, 105-117.

Succar, B. (2013). "Building Information Modelling: Conceptual constructs and performance improvement tools", Ph.D. Thesis, University of Newcastle.

Tan, Y., Fang, Y., Zhou, T., Gan, V. J. L. and Cheng J.C.P. (2019). "BIM-supported 4D acoustics simulation approach to mitigating noise impact on maintenance workers on offshore oil and gas platforms", *Automation in Construction*, 107, 1-10.

Tan, Y., Song, Y., Zhu, J., Long, Q., Wang, X. and Cheng, J.C.P. (2018). "Optimizing lift operations and vessel transport schedules for disassembly of multiple offshore platforms using BIM and GIS", *Automation in Construction*, 94, 328-339.

Tan, Y., Song, Y., Liu, X., Wang, X. and Cheng, J.C.P. (2017). " A BIM-based framework for lift planning in topsides disassembly of offshore oil and gas platforms", *Automation in Construction*, 79, 19-30.

Tsai, Y.H., Wang, J., Chien, W.T., Wei, C.Y., Wang, X. and Hsieh, S.H. (2019). "A BIM-based approach for predicting corrosion under insulation", *Automation in Construction*, 100, 102-123.

Teo, E.A.L, Ofori, G., Tjandra, I.K. and Kim, H. (2016). " The use of BIM in the Singapore construction industry: Opportunities and challenges", *Proceedings of the 20th World Building Congress*, Vol. 4, pp. 141-152, Tampere, Finland.

United Nations Industrial Development Organization (UNIDO), (2009). "Practice on roadmapping", Retrieved from https://www.tc.cz/files/istec_publications /practice_on_roadmapping_1265908167.pdf.

Wang, J., Shou, W., Wang, X. and Wu, P. (2016). "Developing and evaluating a framework of total constraint management for improving workflow in liquefied natural gas construction", *Construction Management and Economics*, 34(12), 859-874.

Wang, X., Truijens, M., Hou, L., Wang, Y. and Zhou Y. (2014). " Integrating augmented reality with building information modeling: Onsite construction process controlling for liquefied natural gas industry", *Automation in Construction*, 40, 96-105.

Xue, C. (2015). "Technology integration capability in the oil/gas industry: Cross case study of iRing and BIM technologies", Master's Thesis, Delft University of Technology (TU Delft).

Zhou, Y., Ding, L., Wang, X., Truijens, M. and Luo, H. (2015). "Applicability of 4D modelling for resource allocation in mega liquefied natural gas plant construction", *Automation in Construction*, 50, 50-63.

Civil Engineering Infrastructures Journal 2021, 54(2): 301-317
DOI: 10.22059/CEIJ.2020.297661.1656

RESEARCH PAPER

An Investigation of the Relationship among Skid Resistance, Mean Texture Depth and Abrasion Resistance for Different Macrotextures of Concrete Pavements

Jalalkamali, R.[1], Dibaee, M.M.[2], Hassani, A.[3*] and Jalal Kamali, M.H.[4]

[1] Assistant Professor, Civil Engineering Department, Shahid Bahonar University of Kerman, Kerman, Iran.
[2] Ph.D. in Highway Engineering, Civil and Environmental Engineering Faculty, Tarbiat Modares University, Tehran, Iran.
[3] Professor in Highway Engineering, Civil and Environmental Engineering Faculty, Tarbiat Modares University, Tehran, Iran.
[4] Ph.D. in Highway Engineering, Tarbiat Modares University, Tehran, Iran; Currently: Assistant Professor, Civil Engineering Department, University of Gonabad, Gonabad, Iran.

Received: 10 Feb. 2020; Revised: 14 Oct. 2020; Accepted: 31 Oct. 2020

ABSTRACT: Road accidents are one of the ten major causes of death in the world. Lack of enough friction and skid resistance of the pavement surface are known as important factors in traffic accidents. In this study, to evaluate the relationship between skid resistance and pavement surface macrotexture, five methods of creating macrotexture on concrete pavements were used. Sand Patch test, British Pendulum and Wide Wheel Abrasion tests were employed to obtain mean texture depth, skid resistance and abrasion resistance of the surface, respectively. Results showed that brushing on fresh concrete surface (parallel or perpendicular to the traffic direction) can improve frictional properties of pavement surface, drastically. This method increased British Pendulum Number (BPN) and friction coefficient by 32% and 38% (in average), respectively. Friction coefficient of parallel brushing was quite similar to perpendicular (0.2% discrepancy), while its abrasion resistance was 4% higher. Hence, as a finding, parallel brushing is the most recommended texturing technique in respect to friction. Generally, concrete pavement texturing decreases surface abrasion resistance, but burlap dragging improved this index by 2.5%. Nevertheless, burlap dragging results could be deceptive due to the high sensitivity to initial setup conditions. In other words, measurement scale of the studied testing procedures are small in respect to the scale of protuberances caused by burlap dragging method.

Keywords: Abrasion Resistance, British Pendulum Number, Macrotexture, Mean Texture Depth, Skid Resistance.

[*] Corresponding author E-mail: jalalkamali@gonabad.ac.ir

1. Introduction

According to the official records reported by Legal Medicine Authority of Iran, more than 14500 people lost their lives in road accidents in 2019 in Iran (ILMO, 2020). In a research, carried out on casualties of road accidents in Iran, Rasouli et al. (2008) showed that death toll rates of the accidents have increased from 22.1 in 1997, to 40.5 per 100,000 people in 2005, which categorizes Iran under high-risk countries in the area of road accidents.

Any life, lost in road accidents, costs the country's economy a huge loss, which was estimated, in 2012, to be 8.53 billion Rials (244,000 USD) per person, in Iran (Monajjem et al., 2013). The investigation showed that many road geometrical parameters and pavement characteristics such as skid resistance, have a great impact on accidents rate (Viner et al., 2004). Four important factors affecting the friction between road surface and vehicle tires are surface specifications, vehicle performance specifications, tire characteristics and environmental conditions (Wu et al., 2012; Hall et al., 2009).

2. Literature Review

2.1. The Relationship between Friction Coefficient and Accidents

Friction coefficient plays an important role in the frequency and severity of traffic accidents. Surface friction constitutes skid resistance providing maneuver ability of the vehicle, which is a vital factor of road safety, especially during braking and turning on curves. Therefore, many countries have specified a minimum friction coefficient in the regulations for road construction (Teekman, 2012).

The frictional properties of road pavements have a great impact on drivers' reaction. It has been proved that most drivers have violent reaction (such as braking, steering, accelerating or combination of these actions) when they encounter a hazardous situation. All these action are related to frictional properties of road pavements (Ahmadinejad et al., 2018; Monajjem et al., 2013)

Several studies have been carried out on the relationship between friction coefficient of pavement surface and road accidents, all indicating that increasing the friction coefficient improves road safety. Table 1 presents the relationship between surface friction and accident rate, studied in a research, performed in Sweden. It was found that an increase in pavement friction significantly reduces the rate of accidents (Wallman et al., 2001). Other studies have also yielded similar results (Viner et al., 2004).

Table 1. Changes in rate of accidents with respect to changes in friction coefficient (Wallman et al., 2001)

Accidents rate (Accidents per million vehicle-kilometers)	Friction coefficient range
0.80	Less than 0.15
0.55	Between 0.15 and 0.24
0.25	Between 0.25 and 0.34
0.2	Between 0.35 and 0.44

2.2. Skid Resistance of the Pavement

Resistance to skidding, i.e. friction between the locked wheel of a vehicle and pavement surface is called "skid resistance". It can be measured by the British pendulum test, and the value is expressed in form of Skid Number (SN). SN is equal to friction coefficient (in percent), measured using locked wheel test (flat or ribbed) (Wallman et al., 2001).

The British Pendulum Number (BPN), which is also measured by British pendulum apparatus, is another commonly used criterion to measure skid resistance of pavements. In many references, BPN is considered as an index of friction at low speeds (less than 64 km/h) indicating the microtexture of pavement (ASTM E303, 2013; Lu et al., 2006; Kuttesch, 2004).

Hence the pavement surface is directly in contact with vehicle tire, skid resistance properties (as an important factor affecting the road safety) need to be investigated to be used in Pavement Management System

(PMS) analysis. Prediction of pavement behavior (including frictional and abrasion properties) is vital during its service life for providing appropriate rehabilitation procedures to prevent the pavement from reaching critical condition (Solatifar and Lavasani, 2020).

Many researches have been done to investigate the parameters affecting skid resistance. Some of them concluded that aggregate polishing resistance and bitumen aging status have impact on skid resistance of asphalt pavement. Aging of asphalt binder, while it is not still removed from aggregates surface, results in higher friction coefficient in asphalt pavements (Dan Zhao et al., 2010). Others have investigated skid resistance variation during time and derived the following factors, as the most determinant parameters affecting frictional properties of the surface: Surface polishing of the asphalt pavement, seasonal variation, binder removal, and bitumen aging (Do et al., 2007).

Do et al. (2009) studied the impact of aggregate polishing properties introducing aggregate hardness parameter, based on mineralogical composition, and showed that micro-texture of aggregates with higher mineralogical hardness are less vulnerable to polishing, which results in more endurable friction (Do et al., 2009b). Moreover, Do et al. (2009a) investigated the effect of aggregate asperity properties on surface polishing of asphalt pavements. Three key factors were employed to represent surface roughness: The profile root mean square, and two introduced texture angularity parameters, named shape and relief of surface asperity.

Although BPN is believed, in some studies, to be solely related to pavement microtexture, detailed analysis of British Pendulum Test procedure, supports the hypothesis of existence of a relationship between BPN and the pavement macrotexture. In this test method, a rubber slider, dimensioned at 2.54 cm by 7.6 cm, is dragged 12.5 cm on the pavement surface, traversing an area of 95 cm^2. Clearly, the pendulum slider can engage pavement macrotexture and affect the pendulum number under any circumstances (Jalal Kamali et al., 2019a)

A study conducted in 2008, to investigate the relationship between macrotexture and skid resistance of grooved concrete pavements, showed that pendulum number has a rather good correlation with texture depth (R^2 = 0.86). The research considered the maximum effective mean texture depth to be 1.8 mm, and showed that by increasing the mean texture depth, the pendulum number initially increases and then decreases (Ahammed et al., 2008).

In another research, pavement macrotexture was manually created by grooving, and it was concluded that BPN strongly depends on the macrotexture. It was indicated that BPN increases by increasing the number and width of the grooves, especially the transverse ones (Pancar and Karaca, 2016).

Skid resistance and noise characteristics on concrete pavements were investigated by Fang et al. (2020) and the results declared that traditional grooved cement concrete pavement had poor skid resistance. The initial skid-resistance level was high, but the skid-resistance level decreased rapidly soon after exposure to traffic.

By evaluating the effect of aggregates gradation and various methods of creating grooves to improve skid resistance of concrete pavements, Fakhri and Taribakhsh (2012) found that macrotexture parameters, including the largest aggregate size in concrete, grooving angle and width of the grooves, can affect BPN value. It was also discussed that grooving is a good choice to enhance the surface friction of concrete pavements.

By investigating the relationship between Mean Texture Depth and BPN in a new constructed highway, Jalal Kamali et al. (2020) showed that increasing MTD leads to BPN decrease and then increase. It was also illustrated that the asphalt content of Hot Mix Asphalt has the similar effect on BPN (the lowest BPN occur at 4.4% of

asphalt content).

As mentioned before, BPN is a good indicator of friction at speeds below 64 km/h. Considering the fact that friction plays a very important role in frequency and severity of road accidents, it seems vital to estimate the BPN value as well as the amount of friction during pavement construction. In this study, different types of conventional textures in concrete pavements are compared in terms of mean texture depth, BPN and abrasion resistance, and the best type of texture is introduced according to the mentioned factors.

2.3. Macrotexture in Concrete Pavements

During pavement lifetime, traffic loading polishes the microtexture, sooner or later. Therefore, adequate macrotexture should be created during/after construction, on the surface, to provide satisfactory friction during pavement life span. Various factors such as traffic characteristics, type and gradation of aggregates, weather conditions, pavement surface noise, and the amount of friction required need to be considered to choose the type of arranged macrotexture (Hall et al., 2009).

Depth, spacing and orientation of pavement macrotexture have significant impact on frictional properties, noise and ride quality (Ardani, 2006). As for macrotexture orientation, longitudinal texturing is more effective on lateral slopes and horizontal curves, while, transverse texture provides higher head-on skid resistance. Concerning rainfall drainage and highway lateral slopes, transversal texturing discharges the water faster and thus, a hydroplaning incident is less likely to occur (ACI-211, 2002).

Concrete pavement macro texture can be arranged using several methods. The most common ones are (ACI-211, 2002):

- Dragging artificial turf transversally and longitudinally on fresh concrete;
- Longitudinal or transversal brushing on fresh concrete;
- Longitudinal or transverse brooming on fresh concrete;
- Burlap dragging on the surface of fresh concrete;
- Grooving or grinding the hardened concrete.

2.4. Surface Abrasion and the Impact on Friction

Abrasion resistance in concrete is a term to address the ability of the surface to resist being worn away by rubbing and friction. A concrete with high abrasion resistance must possess both parameters of abrasion resistance and macrotexture durability under traffic.

Wang et al. (2014) counted the abrasion of an asphalt pavement surface, as one of the factors affecting friction and presented a model to predict the surface skid resistance, based on initial surface skid resistance and abrasion duration. They found that the skid resistance of surface decrease by the abrasion of pavement surface and the rate of skid resistance changes decrease by abrasion duration increases.

Kassem et al. (2013) determined the drop rate of International Friction Index (IFI) in regard to the number of abrasion cycles, by studying skid resistance reduction of hot mix asphalt. The IFI index may drop up to 60% depending on the type of aggregate and mix design.

The effect of fly ash on the abrasion resistance of concrete pavements has been investigated in another study. Based on the results, wet conditioned BPN decreases during the abrasion for the majority of specimens. As explained before, BPN reduction indicates the reduction of friction and skidding resistance (Yoshitake et al., 2016).

The impact of Nanomaterials on abrasion resistance of concrete pavements was also studied in a research, and it was shown that both micro and macrotexture significantly affect the surface friction. The research focused on the need for creating macrotexture with high resistance against abrasion. It was noted that macrotexture resistance against abrasion can reduce the

costs of providing friction during pavement maintenance process (Gonzalez et al., 2014).

Jalal Kamali et al. (2019b) investigated the effect of abrasion on five type of concrete macro textures. It was showed that brushed sample (transverse or longitudinal) experience the most abrasion among other macro texture. On the other hand, the brushed surfaces have the most skid resistance.

Long-term skid resistance of concrete pavements was investigated by Rith et al. (2020). The results showed that the decreasing rate of skid resistance in transverse and longitudinal tining was more rapid than the exposed aggregate concrete texture under traffic loading.

Najafi Alamdarlo and Hesami (2019) investigated the effect of pavement Porosity filling on skid resistance by field test and numerical model. The results showed that between 1-4% reduction in mean texture depth results in 2% reduction in skid number in HMA pavements.

To summarize, skid number is a key parameter in road safety and it completely depends on pavement surface properties. On the other hand, concrete pavement properties are affected by many parameters such as material properties, aggregate gradation, and surface finishing. In concrete pavements, the surface is textured in order to improve frictional properties. Determination of the skid resistance of each texture type is vital to evaluate road safety characteristics.

3. Laboratory Procedure

In this section, properties of the material, used in the study, as well as laboratory procedures including concrete mix design, sample preparation, texture creation and testing procedures have been briefly described.

3.1. Aggregates

Coarse-grained and fine-grained aggregates required for performing the tests were all supplied from Metosak mine, located in the southwest of Tehran (Shahriar area). Common conventional tests were implemented on them and the results are given below. Some mechanical properties such as abrasion resistance values of aggregates, acquired from Los Angeles abrasion test, as well as the impact resistance for coarse-grained aggregates were determined as follows:

Aggregate Soundness: weight loss values in Soundness test for the aggregate with magnesium and sodium sulfate have been presented in Table 3.

Coarse-grained aggregates grading curves have been obtained, considering the upper and lower limits of ACI regulation. By taking the average of these two limits and the fine-grained aggregates, there is no need for further gradation with regard to the fact that they were within the permitted limits of regulation. Figure 1 shows gradation diagram of the fine-grained and coarse-grained aggregates used for concrete mixture.

3.2. Cement

The Qazvin's Abyek cement was used to create concrete pavement samples. The physical and chemical properties of the cement were assessed in Tarbiat Modarres University laboratories and their results are reported in Tables 4 and 5.

Table 2. Some specifications of fine-grained and coarse-grained aggregates

Variables	Standard code	Coarse aggregate	Fine aggregate
Specific gravity (g/cm^3)	ASTM C136	2.67	2.67
Bulk Specific gravity (g/cm^3)	ASTM C29	1.64	-
Water absorption in SSD	ASTM C127	1.3	2.6
Fineness modulus	ASTM C136	-	2.85
Sand equivalent	ASTM D2410	-	80
Los Angeles abrasion test	ASTM C131	12%	-
Impact resistance	BS 812	8.1%	-

Table 3. Results of coarse-grained soundness test

Coarse-grained aggregates	Soundness test with sodium sulfate (ASTM C88)	9.5% weight loss
	Soundness test with magnesium sulfate (ASTM C88)	12.6% weight loss

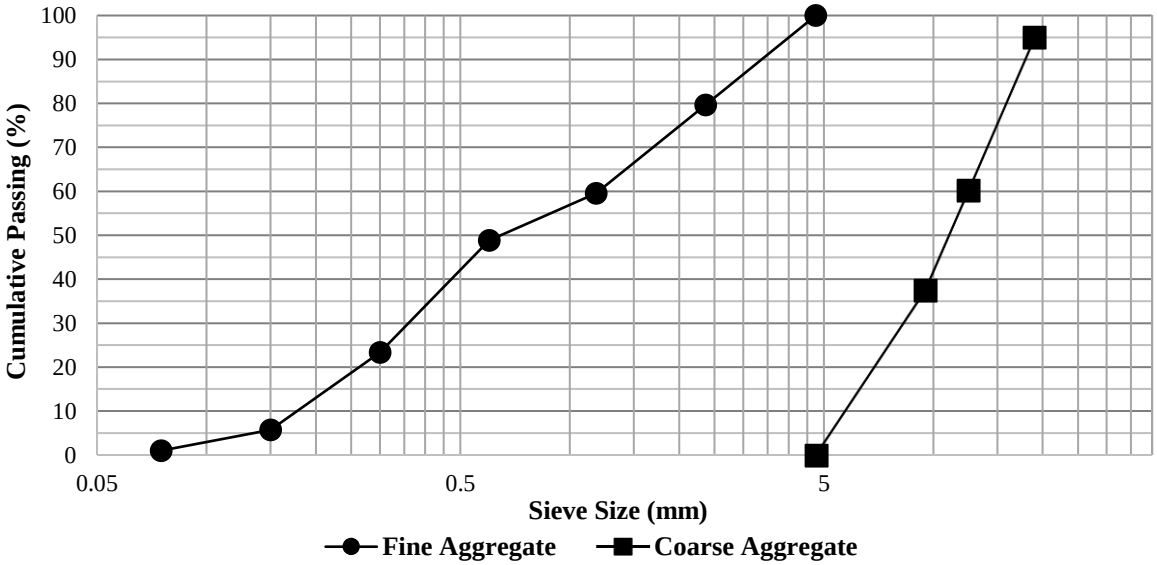

Fig. 1. Gradation diagram for fine-grained and coarse-grained aggregates

Table 4. Physical and mechanical specifications of the used cement

	Specific surface (ASTM C204)	**Specific gravity (ASTM C188)**	**3 day compressive strength (ASTM C109)**	**7 day compressive strength (ASTM C109)**
Minimum requirement	-	-	12 MPa	19 MPa
Abyek cement	3250 cm^2/gr	3.15 gr/cm^3	12.5 MPa	21.9 MPa

Table 5. Constituent compounds of the used cement

Component	L.O.I	CaO	Si2O	Al2O3	Fe2O3	SO3	MgO	K_2O	Ti_2O	Cl	**Total**
Percentage	1.85	62.21	18.492	4.026	3.777	3.208	2.731	0.811	0.366	0.173	97.642

3.3. Concrete Mix Design

The concrete mixture proportions are designed according to ACI-211 regulation. During design process, based on the dimensions of sample molds, the maximum aggregate size was chosen to be ¾ inch. Since the achievements, obtained in this research, may be used in concrete pavements construction, specifications of the designed mix should be as similar as possible to conventional concretes, used in pavements all over the world. Therefore, minimum compressive and flexural strength of concrete in the design process were considered to be 40 and 4.5 MPa, respectively (Delatte, 2014). Also, slump value was assumed to be between one and two inches. With regard to aggregates properties and expected specifications of the concrete, an initial mixture design was selected. After several modifications, final mixture proportions of the concrete were eventually determined, according to Table 6.

3.4. Preparation of Specimens

In this study, according to the achieved concrete mix design, forty eight 10×10×50 cm beams were constructed, and different macrotextures were created on them. As stated before, the created textures are among the most common methods for creating macrotexture on concrete surfaces (ACI-211, 2002). The following notation is used to address different types of texture:

- Without texture (no texture): NT;
- Texture created by dragging artificial turf (Turf dragging): TD;
- Texture created by grooving (Grooving): G;

- Texture created by dragging plastic brush parallel to traffic path (Parallel Brushing): ParB;
- Texture created by dragging plastic brush perpendicular to traffic path (Perpendicular Brushing): PerB;
- Texture created by dragging burlap parallel to traffic path (Burlap dragging): BD.

After being cured for 28 days, concrete beams were sawed into 10×10×15 cm pieces to obtain 127 samples (excluding wasted specimens). Afterward, the concrete beams were subjected to British Pendulum, Sand Patch and Wide Wheel Abrasion tests.

3.5. Wide Wheel Abrasion Test

In this research, an abrasion device made according to BS EN 1338: 2003 standard, was used to abrade the concrete specimens with different textures. According to the above-mentioned standard, the surface of concrete specimen was abraded in the vicinity of a steel wheel in the presence of alumina oxide (corundum). Figure 2 shows the abrasion device used in this research.

When the concrete sample was abraded for one minute, size of the groove left by the abrasion process was measured accurately. In this research, in order to increase the accuracy and also to facilitate the measurement of dimensions of the created groove, a high-quality photo was taken from the surface of specimen with a ruler placed next to it. Then, using AUTOCAD software and by performing the related calculations, dimensions of the groove were measured. Also, to enhance the accuracy of picture, the specimens were wetted before taking the photos to make the abraded area well defined and specified. Figure 3 shows a concrete specimen that has been textured by dragging artificial turf on fresh concrete after performing the abrasion test in both wet and dry condition.

Fig. 2. The employed abrasion machine

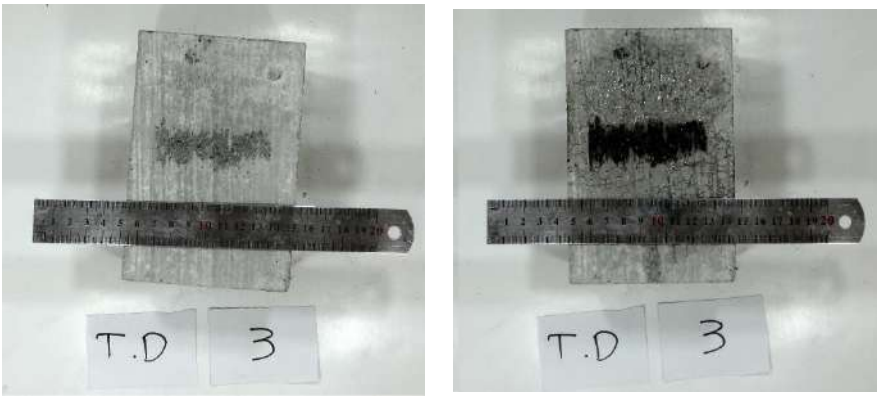

(a) **(b)**

Fig. 3. Concrete specimen (Turf dragged) after abrasion in: a) Dry; and b) Wet condition

Table 6. Mix design of the employed concrete

	Gravel (kg/m^3)	Sand (kg/m^3)	Cement (kg/m^3)	Water (kg/m^3)	W/C ratio
Mix design proportion	1091	670	400	176	0.44

3.6. Measuring Friction by Tribometer

In this research the tribometer produced in Tarbiat Modares University (Kashani et al., 2011; Kashani and Nisiany, 2011), shown in Figure 4, was utilized to measure the friction coefficient of concrete pavements. The output data of the test for a specimen, over time, is depicted in Figure 5. In this procedure, the friction of surface is measured by rotating a rubber ring (with specific composition) on the surface at standard speed and vertical force. The area of the ring is 260.93 mm^2 and the traveling speed of rubber over specimen surface can vary between 1 to 2200 mm/sec. The applied vertical force can be set between 0.1-1.25 MPa.

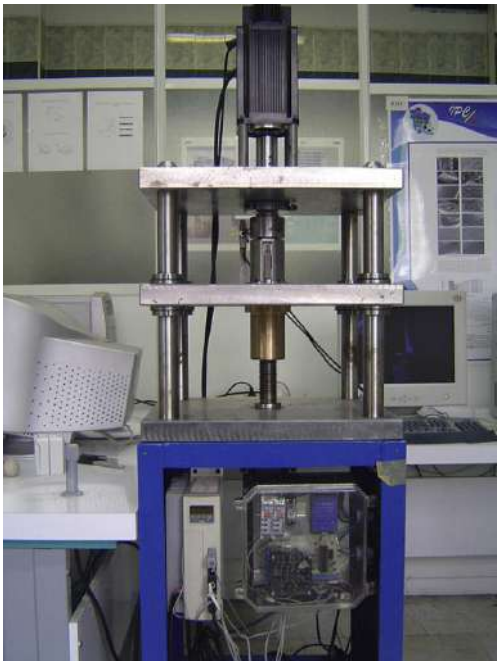

Fig. 4. Friction Test Machine (Kashani et al., 2011)

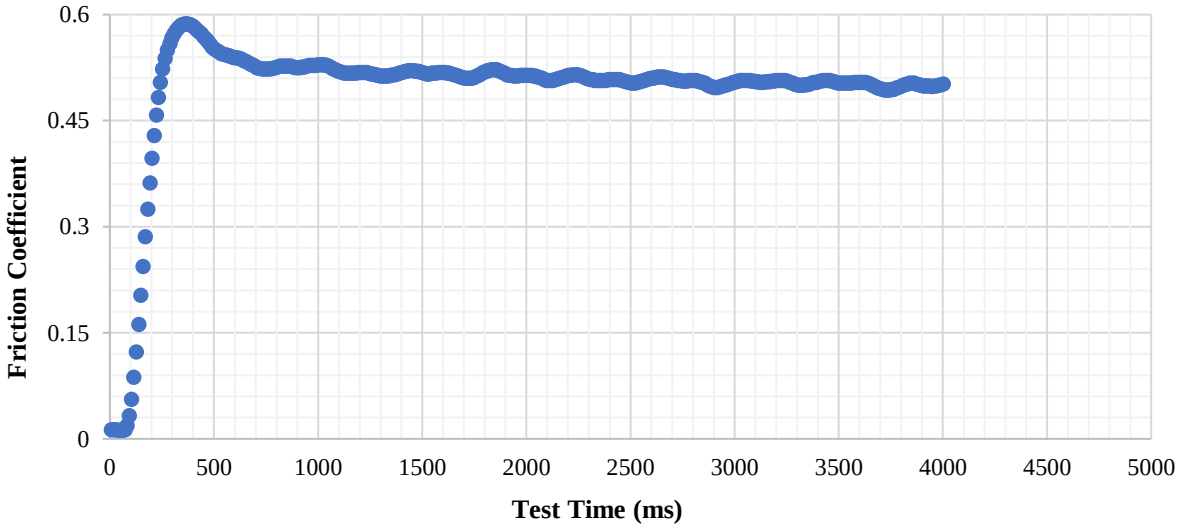

Fig. 5. Wet friction coefficient of the G sample

4. Results

After performing British pendulum, sand patch, abrasion resistance and friction coefficient tests on concrete specimens, the mean values of BPN, MTD, Abrasion Resistance and Friction Coefficient for each specimen of the pavement texture were calculated, which are given in Figures 6 to 9, respectively. As predicted, the pavement with no macrotexture created on it, has allocated the lowest amount of BPN, MTD and Friction Coefficient to itself.

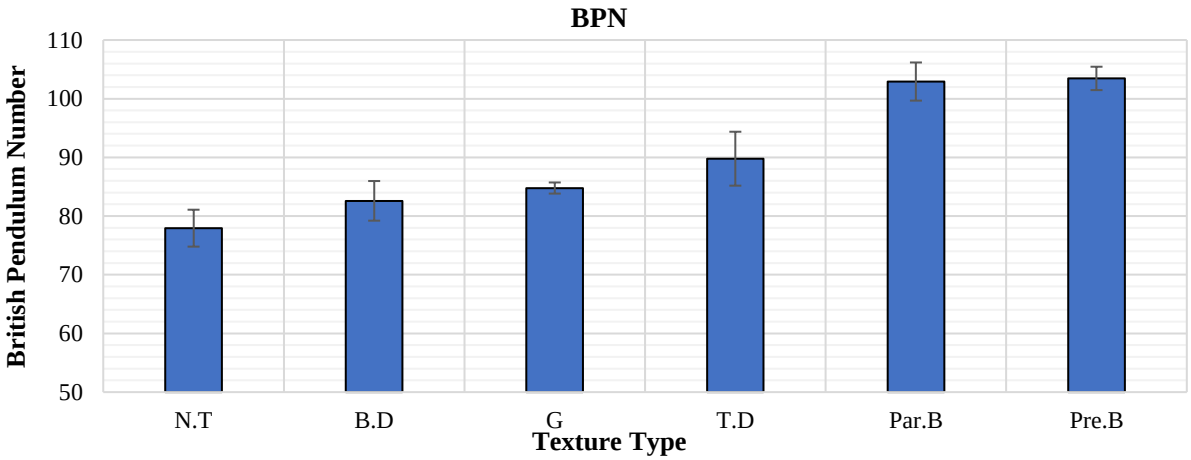

Fig. 6. Comparison of BPN values for different pavement texture

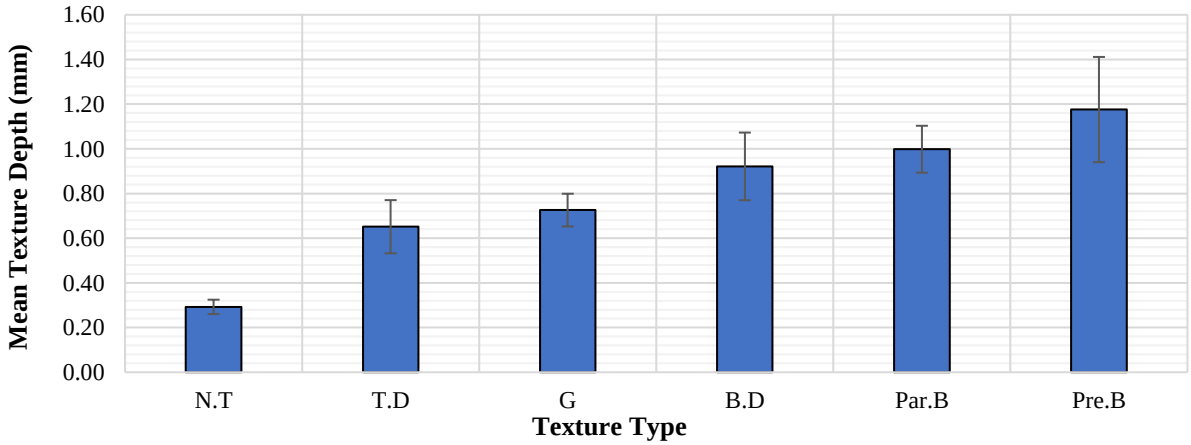

Fig. 7. Comparison of MTD values for different pavement texture

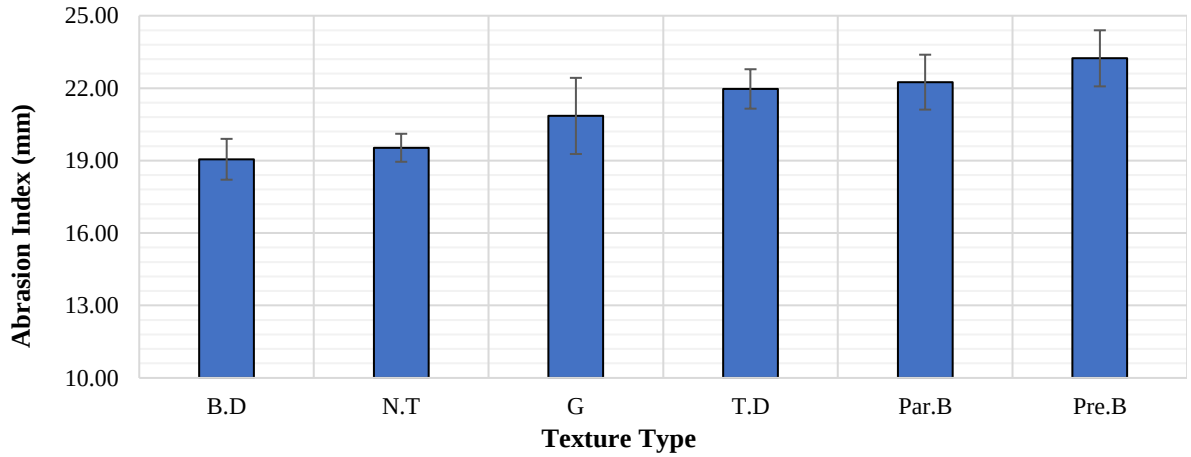

Fig. 8. Comparison of abrasion index values for different pavement texture

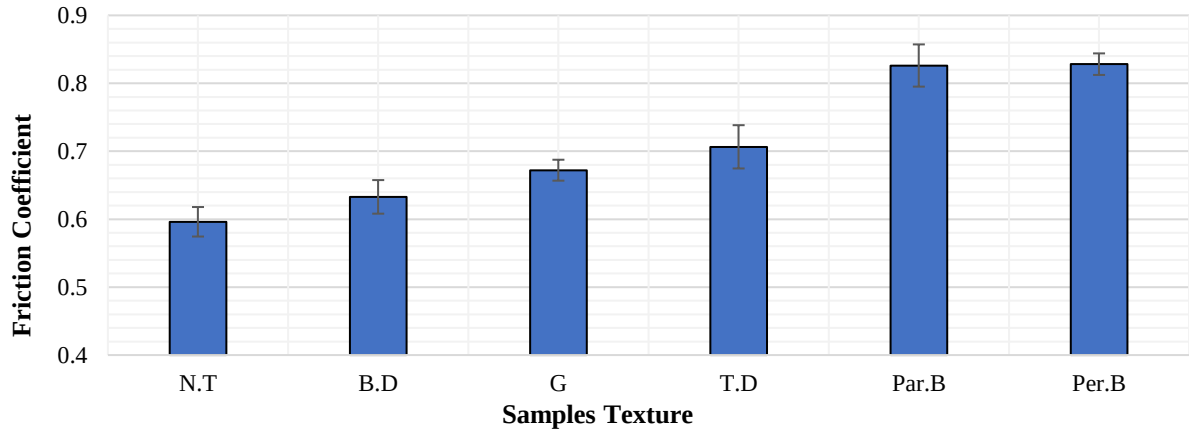

Fig. 9. Comparison of friction coefficient values for different pavement texture

Table 7. ANOVA statistical analysis on the test results

		Sum of squares	df	Mean square	F	Sig.
MTD	Between groups	10.249	5	2.050	103.941	0.000
	Within groups	2.386	121	0.020		
	Total	12.636	126			
BPN	Between Groups	12194.862	5	2438.972	234.369	0.000
	Within groups	1259.192	121	10.407		
	Total	13454.054	126			
A.I	Between groups	285.252	5	57.050	40.056	0.000
	Within groups	172.335	121	1.424		
	Total	457.587	126			
Friction	Between groups	1.015	5	0.203	321.541	0.000
	Within groups	0.076	121	0.001		
	Total	1.091	126			

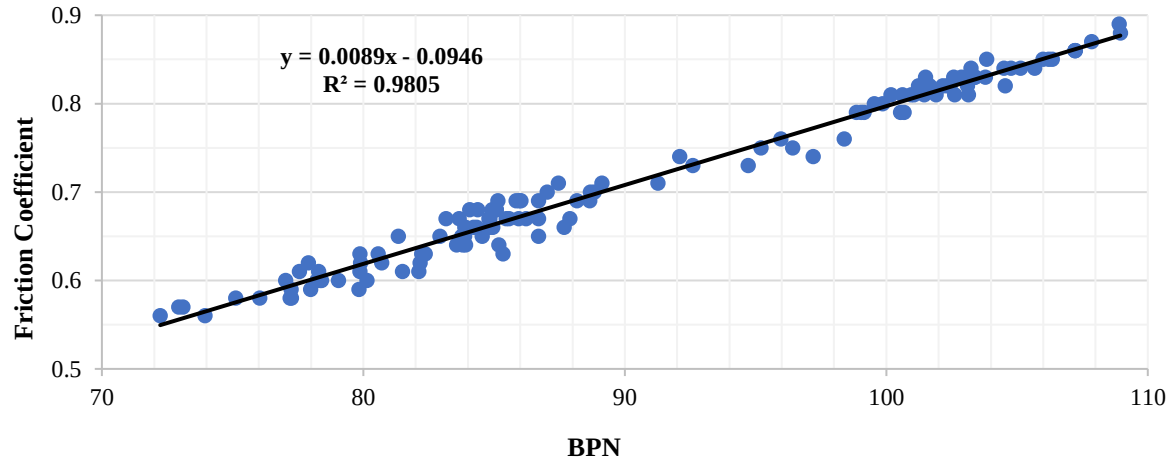

Fig. 10. The relationship between BPN and friction coefficient

Table 7 shows the ANOVA statistical analysis on the results of the sand patch, British pendulum number and wide wheel abrasion tests. With regard to the numerical values of the F and Sig. statistics, it is determined that the difference of the means reported for each of the values of BPN, MTD, AI (Abrasion Index) and friction coefficient is statistically significant. Figure 10 shows the relationship between friction coefficient and BPN in all differently textured samples. As expected, the friction coefficient directly depends on BPN (R^2 = 0.9805).

For concrete specimens constructed with different types of texture, the diagram of the

variations of the pendulum number versus Mean Texture Depth has been depicted, which its governing relationships have been described in detail in the discussion and conclusion section. In Figures 11 to 16 the best line or second-degree parabola that can express the relationship between these two variables has been drawn and its equation has also been mentioned. The R^2 parameter was also reported as an indicator of the amount of correlation between the two abovementioned variables.

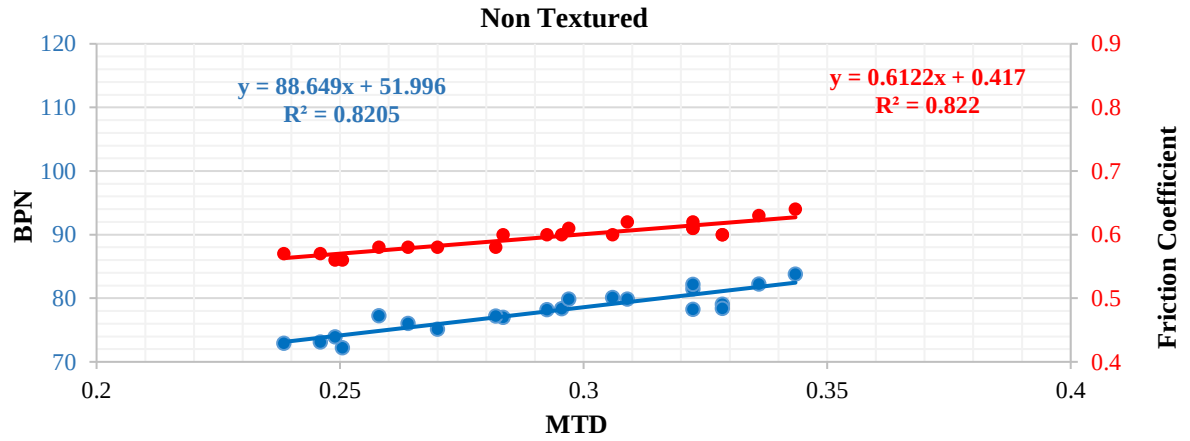

Fig. 11. The relationship between BPN and friction coefficient in N.T. pavement

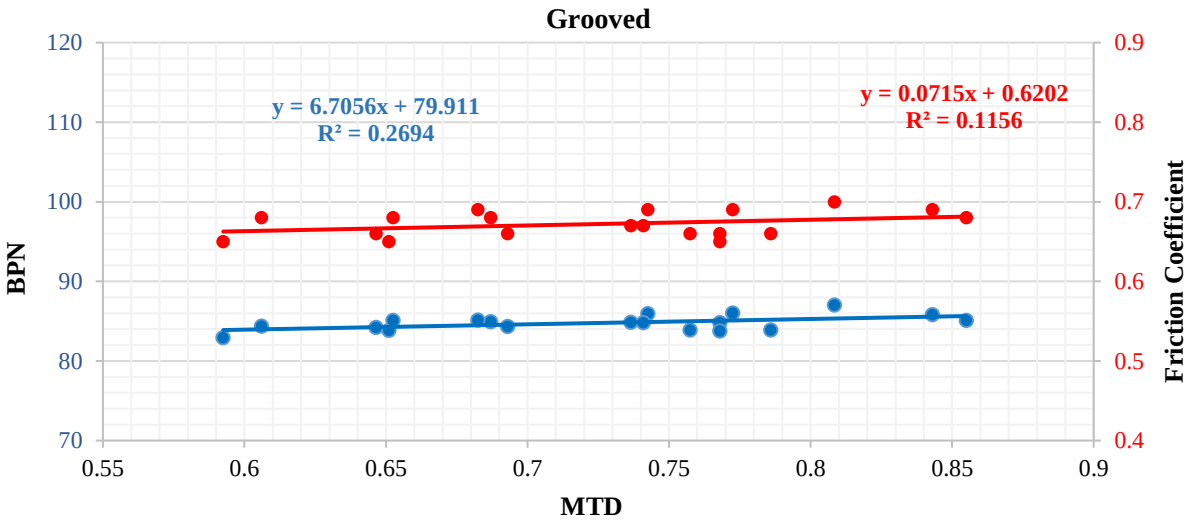

Fig. 12. The relationship between BPN and friction coefficient in G. pavement

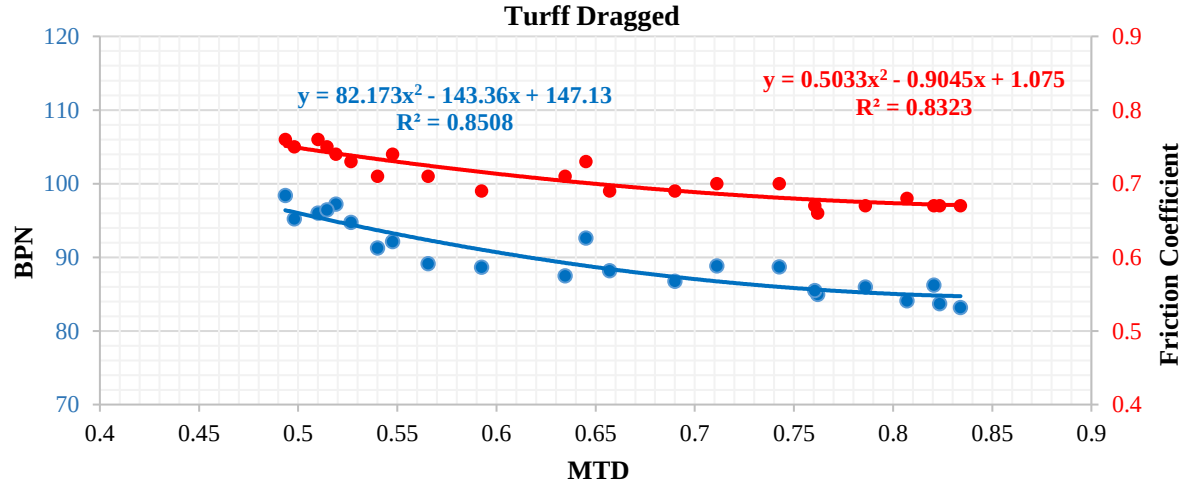

Fig. 13. The relationship between BPN and friction coefficient in T.D. pavement

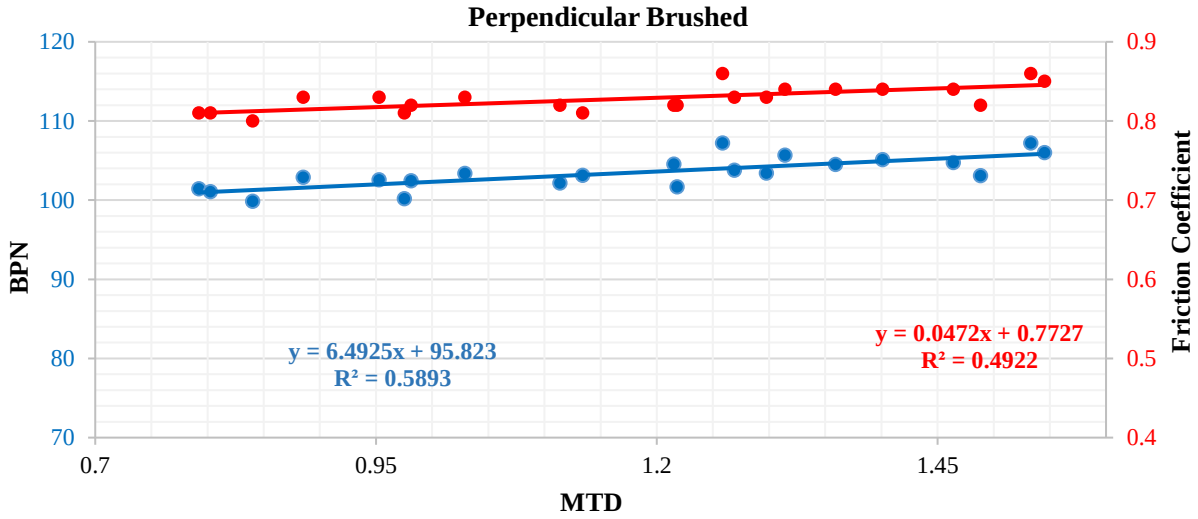

Fig. 14. The relationship between BPN and friction coefficient in Per.B. pavement

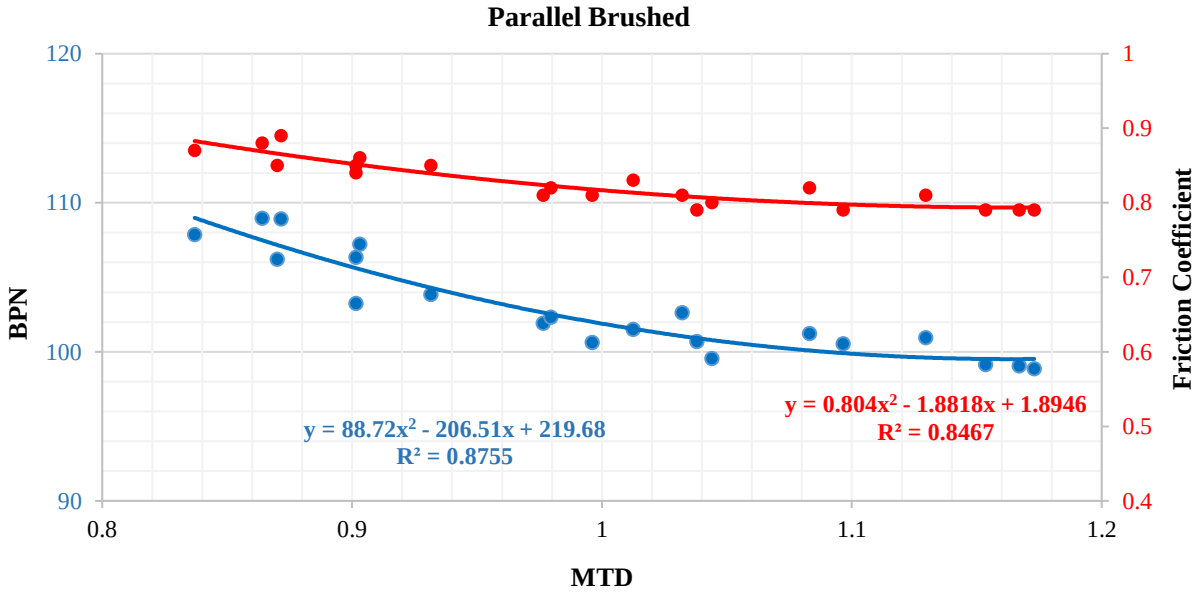

Fig. 15. The relationship between BPN and friction coefficient in Par.B. pavement

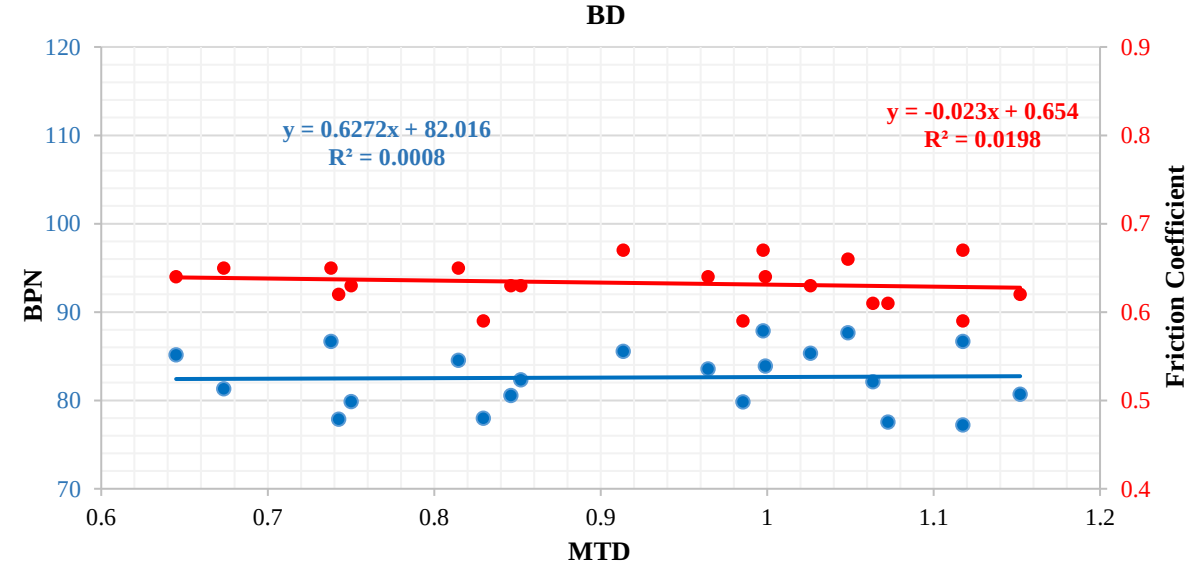

Fig. 16. The relationship between BPN and friction coefficient in B.D. pavement

5. Discussion

Figures 11-16 depict British Pendulum Number (BPN) and friction coefficient variations versus Mean Texture Depth (MTD). With regard to different behaviors of BPN against MTD, this section the relationship between these two variables is investigated in the following four subsections and afterward, the results of Wide Wheel Abrasion test are also assessed.

5.1. The Relationship between BPN and MTD in Per.B and N.T Samples

In untextured samples, the surface of pavement is approximately smooth and the mean texture depth is very small (less than 0.4 mm). In this type of texture, with an increase in amount of MTD, BPN also increases. By increasing 0.1 mm of MTD, the BPN increase about 8.9 units. MTD in these specimens is very small and the pendulum rubber slider drags its path easily. Figure 6 confirms that the average BPN for these pavements is much lower than other pavements. By increasing MTD of pavement, on a very small scale, coarseness is added to the surface of pavement. Interaction of this coarse surface with the rubber causes an increase in the friction coefficient. The opposite trend can be seen in parking lots with concrete paving where usually the pavement is constructed without texture so the surface friction decreases rapidly due to abrasion caused by vehicle traffic. In a pavement that has acquired a macro texture by brushing in perpendicular direction, MTD is higher than the other texturing types, which causes the rubber, while dragging the surface of the pavement, to get stuck in fine grooves created on the concrete that are perpendicular to traffic direction. This leads to an increase in longitudinal friction coefficient and consequently BPN. In Figure 17, which shows a perpendicularly brushed pavement, the created grooves are clearly distinguishable. Given that brushing is performed when the concrete is wet, sometimes during the brushing process some of mortar on the surface transfigure and after hardening, they become an obstacle to the movement of tires.

5.2. The Relationship between BPN and MTD in T.D and Par.B Samples

Artificial turf and plastic brush have similar behaviors when pulled over fresh concrete. Having thin fibers, they both leave thin grooves by passing over fresh concrete, but due to different structure of plastic brush and artificial turf, depths of these grooves are slightly different. As can be observed in Figure 18 the grooves created by artificial turf have lower depth.

Since rubber is a flexible material when compressed in one direction, if there is an empty space, its volume increases in the other directions. In other words, when the rubber under pressure from the vehicle (in this research, under standard pressure of British Pendulum) passes over the pavement with grooves (longitudinal or transverse), due to compression of the rubber, a part of rubber that is on the empty space between the two grooves slightly increases in volume and penetrates in it.

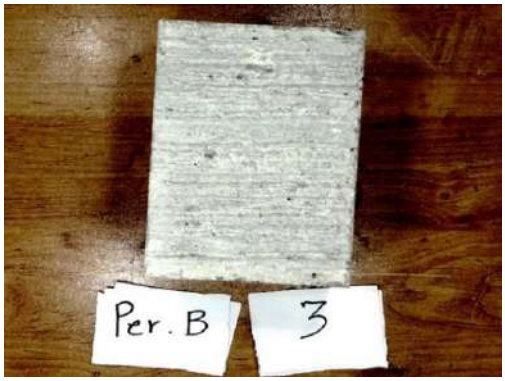

Fig. 17. A specimen with perpendicular brushing texture on it

In these cases, since grooves are parallel to rubber movement (or traffic) direction, when the depth of groove is small, the rubber which is pulled between the two grooves is dragged against its walls and bottom and as a result, the friction between rubber and pavement is high. But when these grooves get deeper, the rubber no longer comes in contact with the bottom of the groove when passing over and the friction between the rubber and the concrete surface decreases. Thus, with an increase in depth of parallel grooves (produced by artificial turf dragging or plastic brushing), BPN slightly decreases. It is worth mentioning that this decrease has a higher rate at first and with a further increase in depth of the groove, the rate of decrease in BPN decreases, as well. This is clearly evident in Figures 13 and 15.

5.3. The Relationship between BPN and MTD on G Samples

The grooving of specimens is performed after hardening of the concrete and, due to spacing between the grooves (2.5 cm in average), a major section of surface is similar to untextured pavement. But the presence of grooves has caused BPN to increase by seven units on average. The trend of changes in BPN versus the changes in MTD of pavement is similar to that of untextured pavements, but the equations governing these two cases are completely different which can be attributed to different variation range of macrotexture. Due to relative similarity of distance and depth of the grooves, the amount of increase in MTD is approximately limited.

Contrary to brush or turf dragging specimens, depth of the grooves in grooved specimens is much higher and practically the rubber does not come in contact with the bottom of the groove when it passes over it. In fact, as explained earlier, a further increase in depth of the grooves does not lead to an increase in skid resistance. It is worth noting that deeper grooves have a significant effect on proper drainage during the rain and prevent the occurrence of hydroplaning which is not the subject of this research.

A weak correlation coefficient shows that we cannot make an accurate judgment with regard to the exact amount of slope of the line or ratio of the changes in BPN versus MTD. But what is clear is an increase in BPN versus an increase in MTD.

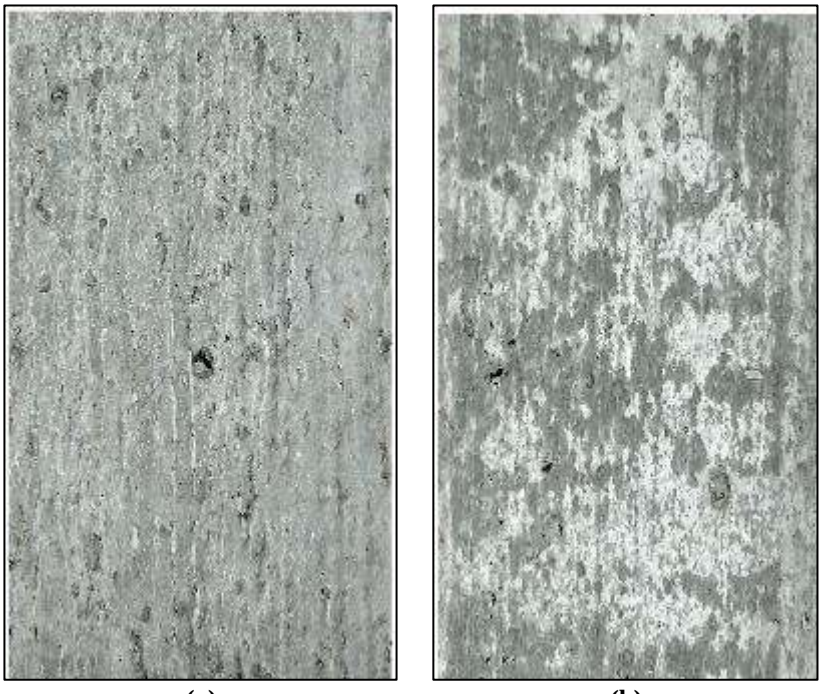

(a) **(b)**

Fig. 18. Specimen with: a) Parallel brushing; and b) Turf dragging texture on it

5.4. The Relationship between BPN and MTD in B.D Samples

As it can be seen in Figure 16 in burlap dragged pavements the variations of MTD and BPN occur in relatively large ranges and no specific relationship is observable between these two parameters. Lack of uniformity of the process of texturing by burlap dragging can be mentioned as one of the reasons for extensive variations in MTD and BPN. Although burlap used in this research were made of the same material, they showed different patterns when dragged on concrete. Displacement of fine grains (granules) of the surface of the concrete by burlap can be mentioned as one of the reasons for this matter. These displacements cause the track of dragging to remain on concrete and consequently major variations in MTD and BPN. Figure 19 shows a concrete specimen textured with burlap dragging where the path of movement of some of the granules on the surface of concrete is distinguishable.

5.5. Abrasion Resistance in Various Textures of Concrete Pavements

As mentioned before, in the current research, the abrasion test is implemented in accordance with BS EN-1338 to measure abrasion resistance of various textures created on concrete pavements. For each specimen of each texture, the height of abraded section was determined and its average has been shown in Figure 8. According to EN 1338, the height of abraded part should not exceed 23 mm. By considering the results of this research, it can be concluded that perpendicular brushed texture, with an average of 23.2 mm, is not an abrasion resistant texture. On the other hand, dragged burlap and untextured pavement, with an abrasion less than 20 mm, are classified in the category of pavements with suitable abrasion resistance.

Although for each texture, abrasion increases with an increase in MTD, this trend is not valid among all data obtained from different textures. In other words, an increase in MTD in each particular texture will cause an increase in the amount of abrasion (abrasion resistance decrease) of the pavement.

6. Conclusions

- Macrotexture of the concrete pavement had significant effect on wet skid resistance of the surface. Thus, it is possible to achieve the desired skid resistance using different methods of creating macrotexture on concrete pavements.
- For untextured pavements, the rate of BPN variation versus MTD was severe (87 unit change of BPN versus 1 mm change of MTD). Despite good abrasion resistance, these pavements are not recommended for use in roads due to low skid resistance.
- Brushing on fresh concrete parallel and perpendicular to traffic direction resulted in the highest skid resistance (minimum increase of friction coefficient to 0.8). Shallow grooves appeared on the concrete using these methods led to higher engagement of tire and surface of the pavement as a result of an increase in the skid resistance.

Fig. 19. Specimen with burlap dragging on it

- Dragging artificial turf on the concrete created a macrotexture similar to the texture of parallel brushing, with the difference that the turf dragged specimen had lower mean texture depth, lower skid resistance and consequently lower friction coefficient.
- Macrotexture created by turf dragging and brushing perpendicular to traffic direction can be used on the roads with medium traffic volume due to large amounts of BPN as well as proper abrasion resistance.
- Depth of the grooves created on hardened concrete had no significant effect on skid resistance of the concrete, but deeper and wider grooves can provide better drainage of overland flow and prevent the occurrence of hydroplaning during rain.
- Burlap dragging is not a good texturing method in the concrete pavements because of the lack of uniformity in the created texture. But, this type of texturing led to abrasion resistant pavement. Burlap dragging does not create a uniform texture due to displacement of some granules by the burlap dragging on the fresh concrete. This method showed better abrasion resistance compared to other texturing methods, so it can be used as a suitable method provided that some modifications are applied to the procedure of achieving a more uniform surface.

7. Acknowledgement

Authors wish to express their gratitude to Ms. Moshtaghi for her assistance.

8. References

ACI Committee 211. (2002). *Standard practice for selecting proportions for normal, Heavy weight and mass concrete (ACI 211.1-91)*, Detroit, MI: American Concrete Institute.

Ahammed, M.A. and Tighe, S.L. (2008). "Pavement surface mixture, texture, and skid resistance: A factorial analysis", In: *Airfield and Highway Pavements: Efficient Pavements Supporting Transportation's Future*, Bellevue, Washington, United States, pp. 370-384.

Ahmadinejad, M., Afandizadeh Zargari, S. and Jalalkamali, R. (2018). "Are deceleration numbers a suitable index for road safety?", *Proceedings of the Institution of Civil Engineers*, 171(5), 247-252.

Alamdarlo, M.N. and Hesami, S. (2020). "Measuring the effect of pavement porosity filling on skid resistance by numerical model and field test", *Measurement*, 152, 107269.

Ardani, A.A. (2006). "Implementation of Proven PCCP Practices in Colorado", No. CDOT-DTD-R-2006-9, Colorado Department of Transportation Research Branch, United States.

ASTM E303-93. (2003). *Standard method for measuring frictional properties using the British Pendulum Tester*, Annual Book of ASTM Standards, Road and Paving Materials.

ASTM E965-96. (2006). *Standard test method for measuring pavement macrotexture depth using a volumetric technique*, Annual Book of ASTM Standards, Road and Paving Materials.

Delatte, N.J. (2014). *Concrete pavement design, construction, and performance*, CRC Press.

Do, M.T., Kane, M., Tang, Z. and de Larrard, F. (2009a). "Physical model for the prediction of pavement polishing", *Wear*, 267(1-4), 81-85.

Do, M. T., Tang, Z., Kane, M. and de Larrard, F. (2007). "Pavement polishing, Development of a dedicated laboratory test and its correlation with road results", *Wear*, 263(1-6), 36-42.

Do, M.T., Tang, Z., Kane, M. and de Larrard, F. (2009b). "Evolution of road-surface skid-resistance and texture due to polishing", *Wear*, 266(5-6), 574-577.

Fakhri, M. and Taribakhsh, M. (2012). "Influence of aggregate grading and creation of macrotexture with the tinning method on the skid resistance of concrete pavements", *Journal of Transportation Research*, 9(3), 293-312.

Fang, J., Tu, J. and Wu, K. (2020). "Analysis of skid resistance and noise characteristics for varieties of concrete pavement", *Advances in Materials Science and Engineering*, Vol. 2020, 8 p.

Gonzalez, M., de Oliveira Lima, A. and Tighe, S.L. (2014). "Nanoconcrete for rigid pavements: abrasion response and impact on friction", *Transportation Research Record*, 2441(1), 28-37.

Hall, J.W., Smith, K.L. and Littleton, P.C. (2009). *Texturing of concrete pavements*, Vol. 634, Transportation Research Board.

Iranian Legal Medical Organization (ILMO). (2020). http://www.lmo.ir/ (in Persian).

Jalal Kamali, M.H., Hassani, A. and Sodagari, J. (2019a). "Investigation the relation between skid resistance and mean texture depth in concrete pavements", *Concrete Research*, 12(1), 27-38, (in Persian).

Jalal Kamali, M.H., Hassani, A. and Sodagari, J. (2020). "Investigating the relation among British pendulum number, mean texture depth and asphalt content in hot mix asphalt", *Journal of Rehabilitation in Civil Engineering*, 8(1), 87-96.

Jalal-Kamali, M.H., Hasani, A. and Sodagari, J. (2019b). "Introduction and application of rotational abrasion device to determine concrete pavement Abrasion", *Civil Engineering Infrastructures Journal*, 52(2), 295-308.

Kashani, M.R. and Nisiany, R.E. (2011). "Design, construction, and evaluation of rubber friction tester", *Science and Technology*, 24(2), 153-164.

Kashani, M.R., Behazin, E. and Fakhar, A. (2011). "Construction and evaluation of a new tribometer for polymers", *Polymer Testing*, 30(3), 271-276.

Kassem, E., Awed, A., Masad, E.A. and Little, D.N. (2013). "Development of predictive model for skid loss of asphalt pavements", *Transportation Research Record*, 2372(1), 83-96.

Kuttesch, J.S. (2004). "Quantifying the relationship between skid resistance and wet weather accidents for Virginia data", Doctoral Dissertation, Virginia Tech.

Lu, Q. and Steven, B. (2006). "Friction testing of pavement preservation treatments: Literature review", Technical Memorandum No. UCPRC-TM-2006-10, UC Davis, University of California Pavement Research Center, Retrieved from https://escholarship.org/uc/item/3jn462tc.

Monajjem, M.S., Jalal Kamali, M.H. and Ayubirad, M.S. (2013). "Studying the effect of spiral curves and intersection angle, on the accident ratios in two-lane rural highways in Iran", *Promet-Traffic andTransportation*, 25(4), 343-348.

Pancer, E.B. and Karaca, Z. (2016). "Reliability of British pendulum test on macrotextured surfaces", *International Journal of Innovation Sciences and Research*, 5(1), 611-616.

Rasouli, M.R., Nouri, M., Zarei, M.R., Saadat, S. and Rahimi-Movaghar, V. (2008). "Comparison of road traffic fatalities and injuries in Iran with other countries", *Chinese Journal of Traumatology* (English Edition), 11(3), 131-134.

Rith, M., Kim, Y.K. and Lee, S.W. (2020). "Characterization of long-term skid resistance in exposed aggregate concrete pavement", *Construction and Building Materials*, 256, 119423.

Solatifar, N. and Lavasani, S.M. (2020). "Development of an Artificial Neural Network model for asphalt pavement deterioration using LTPP data", *Journal of Rehabilitation in Civil Engineering*, 8(1), 121-132.

Teekman, E. (2012). "The determination of the relationship between friction and traffic accidents", M.Sc. Thesis, Faculty of Business Economics, University of Hasselt.

Viner, H., Sinhal, R. and Parry, T. (2004). "Review of UK skid resistance policy", In: *Symposium on Pavement Surface Characteristics [of Roads and Airports]*, 5th, Toronto, Ontario, Canada.

Wallman, C.G. and Åström, H. (2001). "Friction measurement methods and the correlation between road friction and traffic safety: A literature review (VTI meddelande 911A)", Swedish National Road and Transport Research Institute (VTI).

Wang, H. and Liang, R.Y. (2014). "Predicting field performance of skid resistance of asphalt concrete pavement", In: *Proceedings of the Geo-Shanghai International Conference: Pavement Materials, Structures, and Performance*, Shanghai, China, pp. 296-305.

Wu, Z., King, B., Abadie, C. and Zhang, Z. (2012). "Development of design procedure to predict asphalt pavement skid resistance", *Transportation Research Record*, 2306(1), 161-170.

Yoshitake, I., Ueno, S., Ushio, Y., Arano, H. and Fukumoto, S. (2016). "Abrasion and skid resistance of recyclable fly ash concrete pavement made with limestone aggregate", *Construction and Building Materials*, 112, 440-446.

Zhao, D., Kane, M. and Do, M.T. (2010). "Effect of aggregate and asphalt on pavement skid resistance evolution", In: *Proceedings of the Geo-Shanghai International Conference: Paving Materials and Pavement Analysis*, Shanghai, China, pp. 8-18.

Civil Engineering Infrastructures Journal 2021, 54(2): 319-330
DOI: 10.22059/CEIJ.2020.297941.1657

RESEARCH PAPER

The Effects of Cold-Drawn Crimped-End Steel Fibers on the Mechanical and Durability of Concrete Overlay

Sobhani, J.[1]* and Pourkhorshidi, A.[2]

[1] Associate Professor, Road, Housing and Urban Development Research Center (BHRC), Tehran, Iran.
[2] Ph.D. Candidate, Road, Housing and Urban Development Research Center (BHRC), Tehran, Iran.

Received: 15 Feb. 2020; Revised: 21 Apr. 2020; Accepted: 15 Jun. 2020

ABSTRACT: A bonded concrete overlay consists of a new concrete overlay placed directly on top of an existing concrete pavement. The properties of such layer have a distinguished factor for reliable service-life extending of concrete pavements repairing systems. In this paper, the engineering properties of cold-drawn crimped-end steel fiber reinforced (CFCSF) concrete mixtures as overlays are evaluated. To this end, CFCSF mixtures are made with fiber contents of 15 and 25 kg/m^3 with diameters of 0.8 and 1 mm and water-cement ratio of 0.5 in comparison with reference concrete. The engineering properties of these types of concrete in the properties of the fresh and the hardened concrete including Compressive Strength (CS), Tensile Strength (TS), flexural strength (FS), Modulus of Elasticity (ME), depth of Water Penetration (WP), Impact (IR) and Abrasion Resistance (AR) are investigated. The results show that at an early age, the addition of fibers had no significant effects on the CS but at higher ages, the samples containing steel fibers have higher compressive TS and FS than the control ones. Also, the use of steel fibers increases the ME, IR and AR of CFCSF specimens. Moreover, models are developed to correlate the mechanical properties of mixtures with AR and IR. The comparison between the relation of AR and IR to other mechanical properties, made of the linear regression and polynomial relationships in aspects of R^2, indicates that stronger relations are available between TS with IR and AR with ME.

Keywords: Abrasion Resistance, Concrete Overlay, Impact Resistance, Mechanical Properties, Steel Fiber.

1. Introduction

Concrete overlays, are defined as a suitable solution which have long life and high durability, lead to fewer repairing and replacing cycles and lower related expenses, and fewer raw materials, energy, and resources used with the passage of time. Two options regarding concrete overlays exist: bonded and unbonded. Bonded concrete overlays are comparatively thin (50-150 mm). The overlay and the existing pavement when bonded, perform as one integrated system. To ensure a good performance, it is needed a strong bond between the pavement and overlay. Such

* Corresponding author E-mail: ja_sobhani@yahoo.com

bonded system ensures the load-bearing capacity of whole composite pavement system. (Harrington and Fick, 2014; Isla et al., 2015).

Nowadays, the technology developed in the field of pavement resurfacing systems. Many of the technological changes and advances predicted in previous studies have been realized because the pavement technologist and engineers cooperated to better design and present the required specifications for different types of concrete pavements.

Among recent developments, a better definition has been proposed to evaluate existing pavements for concrete pavements. A novel technique proposed, is the application of synthetic and steel fiber technology in this field. This technology has recently received a great attention due to the performance of thin concrete resurfacing. Fiber reinforcement increase the structural integrity of concrete attributed to the improved toughness and durability of the concrete. Some research studies have been carried out, providing solutions of bonded and un-bonded concrete overlays for road pavements (Isla et al., 2015).

Tavakoli et al. (2016) investigated the mechanical behavior of the fiber reinforce of SCC with steel and synthetics fibers. They found that, polyphenylene sulfide (PPS) and glass fibers can make better the mechanical performance like the flexural and the tensile strength, toughness and fracture performance of FRC concretes; although the compressive strength is declined due to application of fibers. Moreover, steel fibers significantly increased properties of absorbing the energy.

LaHucik et al. (2017) studied the mechanical properties of ordinary FRC with fiber-reinforced RCC using different types of fibers. They found that, the compressive, splitting tensile and flexural strengths increased at low fiber content, then decreased at a higher contents.

Jafarifar et al. (2016) studied the impact of cracks regarding shrinkage on the capacity of load bearing of RCC pavement with steel fibers (SFRRCCP). They found that by neglecting the impact of shrinkage, the SFRRCCP capacity is overestimated by approximately two times.

Madhkhan et al. (2012) studied the impacts of mixed PP fibers and steel fibers in roller compacted concrete containing a kind of Iranian pozzolan. They concluded that compressive strength improved with the increasing amount fibers. Also, the flexural strength reduce with the fiber content so long as indices of the toughness increased with the fiber content.

Sukontasukkul et al. (2019) presented a case study on applying steel fibers in RCC pavement. The experimental program includes the compression and flexural strength, density of the strain energy, toughness, and energy dissipation at various ages. The results demonstrated that the water and the density of mixtures reinforced with fiber were more than ones of normal RCC mixtures to a certain extent. The compression strength was decreased with an increase of fibers. Although, flexural strength, toughness, and residual strength increased significantly with applying steel fibers.

Fwa and Paramasivam (1990) studied the thin steel fibre composite overlay for the repair of surface-distressed concrete pavements. The experimental study utilized to investigate the properties of proposed composite overlays. They found that 1% steel fiber would satisfactorily in this regard, and proposed the preferable thickness of overlay.

Atis et al. (2009) presented relations among strength features including compressive and flexural, and abrasion resistance of polymer-based fibers and steel fibers reinforced with fly ash contained concrete. Various replacements of cementitious material and fiber (both steel and polypropylene) were studied. They suggested some models to relate the mentioned properties and compared them with their accuracies.

Zhang et al. (2004) investigated the

impact, toughness and other features like density, tensile and compressive characteristics, and elastic modulus, of both normal and lightweight aggregate concrete reinforced with fibers. Their study revealed that density and high compressive strength have beneficial effects on impact resistance, and the inclusion of the steel fibers substantially made better the impact strength.

Neves and Fernandes de Almeida (2005) studied the effects of strength of the cement matrix, the fiber content and the fiber diameter on the compression strength of steel FRC mixtures. They concluded that adding fibers to concrete enhances its energy absorption capacity, although it can moderately decrease the elastic modulus. Furthermore, analytical model proposed to estimate the stress–strain relationship for steel FRC in compression. The model results are compared with experimental stress-strain curves.

Ramezani and Esfahani (2018) evaluated the effects of hybrid FRC against the freezing/thawing action. The elite mixtures (steel fibers with the amount of 0.75% and PP fibers with the amount of 0.4%) showed the highest freezing/thawing scaling resistances as the materials which were scaled in this mix were approximate half of scaled materials from the normal mixture after cycling of freezing/thawing.

Song et al. (2004) presented a statistical model for the resistance against impact regarding steel-FRC with two fiber volumes, in comparison with ordinary samples. The results revealed that density and high compressive strength are favorable for this purposes.

Shadafza and Jalali (2016) investigate the elastic modulus of SFRC. Results showed that random distribution of fibers and aggregate and the lack of the homogeneity of the matrix have great effects in this content.

Thus, present research purposes to study effects of cold-drawn crimped-end steel fiber reinforced (CFCSF) on the behavior of concrete mixtures. To this end, CFCSF mixtures were made with fiber contents of 15 and 25 kg/m^3 with diameters of 0.82 and 0.99 mm and water - cement ratio of 0.5 compared to reference concrete. To interpret the trends of results, regression models would be developed and compared.

2. Material and Methods

2.1. Materials

An ordinary Portland cement type II, which was locally available is conforming provisions of ASTM C150 (2019). The physical and chemical features of the cement utilized for this study are presented in Table 1.

Limestone aggregates were locally provided from available sources. The coarse aggregates (coarse and fine gravel) were consumed had following features of maximum size of 19 mm and a saturated surface dry specific gravity of 2520 kg/m^3 and water absorption percentage of 1.8. The river sand was also consumed which had the specific gravity of 2570 kg/m^3. The sand water absorption was obtained 2.9%. Their SSD gravity was 2635 kg/m^3. The utilized steel fibers are of cold-drawn crimped-end steel fiber type conforming Type I ASTM A820 (2016) as presented in Table 2.

2.2. Mixture Proportion

Table 3 presents a summary of proportions of the concrete mixture. Furthermore, the control concrete without natural steel fibber (SW), four mixtures were made by using 0.83 and 0.99 mm diameter fiber with 15 and 25 kg/m^3 fiber.

2.3. Preparing Specimens

At first, Materials in dry form were mixed together, after that water was added into the mix. Afterwards, the steel fiber was added to the mixture if available. The mixed concrete was poured into the mold immediately, and consolidated by using a shaking table. After molding, all of samples were left covered during next 24 hours in the casting room. Henceforth, experimental specimens were demolded and cured at 23

± 1 °C and a moist situation during the determined age for every test according to the ASTM C192 (2019).

3. Discussions of Experimental Results

3.1. Fresh Characteristics

The fresh characteristics of the mixed concrete including density and air content are depicted in Table 4.

3.2. Mechanical and Durability Tests

To evaluate the properties of CFCSF mixtures, mechanical and physical tests including the tensile and compressive strength, flexural strength, impact resistance, elastic modulus, water penetration depth and abrasion resistance carried out as following methods:

3.2.1. Compressive Strength

The compression strength of the mixed concrete was determined for cubic specimens of 150×150×150 mm and the results are reported in Table 5 for 7-day, 28-day and 56-day compressive strength.

3.2.2. Tensile Strength

The tensile strength of the mixtures evaluated via ASTM C496 (2014) at 7-day, 28-day and 56-day, are presented in Table 6.

Table 1. Features of the cement utilized in this study

Compound/ Property	Cement Type II
Chemical analysis, %	
Calcium oxide (CaO)	61.68
Silica (SiO_2)	22.58
Alumina (Al_2O_3)	4.45
Iron oxide (Fe_2O_3)	4
Magnesium oxide (MgO)	3.05
Sodium oxide (Na_2O)	0.48
Potassium oxide (K_2O)	0.4
Sulfur trioxide (SO_3)	1.71
Other properties	
3-day compressive strength, MPa	17.8
7-day compressive strength, MPa	26.2
28-day compressive strength, MPa	38.4
Initial time of setting, min	164
Final time of setting, min	245
Specific gravity (g/cm^3)	3.15
Specific surface, m^2/gr	2805
Loss on ignition (975°C)	1.07

Table 2. Features of utilized steel fibers

Name	Diameter (mm)	Length/Area ratio	Tensile strength (MPa)
CFCSF8	0.82	0.51	1220
CFCSF10	0.99	0.79	1201

Table 3. Proportions of concrete mixture [+]

Mixture identification	Definition	Steel fiber (kg/m^3)	Cement (kg/m^3)	Coarse aggregate[*] (kg/m^3)	Fine aggregate[*] (kg/m^3)	Water (kg/m^3)
SW	Reference	-	350	850	960	175
SW0.8-15	0.83 mm fiber	15	350	850	960	175
SW0.8-25	0.83 mm fiber	25	350	850	960	175
SW1.0-15	0.99 mm fiber	15	350	850	960	175
SW1.0-25	0.99 mm fiber	25	350	850	960	175

[+] w/c ratio = 0.5, [*] SSD condition

Table 4. Fresh characteristics of the mixed concrete

Mixed concrete identification	Density (kg/m^3)	Air content (%)
SW	2345	1.5
SW0.8-15	2365	2.4
SW0.8-25	2375	2.6
SW1.0-15	2369	2.5
SW1.0-25	2380	2.7

3.2.3. Flexural Strength

The flexural strength of the mixtures evaluated via ASTM C78 (2018) at 7-day, 28-day and 56-day, are given in Table 7.

3.2.4. Modulus of Elasticity

The modulus of elasticity of mixtures was calculated via ASTM C469 (2014) at 28-day, are reported in Table 8.

3.2.5. Impact Resistance

The resistance against impacts for mixtures was measured by drop-weight test method mentioned in ACI 544.2R (1989) at 28 day and presented in Table 9.

3.2.6. Depth of Water Penetration

The water penetration depth of the specimens was determined based on BS EN 12390-8 (2019) at 28-day and 56-day and presented in Table 10.

3.2.7. Abrasion Resistance

The resistance against abrasion of mixture surfaces was determined according to ASTM C779 (2019) (procedure A at 28 day after 15 and 30 minutes) and presented in Table 10.

4. Results and Discussion

4.1. Fresh Statute

Based on the fresh properties summarized in Table 4, the air content of specimens increased with application of fiber.

Table 5. Compressive strength

Mixture identification	7-day (MPa)	28-day (MPa)	56-day (MPa)
SW	21.5	32.0	33.0
SW0.8-15	22.0	35.6	37.4
SW0.8-25	23.0	35.8	38.0
SW1.0-15	23.5	36.8	38.5
SW1.0-25	24.0	36.9	38.6

Table 6. Tensile strength

Identification of mixed concrete	7-days (MPa)	28-days (MPa)	56-days (MPa)
SW	2.8	3.4	3.5
SW0.8-15	3.0	4.8	5.4
SW0.8-25	3.5	6.5	6.7
SW1.0-15	3.1	5.5	5.6
SW1.0-25	3.6	7.7	7.8

Table 7. Flexural strength

Mixture identification	7-day (MPa)	28-day (MPa)	56-day (MPa)
SW	2.2	4.3	4.5
SW0.8-15	2.8	5.8	6.0
SW0.8-25	3.1	7.7	7.9
SW1.0-15	3.6	5.9	6.2
SW1.0-25	4.5	7.9	8.0

Table 8. Modulus of elasticity

Mixture identification	28-day (GPa)
SW	29.0
SW0.8-15	35.4
SW0.8-25	39.5
SW1.0-15	36.5
SW1.0-25	51.3

Table 9. Water penetration depth

Mixture identification	Penetration depth of water under pressure (mm)	
	28-day	56-day
SW	16	14
SW0.8-15	17	16
SW0.8-25	19	17
SW1.0-15	18	17
SW1.0-25	19	18

Table 10. Abrasion resistance

Mixture identification	Abrasion (mm) after	
	15 min.	30 min.
SW	1.1	1.6
SW0.8-15	0.79	0.83
SW0.8-25	0.75	0.77
SW1.0-15	0.81	0.83
SW1.0-25	0.74	0.75

4.2. Hardened Properties

4.2.1. Compressive Strength

As shown in Figure 1, although at 7 days of age, CFCSF specimens did not exhibit much compressive strength compared to the control concrete, but at 28-day and 56-day, such samples showed greater compression strength than reference specimens. However, there cannot be seen any improvements with variation of fiber type and content.

4.2.2. Tensile Strength

As shown in Figure 2, using steel fibers augmented the tensile strength at age of 28 day and 56 day. An increment regarding tensile strength was nearly twice that of fibers at the same age compared to control specimens.

4.2.3. Flexural Strength

As shown in Figure 3, the application of steel fibers augmented the flexural strength of samples. An increase regarding flexural strength of CFCSF specimens at 28 day and 56 day was more than twice when compared to the reference specimen.

4.2.4. Modulus of Elasticity

As presented in Figure 4, using steel fibers raised the modulus of elasticity in mixed concrete. The modulus of elasticity of CFCSF specimens also increased with increasing fiber content.

4.2.5. Depth of Water Penetration

The results of Table 9 show that consuming steel fibers had little impact on the permeability depth under water pressure.

4.2.6. Impact and Abrasion Resistance

According to the results presented in Tables 8 and 10, the impact strength as well as the abrasion resistance of CFCSF samples was higher than the abrasion resistance of the reference samples. The increase in impact and abrasion resistance is much more prominent at older ages.

5. Developing Relationships of Data and Comparisons

To determine the relationship between existing parameters, at first, the correlation between existing parameters should be specified. The correlation coefficient is expressed for test data by:

$$MCF = Correl(X,Y) = \frac{\sum (x-\bar{x})(y-\bar{y})}{\sqrt{\sum (x-\bar{x})^2 \sum (y-\bar{y})^2}} \quad (1)$$

where x and y: are the parameters under consideration in this study, $\bar{x}$ and $\bar{y}$: are their average values. Using Eq. (1) the correlation coefficients among different parameters are specified and reported in Table 11. Considered parameters are Tensile Strength (TS), Compressive

Strength (CS), Flexural Strength (FS), elastic modulus (ME), Water Penetration depth (WP), Impact Resistance (IR) and Abrasion Resistance at 15 and 30 min (AR15, AR30). All of these parameters are of age 28 day.

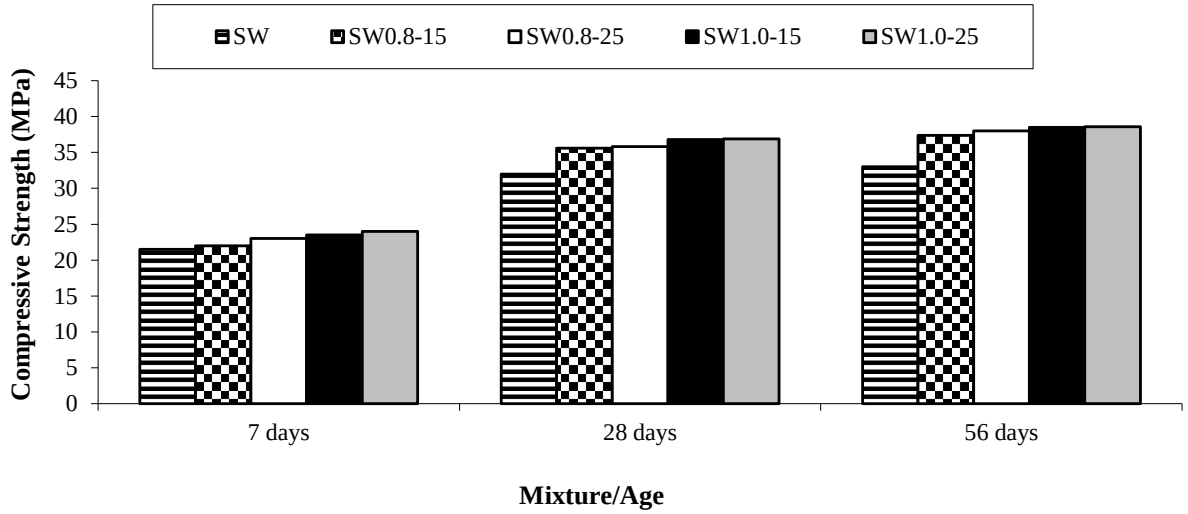

Fig. 1. Compressive strength of CFCSF mixtures compared to reference mixture

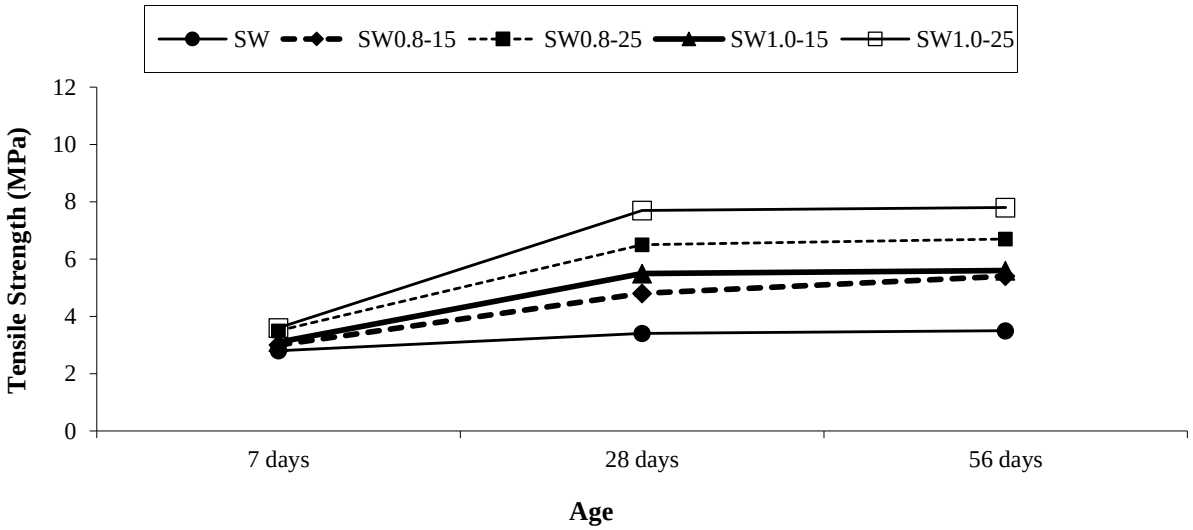

Fig. 2. Comparison of tensile strength of CFCSF mixtures with reference

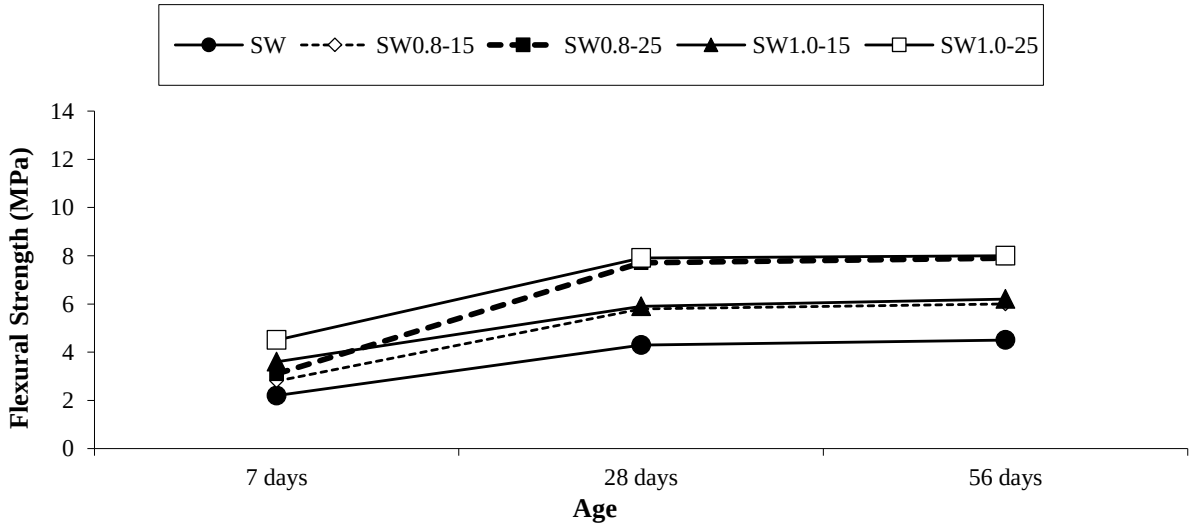

Fig. 3. Comparison of flexural strength in CFCSF mixtures with reference

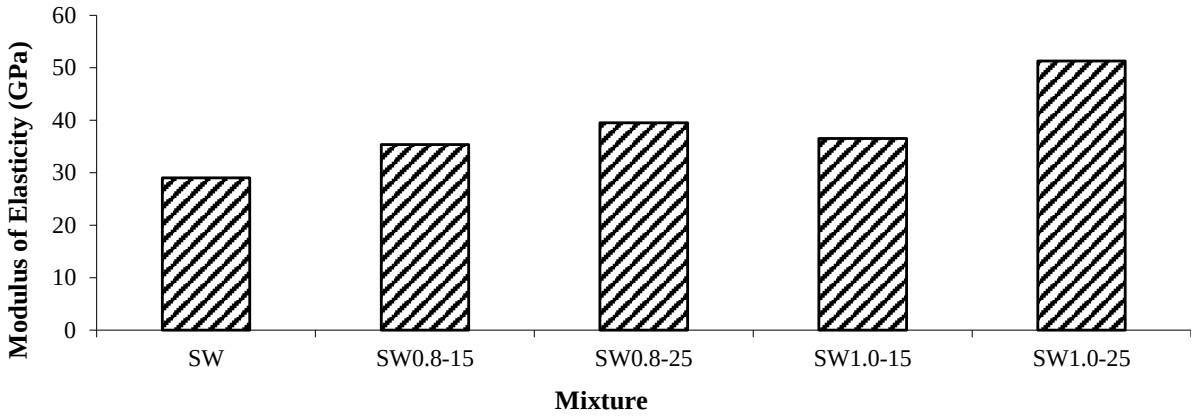

Fig. 4. Comparison of elastic modulus of CFCSF mixtures with reference

Calculated correlation parameters are various ranging from -1 to 1. Whenever the MCF becomes closer to ±1, it can be understand there is a higher correlation among actual data and outputs of model. Results reported in Table 11, reveal that it is feasible to find a relationship among results. This subject is carried out through the regression analysis by implementing the defined model as follows:

$$Y = f(b_i \times x_i) \quad (2)$$

where b_i : stands for the multipliers and x_i : indicates impressive input parameters.

In Figure 5, the relations between tensile and compressive strength, flexural strength, elastic modulus with impact resistance are demonstrated. As seen linear models were fitted to data which emphasized a direct correlation between different mechanical properties and impact resistance. As depicted, tensile strength has the most relation with impact resistance with R^2 of 0.89.

Song et al. (2004) concluded that linear regression models are accounting for most of variabilities in the impact resisting with a failure strength. However the similar trend, the gained results of current research, emphasized stronger relationship for impact resistance with tensile strength.

Also in Figure 6, relations between tensile and compressive strength, flexural strength, elastic modulus, resistance against impact and abrasion at 15 min/30 min were presented. As seen polynomial model were fitted to the experimental results with higher accuracy as depicted for abrasion resistance with modulus of elasticity.

Atis et al. (2009) compared relationships of abrasion to flexural tensile strength and abrasion to compressive strength and proposed that the relationship which is available between flexural tensile strength and abrasion is stronger than the relationship between compressive strength of the concrete and abrasion including either fibers or fly ash, or both of them. The gained results of the current study could be verified by their results; however, found relation between abrasion resistances with the modulus of elasticity proposed a better R^2 considering different utilized methods and materials.

Table 11. Correlations among results of determined parameters

MCF	CS	TS	FS	ME	IR	WP	AR15	AR30
CS	1	0.817682	0.955865	0.853068	0.874839	0.887672	-0.7384	-0.73915
TS	0.817682	1	0.79009	0.903284	0.946815	0.961204	-0.78053	-0.72952
FS	0.955865	0.79009	1	0.932148	0.845479	0.804303	-0.71933	-0.7113
ME	0.853068	0.903284	0.932148	1	0.889879	0.836315	-0.74145	-0.69982
IR	0.874839	0.946815	0.845479	0.889879	1	0.972718	-0.93163	-0.90616
WP	0.887672	0.961204	0.804303	0.836315	0.972718	0.972718	-0.93163	-0.90616
AR15	-0.7384	-0.78053	-0.71933	-0.74145	-0.93163	0.972718	-0.93163	-0.90616
AR30	-0.73915	-0.72952	-0.7113	-0.69982	-0.90616	0.972718	-0.93163	-0.90616

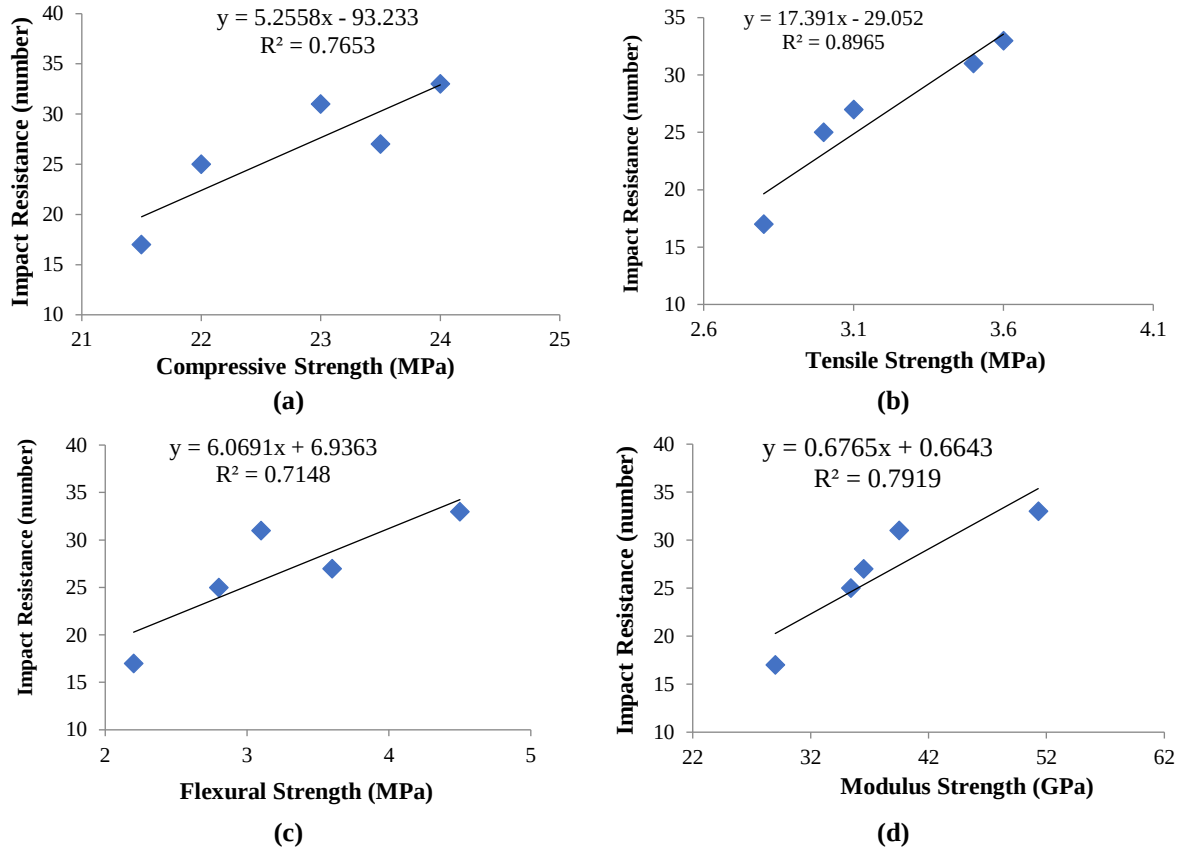

Fig. 5. Relations between: a) Compressive strength; b) Tensile strength; c) Flexural strength; and d) Elastic elasticity modulus with impact resistance

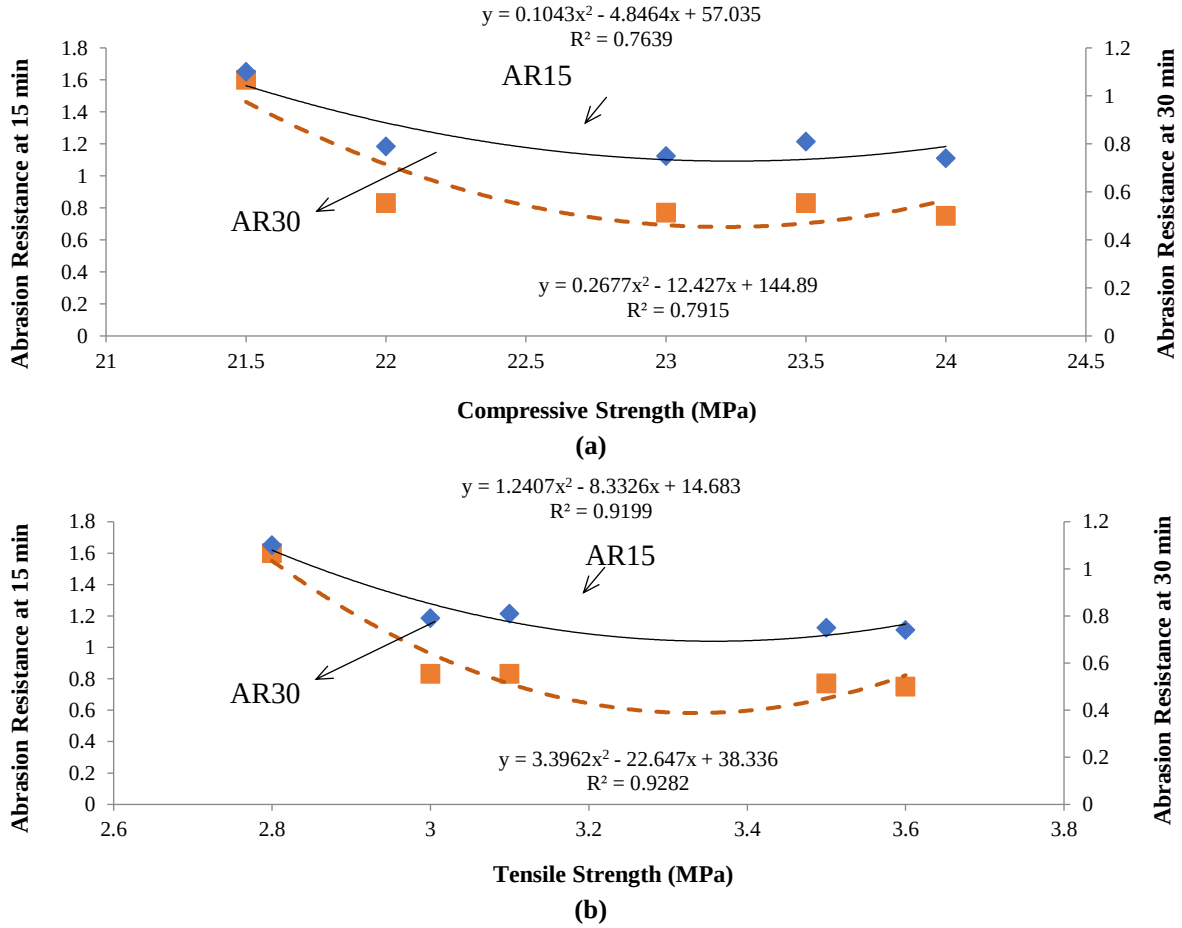

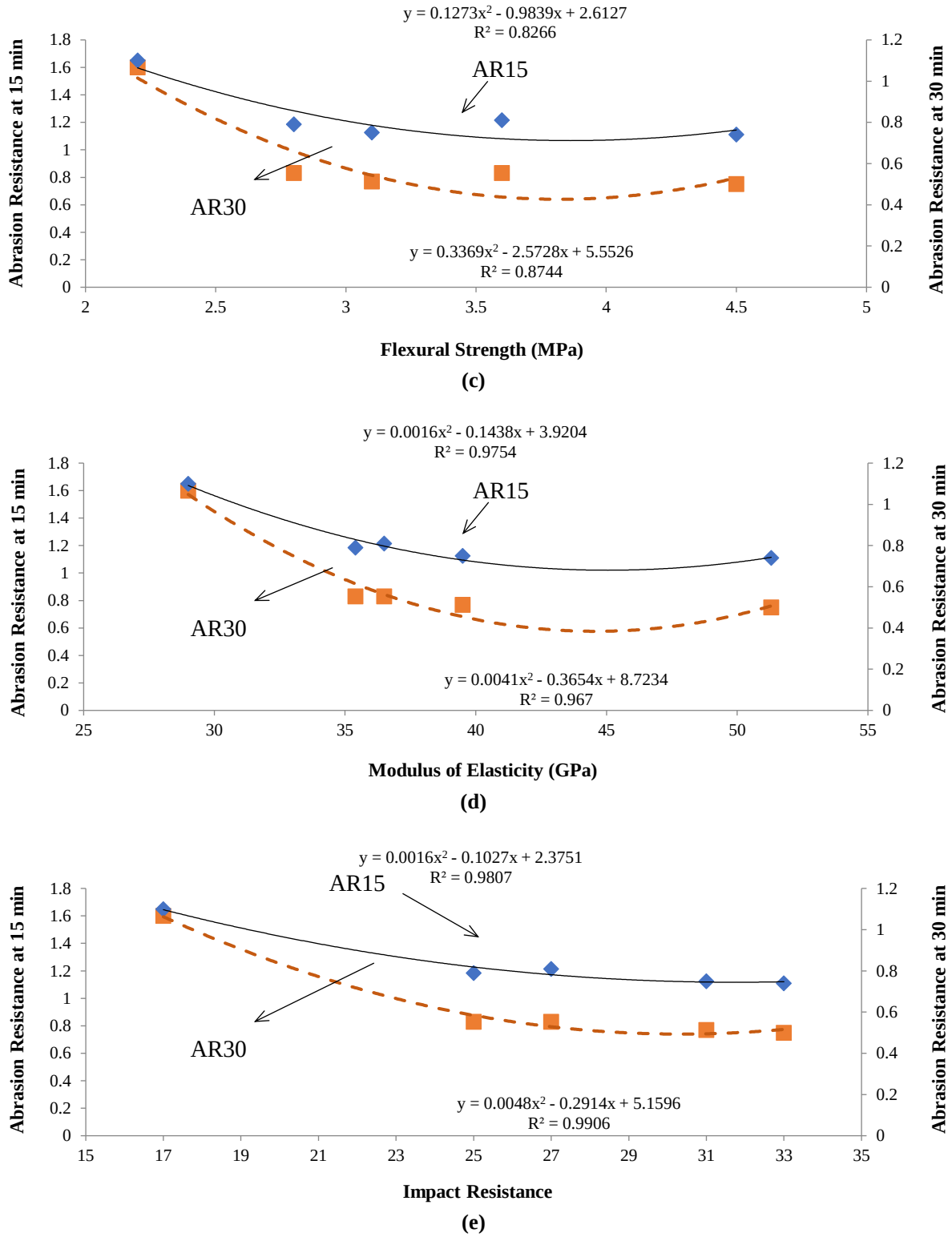

Fig. 6. Relations between compressive strength: a) Tensile strength; b) Flexural strength; c) Elasticity modulus; d) Impact resistance; and e) With abrasion resistance at 15 min/30 min

6. Conclusions

In this paper, the effects of using cold-drawn crimped-end steel fibers (CFCSF) on the durability and mechanical properties of concrete overlay was studied. Accordingly, according to the limited test results, these conclusions could be drawn as follows:

- However at the age of 7 days, steel-containing specimens did not exhibit much compressive strength in comparison with the control concrete,

but at 28 and 56 days, the compressive strength of CFCSF specimens is higher than the compressive strength of control concrete.

- The use of steel fibers has increased tensile strength at 28 and 56 days. An increase in tensile strength was about twice that of fibers at 28 and 56 days of age compared to control ones.
- Application of steel fibers has increased flexural strength. The increase in flexural strength of steel fiber samples at 28 and 56 days was more than 100% compared to the control.
- The use of steel fibers increases the elastic modulus regarding concrete. The elastic modulus of fibers containing specimens also increased with increasing fiber content.
- Using steel fibers showed a little impact on the permeability depth under water pressure.
- Impact resistance as well as abrasion resistance of fibers is higher than those of control. The increase in impact and wear resistance is much more pronounced at older ages.
- Permeability results at 56 days prove the effect of using steel fibers in hardened concrete.
- Developed models between the relation of abrasion and impact resistance to other mechanical properties, made in terms of R^2 of the linear regression and polynomial relationships, showed that stronger relations were available between impact resistance and tensile strength and abrasion resistance with modulus of elasticity.

7. Acknowledgments

The authors acknowledge the Road, Housing and Urban Development Research Center of Iran (BHRC) for its experimental supports of the studies.

8. References

ACI 544.2R-89. (1989). *Measurement of properties of fiber reinforced concrete*, American Concrete Institute.

ASTM A820/A820M. (2016). *Standard specification for steel fibers for fiber-reinforced concrete*, ASTM International, West Conshohocken, PA.

ASTM C150/C150M. (2019). *Standard specification for Portland cement*, ASTM International, West Conshohocken, PA.

ASTM C192/C192M. (2019). *Standard practice for making and curing concrete test specimens in the laboratory*, ASTM International, West Conshohocken, PA.

ASTM C469/C469M. (2014). *Standard test method for static modulus of elasticity and Poisson's ratio of concrete in compression*, ASTM International, West Conshohocken, PA.

ASTM C496/C496M. (2017). *Standard test method for splitting tensile strength of cylindrical concrete specimens*, ASTM International, West Conshohocken, PA.

ASTM C779/C779M. (2019). *Standard test method for abrasion resistance of horizontal concrete surfaces*, ASTM International, West Conshohocken, PA.

ASTM C78/C78M. (2018). *Standard test method for flexural strength of concrete (using simple beam with third-point loading)*, ASTM International, West Conshohocken, PA.

Atis, C.D., Karahan, O., Ari, K., Sola, Ö.C. and Bilim, C. (2009). "Relation between strength properties (flexural and compressive) and abrasion resistance of fiber (steel and polypropylene) reinforced fly ash concrete", *Journal of Materials in Civil Engineering*, 21, 402-408.

BS EN 12390-8. (2019). *Testing hardened concrete. Depth of penetration of water under pressure*, BS Standards.

Fwa, T.F. and Paramasivam, P. (1990). "Thin steel fiber cement mortar overlay for concrete pavement", *Cement and Concrete Composites*, 12, 175-184.

Harrington, D. and Fick, G. (2014). "Guide to concrete overlays sustainable solutions for resurfacing and rehabilitating existing pavements", 3rd Edition, ACPA Publication.

Isla, F. Luccioni, B. Ruano, G. Torrijos, M.C. Morea, F. Giaccio, G. and Zerbino, R. (2015). "Mechanical response of fiber reinforced concrete overlays over asphalt concrete substrate: Experimental results and numerical simulation", *Construction and Building Materials*, 93, 1022-1033.

Jafarifar, N., Pilakoutas, K. and Bennett, T. (2016). "The effect of shrinkage cracks on the load bearing capacity of steel-fiber-reinforced roller-compacted-concrete pavements", *Materials and Structures*, 49, 23-29.

LaHucik, J. Dahal, S. Roesler, J. and Amirkhanian, A.N. (2017). "Mechanical properties of roller-

compacted concrete with macro-fibers", *Construction and Building Materials*, 135, 440-446.

Madhkhan, M., Azizkhani, R. and Torki Harchegani, M.E. (2012). "Effects of pozzolans together with steel and polypropylene fibers on mechanical properties of RCC pavements", *Construction and Building Materials*, 26(1), 102-112.

Neves, R.D. and Fernandes de Almeida, J.C.O. (2005). "Compressive behaviour of steel fiber reinforced concrete", *Structural Concrete*, 6(1), 1-8.

Ramezani, A.R. and Esfahani, M.R. (2018). "Evaluation of hybrid fiber reinforced concrete exposed to severe environmental conditions", *Civil Engineering Infrastructures Journal*, 51(1), 119-130.

Shadafza, E. and Saleh Jalali, R. (2016). "The elastic modulus of steel fiber reinforced concrete (SFRC) with random distribution of aggregate and fiber", *Civil Engineering Infrastructures Journal*, 49(1), 21-32.

Song, P.S., Hwang, S. and Sheu, B.C. (2004). "Statistical evaluation for impact resistance of steel-fiber-reinforced concretes", *Magazine of Concrete Research*, 56(8), 437-442.

Sukontasukkul, P., Chaisakulkiet, U., Jamsawang, P., Horpibulsuk, S., Jaturapitakkul, C. and Chindaprasirt, P. (2019). "Case investigation on application of steel fibers in roller compacted concrete pavement in Thailand", *Journal of Case Studies in Construction Materials*, 11, e00271.

Tavakoli, H.R., Fallahtabar Shiadeh, M. and Parvin, M. (2016), "Mechanical behavior of self-cnthetics and steel fibers", *Civil Engineering Infrastructures Journal*, 49(2), 197-213.

Zhang, M.H., Li L. and Paramasivam, P. (2004). "Flexural toughness and impact resistance of steel-fiber-reinforced lightweight concrete", *Magazine of Concrete Research*, 56(5), 251-262.

Civil Engineering Infrastructures Journal 2021, 54(2): 331-350
DOI: 10.22059/CEIJ.2021.298632.1659

RESEARCH PAPER

Numerical Investigation of Nailing Pattern Effect on Nailed Wall Performance

Shahir, H.[1]* and Delfan, S.[2]

[1] Associate Professor, Department of Civil Engineering, Faculty of Engineering, Kharazmi University, Tehran, Iran.
[2] M.Sc., Department of Civil Engineering, Faculty of Engineering, Kharazmi University, Tehran, Iran.

Received: 29 Feb. 2020; Revised: 10 Sep. 2020; Accepted: 14 Dec. 2020

ABSTRACT: In this paper, the performance of soil nailed walls with various nail patterns has been studied to find an optimum layout based on the deformation criterion. To this end, parametric analysis on soil nailed walls with various nailing patterns is performed. Nine patterns including one uniform and eight variable nails length are considered. For each pattern, parametric analysis on different parameters including wall height, surcharge, nails spacing is implemented to find an optimum pattern based on the deformation criterion. The simulation results indicate that using the variable layout with long nails at the top of the wall not only reduces the lateral deformation of soil nailed wall but also decreases the density of nails.

Keywords: Deformation, Finite Element, Optimum Pattern, Safety Factor, Soil Nailing.

1. Introduction

Soil nailing is a common method to stabilize excavated slopes and walls. Where buildings or underground facilities exist near the excavation, in addition to checking the overall stability, the amount of deformations shall also be evaluated to ensure the appropriate performance of the wall and nearby structure.

Deformation of soil nailed walls has been studied by various researchers using experimental or numerical approaches. Plumelle et al. (1990), Tei et al. (1998) and Chu and Yin (2005) studied the response of soil-nailed walls using full-scale and centrifuge experiments. Numerical modeling has been successfully applied to model the behavior of soil nailed walls and slopes (Unterreiner et al., 1997; Seo et al., 2014; Ardakani et al., 2014; Liu et al., 2016; Moniuddin et al., 2016; Rawat and Gupta, 2016; Hitha et al., 2019; Rashidi et al., 2019; Rashidi and Shahir, 2019; Gharedaghi and Shahir, 2019; Hajiazizi and Mirzazadeh, 2020; Abbas et al., 2020). A verified numerical model makes it possible to study the effects of various parameters such as nails length and spacing.

The effects of spacing and length of nails on the performance of soil nailed wall have been studied by a few researchers. Fan and Luo (2008) performed numerical study on the optimal nails layout for various slope angles in terms of factor of safety using 2D finite element program. Their study showed

* Corresponding author E-mail: shahir@khu.ac.ir

that the nails length at the lower 1/3 part of the slope has a significant impact on the overall stability, especially for soil nailed walls. They also concluded that the effect of vertical spacing of nails on the stability of soil nailed slopes is insignificant if the length and number of nails remain unchanged. Yang and Drumm (2000) using 3D finite element modeling, concluded that the short nails are not effective because the long term deformations occurs in the upper part of the soil nailed slope. Zhang et al. (1999) developed a 3D finite element model for the deformation analysis of soil nailed walls and investigated the effects of nail length and spacing on horizontal deflection. Uniform distribution of nails was considered. They indicated that the horizontal deflection decreases with increasing nails length and decreasing nails spacing.

In the previous studies, an inclusive study on the effect of the nailing arrangement on the wall deformation considering various wall heights and nail spacing and determination of the optimum pattern based on the deformation criterion have not been accomplished. Halabian et al. (2012) used a 3D numerical model to evaluate the earth pressure distribution during and after excavation. They also studied the effects of different crucial factors such as nail inclination, nail length, length pattern, slope inclination and nail bars arrangement on the performance of soil-nailed structures. The research implied that using nails with inclination angle varying in the range of 0 to 15 deg results in a reduction of lateral earth pressure. To study the effect of nails length and pattern, they assumed that nails are placed horizontally. The results showed that nails with longer length placed in the upper third part of the wall contribute more in the wall horizontal displacement reduction while nails with longer lengths placed in lower part of the wall provide more stability to the structure as well as reduction in horizontal displacements.

Sharma and Ramkrishnan (2020) studied potential parametric optimization in soil nailing. They considered reduced nail length pattern to study the possible optimization of nail length. Their study showed that the nail length for the lower-third portion could be reduced by 10-20% of their lengths than in the upper-third and middle-third portion of the wall.

To study the effects of pullout strength on horizontal displacement, uniform pattern and reduced nail length pattern were considered by the researchers. Their study showed that the middle third portion which is more susceptible to pull-out failure undergo maximum displacements and using reduced nail length pattern marginally increases the horizontal displacements. In the above mentioned studies, the effects of various nailing arrangements, nails spacing and wall height on the wall deformations have not been completely studied and only three patterns have been considered. Also, the effects of excavation-induced ground movements on the performance and serviceability of the adjacent buildings have not been studied.

In this study, nine patterns including one uniform and eight variable nails length have been considered. For each pattern, parametric analysis on different parameters including wall height, surcharge, nails spacing was done. The nailed walls were designed using limit equilibrium method according to recommendation procedure and safety factors in the nailing manual of FHWA (Lazarte et al., 2015), for temporary conditions. After determination of the required nails length, nailed wall deformations were predicted using the non-linear finite element analysis. To verify the employed model, a two-dimensional finite element analysis of a full-scale experimental soil nailed wall was performed and compared with the field measurements.

2. Description and Verification of the Numerical Model

To analyze the deformation of nailed walls,

the wall has been modeled in the plane strain condition. In the two-dimensional analysis, nails are modeled using the "equivalent plate" approach. In this method, the discrete nails are replaced by a continuous plate with the stiffness equal to the stiffness of the nail divided by the horizontal spacing. For the grouted nails, an equivalent modulus of elasticity (E_{eq}) can be determined as follow:

$$E_{eq} = E_n\left(\frac{A_n}{A}\right) + E_g\left(\frac{A_g}{A}\right) \quad (1)$$

where E_n and E_g: are the elastic modulus of the bar and grout material, respectively. A: is the total cross-sectional area of grouted nails. A_n and A_g: are the cross-sectional area of bar and grout cover, respectively. It should be noted that due to the insignificant tensile strength of the grout, the effect of grout has been neglected in the calculation of equivalent *EA*. Also, the bending stiffness of nails is neglected. The axial stiffness of nails can be determined as follow:

$$EA(kN/m) = \frac{E_{eq}}{S_h}A \quad (2)$$

where S_h: is the horizontal spacing of nails.

The hardening soil model (HS model) has been used to simulate the soil behavior. It is an advanced constitutive model that can be used for both soft and stiff soils. This model is able to simulate stress dependency of soil stiffness. Limit state of stress are described by means of the friction angle (ϕ) and cohesion (c). The soil stiffness is described using three moduli: the triaxial loading modulus, E_{50}, the triaxial unloading modulus, E_{ur} and the oedometer loading modulus, E_{oed}. The stress dependency of these three moduli is defined by the following equation:

$$E = E^{ref}\left(\frac{c\cos\phi + \sigma_3^{'}\sin\phi}{c\cos\phi + p^{ref}\sin\phi}\right)^m \quad (3)$$

where m: is the fabric parameter used to determine the amount of stress dependency of stiffness, E^{ref}: is the reference stiffness modulus corresponding to the reference confining pressure p^{ref}, and σ_3': is the confining pressure in a triaxial test. As a default, $p^{ref} = 100\,kPa$ is used. Schanz and Vermeer (1998) indicated that E_{oed}^{ref} can be considered equal to E_{50}^{ref} for sand and gravel soils. As an average value for various soil types, E_{ur}^{ref} is assumed equal to $3E_{50}^{ref}$.

To verify the utilized numerical model, a full-scale test called Clouterre (FHWA, 1993; Plumelle et al., 1990; Unterreiner et al., 1997) was simulated. The French national project Clouterre was conducted from 1986 to 1991 to study the behavior of soil nailed walls during construction, in service and at failure. The schematic cross-section of the constructed soil-nailed wall in the Clouterre test is shown in Figure 1 (Unterreiner et al., 1997). The nailed wall is 7.3 m high and 7.5 m wide that is restricted between two lateral walls covered with a double layer of polyethylene sheet greased to ensure plane strain condition. The wall was constructed by excavation steps of 1 m height with the installation of nails at the horizontal spacing of 1.15 m. Hollow aluminum tubes with various diameter, thickness and length were used as nail elements in this test. Inclination of nails is 10 deg and their length range from 6 to 8 m. Each nail was fixed to 80 mm thick shotcrete facing. The facing, made of mesh-reinforced shotcrete, was installed after placing the nails. Properties of the nails and shotcrete facing used in the finite element analysis are listed in Tables 1 and 2.

Table 1. Properties of nails used in the simulation of Clouterre test

Parameter	Symbol	Unit	Type A	Type B	Type C
Tube thickness	e	mm	1	2	1
Tube diameter	φ	mm	16	30	40
Axial stiffness	EA	kN/m	2870	10700	7500
Yield force	N_p	kN/m	4.52	16.8	11.7

Table 2. Properties of shotcrete facing used in the simulation of Clouterre test

Parameter	Symbol	Unit	Value
Unit weight	γ	kN/m^3	24
Young's modulus	E	kPa	25×10^6
Axial stiffness	EA	kN/m	2×10^6
Bending stiffness	EI	$kN.m^2/m$	1067
Shotcrete thickness	d	m	0.08
Poisson ratio	ν	-	0.2

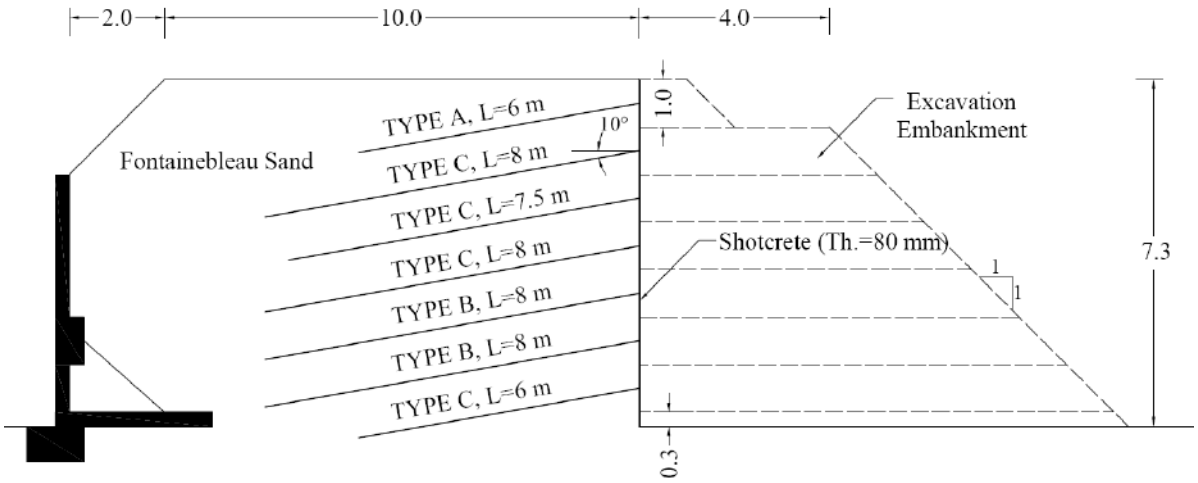

Fig. 1. Cross-section of the soil-nailed wall in the Clouterre test (Unterreiner et al., 1997)

In the Clouterre test, backfill and foundation soils are the Fontainebleau sand with different densities. The physical and mechanical properties of backfill and foundation soils were reported by Unterreiner et al. (1997) as presented in Table 3.

The stiffness parameters of the HS model can be evaluated based on the results of the conducted pressuremeter tests. The results of pressuremeter tests within the backfill soil before construction of the nailed wall (Plumelle et al., 1990; Unterreiner et al., 1997) are presented in Table 3. Unterreiner et al. (1997) compared the results of pressuremeter tests with the results of compression triaxial tests performed on the medium to dense Fontainebleau sand samples by Dupla and Canou (1994). Their comparison showed that the ratio (α) of soil stiffness modulus (E) to the Menard pressuremeter modulus (E_M) varies from 2.2 to 2.8 with depth which is in agreement with the recommended values by Plumelle et al. (1990) and Unterreiner et al. (1997).

$$E_{soil} = \alpha \times E_M \tag{4}$$

To obtain the parameters of the HS model, the values of soil stiffness at different depths have been calculated using the aforementioned ratio. By applying the following equation, E_{50}^{ref} and m can be determined by curve-fitting to the soil stiffness modulus as shown in Figure 2.

Table 3. Summary of calculations of the stiffness parameters of backfill soil

Depth (m)	E_M (MPa)	α	$E_{50}=\alpha . E_M$ (MPa)	σ_c (kPa)	β
1	7.0	2.2	15.4	9.5	0.13
2	6.5	2.3	15.0	19.0	0.22
3	11.0	2.4	26.4	28.5	0.31
4	12.0	2.5	30.0	38.0	0.40
5	10.5	2.6	27.3	47.5	0.49
6	14.5	2.7	39.2	57.0	0.59

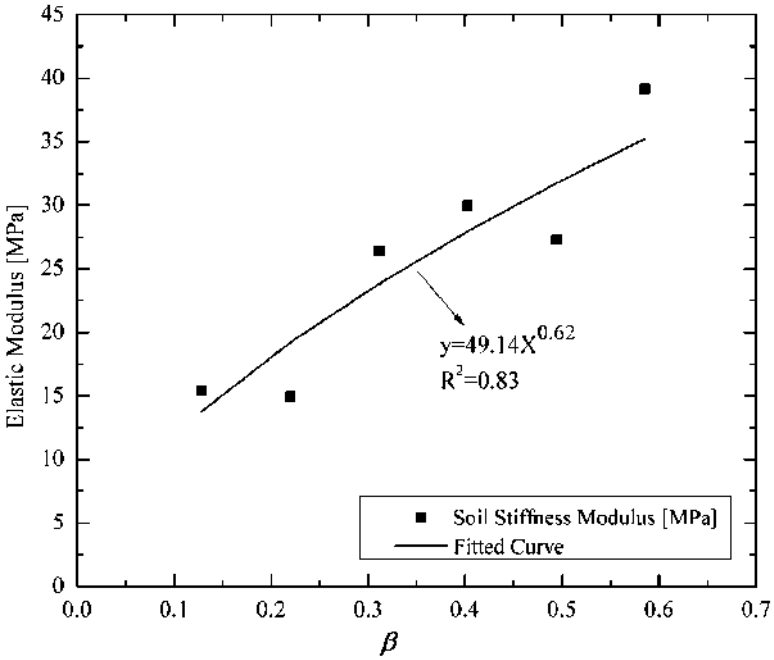

Fig. 2. Evaluation of stiffness parameters of backfill soil based on the pressuremeter results

$$E_{soil} = E_{50} = E_{50}^{ref}\left(\frac{c\cos\phi + \sigma_3^{'}\sin\phi}{c\cos\phi + p^{ref}\sin\phi}\right)^m = E_{50}^{ref} \times \beta^m \quad (5)$$

$$\beta = \frac{c\cos\phi + \sigma_3^{'}\sin\phi}{c\cos\phi + p^{ref}\sin\phi}$$

where c and φ: are the cohesion and friction angle of soil, respectively. σ_3': is the confining soil pressure which can be calculated by the following equation:

$$\sigma_3^{'} = \sigma_v^{'}\left(\frac{1+2k_0}{3}\right) \quad (6)$$

where σ_v': is the vertical soil stress and k_0: is the coefficient of earth pressure at rest. A summary of calculations is presented in Table 3. As shown in Figure 2, the obtained values of E_{50}^{ref} and m from the best fitted curve are 49.1 MPa and 0.62, respectively.

Regarding the foundation soil, two pressuremeter tests were carried out by Schlosser et al. (1993) and the average pressuremeter modulus of the foundation soil in depth of 0 to 7 m was measured as 35 MPa. Therefore, the values of E_{50}^{ref} and m can be determined as above. The evaluated values of the foundation soils parameters are presented in Table 4.

The construction of Clouterre test was interrupted for two months between phases five and six. During the interruption significant creep movement was measured at the top of the wall. In this paper, the instantaneous deformations have been considered and the creep effect was not taken into account. Thus, the first five phases of excavation have been simulated and compared with the measured results. The finite element mesh of the Clouterre wall is shown in Figure 3.

In Figures 4 and 5, the simulation and measured results for the horizontal displacement in the wall height have been compared at the end of phases 3 and 5 where the excavation depths were 3 and 5 m, respectively. The results have also been compared with the results of finite element analysis of Unterreiner et al. (1997). They used the finite element code CESAR–LCPC and a finite element meshes with rectangular 8-node elements and non-associated Mohr–Coulomb constitutive model for both of the foundation and backfill soils.

As depicted in these figures, the simulation results are somewhat more than the measured values in both phases. Acceptable agreement is observed between the curves. It is notable that significant jump

in the measured lateral deformation is observed at the upper part of the wall, while it can be seen the more uniform trend in the predicted results.

Figure 6 shows the tensile force distribution in the nails length for the upper four rows at the end of phase 5. There is an acceptable agreement between simulation results and numerical modeling results of Unterreiner et al. (1997). The maximum difference between two curves for nails No. 1, 3, and 4 is about 0.5 to 1.5 kN. For nail No. 2, this difference is about 3 kN.

Table 4. Parameters of the backfill and foundation soils for the HS model

Parameter	Symbol	Unit	Backfill soil	Foundation soil
Cohesion	c	kPa	3	0
Friction angle	φ	deg	38	36
Dilation angle	ψ	deg	25	20
Unit weight	γ	kN/m^3	16.1	17.0
Reference loading stiffness	E_{50}^{ref}	kPa	4.91×10^4	1.72×10^4
Reference oedometer loading stiffness	E_{oed}^{ref}	kPa	4.91×10^4	1.72×10^4
Reference unloading stiffness	E_{ur}^{ref}	kPa	1.47×10^5	5.16×10^4
Reference confining pressure	P^{ref}	kPa	100	100
Poisson ratio	ν	-	0.39	0.37
Fabric parameter	m	-	0.62	0.62

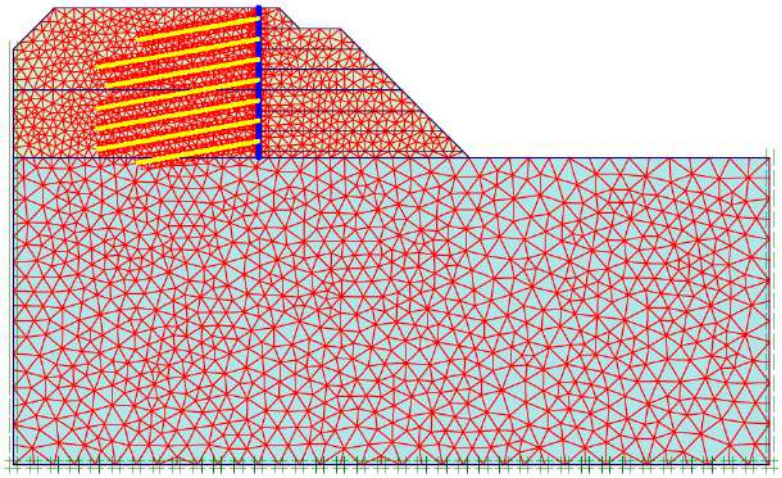

Fig. 3. Finite element mesh of the Clouterre test

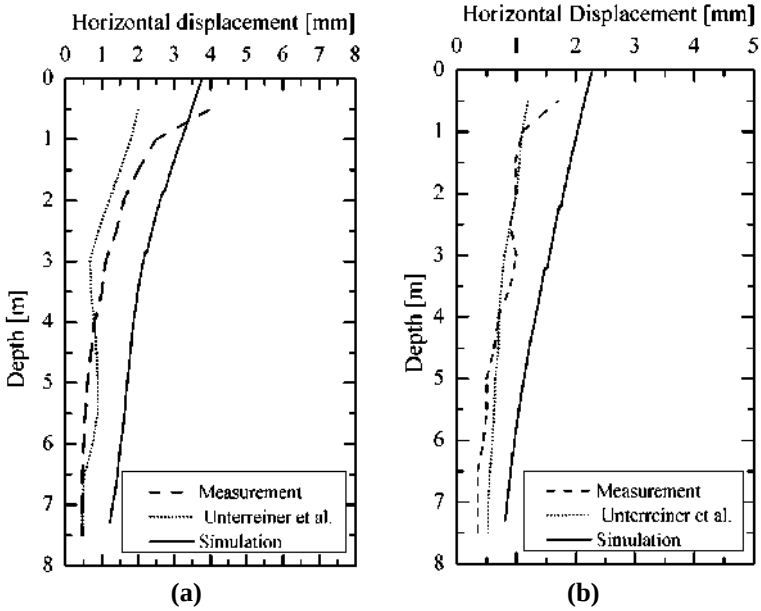

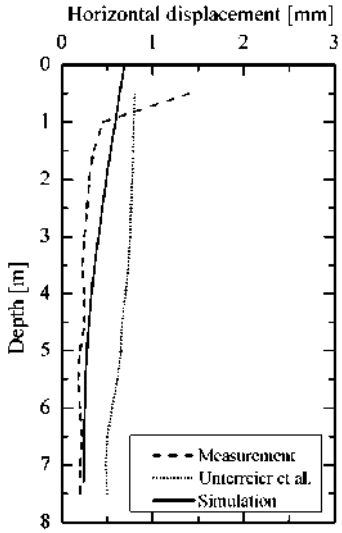

(c)

Fig. 4. Comparison of the predicted horizontal displacements in the backfill with measured results in phase 3 at: a) 2 m; b) 4 m; and c) 8 m behind the wall facing

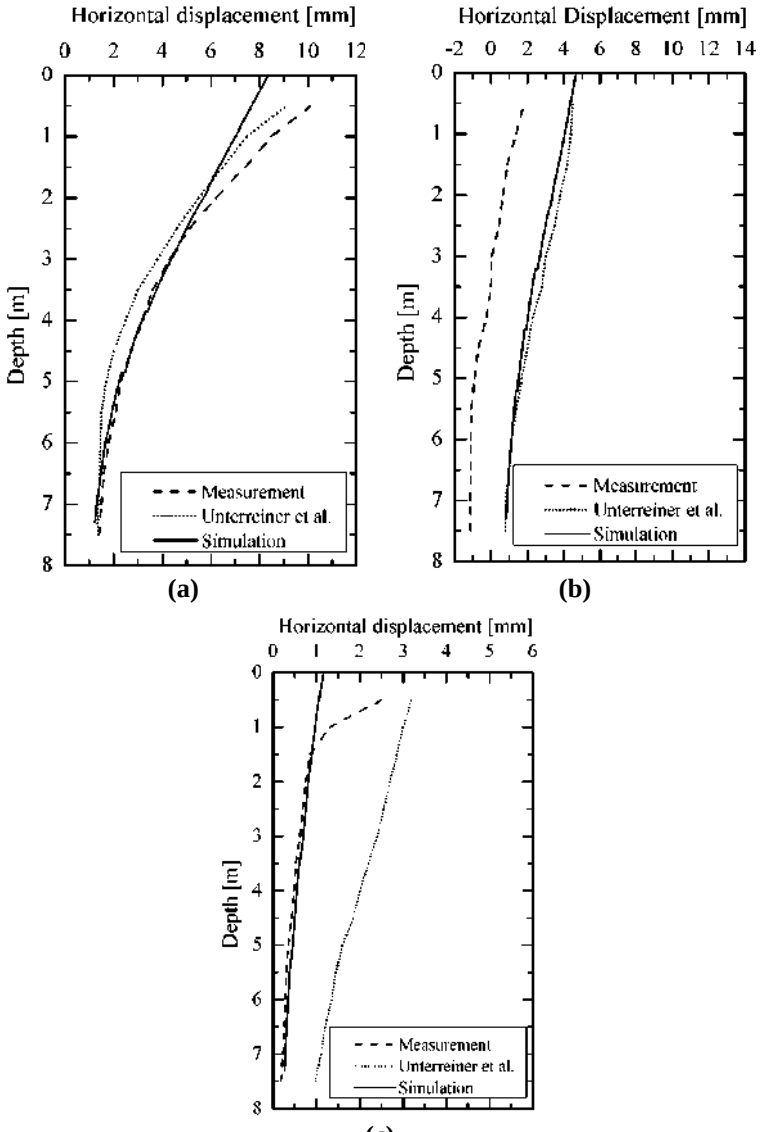

(a) **(b)**

(c)

Fig. 5. Comparison of the predicted horizontal displacements in the backfill with measured results in phase 5 at: a) 2 m; b) 4 m; and c) 8 m behind the wall facing

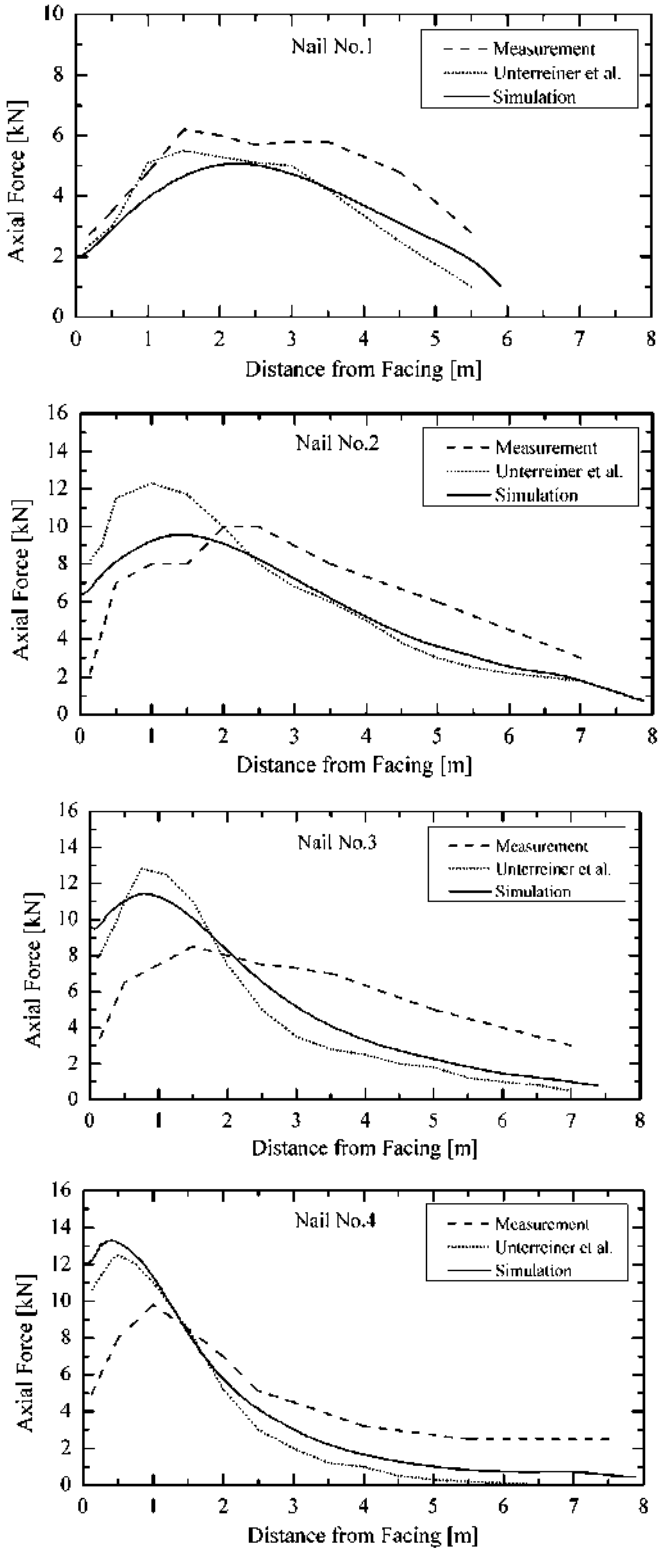

Fig. 6. Tensile force distribution in the nails at the end of phase 5

3. Parametric Analysis on the Nailing Pattern

The nails length can be considered constant in the height of the wall. This approach may not be the best design if the wall deformation is taken into account. To study the effect of nailing pattern on the performance of nailed wall, nine patterns were considered (Figure 7). The nails length in pattern (a) is uniform and equal. In patterns (b) and (c), half and two-thirds of nails are uniformly long nails, respectively and the other nails are short nails. In

patterns (d) and (e), the length of each 3 or 2 nails are linearly decreased from the maximum nail length at the top of the wall to the minimum nail length at the bottom of the wall, respectively. The ratio of length of the shortest nail to the longest nail has been considered 0.5 and 0.7 in all variable patterns.

In addition to the nailing pattern, the other factors which have effect on the wall deformation are nails spacing, wall height and surcharge load. The considered values for these parameters are presented in Table 5. So, parametric analysis was conducted to determine the effects of these parameters on the wall deformation with various nailing layouts.

Figure 8 shows the typical geometry of the wall used for the parametric analysis. These dimensions are chosen in such a way that minimizes the effects of boundary conditions on simulation results. The stability of nailed walls was analyzed using the limit equilibrium method. The overall stability of all patterns has been analyzed according to the recommended procedure and safety factors in the nailing manual of FHWA (Lazarte et al., 2015) for temporary condition. The objective of limit equilibrium analysis was determination of nails length in such a way that all models have the same safety factor of overall stability equal to 1.35.

The diameter of nail bar has been considered 32 and 40 mm for the 12 and 18 m walls, respectively. The nail bar is surrounded by 10 cm cement grout. The nail orientation relative to horizontal plane is 15 deg. The thickness of shotcrete facing is 10 cm. The properties of nail and shotcrete used in the parametric analysis are shown in Tables 6 and 7.

Table 8 shows the soil properties used in the parametric analysis. These parameters are matching with the properties of dense clayey sand and gravel soils. The hardening soil model was used to simulate the stress-strain behavior of soil.

After creating geometry of the model, defining material properties and mesh generation, the initial condition of stress and stage construction should be defined. Each stage construction involved two phases: excavation with 2 m height and activation of nail and shotcrete elements. This process has been continued until reaching to base of the wall.

Table 5. Variable parameters in parametric analysis

Parameter	Symbol	Unit	Values
Wall height	H	m	12, 18
Surcharge	q	kPa	0, 50
Nails spacing	$S_h = S_v$	m	1.5, 2

Table 6. Properties of nails used for the parametric analysis

Parameter	Symbol	Unit	H=12 m	H=18 m
Diameter	φ	mm	32	40
Yield force	F_y	kN	320	500
Bond diameter	d	m	0.1	0.1
Bond skin friction	α	kPa	200	200
Axial stiffness	EA	kN	3.17×10^5	4.93×10^5
Poisson ratio	ν	-	0.2	0.2

Table 7. Properties of shotcrete facing used for the parametric analysis

Parameter	Symbol	Unit	Value
Unit weight	γ	$\mathrm{kN/m^3}$	24
Young's modulus	E	kPa	21×10^6
Axial stiffness	EA	kN/m	2.1×10^6
Bending stiffness	EI	$\mathrm{kN.m^2/m}$	1750
Shotcrete thickness	d	cm	10
Poisson ratio	ν	-	0.2

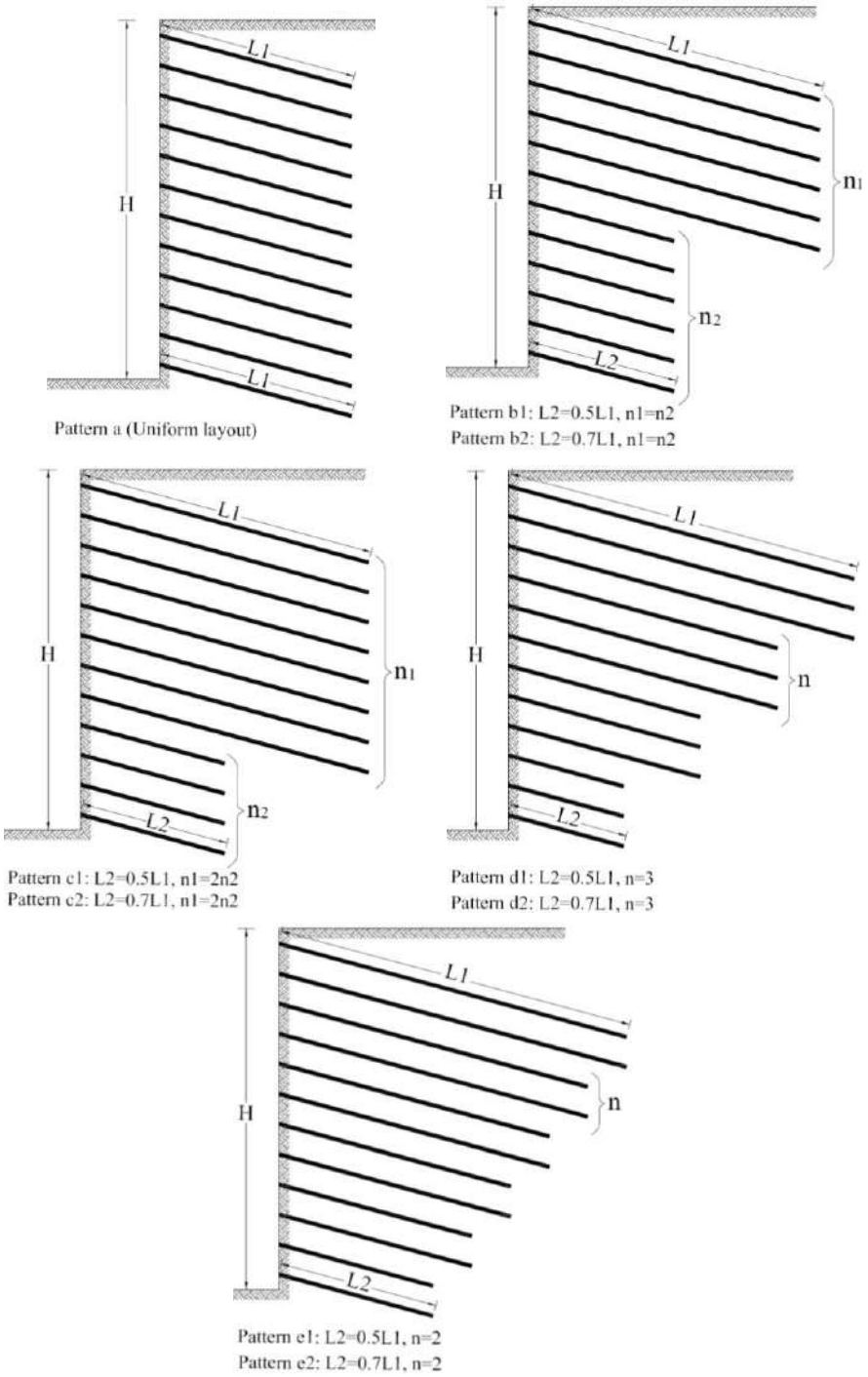

Fig. 7. Nailing patterns for parametric analysis

Table 8. Soil properties used in the parametric analysis

Parameter	Symbol	Unit	Value
Cohesion	c	kPa	30
Friction angle	φ	deg	36
Dilation angle	ψ	deg	6
Unit weight	γ	kPa	20
Reference loading stiffness	E_{50}^{ref}	kPa	7.0×10^4
Reference oedometer loading stiffness	E_{oed}^{ref}	kPa	7.0×10^4
Reference unloading stiffness	E_{ur}^{ref}	kPa	2.1×10^5
Reference confining pressure	P^{ref}	kPa	100
Poisson ratio	ν	-	0.3
Fabric parameter	m	-	0.5

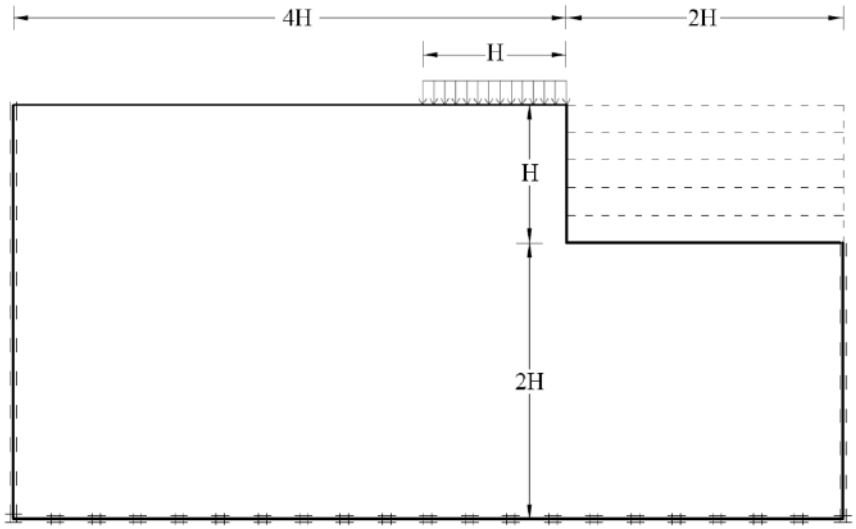

Fig. 8. Geometry of nailed walls used for the parametric study

4. Results and Discussion

4.1. Density of Nails

In Figure 9, the normalized maximum nail lengths for various patterns are presented. Also, nail density per unit area of wall facing for the various patterns is shown in Figure 10. The density of nail is defined as follows:

$$Nail\ density = \frac{\sum L_{nail}}{S_h \times H} \quad (7)$$

where $\sum L_{nail}$: is the summation of all nails length in a vertical row, S_h: is the horizontal spacing of the nails and H: is the wall height.

As observed in Figure 9, pattern (a) has the minimum nail length and patterns (b1), (d1) and (e1) has the maximum nail length. The maximum nail length of the patterns 2 (in which $L_2 = 0.7L_1$) are less than patterns 1 (in which $L_2 = 0.5L_1$). The results of analyses indicate that by increasing the nail spacing to 2 m, the nails length increases. As seen in Figure 9, the normalized nails length increases by increasing the height of wall and surcharge load.

As it is observed in Figure 10, the nailing pattern has minor influence on the nail density and its variation is between 5 to 15 percent. However, nails spacing has considerable effect on nail density. By increasing the nail spacing from 1.5 m to 2 m, the nail density decreases about 20 to 40 percent. This indicates that despite of the increasing of the maximum nail length, the nail density decreases by increasing of nails spacing. In fact, by increasing the spacing of nails from 1.5 m to 2 m, the effective area of each nail increases from 2.25 to 4 m^2, i.e. 78 percent. However, the length of the nails does not increase with this ratio according to the Figure 10. As a result, increasing the nail spacing will reduce the density of nail and optimize the design of soil-nailed wall economically. Also, the nail density increases considerably by increasing the height of the wall and surcharge load.

4.2. Deformations of Nailed Walls

The results of deformation analysis are presented in Figures 11 and 12 in the form of normalized deformations at the top of the wall (δ_h/H and δ_v/H). As can be seen in these figures, the deformations of uniform pattern in various conditions are significantly greater than that of the variable patterns. Among the variable patterns, patterns 1 have relatively less deformation than patterns 2. Also, it can be seen that the patterns (d1) and (e1) in most cases have the least deformations in comparison to other variable patterns.

As mentioned above, the nail density in uniform and variable patterns is approximately equal. Thus, it can be concluded that these observations are

related to the maximum length of the nail in the upper rows. The patterns in which the nails lengths are more variable, the length of the upper nails should be increased to provide the required safety factor of stability. Increasing the nails length in the upper rows will cause more constraint for the wall and reduce deformations, especially horizontal deformations.

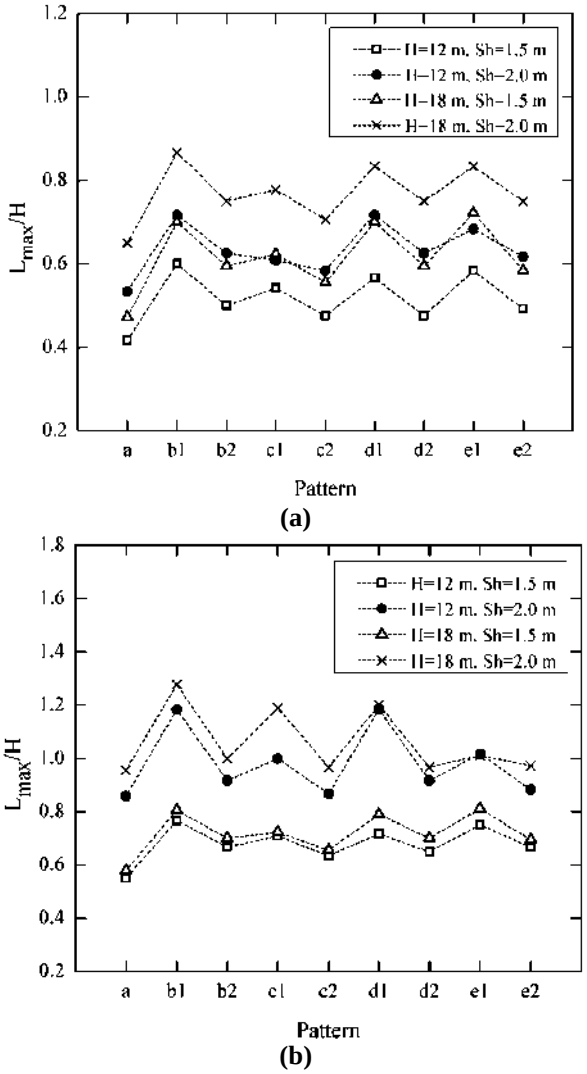

Fig. 9. Maximum length of nails for different patterns: a) q = 0 kPa; and b) q = 50 kPa

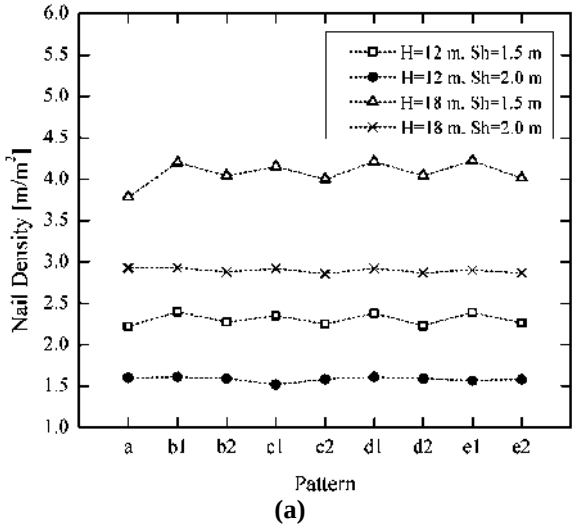

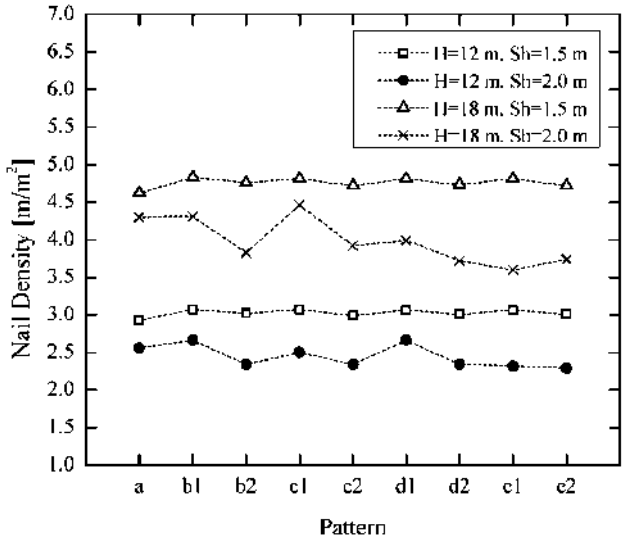

(b)

Fig. 10. Nail density for different patterns: a) q = 0 kPa; and b) q = 50 kPa

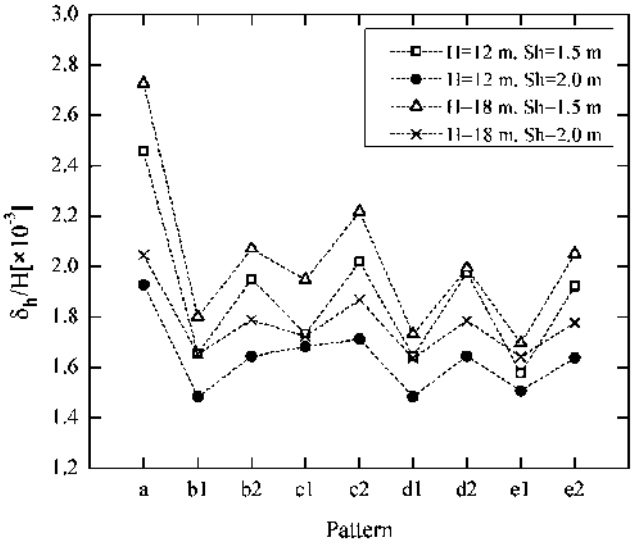

(a)

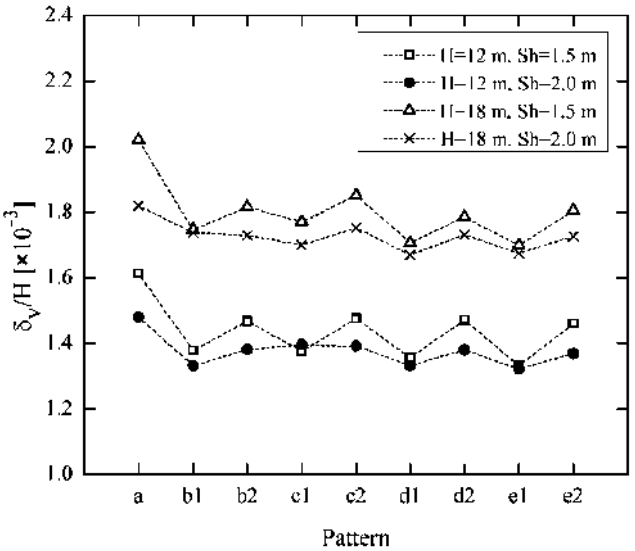

(b)

Fig. 11. Normalized maximum wall deformation for different patterns (q = 0 kPa): a) Horizontal displacement; and b) Vertical displacement

As stated, the nailed walls were designed based on the FHWA manual and the target safety factor of stability in all of walls is the same. This implies that the nails length should be increased by increasing of nails spacing. Regarding the nails spacing, important point that can be seen in Figures 11 and 12 is that the wall deformation is reduced by increasing the spacing of nails which is directly related to the long nails in the sparse layouts. In this case, it should be noted that although the maximum length of the nail increases, the density of nails per unit area of wall facing decreases. Therefore, it can be concluded that the length of the upper nails is more effective than the nail density on reducing deformation. However, these two factors are more effective on horizontal displacement of the wall and in the case of vertical displacement; they balance the effects of each other. Consequently, the amount of the settlement has not changed much by changing the nails spacing.

In Figure 13, the horizontal deformation at the top of the wall is plotted versus the maximum nail length for all analyses. These two parameters were normalized in terms of the height of wall, so that all of the results can be presented in one graph for various heights of the wall. This plot shows the effect of the maximum length of the nails on the horizontal displacement of the nailed wall more accurately. The general trend of data in this figure indicates that with increasing the maximum length of the nails, the horizontal deformation of the wall decreases.

Regarding the above discussions, it can be concluded that the optimal pattern for reducing the nailed wall deflections is that the long nails should be installed at the top of the wall and nails length reduced in the wall height. The linear reduction of the nails length at the wall height (for example pattern e1) can be considered as an optimal pattern, because the nails length changes according to the slip surface inclination. Also, designing of nailed wall with the greater nails spacing leads to reduction of wall deformation and optimal economical design.

4.3. Damage Severity

There are various criteria for assessing the effects of excavation-induced ground movements on the performance and serviceability of the adjacent buildings. One of the most famous criteria for this purpose is angular distortion criterion that is proposed by Boscardin and Cording (1989). Boscardin and Cording (1989) considered both vertical and horizontal ground deformations for evaluating the damage of adjacent structures due to excavation-induced ground movements. As can be seen in Figure 14, the severity of damages is divided into four zones based on horizontal extension strain and angular distortion, namely Negligible damage (NEGL.), Very slight damage (V.SL.), Slight damage, and Moderate to Severe damage. The horizontal extension strain (ε_v) and angular distortion (β) are defined as follows:

$$\beta = (\delta_{v1} - \delta_{v2})/L \quad (8a)$$

$$\varepsilon_h = (\delta_{h1} - \delta_{h2})/L \quad (8b)$$

where L: is the length of adjacent structure, and δ_v and δ_h: are the vertical and horizontal displacement at two edges of structure, respectively.

It should be noted that the ground movements at the ground surface on the top of the wall varies non-linearly with the distance from the wall edge. In the vicinity of the nailed wall, the rate of variations is greater, and by increasing the distances from the wall, deformation values and their rate of variation are reduced. Therefore, there are various values of horizontal extension strain and angular distortion by changing the distance from the wall. In order to consider the proper estimation for L in the above equations, the influence zone of excavation should be considered that depends on various conditions such as soil type and excavation depth. The results of the analyses indicate that the main effects of excavation usually occur at a distance equal

to the height of the wall. Therefore, to obtain the proper values for the horizontal strain and angular momentum parameters, the rate of variation of the deformation at the distance of H from the wall edge was used.

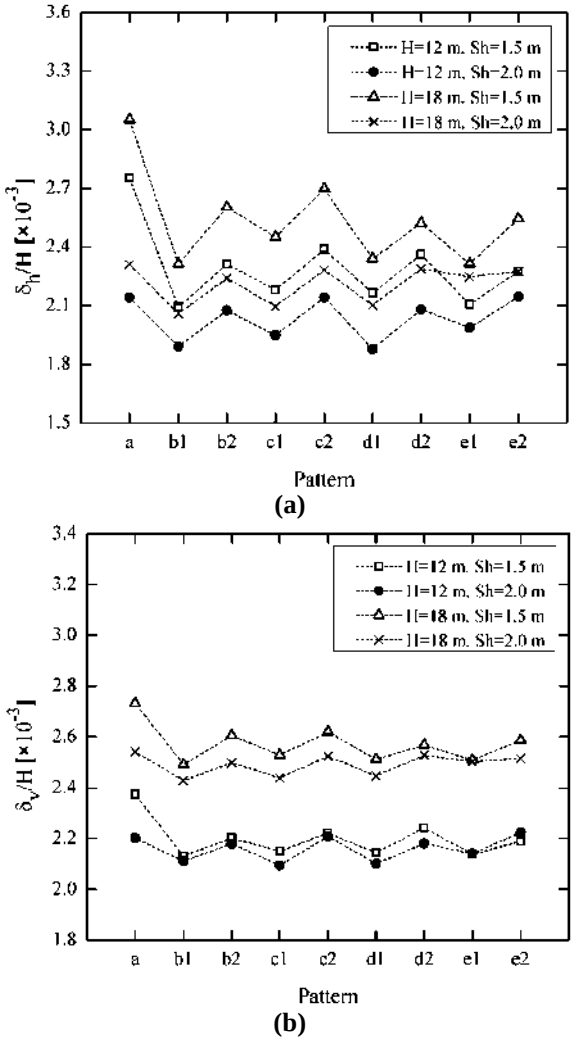

Fig. 12. Normalized maximum wall deformation for different patterns (q = 50 kPa): a) Horizontal displacement; and b) Vertical displacement

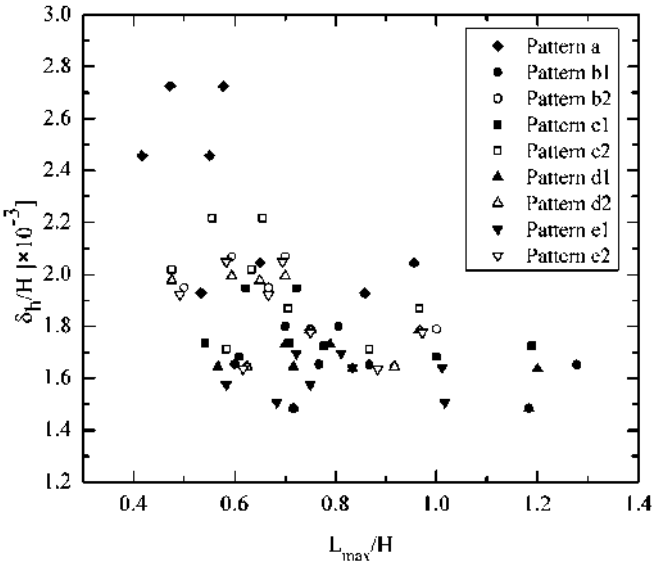

Fig. 13. Relationship between maximum horizontal displacement and maximum length of nails for different patterns

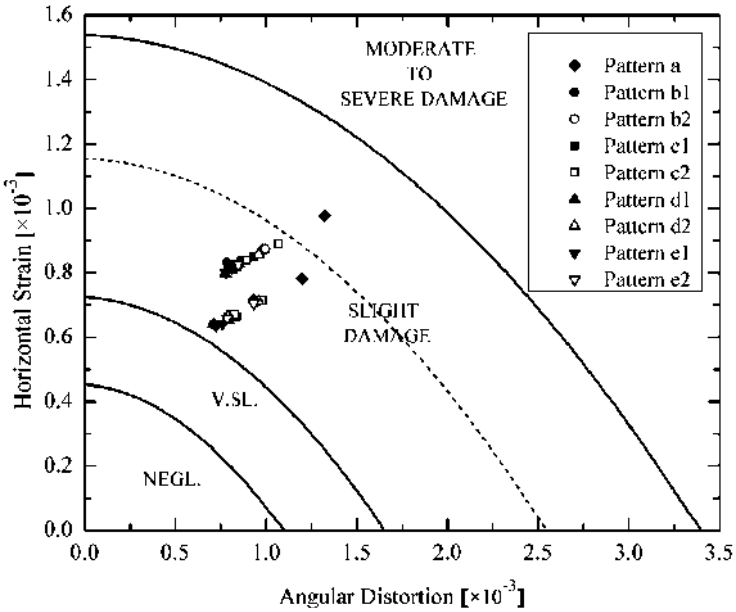

Fig. 14. Relationship between angular distortion and horizontal strain for damage category (q = 0 kPa)

In Figures 14 and 15 the values of the horizontal extension strain and the angular distortion for all the models were plotted in the Boscardin and Cording graph. Figures 14 and 15 are related to the models without surcharge and with surcharge of 50 kPa, respectively. As seen, in case of no surcharge (q = 0), the severities of displacements are located in the lower half of slight damage region while in the presence of surcharge they are located in the upper half of the slight damage region. As shown in these figures the severity of damages in the uniform patterns are more than variable ones. Even in Figure 15, one point is located in moderate to severe damage region. This point is related to the uniform pattern with the wall height of 18 m and the nails spacing of 1.5 m.

These graphs assist in considering the appropriate safety factor to achieve the allowable displacement. As seen in Figure 14, in the case of no surcharge, the excavation-induced displacements can be considered allowable. Specially, by taking into account the recommendations of the previous section (using the variable patterns and increasing the length of upper nails), it is possible to reduce deformations up to very slight damage region. Therefore, considering the stability safety factor equal to 1.35 can be appropriate in the case of no surcharge. But as seen in Figure 15, the existence of surcharge increases the wall deformations. On the other hand, due to the presence of the structure in the vicinity of the wall, the allowable deformations are less than the no surcharge case. Therefore, the safety factor equal to 1.35 is not a good criterion for design of nailed walls adjacent to the structures.

In order to investigate the deformations of nailed walls with different safety factors of stability, the optimal case in the previous section (Pattern e1 and nails spacing of 2 m) was considered and the nailed wall was designed considering different safety factors of stability. The wall height of 18 m and 50 kPa surcharge were considered. Afterwards, the wall deformations were calculated using finite element analysis and the amount of horizontal strains and angular distortions were plotted on the Boscardin and Cording (1989) graph and its distance from the boundary of the very slight damage (V.SL.) region were measured. In Figure 16, the method of calculation is schematically shown.

The variation of distance from the V.SL. boundary versus safety factor of stability is shown in Figure 17. As seen, the deformations reduce by increasing the safety factor and approach to the V.SL. boundary. It can be concluded from this

graphs that the deformations of nailed walls with surcharge will be located in the V.SL. region if the safety factor of stability is considered greater than 1.5. These deformations can be acceptable for the ordinary structures. It should be noted that this conclusion is depended on the various conditions such as soil type, the height of the wall, and the amount of the surcharge load. So, the permissible deformations cannot be guaranteed by taking into account only the proposed safety factor and deformation analysis is necessary. The proposed safety factor can be considered as a preliminary guide for design of optimal and safe soil nailed walls in the urban areas.

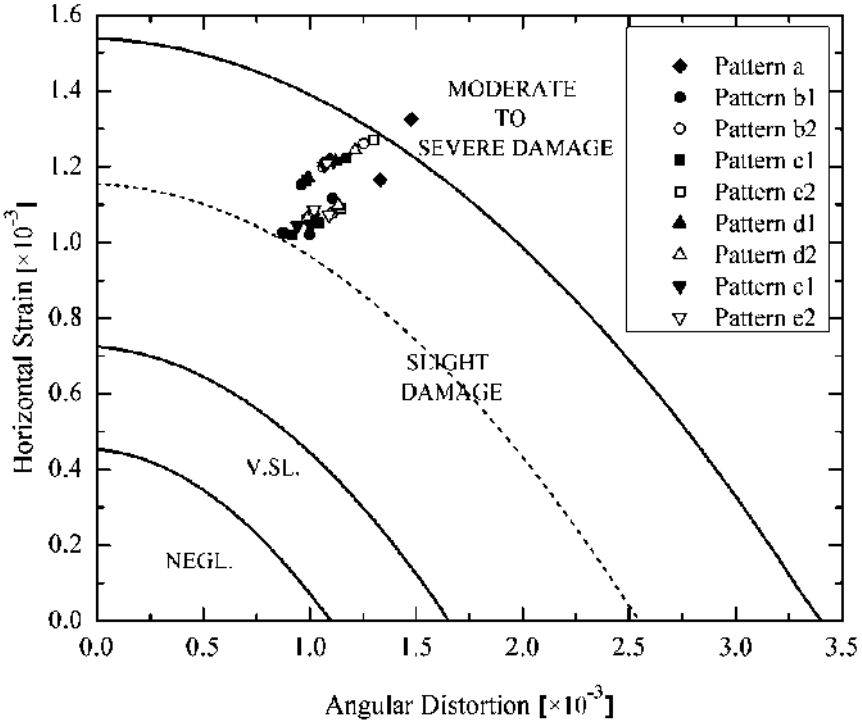

Fig. 15. Relationship between angular distortion and horizontal strain for damage category (q = 50 kPa)

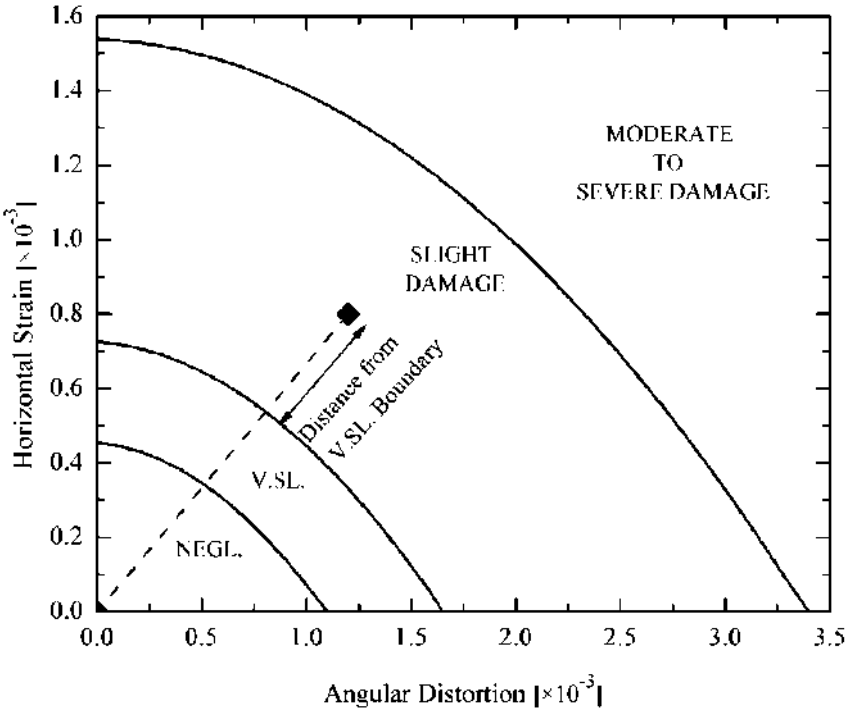

Fig. 16. Definition of distance from the boundary of the V.SL. region

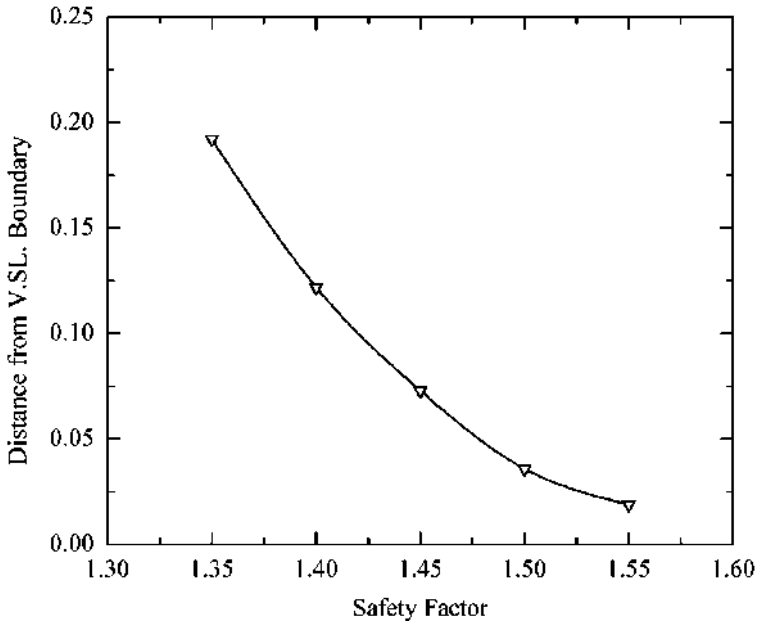

Fig. 17. The variation of distance from the V.SL. boundary versus safety factor

5. Conclusions

In this study, the effects of the nailing pattern on the wall deformation were studied using the non-linear finite element analysis. Major results concluded from this study are summarized as follow:

- The nailing pattern has minor influence on the nail density. It can be indicated that this conclusion is related to the maximum length of the nail in the upper rows. The patterns in which the nails lengths are more variable, the length of the upper nails should be increased to provide the required safety factor of stability.
- Nails spacing has considerable effect on the nail density. This indicates that despite of the increasing of the maximum nail length, the nail density decreases by increasing of nails spacing. As a result, increasing the nail spacing will reduce the density of nail and optimize the design of nailed wall.
- The deformations of uniform pattern in various conditions are significantly greater than that of the variable patterns. The simulation results indicate that using the variable pattern with long nails at the top of the wall reduces the lateral deformation and the density of nails of soil nailed wall. Increasing the nails length in the upper rows will cause more constraint for the wall and reduce deformations, especially horizontal deformations.
- To achieve the optimal nailing pattern for reducing the nailed wall deflections, the long nails should be installed at the top of the wall and nails length should be reduced in the wall height. The linear reduction of the nails length at the wall height (for example pattern e1) can be considered as an optimal pattern.
- Based on the angular distortion criterion that is proposed by Boscardin and Cording (1989), the severity of damages in the uniform patterns are more than variable ones.
- Deformation analysis of optimal pattern in this study with different safety factors of stability indicated that considering the stability safety factor equal to 1.35 can be appropriate in the case of no surcharge. However, it is not a good criterion for design of nailed walls adjacent to the structures. The minimum safety factor of 1.5 can be considered as a preliminary guide for design of optimal and safe soil nailed walls in the urban areas.

6. Acknowledgment

The authors gratefully acknowledge the financial support of Kharazmi University (Grant Number: 4/28941).

7. References

Abbas, H., El Sherbiny, R. and Salam, A. (2020). "Numerical analysis of soil nail walls in hybrid retaining wall systems", *Geo-Congress 2020*, Minneapolis, Minnesota.

Ardakani, A., Bayat, M. and Javanmard, M. (2014). "Numerical modeling of soil nail walls considering Mohr Coulomb, hardening soil and hardening soil with small-strain stiffness effect models", *Geomechanics and Engineering*, 6(4), 391-401.

Boscardin, M.D. and Cording, E.G. (1989). "Building response to excavation-induced settlement", *Journal of Geotechnical Engineering*, ASCE, 115(1), 1-21.

Chu, L.M. and Yin, J.H. (2005). "Comparison of interface shear strength of soil nails measured by both direct shear box tests and pull-out tests", *Journal of Geotechnical and Geoenvironmental Engineering*, ASCE, 131(9), 1097-1107.

Dupla, J.C. and Canou J. (1994). "Caractérisation mécanique du sable de Fontainebleau à partir d'essais triaxiaux de compression et d'extension", Rapport Interne Clouterre II, CERMES–ENPC.

FHWA (1993). "Recommendations Clouterre 1991 (English translation): Soil nailing recommendations", Report No. FHWA-SA-93-026, Federal Highway Administration, Washington, D.C.

Fan, C.C., and Luo, J.H. (2008). "Numerical study on the optimum layout of soil-nailed slopes", *Computers and Geotechnics*, 35(4), 585-599.

Gharedaghi, H. and Shahir, H. (2019). "Parametric assessment of lateral pressure on piles and laggings in an anchorage system", *Journal of Geoengineering*, 14(1), 11-20.

Hajiazizi, M. and Mirzazadeh, Z. (2020). "Determination of creep-induced displacement of soil slopes based on LEM", *Civil Engineering Infrastructures Journal*, 53(2), 341-358.

Halabian, A.M., Sheikhbahaei, A.M. and Hashemolhosseini, S.H. (2012). "Three dimensional finite difference analysis of soil-nailed walls under static conditions", *Geomechanics and Geoengineering*, 7(3), 183-196.

Hitha, S., Vijayshree, S., Animesh, S. and Ramkrishnan, R. (2019). "Regression analysis of soil nailing parameters using finite element and limit equilibrium methods", *Australian Geomechanics Journal*, 54(3), 137-147.

Lazarte, C.A., Robinson, H., Gómez, J.E., Baxter, A., Cadden, A. and Berg, R. (2015). "Geotechnical engineering circular No. 7: Soil nail walls - Reference manual", Report No. FHWA-NHI-14-007, National Highway Institute, US Department of Transportation, Federal Highway Administration, Washington D.C.

Liu, J., Shang, K. and Wu, X. (2016). "Stability analysis and performance of soil-nailing retaining system of excavation during construction period", *Journal of Performance of Constructed Facilities*, ASCE, 30(1), C4014002.

Moniuddin, Md. K., Manjularani, P, and Govindaraju, L. (2016). "Seismic analysis of soil nail performance in deep excavation", *International Journal of Geo-Engineering*, 7(1), 1-10.

Plumelle, C., Schlosser, F., Delage, P. and Knochenmus, G. (1990). "French national research project on soil nailing: Clouterre", *Proceedings of Conference of Design and Performance of Earth Retaining Structures*, ASCE Geotechnical Special Publications No. 25, 660-675.

Rashidi, F., Shahir, H. and Arefizade, H. (2019). "Comparative study of anchored wall performance with two facing designs", *Civil Engineering Infrastructures Journal*, 52(1), 23-40.

Rashidi, F. and Shahir, H. (2019). "Numerical investigation of anchored soldier pile wall performance in the presence of surcharge", *International Journal of Geotechnical Engineering*, 13(2), 162-171.

Rawat, S. and Gupta, A.K. (2016). "Analysis of a nailed soil slope using limit equilibrium and finite element methods", *International Journal of Geosynthetics and Ground Engineering*, 2(4), 1-23.

Schanz, T. and Vermeer, P.A. (1998). "On the stiffness of sand", In: *Pre-Failure Deformation Behaviour of Geomaterials*, London, 383-387.

Schlosser, F., Unterreiner, P. and Plumelle, C. (1993). "Validation des méthodes de calcul de clouage par les expérimentations du projet national Clouterre", *Revue Française de Géotechnique*, 64, 11-20.

Seo, H.J., Lee, I.M. and Lee, S.W. (2014). "Optimization of soil nailing design considering three failure modes", *KSCE Journal of Civil Engineering*, 18(2), 488-496.

Sharma, A. and Ramkrishnan, R. (2020). "Parametric optimization and multi-regression analysis for soil nailing using numerical approaches", *Geotechnical and Geological Engineering*, 38, 3505-3523.

Tei, K., Taylor N.R. and Milligan G.W.E. (1998). "Centrifuge model tests of nailed soil slopes", *Soils and Foundations*, Japanese Geotechnical

Society, 38(2), 165-177.
Unterreiner, P., Benhamida, B. and Schlosser, F. (1997). "Finite element modeling of the construction of a full scale experimental soil-nailed wall", *French National Research Project Clouterre-Ground Improvement*, 1(1), 1-8.
Yang, M.Z. and Drumm, E.C. (2000). "Numerical analysis of the load transfer and deformation in a soil nailed slope", In: *Numerical Methods in Geotechnical Engineering*, pp. 102-115.
Zhang, M., Song, E. and Chen, Z. (1999). "Ground movement analysis of soil nailing construction by three-dimensional (3-D) finite element modeling (FEM)", *Computers and Geotechnics*, 25(4), 191-204.

Civil Engineering Infrastructures Journal 2021, 54(2): 351-364
DOI: 10.22059/CEIJ.2020.298837.1661

RESEARCH PAPER

Development of a Bridge Maintenance System Using Bridge Information Modeling

Samadi, D.[1], Taghaddos, H.[2*], Nili, M.H.[3] and Noghabaei, M.[4]

[1] M.Sc., School of Civil Engineering, College of Engineering, University of Tehran, Tehran, Iran.
[2] Assistant Professor, School of Civil Engineering, College of Engineering, University of Tehran, Tehran, Iran.
[3] Ph.D., School of Civil Engineering, College of Engineering, University of Tehran, Tehran, Iran.
[4] Ph.D. Student, Department of Civil, Construction, and Environmental Engineering, North Carolina State University, Raleigh, USA.

Received: 04 Mar. 2020; Revised: 12 Oct. 2020; Accepted: 31 Oct. 2020

ABSTRACT: Bridges play a critical role in the transportation system network; accordingly, assuring satisfaction with the service level of these structures is vital for bridge maintenance managers. Thus, it is vital to determine the optimum bridge maintenance plan (i.e., the optimum timing and type of repair activities applied to the bridge elements) considering the budget limitations. To optimize the bridge maintenance plan, some researchers have focused on developing optimization models, including the Genetic Algorithm (GA). However, a few studies have employed Bridge Information Modeling (BrIM) to enhance bridge maintenance management. This study focuses on developing an integrated framework based on BrIM and bridge maintenance optimization to utilize visualization capabilities of BrIM to assist maintenance managers in making decisions. The presented framework optimizes the bridge maintenance plan at the sub-element level. The BrIM automatically feeds into the developed GA optimization system. The introduced framework is successfully verified using a real-world case study.

Keywords: Bridge Information Modeling (BrIM), Bridge Maintenance Plan, Genetic Algorithm (GA), Maintenance Optimization.

1. Introduction

Civil infrastructure systems have direct impacts on the sustained economic growth and social development of modern society. The highway transportation system is especially critical within the infrastructure system. Among the many elements of an infrastructure system, bridges are necessary economic and human connectors; their failure, or partial closure, may cause various public or private losses.

Few constructed facilities are genuinely maintenance-free. Most require regular maintenance and occasional repairs to keep them operable and in a good appearance (Nili et al., 2020). Bridges are no exception. Although some structures have a long

* Corresponding author E-mail: htaghaddos@ut.ac.ir

period of usability, overwhelming loads exceeding bridge design and environmental conditions have caused many to perform below their intended function (Miyamoto and Motoshita, 2015). As reported in the literature, the application of effective repair activities is critical for a bridge to reach its expected service life (Chen and Duan, 2014). For instance, in Iran, the national bridge network comprises over 330,000 bridges, and more than 50% of them are more than 30 years old (Sahrapeyma and Hosseini, 2013). Heavy traffic and the absence of a proper bridge maintenance plan have deteriorated many of these bridges (Gholami et al., 2013).

Many researchers have endeavored to develop optimum bridge maintenance plans, including De Brito et al. (1997), Furuta et al. (2004), Hong and Hastak (2007), Elbehairy et al. (2009), and Kim et al. (2013). However, current practices in this area suffer the following limitations:

- Data entry in the developed systems does not enjoy a neat visual interface, even though data visualization facilitates decision making by maintenance managers.
- In current bridge maintenance practices, project life cycle data are scattered over different data sources, which produce a high probability of data loss from one project phase to another.
- Bridge maintenance planning is optimized at the element-level. In other words, all of the bridge elements with a common type are represented by a single element in the optimization process. For instance, in the optimization process, the optimum timing and type of repair activities for a deck element, which represents the full deck of the bridge, is found.

Building Information Modeling (BIM) is one of the most promising developments in the architecture, engineering, and construction (AEC) industries (Eastman et al., 2011). BIM improves upon planning, design, construction, operation, and maintenance processes using a standardized machine-readable information model for each facility. BIM contains appropriate information created or gathered about that facility in a format useable by all stakeholders throughout its life cycle (NIBS, 2008).

The need for BIM in maintenance management has been acknowledged by various researchers and practitioners (Becerik-Gerber et al., 2011). However, BIM is not yet effectively utilized in this phase (Ilter and Ergen, 2015). BIM in bridges, sometimes also called Bridge Information Modeling (Ghadiri Mohghaddam, 2014), is an active topic in bridge maintenance management. The BrIM is not only a geometrical representation of bridges but also an intelligent representation of bridges containing all relevant information throughout their life cycles (Marzouk and Hisham, 2011). BrIM can effectively facilitate the inspection and evaluation of bridges. It can also enable transportation agencies to manage bridge inventories more efficiently. In short, BrIM can lead to a more automated and integrated practice in the design, construction, and operation phases of a bridge life cycle (McGuire et al., 2016). However, developing a framework integrating BrIM and optimization models to enhance bridge maintenance management is neglected in the literature.

This paper utilizes BrIM as a powerful tool to gather data related to the whole life cycle. The obtained data is utilized in maintenance optimization. Moreover, the developed framework provides optimized repair and generates effective visualization of the results to aid bridge managers in decision making. Finally, the optimum bridge maintenance plan is found in the sub-element level. In other words, in the presented framework, instead of finding the optimum timing and type of repair activities for the deck, the deck is divided into some sub-elements. Then, the maintenance plan is optimized for each of the deck sub-elements.

The framework includes an Inspection Module, an Optimization Module, a Visualization Module, and a Maintenance Database. It also incorporates a graphical user interface to facilitate data entry and visualize optimized repair activities in the BrIM model.

2. Literature Review

To determine optimum repair activities for bridges, many researchers have utilized optimization algorithms. De Brito et al. (1997) used single-objective maintenance optimization in a bridge network, maximizing total expected benefits less expected repair and failure costs. They assumed that for each bridge, only one repair type would be implemented. Elbehairy et al. (2009) also proposed a single objective optimization bridge management system utilizing a year-by-year optimization formulation. Their developed system maximizes the benefit/cost of repair activities as well as the overall network condition. Farran and Zayed (2015) developed a multi-objective decision support system (MODSS), which handles two objective functions, including cost and performance, simultaneously, utilizing a normalization technique. Alikhani and Alvanchi (2019) presented a framework to find the optimum bridge maintenance plan at the bridge-level and network-level, which minimizes the ratio of repair costs to repair improvements.

In addition to single-objective optimization, some researchers have developed multi-objective optimization. For example, Frangopol and Liu (2007) optimized maintenance activities, both in an individual bridge and in a bridge network. They considered the objectives of minimizing the maximum condition index, maximizing the minimum safety index, and minimizing lifecycle cost. Kim et al. (2013) proposed a probabilistic framework for optimum inspection and maintenance planning for deteriorating structures, including bridges. The optimum inspection and maintenance types and times are obtained through an optimization, maximizing the expected service life and minimizing the expected total lifecycle cost. Mirzaei and Adey (2018) developed a framework to find the most sustainable bridge maintenance program in a bridge network. The developed model considered agency costs, user costs, and costs related to sound emission, air pollution, and climate change.

An important factor influencing the optimum bridge maintenance plan is bridge deterioration rates. The bridge deterioration is a complex process affected by many factors such as material aging, overload, and aggressive environmental conditions such as chloride contamination, corrosion, and shrinkage. Therefore, calculating the deterioration of elements based on its causes is a complicated task. Thus, the deterioration rate has been modeled in the literature via different statistical techniques, such as linear (Frangopol and Liu, 2007) and nonlinear (Miyamoto et al., 2000) deterioration, or by using the Markov chain (Morcous and Lounis, 2005). Some researchers have utilized a combination of the methods mentioned above (Elbehairy et al., 2009). In some studies, the deterioration model is specific to the deterioration mechanisms, such as chloride-induced corrosion (Frangopol and Soliman, 2016). From another perspective, the effect of repair activities on the elements' PI values is modeled differently in the literature. Some researchers have assumed that repair activities enhance the elements' PI values (Hong and Hastak, 2007), while others have considered a decrease in the deterioration rates (Farran and Zayed, 2015). Table 1 summarizes some of the conducted research in the field of bridge maintenance optimization.

In utilizing BIM to improve maintenance planning, some researchers have introduced BIM to FM practices, mostly focusing on visualization capabilities. Chen and Wang (2009) proposed a 3D visualized approach for the maintenance and management of facilities.

Table 1. Summary of some of the previous research efforts in bridge maintenance optimization

Reference	Optimization level	Deterioration modeling	Improvement effect
De Brito et al. 1997)	Network-level	Chloride corrosion formulation	Enhancing elements' PI values to the best
Furuta et al. (2004)	Bridge-level	Linear	Enhancing elements' PI values, delaying deterioration rates
Frangopol and Liu (2007)	Bridge-level, network-level	Markov	Enhancing elements' PI values, delaying deterioration rates
Hong and Hastak (2007)	Bridge-level	Linear	Enhancing elements' PI values
Elbehairy et al. (2009)	Bridge-level, network-level	Linear, Markov	Enhancing elements' PI values
Huang and Huang (2012)	Bridge-level	Linear	Enhancing elements' PI values
Kim et al. (2013)	Bridge-level	Time-dependent deterioration rates	The extension of bridge service life
Sahrapeyma and Hosseini (2013)	Network-level	Markov	Enhancing elements' PI values to the best
Farran and Zayed (2015)	Bridge-level	Markov	Different Markov deterioration rates are utilized
Alikhani and Alvanchi (2019)	Network-level	Markov	Enhancing the elements' PI values to the best
Mirzaei and Adey (2018)	Bridge-level	Markov	Enhancing elements' PI values to the best

A 3D facility model was provided in the system as the interface for accessing various maintenance-related data intuitively. The 3D model provided users an intuitive understanding of the state of the facility from different aspects. Liu and Issa (2012) focused on automatic bidirectional communications between Computerized Maintenance Management Systems (CMMS) and BIM models on a database level. Lin and Su (2013) proposed a BIM-based Facility Maintenance Management (BIMFMM) system, which helped maintenance staff access and review 3D BIM models to update related maintenance records digitally. Motamedi et al. (2014) utilized BIM visualization capabilities to provide FM technicians with visualizations to utilize their cognitive and perceptual reasoning for problem-solving. Marzouk and Abdelaty (2014) utilized BIM along with a global ranking system to monitor Indoor Environmental Quality (IEQ) in subway stations. In the proposed framework, a Wireless Sensor Network (WSN) is deployed in a subway station and connected to a BIM-based model. WSN readings and particulate matter concentration levels are visualized in the BIM-based model.

Further to FM, some researchers have utilized BIM capabilities for the bridge, which is called BrIM. Most of these studies address the visualization capabilities of BrIM. Hammad et al. (2006) discussed the requirements for developing a Mobile Model-Based Bridge Life-cycle Management System (MMBLMS). The system would link information about the life cycle stages of a bridge (e.g., design, construction, inspection, and maintenance) to a 4D model of the bridge and provide user interfaces that facilitate the use of the 4D models. Marzouk and Hisham (2011) presented a BrIM framework that visualized maintenance information relative to each bridge component. Ghadiri Mohghaddam (2014) proposed a framework to improve bridge maintenance information documentation, storage, and visualization. In their framework, inspection observations are added to the BrIM by the inspector directly interacting with the model at the inspection site.

Few papers have explored other benefits of BrIM for bridge maintenance. McGuire

et al. (2016) investigated the use of BrIM to link and analyze data related to the inspection, evaluation, and management of bridges. In the proposed method, information on damage type, amount, severity, and location were gathered during bridge inspection by an inspector using a custom software add-in. Next, a custom tool in Microsoft Excel evaluated the structural performance, provided load ratings of the inspected bridge, and offered maintenance recommendations for selected superstructure elements. Also, Chan et al. (2016) integrated BrIM and imaging techniques to detect defects such as cracking, corrosion, or settlement to create a consistent means of inspecting structures by processing images collected from the visual inspection and housed in the BrIM-asset management model.

To conclude, although the use of BrIM in the maintenance phase of bridges is increasing, integration of BrIM and optimization to enhance bridge maintenance planning has been neglected. In the following sections, a framework integrating BrIM and maintenance optimization is proposed and is applied to a real-world case study.

3. General Framework: Integrating BrIM with Maintenance Optimization

3.1. Overview

As discussed above, the integration of BrIM and bridge maintenance optimization should be implemented to economically maintain a bridge at desired performance levels while facilitating bridge maintenance management. Using Autodesk Navisworks Manage and Visual Studio software, the presented framework has been structured to integrate BrIM and bridge maintenance planning. The components of the proposed framework are a maintenance database, an inspection module, an optimization module, and a visualization module (Figure 1). The framework is coded in Visual Basic.NET (VB.NET) programming language utilizing an Application Programming Interface (API). API enables users to create add-ins to tailor and enhance a program-here, the BrIM software. In the following paragraphs, the components of the framework are discussed.

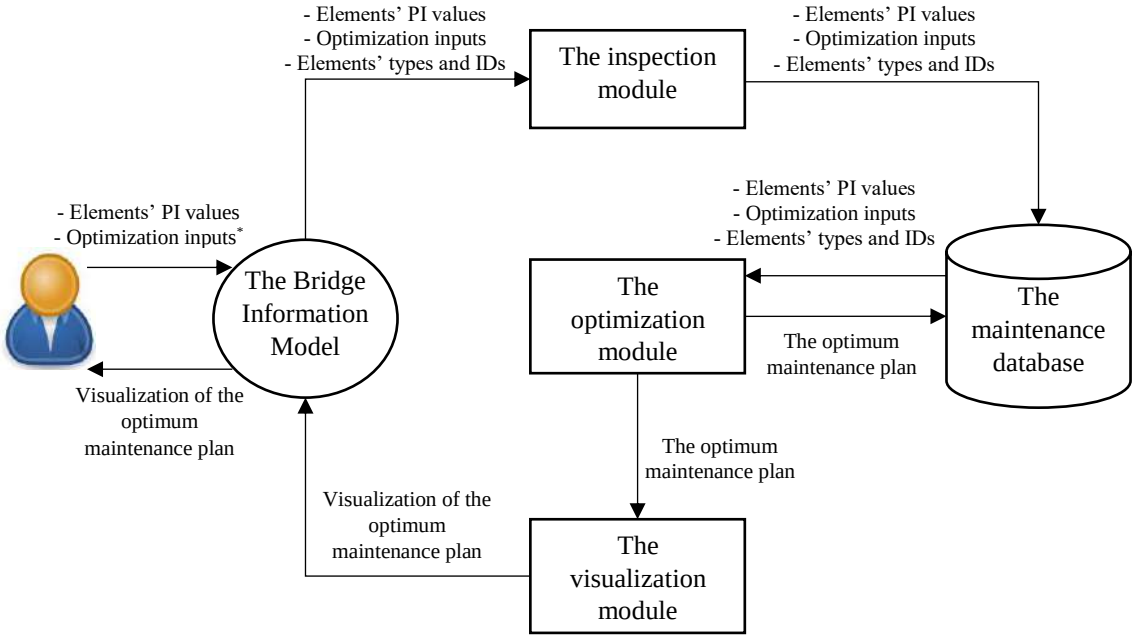

* Optimization inputs include: Elements' weights, available budget, maintenance planning horizon, inflation rate, deterioration rates, repair methods data, GA stop rules, generation length, and chromosome length

Fig. 1. The proposed framework

3.2. The Maintenance Database

The maintenance database acts as a repository in which data required for the proposed framework can be recorded and then retrieved when needed. The input data obtained by the inspection module, and the results of the framework, found by the optimization module, are recorded in the database (Figure 1).

3.3. The Inspection Module

The inspection module obtains the input data required for bridge maintenance planning from the user (Figure 1). For this purpose, this module prepares a graphical user interface by providing a VB form in the BrIM software environment (Figure 2). The provided form allows the user to enter the inspection data for each element in the BrIM environment. Additionally, the entered is saved in the maintenance database automatically through Object Linking and Embedding Database (OLEDB).

The inspection module obtains the bridge elements' types from the user. In this paper, similar to some previous studies in the literature (e.g., Yanev and Testa (1997) as depicted in Table 2), the proposed framework considers a particular weight for each element type. In the bridge maintenance optimization (which is conducted by the optimization module), elements with higher weights get a higher probability of repair. The assigned element type's weight depend on the impact of the element on the overall condition of the bridge.

Table 2. Element types and weights (based on Yanev and Testa, 1997)

Elements	Weight
Road	4
Deck	8
Barrier	1
Railing	1
Abutment	8
Pier	8
Joint	4
Sidewalk	2
Bearing	6

Another input data obtained from the user are elements Performance Index (PI) values. Various methods are utilized to evaluate condition rating in bridge inspection. For instance, the Bridge Condition Index (BCI) demonstrates the overall condition of a bridge, or the Bridge Criticality and Urgency (BCU) demonstrates the risk level of a bridge (Evans, 2018). For the evaluation and condition rating of bridge elements, suitable performance indices are needed to describe the performance of each element over time. One of the most applicable performance indices is a visual condition index. A common type of condition index is the component condition rating published by the National Bridge Inventory (NBI), which classifies the condition of an element on a 0-9 scale. A condition rating of 0, and a condition rating of 9, represent the failure and new status of the element, respectively. The weaknesses of the NBI rating is that it does not consider element condition rating, and it provides the rating only for primary elements such as the deck, superstructure, and substructure. The Michigan Department of Transportation has published a guideline providing NBI ratings within an element-level condition rating (Michigan Department of Transportation, 2016), in which each element condition rating is described qualitatively. A specific condition rating guide is presented for each element type. For illustration, the pier condition rating guide is shown in Table 3. In this study, the condition rating provided by Michigan Department of Transportation (2016) is applied as a performance index.

The maintenance planning horizon is another input parameter of the developed framework. However, various approaches have been adopted in the literature to consider the planning horizon. Some researchers have taken the bridge life as this period (Furuta et al., 2006; Kim et al., 2013). Chassiakos et al. (2005) and Elbehairy et al. (2009) have evaluated maintenance activities over a 10-year and 5-year period, respectively.

In the proposed framework, the optimum bridge maintenance plan is found for a short horizon (e.g., five years). This assumption is fully compatible with environments having high inflation rates. Also, in Iran, visual inspections are not reliable enough to be considered a basis for long-term maintenance planning. However, it should be noted that the proposed framework is flexible enough to be expanded for long-term maintenance planning.

3.4. The Optimization Module

The optimization module obtains the data required for the maintenance database (Figure 1), including the deterioration rates and the repair data. Moreover, the optimization module contains an optimization algorithm to find the optimum bridge maintenance plan. In the following, the main attributes of the optimization module are described in the following paragraphs.

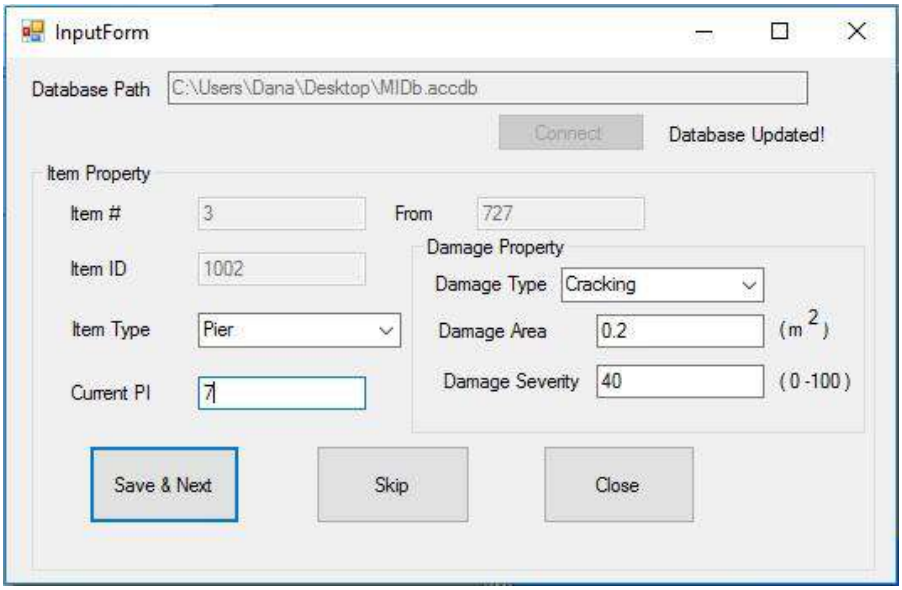

Fig. 2. Sample of Input Form

Table 3. Pier condition rating based on bridge safety inspection NBI rating guidelines

PI	Condition	Description
9	NEW	No deficiency exists in any of the structural components.
8	GOOD	All structural components are sound and functioning as designed. There may be superficial cracking or weathering of components.
7	GOOD	Insignificant cracks or moderate cracks that are sealed have occurred.
6	FAIR	Unsealed moderate-width or map cracks. Minor delamination, spalling, or efflorescence without build-up or rust staining.
5	FAIR	Moderate delamination, spalling, or efflorescence. Reinforcement exposure without section loss.
4	POOR	Considerable cracking, spalling, and efflorescence with massive build-up or rust staining exist.
3	SERIOUS	Considerable areas of spalling exposed reinforcement with section loss, or heavy rust staining.
2	CRITICAL	Deterioration has progressed to the point where the structure will not support design loads and posting emergency repairs.
1	IMMINENT FAILURE	The bridge is closed to traffic due to pier failure, but corrective action may put it back in service.
0	FAILURE	The bridge is closed due to its condition.

Because in Iran, no comprehensive bridge management system is defined and no deterioration rate is developed (Akbari and Maalek, 2017), in this study, a linear function has been employed to model the deterioration rate for each bridge element type. The relation between the current PI and future PI is shown in Eq. (1).

$$\begin{aligned}\Delta PI = PI_{at\ the\ end\ of\ period} \\ - PI_{current} \\ = a_{type} \times \Delta t\end{aligned} \quad (1)$$

where $PI_{at\ the\ end\ of\ period}$: is the PI of the element after Δt period has been elapsed. $PI_{current}$: is the current PI of the element and a_{type}: is the deterioration rate.

The proposed framework assumes that each element is repaired at most one time in the planning horizon (e.g., five years). This assumption is fully compatible because, in most agencies responsible for bridge management, a maximum of one repair activity is applied to an element in a five-year horizon.

Six repair methods have been considered for each element to define repair methods. These have been adapted from Elbehairy et al. (2009) with small modifications, including: "Do nothing;" "Semi-light repair;" "Light repair;" "Medium repair;" "Heavy repair;" and "Replace." Table 4 shows the defined repair methods for pier elements and their related costs and impact on element PI.

The cost of a repair method applied to an element is calculated as a proportion of the element construction cost. Thus, in the proposed framework, the indirect costs of repair activities, including traffic closure and mobilization costs, are not considered.

Finally, it should be noted that the framework is flexible in considering different input data in the optimization (e.g., other repair methods, repair costs, repair effects, weights, and deterioration rates).

3.5. Optimization Algorithm

The main question in a bridge maintenance optimization is to decide which elements are repaired each year of the planning horizon, and which repair methods are applied. However, a complete mathematical solution does not exist for such a Non-deterministic Polynomial-time Hard (NP-Hard) problem. Thus, a meta-heuristic algorithm is chosen to solve and to optimize the problem.

Recent related studies such as Miyamoto et al. (2000) and Elbehairy et al. (2009) utilized GA to find the optimum bridge maintenance plan. Besides, GA has shown high performance and excellent results in solving assignments and layout optimization problems. Therefore, GA is chosen for the optimization algorithm of this study.

GA performs occasional search techniques to reach optimal solutions based on natural selection, starting with an initial population. This initial population contains random genes used to encode a particular solution to a given problem. These individuals evolve to form a better population through reproduction. New individuals (offspring) are created by merging two individuals as parents using recombination (crossover). Then, some of the offspring are changed by using a mutation operator.

Table 4. The repair cost of the concrete pier (adapted from Elbehairy et al., 2009)

Repair type	Repair option	Cost	Improving PI
1	Do nothing	0%	0
2	Patch	5%	1
3	Cover repair	25%	2
4	RFT. replace	50%	3
5	Rehabilitation	75%	4
6	Replace	110%	5

Individuals are selected to form a new population-based on a tournament selection. Tournament selections sort individuals based on their fitness function and keep the population size constant by removing individuals with low fitness functions. In other words, taking *n* as the population size, all solutions with an index greater than *n* are removed after sorting. This procedure is repeated as needed to evolve the population toward the optimum solution. The iteration is stopped when the algorithm converges to an optimal solution with the required accuracy.

In this research, utilizing a single objective GA, repair activities for bridge elements have been taken as the genomes forming individuals. Scheduling and assigning repair activities to each element is conducted based on the current PI of the elements, repair types, repair costs, and available budget. In the proposed framework, the input data for the optimization process are the elements and their PI values. The optimization results are repair activities and the year in which the repair activity is applied to each element.

In the GA optimization in the framework, each chromosome is divided into two categories (Figure 3). In the first category, each genome represents the repair activity for the corresponding element. Since six types of repair activities are considered, each genome has an integer value from 0 to 5. In the second category, each genome shows the repair year of the corresponding element. Since the planning horizon contains five years, each genome has an integer value from 1 to 5.

The objective function for the optimization is adapted from (Elbehairy et al. 2009) with some small modifications, and it is formulated by Eq. (2) as below:

$$F = max\left(\frac{\sum_{i=1}^{n}\Delta PI_i \times (\frac{weight_i}{\sum weight})}{Total\ cost}\right) \quad (2)$$

where ΔPI_i: is the difference between PI of the element *i* at the end of the maintenance period and its current PI, considering deterioration (Eq. (1)) and repairs, $weight_i$: is the weight of element *i*. $\sum weight$: is the sum of the weights, $Total\ cost$: is the sum of the cost of the repair activities for all of the elements.

The optimization formulation includes the following constraints:

- The total planned cost should be lower than or equal to the total budget. The total budget is the sum of the available budget for each year based on the Net Present Value (NPV) concept.
- In each year of the planning horizon, the PI value of bridge elements should not be lower than a predefined value, because it would lead to the failure of the bridge or put it in a critical condition. Here, the predefined value is taken as 3.

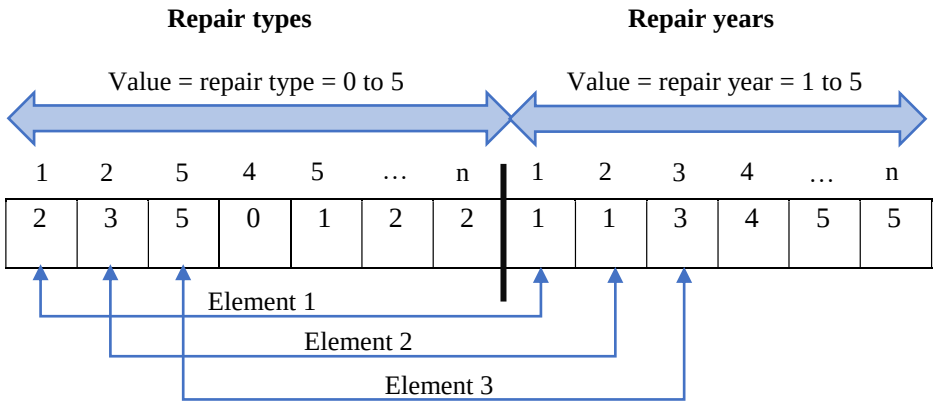

Fig. 3. The structure of the chromosome

A penalty method has been utilized in this study to prevent infeasible chromosomes in the constrained optimization problem. Penalty methods handle the problem to find feasible solutions, as the optimal solution usually happens between the feasible and infeasible regions.

3.6. The Visualization Module

After running the optimization module, the optimized repair activities are recorded in the maintenance database. Then, the PI values of elements are visualized to the user through color-coding in the BrIM environment. Also, the optimum repair method for each element is presented to the user (Figure 4). The prepared visualization tool helps bridge maintenance managers to identify the real condition of the bridge at a simple glance, which is especially beneficial for very long bridges with many elements.

4. Framework Verification

For the sake of validating the optimization module, the optimum repair activities of a hypothetical bridge are found using the provided optimization module and the Microsoft Excel Solver program. Identical inputs were used for both methods. The results obtained from the GA code and Microsoft Excel Solver program are displayed in Table 5, which includes the obtained fitness function and cost related to the optimum repair activities of the bridge. By observing the convergence in the optimization procedure of both of the optimization tools and the closeness of their final answers, it is concluded that the proposed GA code in the optimization module is valid.

5. Case Study

After validating the optimization tool, the framework is applied to a case study in the south-east of Iran. The case study bridge is a concrete bridge with a total length of 700. First, a general in-site visual inspection of the bridge was undertaken. The gathered inspection data for more than 570 identified bridge elements with an average PI value of 5 were recorded in the maintenance database using the inspection module.

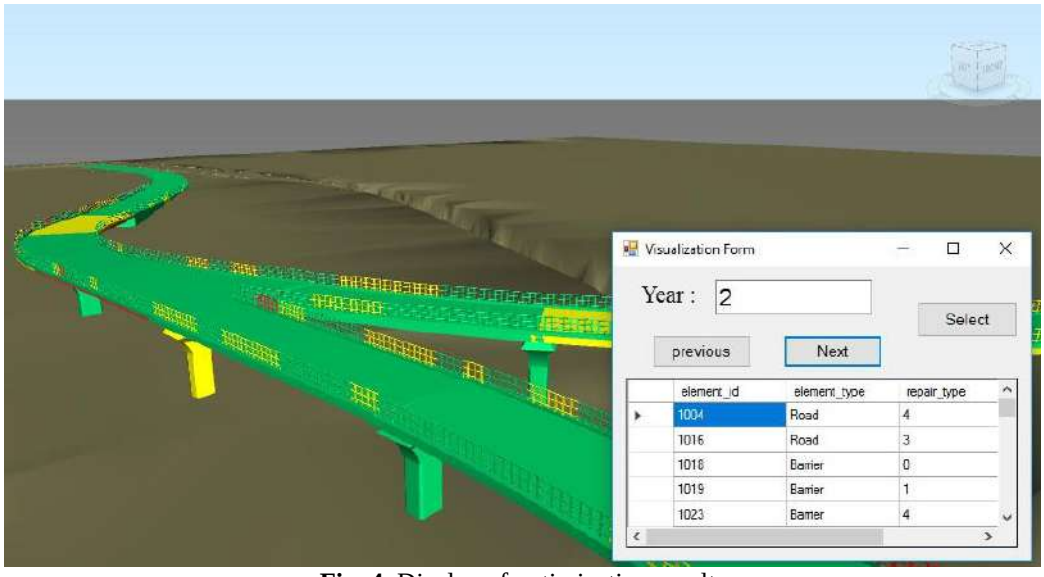

Fig. 4. Display of optimization results

Table 5. Optimization Results

Budget ($)	Optimization tool	Fitness-function	Cost ($)
20,000	API-Code	84	18,623
	Excel-Solver	77.91	19,558
22,500	API-Code	86	21,783
	Excel-Solver	82.87	22,283

Then the optimization module was run for an available yearly budget of $140,000. Maintenance period and an inflation rate are assumed to be a five-year and 20%, respectively. The total available budget was calculated based on the NPV concept, resulting in approximately $500,000 for this case. After running the optimization module, a convergence chart was obtained (see Figure 5a). After the 600th generation, the value of the fitness function converges to 3.47. Thus, the best chromosome of the 600th generation is taken as the optimum bridge maintenance plan.

In the optimization module, the user can apply the "What-if" analysis, e.g., to investigate the optimum bridge maintenance plan related to different available budgets. Figure 5b illustrates the change in the fitness function of the optimum chromosome versus NPV budget. With the increase in budget, the fitness function increases. However, increasing the NPV budget above a specified number (in this example, about $100,000) does not considerably change the fitness function of the optimum chromosome. Thus, the budget of 100,000$ is taken as the maximum required budget for bridge maintenance optimization. Finally, the PI values of bridge elements were visualized using Visualization Module. Figure 6 shows a sample report of repair methods for the case study.

Then, the optimum bridge maintenance plan is evaluated. It was observed that most of the repair activities encompass light repair. Although the average PI value of the elements was 6.8, the elements with higher weights are above the average PI. For example, the average PI of "deck" elements was 7.7, while the corresponding amount for "railing" elements was 6.7. In the end, the optimum repair activities were reported to the bridge maintenance manager, and their rationality was confirmed.

To show the merit of the proposed framework (called scenario #1), the obtained results are compared with a traditional framework (called scenario#2). In the traditional framework, sub-elements with the same type are represented by a single element (i.e., the optimum bridge maintenance plan is found in the element-level). According to Table 6, the optimum plan obtained by the first scenario results in a more excellent fitness function value than the second scenario (about 36%), which means that the current framework finds a more optimum maintenance plan than the traditional frameworks. Moreover, in the first scenario, the average of elements' PI values does not change drastically compared to the second scenario.

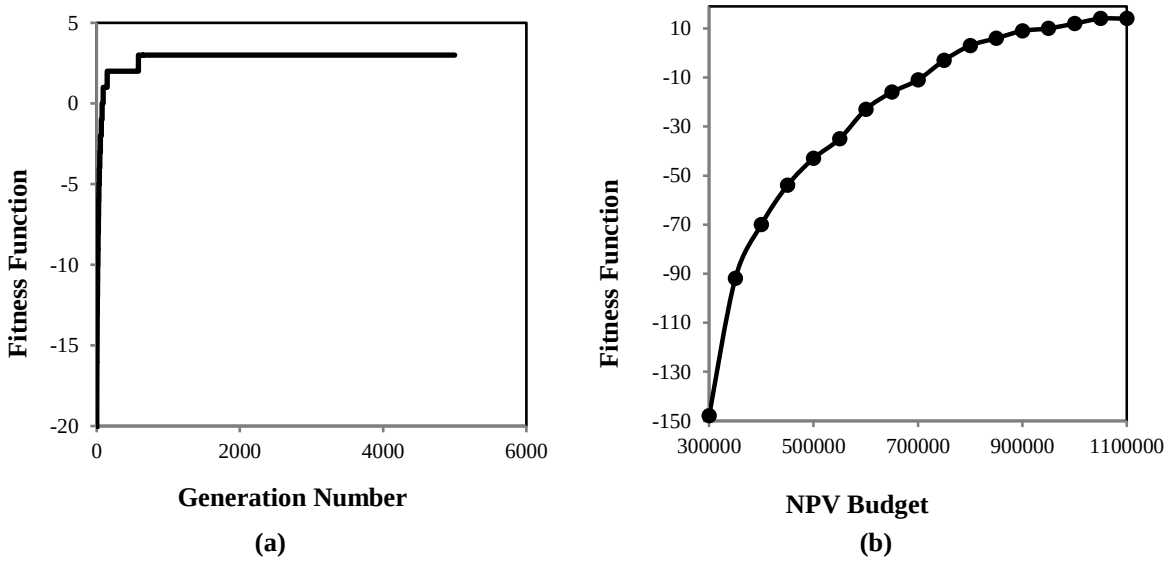

Fig. 5. The process of changing the fitness function: a) The fitness function convergence through generations; and b) Optimized Fitness Function versus different NPV budgets

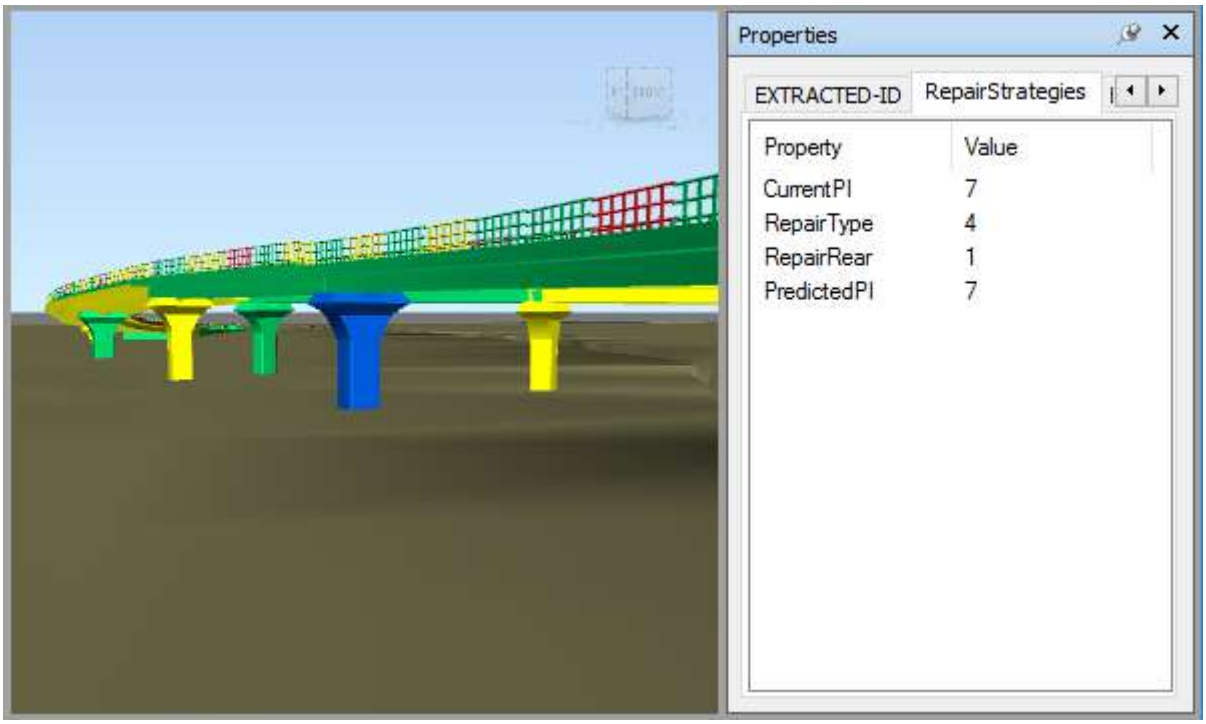

Fig. 6. Sample report of repair strategies

Table 6. Values of the bridge performance index

	Year						Fitness-function
	0	**1**	**2**	**3**	**4**	**5**	
Scenario 1	6.93	7.17	6.97	7	6.99	7.44	3.47
Scenario 2	6.73	6.73	6.23	5.73	5.23	7.76	2.54

6. Conclusions

This paper introduced a framework to enhance bridge maintenance management integrating optimization and BrIM. The proposed framework incorporated four main modules using the developed API: the maintenance database, the inspection module, the optimization module, and the visualization module. The inspection module prepared a graphical user interface, providing a VB form in the BrIM software environment that allows the user to enter the inspection data for each element, and copies the data into the maintenance database. In the optimization module, GA was applied to the information in the database to discover the optimum bridge maintenance plan. The algorithm in the optimization module considered the cost-benefit ratio as the single objective of the optimization.

After optimization, by applying the visualization module, the proposed framework visualized optimum repair activities in the BrIM model to facilitate decision making. Finally, to demonstrate the efficiency of optimization, GA results were compared with results obtained by a code based on the Excel Solver program. Also, to fully validate the proposed framework, it was applied to a real case in Iran. The obtained results were compared with the results obtained by traditional frameworks, and the capability of the developed framework in finding a more optimum bridge maintenance plan was demonstrated. The framework benefits from the use of BrIM in bridge maintenance management, and this result provides a basis for further development in this field.

7. Acknowledgments

The authors would like to sincerely acknowledge the kind supports of the Tecnosa R&D center and Engineer Reza Sadeghi in providing the BrIM model of the case study.

8. References

Akbari, R. and Maalek, S. (2017). "A road map for civil engineers towards bridge engineering through academic education and professional training", *Civil Engineering Infrastructures Journal*, 50(1), 51-73.

Alikhani, H. and Alvanchi, A. (2019). "Using genetic algorithms for long-term planning of network of bridges", *Scientia Iranica A*, 26(5), 2653-2664.

Becerik-Gerber, B., Jazizadeh, F., Li, N. and Calis, G. (2011). "Application areas and data requirements for BIM-enabled facilities management", *Journal of Construction Engineering and Management*, 138(3), 431-442.

Chan, B., Guan, H., Hou, L., Jo, J., Blumenstein, M. and Wang, J. (2016). "Defining a conceptual framework for the integration of modelling and advanced imaging for improving the reliability and efficiency of bridge assessments", *Journal of Civil Structural Health Monitoring*, 6(4), 703-714.

Chassiakos, A., Vagiotas, P. and Theodorakopoulos, D. (2005). "A knowledge-based system for maintenance planning of highway concrete bridges", *Advances in Engineering Software*, 36(11), 740-749.

Chen, H.-M. and Wang, Y.-H. (2009). "A 3-dimensional visualized approach for maintenance and management of facilities", *Proceedings of ISARC09*, Austin, Texas, USA, pp. 468-475.

Chen, W.-F. and Duan, L. (2014). *Bridge engineering handbook: Construction and maintenance*, CRC Press, Boca Raton, Florida, USA.

De Brito, J., Branco, F., Thoft-Christensen, P. and Sørensen, J.D. (1997). "An expert system for concrete bridge management", *Engineering Structures*, 19(7), 519-526.

Eastman, C., Eastman, C.M., Teicholz, P. and Sacks, R. (2011). *BIM handbook: A guide to building information modeling for owners, managers, designers, engineers and contractors*, John Wiley & Sons, Hoboken, New Jersey, USA.

Elbehairy, H., Hegazy, T. and Soudki, K. (2009). "Integrated multiple-element bridge management system", *Journal of Bridge Engineering*, 14(3), 179-187.

Evans, D. (2018). "Bridge inspection report, 2018 Inspection Year", Government of Prince Edward Island, Available at: https://www.princeedwardisland.ca/sites/default/files/publications/bridgeinspection2018.pdf. (Access Date: 2020 June 10)

Farran, M. and Zayed, T. (2015). "Fitness-oriented multi-objective optimisation for infrastructures rehabilitations", *Structure and Infrastructure Engineering*, 11(6), 761-775.

Frangopol, D.M. and Liu, M. (2007). "Maintenance and management of civil infrastructure based on condition, safety, optimization, and life-cycle cost", *Structure and Infrastructure Engineering*, 3(1), 29-41.

Frangopol, D.M. and Soliman, M. (2016). "Life-cycle of structural systems: Recent achievements and future directions", *Structure and Infrastructure Engineering*, 12(1), 1-20.

Furuta, H., Kameda, T., Fukuda, Y. and Frangopol, D.M. (2004). "Life-cycle cost analysis for infrastructure systems: Life cycle cost vs. safety level vs. service life", *Life-cycle Performance of Deteriorating Structures: Assessment, Design and Management*, Lausanne, Switzerland, pp. 19-25.

Furuta, H., Kameda, T., Nakahara, K., Takahashi, Y. and Frangopol, D.M. (2006). "Optimal bridge maintenance planning using improved multi-objective genetic algorithm", *Structure and Infrastructure Engineering*, 2(1), 33-41.

Ghadiri Mohghaddam, D. (2014). "Framework for Integrating Bridge Inspection Data with Bridge Information Model", MSc. Dissertation, Concordia University, Available at: https://spectrum.library.concordia.ca/978607/ (Access Date: 2020 June 10).

Gholami, M., Sam, A.R.B.M. and Yatim, J.M. (2013). "Assessment of bridge management system in Iran", *Procedia Engineering*, 54, 573-583.

Hammad, A., Zhang, C., Hu, Y. and Mozaffari, E. (2006). "Mobile model-based bridge lifecycle management system", *Computer-Aided Civil and Infrastructure Engineering*, 21(7), 530-547.

Hong, T. and Hastak, M. (2007). "Evaluation and determination of optimal MR&R strategies in concrete bridge decks", *Automation in Construction*, 16(2), 165-175.

Huang, Y.-H. and Huang, H.-Y. (2012). "A model for concurrent maintenance of bridge elements", *Automation in Construction*, 21, 74-80.

Ilter, D. and Ergen, E. (2015). "BIM for building refurbishment and maintenance: current status and research directions", *Structural Survey*, 33(3), 228-256.

Kim, S., Frangopol, D.M. and Soliman, M. (2013). "Generalized probabilistic framework for optimum inspection and maintenance planning", *Journal of Structural Engineering*, 139(3), 435-447.

Lin, Y.-C. and Su, Y.-C. (2013). "Developing mobile-and BIM-based integrated visual facility maintenance management system", *The Scientific World Journal*, 2013(7), 124249.

Liu, R. and Issa, R. (2012) "Automatically updating maintenance information from a BIM database", *Proeedings of International Conference on Computing in Civil Engineering*, Florida, USA, pp. 373-380.

Marzouk, M. and Abdelaty, A. (2014). "BIM-based framework for managing performance of subway stations", *Automation in Construction*, 41, 70-77.
Marzouk, M. and Hisham, M. (2011). "Bridge information modeling in sustainable bridge management", *Proceedings of ICSDC*, Lawrence, Kansas, USA, pp. 457-466.
McGuire, B., Atadero, R., Clevenger, C. and Ozbek, M. (2016). "Bridge information modeling for inspection and evaluation", *Journal of Bridge Engineering*, 21(4), 04015076.
Mirzaei, Z. and Adey, B.T. (2018). "Determination of the most sustainable bridge work programs through the improved structure level considerations", *Structure and Infrastructure Engineering*, 14(8), 1123-1139.
Miyamoto, A., Kawamura, K. and Nakamura, H. (2000). "Bridge management system and maintenance optimization for existing bridges", *Computer-Aided Civil and Infrastructure Engineering*, 15(1), 45-55.
Miyamoto, A. and Motoshita, M. (2015). "Development and practical application of a bridge management system (J-BMS) in Japan", *Civil Engineering Infrastructures Journal*, 48(1), 189-216.
Morcous, G. and Lounis, Z. (2005). "Maintenance optimization of infrastructure networks using genetic algorithms", *Automation in Construction*, 14(1), 129-142.
Motamedi, A., Hammad, A. and Asen, Y. (2014). "Knowledge-assisted BIM-based visual analytics for failure root cause detection in facilities management", *Automation in Construction*, 43, 73-83.
NIBS (2008). "United States national building information modeling standard, version 1, Part 1: Overview, principles, and methodologies", Nantional Institute of Building Sciences, USA.
Nili, M.H., Zahraie, B. and Taghaddos, H. (2020). "BrDSS: A decision support system for bridge maintenance planning employing bridge information modeling", *Smart Structures and Systems*, 26(4), 533-544.
Sahrapeyma, A. and Hosseini, A. (2013). "Strategic planning for the national bridge stock of Iran", *Civil Engineering Infrastructures Journal*, 46(1), 51-68.
Michigan Department of Transportation (2016). "NBI rating guideline", Available at: https://www.michigan.gov/documents/mdot/BIR_Ratings_Guide_Combined_2016-3-15_517075_7.pdf (Access Date: 2020 June 5).
Yanev, B. and Testa, R.B. (1997). "Life-cycle performance of bridge components in New York City", *Recent Advances in Bridge Engineering*, 385-392.

Civil Engineering Infrastructures Journal 2021, 54(2): 365-380
DOI: 10.22059/CEIJ.2020.300273.1663

RESEARCH PAPER

Waffle Slab Behavior Subjected to Blast Load

Gorji Bandpey, Gh.[1], Abdollahzadeh, G.R.[2]* and Firoozjaee, A.R.[3]

[1] Ph.D. Student, Faculty of Civil Engineering, Babol Noshirvani University of Technology, Babol, Iran.
[2] Professor of Civil Engineering, Babol Noshirvani University of Technology, Babol, Iran.
[3] Associate Professor, Faculty of Civil Engineering, Babol Noshirvani University of Technology, Babol, Iran.

Received: 02 Apr. 2020; Revised: 13 Jun. 2020; Accepted: 29 Jun. 2020

ABSTRACT: Over the previous years, the use of structure roof systems which can be implemented with long column spans has been welcomed by manufacturers. One of the most widely used roofs is the waffle slab system. Therefore, by reviewing previous studies in the field of roof collapse in reinforced concrete structures under blast, the absence of studies on the performance of waffle slab and comparing its behavior with blast affected RC slabs is observed. Laboratory simulation of this problem requires high cost, high accuracy in model building and much time. In this study, after preliminary model validation with experimental research and two numerical studies in LS-DYNA software, the behavior of waffle slab subjected to blast load and compare its performance with RC slab are investigated. It should be noted that because the blast load is applied to the structure in a very short time, it has a high loading rate. Therefore, the strain rate effects on concrete and reinforcement are considered for achieving real material behavior. The identical volume of concrete and reinforcement used in all roofs is considered in order to evaluate and compare the behavior of the roofs reasonably. Then, the effect of the geometric dimension of waffle molds and the effect of the supporting condition on the Waffle slab responses are studied. Other investigated parameter in this study includes the effect of concrete compressive strength on the behavior of roof under blast load. The mass of the explosive and its distance from the roof surface are other parameters considered in this study. The effect of bar size on the behavior of the roof is also investigated. The results of this study are presented as diagrams and tables showing that given the same volume of concrete and reinforcement in the RC slab and the waffle slab, the central displacement of Waffle slab is reduced to a desirable level. This shows the better behavior of the waffle slab in comparison with the RC slab with the same volume of material under the blast load.

Keywords: Blast Load, Central Displacement, Geometrical Dimension of the Waffle, RC Slab, Strain Rate, Waffle Slab.

* Corresponding author E-mail: g.abdollahzadeh@ymail.com

1. Introduction

Structures are generally designed on the basis of conventional loads, including dead, live, snow, wind and seismic loads, and unconventional loads such as impact, fire and blast are not considered in structural analysis and design. Therefore, during the exposure of the structure to such unusual loads, there would be a great deal of destruction and damage. An example of such damage in recent years in some structures around the world is the twin towers of the World Trade Organization in 2001 collapsed in effect of aircraft collisions with structures followed by blasts and fires. Other structural damage caused by unconventional loads can be attributed to the overall demolition of the Plasco building in Iran in 2017, part of which has been damaged by fire and consequently the loss of strength to roof elements.

One of the most effective elements in controlling the failures caused by unconventional loads is the structural roof that in the case of losing loading capacity of the roof system will lead to the extension of failure in other floors. Many studies have been conducted by researchers on materials as well as blast loads. Steel and concrete are materials that are widely used in construction projects. Concrete has a better strength to blast load than other materials. Therefore, the behavior of reinforced concrete slab due to abnormal loads such as blast is essential to study. Numerical and experimental studies carried out in this area over the last years.

Wang et al. (2013) in an experimental and numerical study, modeled a square reinforced concrete slab under near-field blast. In this study, the mechanism of slab failure under different amounts of explosive was investigated at the distance of 0.4 m from slab surface. Since the blast phenomenon is a type of high-speed dynamic load, they considered the strain rate effects on the behavior of concrete and steel materials. Results of the numerical and experimental models showed good agreement in this study. This study also showed that as the explosive content increased, the failure mode changed from the whole slab to local failure.

Zhao and Chen (2013) conducted a dynamic analysis of the failure mechanism of a reinforced concrete slab under blast load. In this study, they considered dimensions of 1000 × 1000 × 400 mm for reinforced concrete slab with three different amounts of explosives and modeled in LS-DYNA software and compared the results of this numerical study with existing experimental studies. This research was able to estimate the failure mechanism of the slab under blast load, and the result of this study showed that the destruction mechanism would change as the explosive volume changed.

Shuaib and Daoud (2015) investigated the failure mode and deformation of square concrete slabs due to blast load. The slabs studied are two-end fixed. They assumed the distance between the blast center and the center of the slab constant, but the weight of the explosive varied in three modes. They also modeled their studies numerically in LS-DYNA software. Two KCC and Winfrith behavioral models were used to model concrete materials. In this study, the blast load was applied to the slab with Lagrangian method. To ensure the validity of this study, the results were compared with an experimental study. Both concrete behavior models (KCC and Winfrith) showed good estimates of actual concrete behavior and slab deformation. To investigate the slab failure mode, the KCC behavior of the concrete was optimally modeled by bending cracks, but this behavior model was not capable to model the local shear behavior, because the Lagrangian method is not able to consider the interaction of open air and concrete slab.

In the RC structures, the concrete compressive strength is important in the behavior of structural element under blast load. So, Abdollahzadeh et al. (2017) considered two models based on Gene Expression Programming (GEP). These

models predict compressive strength of High Strength Concrete (HSC). They considered composition of HSC, as a mixture of six components (water, cement, super-plastisizer, silica fume, fine aggregate and coarse aggregate). The target of the prediction is the 28-day compressive strength value. Results of this study show that the GEP is a good method for the prediction of compressive strength amounts of HSC concerning to the outcomes of the training.

Pandey et al. (2006) investigated the failure of concrete thin slabs against blast load. In this study, they investigated the effect of deterioration and reduction of hardness of material on concrete behavior and presented the mechanism of possible failure in their research. The results of this study were validated with numerical models that showed good agreement.

The missing of an element can lead to the beginning of progressive collapse in a structure. So, finding the location of this element is very important. Therefore, Kheyroddin et al. (2019) investigated about this topic and following GSA and DoD guidelines for finding the key element of symmetric structures with different floor heights, sensitivity analysis was modified. Results of this study showed that the location of the key element was different in the plan and height of the structure in structures with different floor heights.

Eltehaway (2009) conducted a study to investigate the performance of reinforced concrete slab under the impact loads and the effect of Ferro cement against slab surface damage. The result of this research showed that the Ferro cement has high ductility and high strength to dynamic loads including impact. Also, by increasing slab thickness, energy absorption and slab strength will increase.

Augustsson and Harenstam (2010) presented two simplified methods for designing beams and reinforced concrete slabs subjected to blast loads. These two methods include manual calculation based on energy equations and numerical calculation based on motion equations. Both methods proposed in this study assumed that the structure can be simulated as a degree of freedom system and are valid for elastic, plastic and elastoplastic responses. The result of this study was compared with the result of ADINA finite element software and its validity was confirmed.

Chen et al. (2015) studied the dynamic behavior of a rectangular reinforced concrete beam with simple support under blast load. LS-DYNA finite element software was used for this purpose. Numerical simulation was performed in this study for four groups of reinforced concrete beams. In order to study the behavior of this beam, the maximum displacement, concrete cracking, rebar stress and shear stress of the concrete near the support were investigated and the results were compared with an experimental study.

Xu and Lu (2006) performed the effect of blast on reinforced concrete walls in an analytical study. For this purpose, the wave theory was studied and the strain rate effects on concrete were considered. The studied scenarios included the distance and mass of the explosive. The results showed a good verification with the experimental results related to this research.

Yang et al. (2019) studied the effects of blast on rubber reinforced concrete slab. They considered four types of rubber concrete with different rubber ratios in concrete compositions. This study showed that the tensile failure area of slab concrete in rubber concrete is far less than that of conventional concrete subjected to blast. Finally, rubber-reinforced concrete structural elements exhibited a very favorable behavior against the energy released from large blast.

Zhao et al. (2019) studied the effect of blast on composite slab consisting of concrete, steel plate and stud. For this purpose, three types of slab affected by contact blast were studied experimentally and the mechanism of failure, maximum displacement of slab and its dynamic

responses were investigated. In order to confirm the experimental results, these slabs were simulated in finite element software that the agreement between the failure mechanism and the maximum displacement of the slab indicated the accuracy of the experimental model in this study. The results showed that the composite slab behavior is much better than the conventional concrete slab system under contact blast due to the use of steel plate.

Meng et al. (2019) experimentally and numerically studied environment-friendly geopolymer-reinforced concrete slab under the near-field blast. One of the important aims of this study was investigating the mechanism of destruction and comparing it conventional concrete slab. The results of this study showed that the bars in this type of slab experienced less damage than conventional slabs.

On the other hand, the progressive collapse in the structure will be occur if the slab capacity is lost. Regarding the topic of progressive collapse, Zahrai and Ezoddin (2014) presented an analytical method for calculating progressive collapse potential in typical concrete buildings. They compared four methods for progressive collapse analysis by studying 5 and 10-story intermediate moment-resistant reinforced concrete frame buildings. To evaluate the behavior of RC buildings, three column-removal conditions were performed. Their results showed that dynamic analysis procedures pre sent more accurate results to be performed for progressive collapse determination yielded.

By reviewing previous studies, it is concluded that the alternative load path method is suitable for progressive collapse due to explosion. Tavakoli and KiaKojouri (2015) numerically investigated the steel moment resisting frames for evaluation of fire-induced and threat-independent progressive collapse potential. In this study, number of floors and the location of initial failure were considered. Two different mechanisms were assumed in fire-induced and threat-independent progressive collapse. While column removal alternative load paths play major role in threat-independent, the weight of the structure above the failure region is the most important parameter in fire-induced progressive collapse.

Rezaie et al. (2018) studied about sudden removal of vertical load-bearing elements such as columns in reinforced concrete buildings structures with different floor plans such as floor plans with and without torsional irregularity as well as geometrical regular and irregular floor plans. They considered column sensitivity and displacement sensitivity indexes to compare different cases of column removal in each model. One of the results of this study was that removing shear walls led to much more critical scenarios than removing columns in building with shear walls. As another result, removing the internal columns was less critical than the external columns.

In recent years, there is no research on the behavior of waffle roofs subjected to the blast loads. The use of waffle roof systems with the potential of implementation with columns at high distances has recently been interested by manufacturers. Therefore, this study will investigate the behavior of waffle slab under blast load and compare its performance with that of conventional reinforced concrete slab. For this purpose, after presenting the equations related to the blast load and also developing the relationship between the behavior of concrete and reinforcement materials, the model validation will be investigated with and experimental research and two numerical studies in LS-DYNA software. It should be noted the blast load is applied to the structure in a very short time and the loading rate is high. Therefore, the strain rate effects on concrete and reinforcement are taken into account for achieving real material behavior. The following is intended to compare the behavior of slabs and the volume of concrete. The reinforcement materials in all slabs are similar and then the effect of the geometric dimensions of the waffle molds will be

examined. The other case which is examined is the effect of supporting condition on the waffle slab response. The effect of concrete compressive strength on the behavior of the slab under blast load is also studied. The mass of the explosive and its distance from the slab surface will be other parameters considered in this study. Besides the effect of bar size on slab behavior is examined.

2. Introducing the Blast Load

The blast phenomenon is caused by the rapid release of large amounts of energy in a confined space. In the engineering literature, researchers classify the blast in terms of location into two categories of indoor and outdoor blasts. The sudden release of energy creates a pressure wave in the environment that gradually decreases with a short period of time (Figure 1).

After the occurrence of blast in a short time, the pressure will reach its maximum. In the literature, the pressure due to the pressure difference between the blast pressure and the atmospheric pressure is called pre-pressure. Over the time, the pressure gradually decreases until the blast pressure reaches the atmospheric pressure and this decreasing trend will continue and so-called suction will occur. Thus, the pressure-time diagram includes both positive and negative zones (Figure 2).

A criterion is introduced for determining the degradation severity as a mass-distance scale (Z_G) as follows:

$$Z_G = \frac{R}{\sqrt[3]{M}} \quad (1)$$

where R: is the distance from the blast point and M: is the mass of the explosive equivalent to TNT. The ambient air under the blast is considered an Expression of State (EOS) model. The pressure due to the blast in the environment is calculated from the following relation:

$$P = (\gamma - 1)\rho e \quad (2)$$

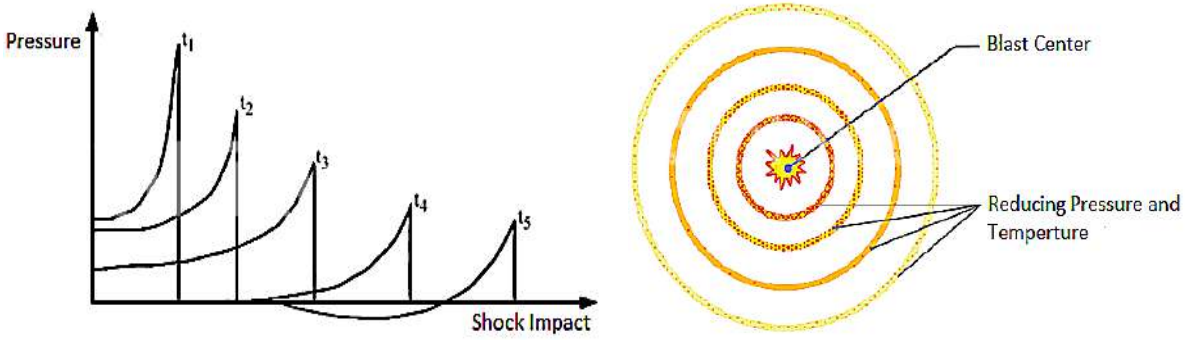

Fig. 1. Reduction of blast pressure over distance

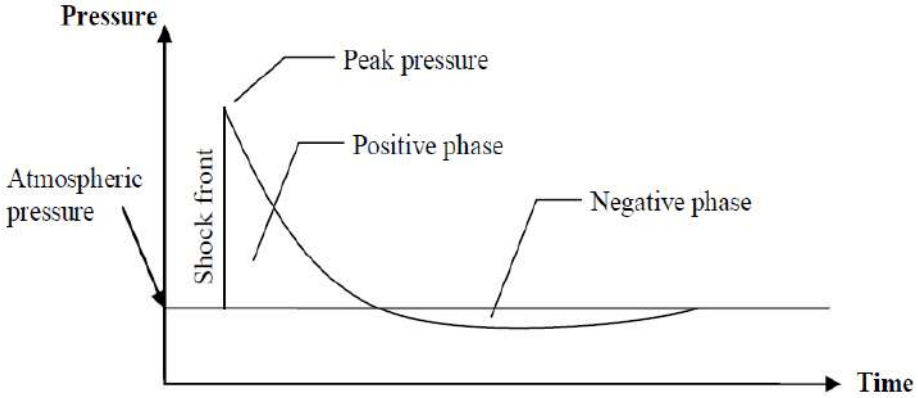

Fig. 2. Idealized shockwave pressure in time (Augustsson and Harenstam, 2010)

where, γ: is the constant value, ρ: is the density of air and e represents the internal energy. In this study, standard air constants are extracted from the library values in (LS-DYNA, 2006) where ρ = 1.225 kg/m^3 and $\gamma = 14$. The initial internal energy of the air in the above equation is e = 2.068×10^5 KJ/kg. Explosives such as TNT are considered to be the Jones-Wilkins-Lee EOS model, which represents the pressure resulting from the chemical energy of a blast and is calculated as follows:

$$P = A\left(1-\frac{\omega}{R_1V}\right)e^{-R_1V} + B\left(1-\frac{\omega}{R_2V}\right) e^{-R_2V} + \frac{\omega E}{V} \quad (3)$$

where P: represents the hydrostatic pressure, V: is the specific volume of TNT, and A, B, R_1, R_2 and ω: are constant values of the material. These constant values have been calculated for several blast samples from dynamic laboratory studies, which are referred to in (LS-DYNA, 2006). In this study, the values A, B, R_1, R_2 and ω are 3.7377 × 10^5 Mpa, 4.15, 3.747 × 10^3 Mpa, 0.9 and 0.35 respectively, for TNT explosives.

3. Characteristics of Materials

In order to obtain the most accurate results, the failure of the material such as concrete under the dynamic load of the blast should be appropriately modeled. Blast loads will affect the behavior of the materials because they are applied to the structure in a very short time and have high loading rates. Therefore, the strain rate effects and inertia on the behavior of concrete and rebar should be taken into account because the higher strain rate increases the strength of such materials (Chen et al., 2015).

The concrete stress tensor is defined as sum of the hydrostatic stress tensor and the deviated stress tensor. The hydrostatic tensor shows the volume changes of the concrete and the deviated tensor shows the concrete deformation (Zhao and Chen, 2013).

In this study, the dynamic failure model of Riedel, Hiermaier and Thoma (RHT) for concrete has been considered. This model is very suitable for studying dynamic behavior of concrete. The RHT model is generally used for brittle materials and includes several features for various mechanisms in the field, including strain hardening, strain rate hardening, pressure hardening, third invariant dependence for tensile and compressive meridians and cumulative damage (strain softening). Conjunction with the exiting tensile crack softening algorithm can be used in this model. The p-α equation of state for volumetric compaction is also considered in this model. As can be seen in Figure 3, the material has three strength surfaces including an elastic limit surface, a failure surface, and the remaining strength surface for the crushed material. For the elastic strength surface, a threshold often exists (Wang et al., 2013).

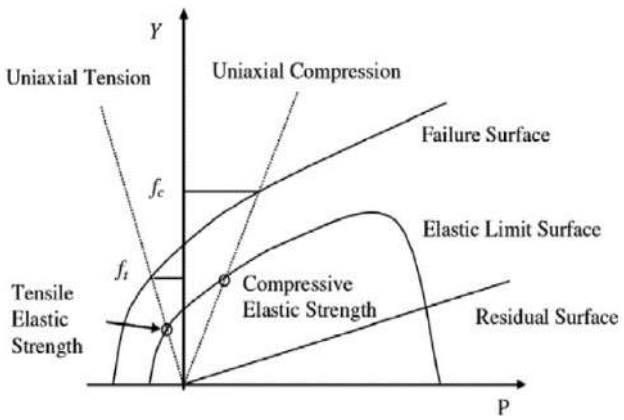

Fig. 3. Ultimate strength, yield strength and residual strength surfaces (Wang et al., 2013)

In Figure 3, *Y*: is the failure surface and defined as a function of pressure *P*, strain rate $\dot{\varepsilon}$ and the load angle θ.

$$Y_f = Y_{(p)}.R_{(\theta)}.F_{RATE(\dot{\varepsilon})} \quad (4)$$

where $Y_{(p)} = f_c\left[A(p^* - p^*_{spall}F_{RATE(\dot{\varepsilon})})^N\right]$, with f_c: being the compressive strength, *A*: the failure surface exponent and p^*: the pressure normalized by f_c, $p^*_{spall} = p^*(f_t / f_c)$. $F_{RATE(\dot{\varepsilon})}$: shows the strain rate function. $R_{(\theta)}$: represents the third invariant dependency of the model as a function of a meridian ratio Q_2 and the second and third stress invariants.

Figure 4 shows the compressive meridian on the stress π plane and the tensile. From the failure surface, the elastic limit surface is scaled as (Wang et al., 2013).

$$Y_e = Y_f.F_e.F_{CAP(p)} \quad (5)$$

where $F_{CAP(p)}$: is a function that limits the elastic deviatoric stresses under hydrostatic compression which is varying within the range of 0 to 1 for pressure. In this range, value 0 is initial compaction and 1 is solid compaction pressures. F_e: is the ratio of the elastic strength to failure surface strength. A residual (frictional) failure surface is defined as following equation (Wang et al., 2013).

$$Y^*_{residual} = B.p^{*M} \quad (6)$$

where *B*: is the constant of residual failure surface and *M*: is the exponent of residual failure surface. It should be explained that additional plastic straining of the material results in damage and strength reduction after the hardening phase. Damage in the material is accumulated by:

$$D = \sum \frac{\Delta\varepsilon_p}{\varepsilon_p^{failure}} = \sum \frac{\Delta\varepsilon_p}{D_1(p^* - p^*_{spall})^{D_2}} \quad (7)$$

where D_1 and D_2: are damage constants and the post-damage failure surface is then interpolated by:

$$Y^*_{fracture} = (1-D)Y^*_{failure} + DY^*_{residual} \quad (8)$$

and the material post-damage shear modulus is interpolated via the following equation:

$$G_{fracture} = (1-D)G_{initial} + DG_{residual} \quad (9)$$

where $G_{initial}$, $G_{residual}$, $G_{fracture}$: are the shear modulus. In the present work, the material constant is based on the typical data for concrete, which compressive strength, f_c = 39.5 Mpa and the material parameters are: shear modulus, *G* = 0.28 Mpa; reference density, ρ = 2.55 g/cm^3; tensile strength, f_t = 4.2 Mpa; and *A*, *N*, *B*, *M*, D_1, D_2 and $\varepsilon_f^{\min}$ are 1.6, 0.61, 0.7, 0.8, 1, and 0.0008, respectively. Also, the failure strain is $\varepsilon_f^{\min} = 0.001$.

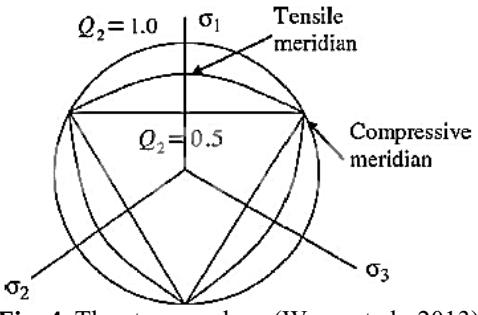

Fig. 4. The stress π plane (Wang et al., 2013)

Specifications of materials in software should be close to the behavior of materials in experimental research. The Abaqus software considers three behavioral models for concrete, including Concrete Smeared Cracking, Brittle Cracking, and Concrete Damaged Plasticity model. In this study, the Concrete Damaged Plasticity model is used because it is close to the actual concrete behavior model. The coefficient of increase of dynamic compressive and tensile strength of concrete is calculated using Eqs. (10-13) (Chen et al., 2015).

$$CDIF = \frac{f_c}{f_{cs}} = \left(\frac{\dot{\varepsilon}}{\dot{\varepsilon}_{cs}}\right)^{1.026\alpha} \quad if \ \dot{\varepsilon} \le 30s^{-1} \qquad (10)$$

$$CDIF = \frac{f_c}{f_{cs}} = \gamma(\dot{\varepsilon})^{1/3} \quad if \ \dot{\varepsilon} > 30s^{-1} \qquad (11)$$

$$TDIF = \frac{f_t}{f_{ts}} = \left(\frac{\dot{\varepsilon}}{\dot{\varepsilon}_{ts}}\right)^{\delta} \quad if \ \dot{\varepsilon}_{td} \le 1s^{-1} \qquad (12)$$

$$TDIF = \frac{f_t}{f_{ts}} = \beta = \left(\frac{\dot{\varepsilon}}{\dot{\varepsilon}_{ts}}\right)^{1/3} \quad if \ \dot{\varepsilon}_{ts} > 1s^{-1} \qquad (13)$$

where f_c: is the dynamic concrete compressive strength at strain rate of $\dot{\varepsilon}$, f_{cs}: represents the concrete static compressive strength at strain rate of $\dot{\varepsilon}_{cs}$, $\log\gamma = 6.156\alpha - 0.49$, $\alpha = 1/(5+3f_{cu}/4)$ and f_{cu}: denotes the compressive strength of the cube concrete sample in MPa. f_t: is the concrete dynamic tensile strength at the strain rate of $\dot{\varepsilon}$ is assumed to be within the range of $1-S\ 10^{-6}\ S^{-1}$ to $160\,S^{-1}$, f_{ts} the concrete tensile strength at the strain rate of $\dot{\varepsilon}_{ts}$, $\log\beta = 6\delta - 2$, $\delta = 1/(1+8f_c'/f_{co}')$ and f_{co}' is equal to 10 MPa (Chen et al., 2015).

Johnson-Cook behavior model has been considered for rebar because it is suitable for studying the behavior of material under high strain rate and heat. This model defines rebar yield stress *Y* as (Johnson and Cook, 1983):

$$\sigma = \left[A + B\varepsilon_p^n\right]\left[1 + C\ln\frac{\dot{\varepsilon}_p}{\dot{\varepsilon}_0}\right]\left[1 - T_H^m\right] \qquad (14)$$

where, ε_p: represents the effective plastic strain, $\dot{\varepsilon}_p^* = \frac{\dot{\varepsilon}}{\dot{\varepsilon}_0}$ is equal to the effective plastic strain rate for $\dot{\varepsilon}_0 = 1s^{-1}$, $T_H = (T - T_{room})/(T_{melt} - T_{room})$, where T_{room} represents the room temperature and T_{melt}: is the melting temperature and also *A, B, C, n* and *m*: are the five material constant (Johnson and Cook, 1983). The density of rebar used in this study is equal to ρ = 7.85 g/cm^3, bulk modulus is *K* = 159 Gpa and shear modulus is *G* = 81.8 Gpa. The coefficient of increase of the dynamic strength of the steel (*DIF*) is calculated from the Eq. (15), where f_y represents the yielding strength of the rebar in MPa.

$$DIF = (\dot{\varepsilon}/10^{-4})^{\alpha}$$
$$\alpha = 0.074 - 0.04\,f_y/414 \qquad (15)$$

4. Modeling

In this study, simulation of reinforced concrete slab and waffle slab under blast load was performed in ABAQUS software. Solid element was used for modeling concrete and Concrete Damaged Plasticity model was used for concrete material behavior in software. In this model, the effects of strain rate and crack on concrete elements are considered. Beam element was used in the rebar and also Johnson-Cook plastic model capable of considering strain rate was used for the behavior of steel material. To model the contact between the concrete and the reinforcements, it was assumed that the reinforcements were buried in the concrete. Therefore, the Embedded region model was used in the software to contact between the two materials. In the blast loading, the loading speed is high and the slip between the concrete and the reinforcements can be neglected. This behavioral model does not take into account the slip between the two materials (Xu and Lu, 2006).

To ensure the accuracy of the simulation performed in ABAQUS software, the results of the experimental model performed by Wang et al. (2013) and the numerical models performed in LS-DYNA software by Zhao et al. (2013) and (Shuaib and Daoud (2015), which a 1000×1000×40 mm reinforced concrete slab, have been compared with the present study. In these studies, the reinforcements are meshed in a row with a diameter of 6 mm at 75 mm intervals. The concrete cover is 20 mm and the compressive strength, tensile strength and modulus of elasticity of concrete are

39.5 MPa, 4.2 MPa and 28.3 Gpa, respectively. The yield stress of the reinforcement is also assumed to be 600 MPa and its modulus of elasticity is 200 Gpa. Figure 5 shows an image of the experimental and numerical model made in Wang et al. (2013), Zhao and Chen (2013) and Shuaib and Daoud (2015).

An illustration of the reinforced concrete slab studied has been shown in Figure 6. As shown in this figure, the explosive is located above the slab 400 mm from the center of the slab and its mass is 0.46 kg.

Figure 7 illustrates an image of the blast load applied to the RC slab at the RP-1 point as a CONWEP blast model in ABAQUS software. Also, the deformed RC slab is presented in Figure 8.

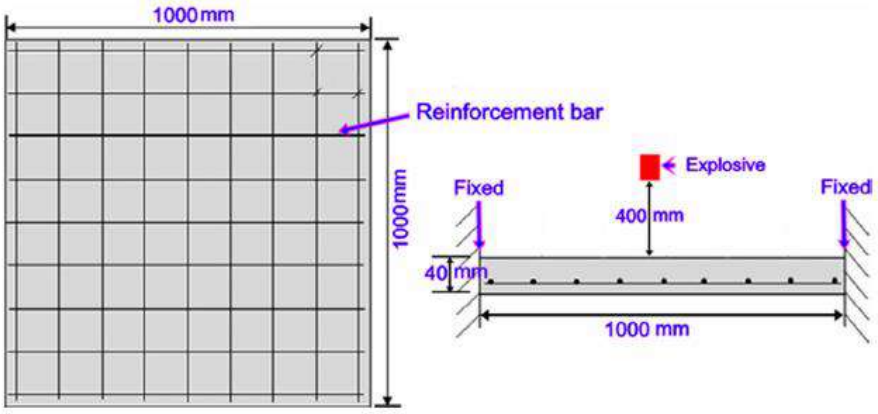

Fig. 5. The geometry of the reinforced concrete slab studied in experimental and numerical references (Wang et al., 2013; Zhao and Chen, 2013; Shuaib and Daoud, 2015)

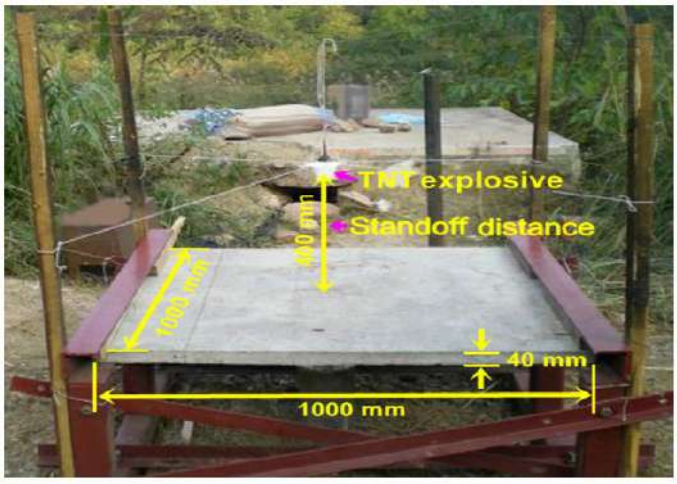

Fig. 6. Laboratory specimen of reinforced concrete slab in reference (Wang et al., 2013)

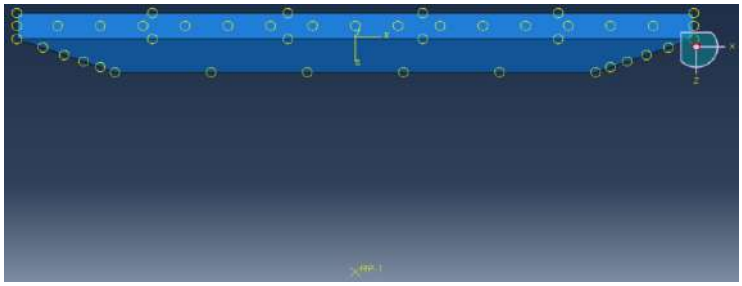

Fig. 7. Applying the blast load to the RC slab at RP-1 point

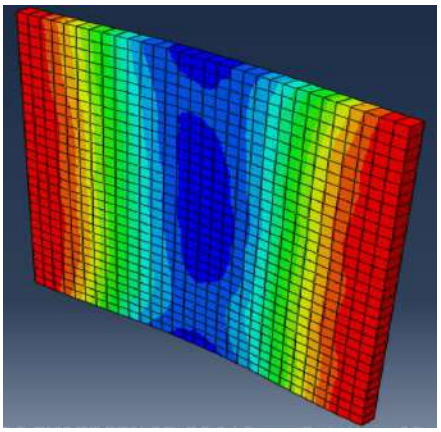

Fig. 8. Deformation of RC slab after blast loading

As is observed in Figure 9, the magnitude of the slab center displacement due to the blast load has a negligible difference with the results obtained from Wang et al. (2013), Zhao and Chen (2013) and Shuaib and Daoud (2015), indicating the accuracy of the modeling performed in ABAQUS software. Now, after verifying the accuracy of the modeling, the behavior of the waffle slab under the blast load is investigated. For this purpose, in order to compare the behavior of the waffle slab with the RC slab subjected to the blast load, a RC slab with dimensions of 5000×5000×200 mm is first considered. The reinforcement in this slab is in the form of mesh in a row with 12 mm diameter and 300 mm intervals. The specifications of the concrete and reinforcement are the same as in the previous slab. In order to uniformize the conditions in terms of volume of concrete and reinforcement materials used in RC slab and waffle slab, the geometrical characteristics of the desired waffle slab are as in Figure 10. The three-dimensional image in ABAQUS software can be seen in Figure 11. It should be noted that the characteristics of the material used in the waffle slab are the same as in the previous specifications.

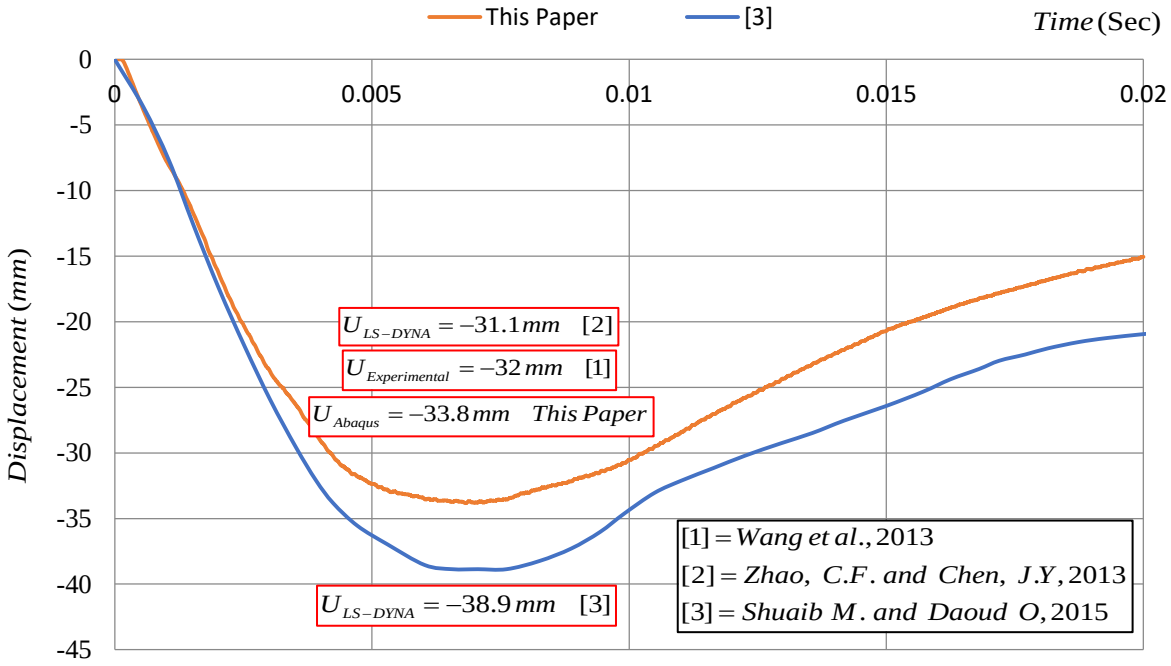

Fig. 9. Comparison of slab center displacement values in ABAQUS software with experimental study and numerical study in LS-DYNA software

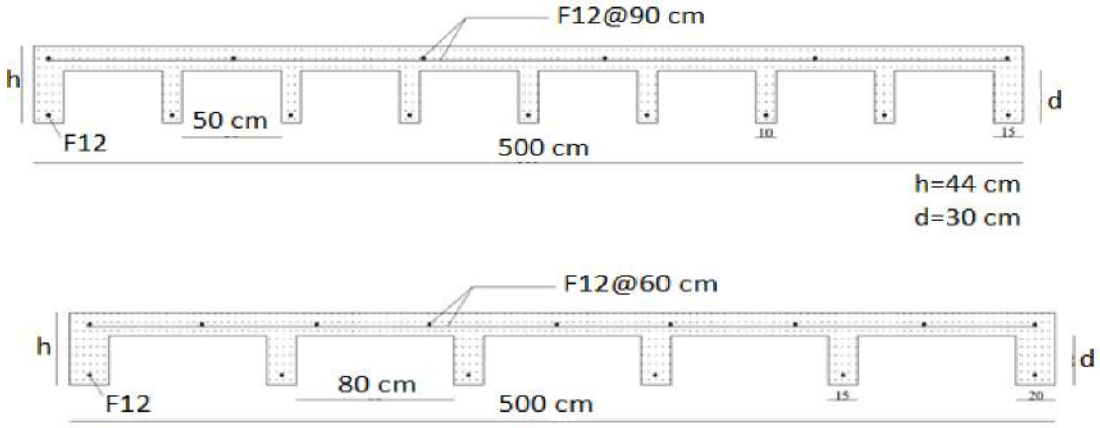

Fig. 10. Geometric properties of waffle slab with molds dimensions of 50×50×30 cm and 80×80×30 cm

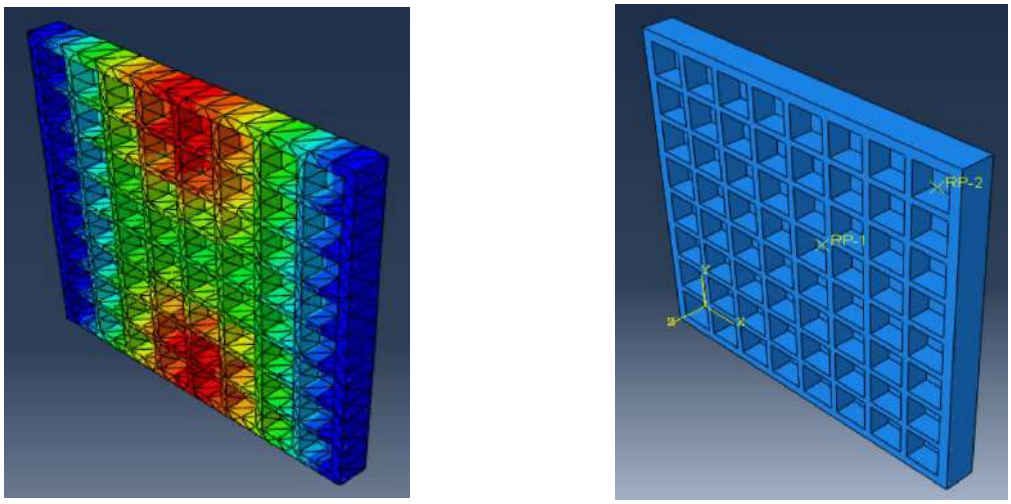

Fig. 11. Three-dimensional view of the waffle slab with molds dimension of 50×50×30 cm

Figure 12 shows a comparison of the displacement of the center of the RC slab and the waffle slab over time. In this comparison, both slabs have two fixed-supported sides, the volume of concrete and reinforcement are same and the mass of TNT is 0.5 kg that is located 2 m from the center of the slabs. As can be seen in this figure, waffle slab shows lower displacement under the blast load. As illustrated in Figure 13, studies on the effect of molds dimensions of waffle slab show that with the same volume of concrete and reinforcement materials, the molds dimensions have little effect on the behavior of the slab under the blast load. Three cases have been considered to investigate the effect of supporting conditions on the behavior of the waffle slab. The first case with two sides of the slab with fixed support (2 Fixed), the second case with four sides of the slab with fixed support (4 Fixed) and the third case with four pinned support sides (4 Pinned).

As can be seen in Figure 14, the displacement of the center of the slab in the second and third cases is less than the first case, indicating that fixing four sides of the slab offers better responses than fixing two sides of the slab and it can reduce the displacement of the slab center. Another point which is evident in this figure is that the type of slab support does not have an effect on the displacement of the center of the slab due to the blast load. In other words, it could show that the damage of the slab under blast has been localized and boundary condition cannot reduce the displacement and therefore local damage to the slab.

Figure 15 presents the effect of concrete compressive strength on the displacement of the center of the slab, which shows that

the slab displacement decreases as the concrete compressive strength increases. It is noteworthy in this figure that the restriction of slab displacement by increasing the strength of concrete decreases its effect approximately from the concrete grade C45 to above. Table 1 shows the effect of the explosive mass on the maximum displacement of the center of the waffle slab. For this purpose, the distance of the blast position is fixed at 2 m, but the mass of the explosive increased from 0.25 kg to 2.5 kg. The results show that with increasing mass of the explosive, the displacement of the center of the slab also increases.

Table 2 shows the effect of explosive distance on the maximum displacement of the center of the waffle slab. Therefore, the mass of the explosive is considered to be constant and equal to 1 kg and its distance varies. The results show that by increasing the distance of the explosive from the center of the slab, the displacement of the center of the slab is reduced. Finally, Figure 16 illustrates the effect of reinforcement size on the displacement of the center of the waffle slab for C30 concrete and the slab on two fixed sides subjected to the explosive with mass of 0.5 kg at a distance of 2 m.

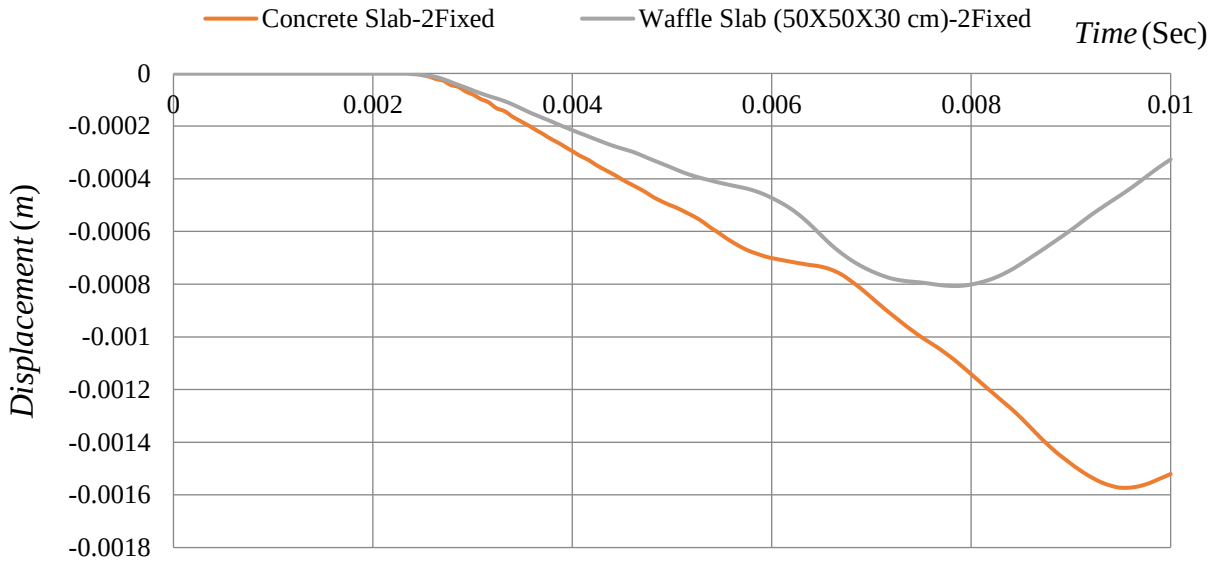

Fig. 12. Comparison of the displacement of the center of RC slab and waffle slab with waffle molds dimension of 50×50×30 cm

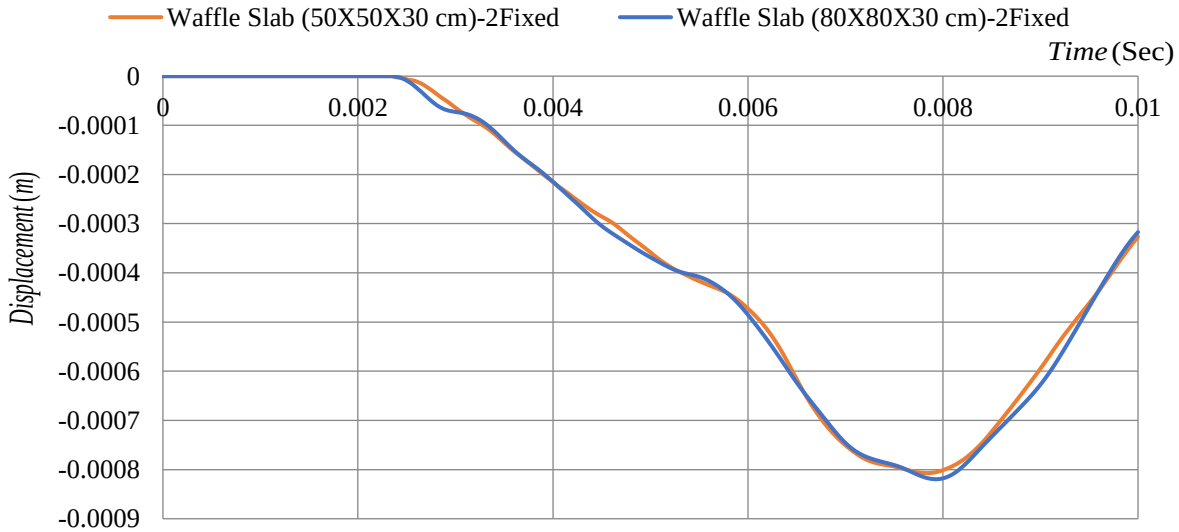

Fig. 13. Comparison of the displacement of the center of waffle slab with the molds dimensions of 50×50×30 cm and 80×80×30 cm

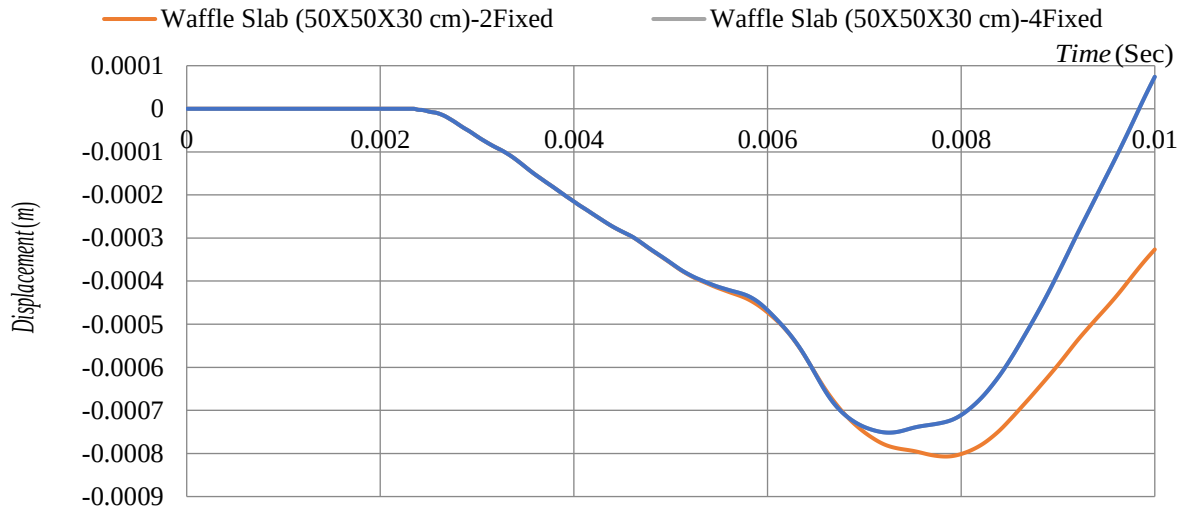

Fig. 14. Effect of supporting conditions on the displacement of the center of waffle slab with molds dimension of 50×50×30 cm

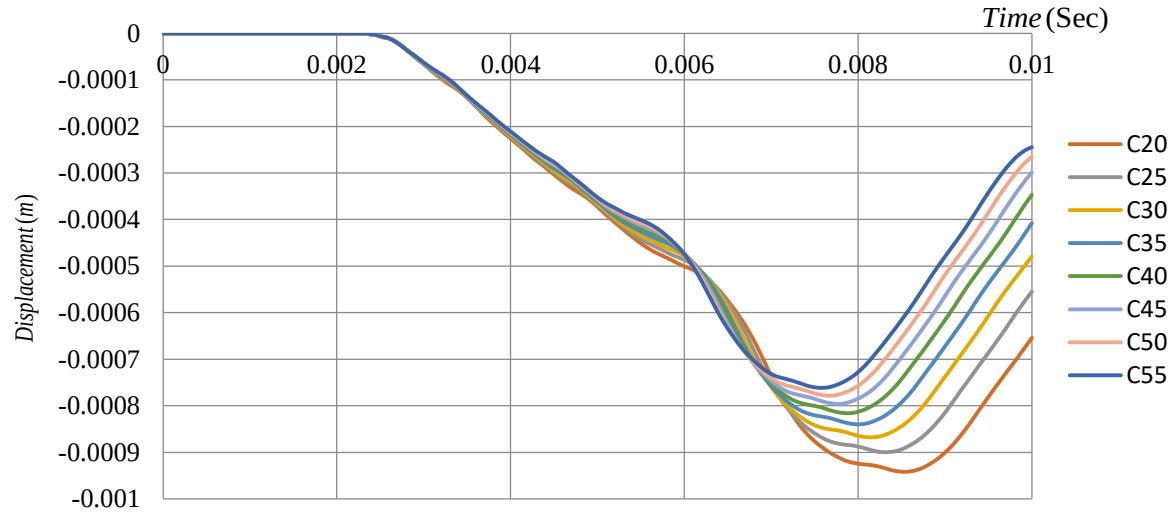

Fig. 15. Effect of compressive strength of concrete on the displacement of center of waffle slab with molds dimension of 50×50×30 cm

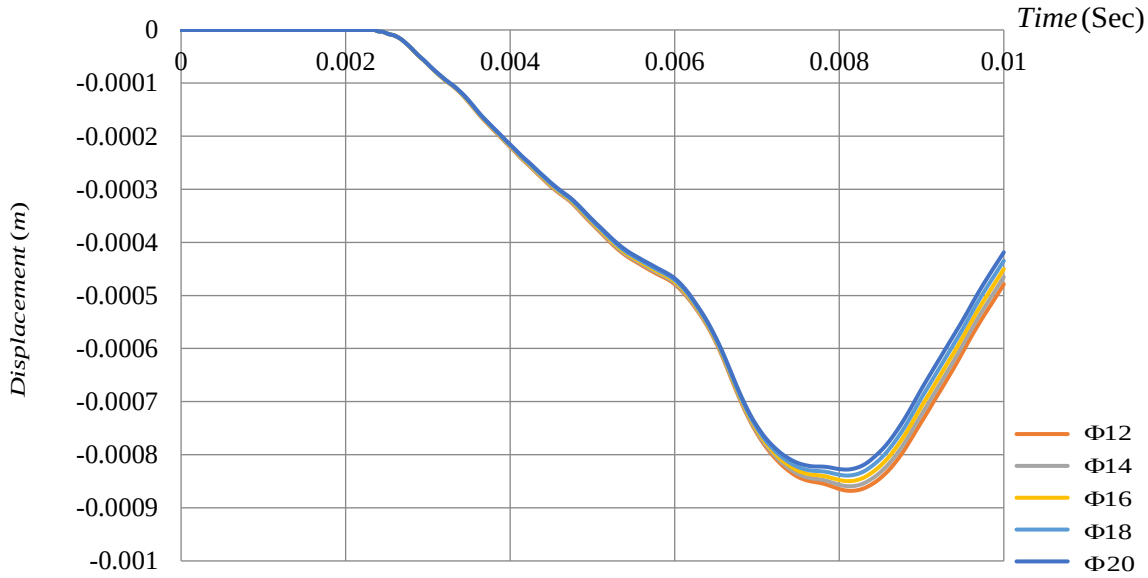

Fig. 16. Effect of reinforcement size on the displacement of center of waffle slab with molds dimension of 50×50×30 cm and C30 concrete

Table 1. Effect of explosive mass on the maximum displacement of the center of the waffle slab with molds dimension of 50×50×30 cm and C30 concrete

Z_i	R_i (m)	M_i (Kg)	U_{iMax} (m)
Z_1=3.1748	R_1=2	M_1=0.25	U_1=0.0005
Z_2=2.5198	R_2=2	M_2=0.5	U_2=0.0009
Z_3=2.2013	R_3=2	M_3=0.75	U_3=0.0012
Z_4=2	R_4=2	M_4=1	U_4=0.0015
Z_5=1.8566	R_5=2	M_5=1.25	U_5=0.0018
Z_6=1.7472	R_6=2	M_6=1.5	U_6=0.0021
Z_7=1.6597	R_7=2	M_7=1.75	U_7=0.0024
Z_8=1.5874	R_8=2	M_8=2	U_8=0.0026
Z_9=1.5263	R_9=2	M_9=2.25	U_9=0.0029
Z_{10}=1.4736	R_{10}=2	M_{10}=2.5	U_{10}=0.0032

Table 2. Effect of explosive distance on the maximum displacement of the center of the waffle slab with molds dimension of 50×50×30 cm and C30 concrete

Z_i	R_i (m)	M_i (Kg)	U_{iMax} (m)
Z_1=3.1748	R_1=3.1748	M_1=1	U_1=0.00090
Z_2=2.5198	R_2=2.5198	M_2=1	U_2=0.00115
Z_3=2.2013	R_3=2.2013	M_3=1	U_3=0.00130
Z_4=2	R_4=2	M_4=1	U_4=0.0015
Z_5=1.8566	R_5=1.8566	M_5=1	U_5=0.00151
Z_6=1.7472	R_6=1.7472	M_6=1	U_6=0.00158
Z_7=1.6597	R_7=1.6597	M_7=1	U_7=0.00164
Z_8=1.5874	R_8=1.5874	M_8=1	U_8=0.00169
Z_9=1.5263	R_9=1.5263	M_9=1	U_9=0.00174
Z_{10}=1.4736	R_{10}=1.4736	M_{10}=1	U_{10}=0.00179

5. Conclusions

This study investigated the behavior of the waffle slab under the blast load and comparison of its performance with that of conventional reinforced concrete slab. For this purpose, after presenting the equations related to the blast load, and the formulation of behavior of concrete and reinforcement materials, the model validation was also investigated by experimental research and two numerical studies in LS-DYNA software. Because the blast load was applied to the structure in a very short time, the loading speed was high. Therefore, the effects of strain rate on concrete and reinforcement were taken into account for achieving real behavior of the materials.

In order to study and compare rationally the behavior of slabs, the volume of concrete and reinforcement materials in all slabs was considered similar and then the effect of geometric dimensions of the molds was investigated. In addition, the effect of supporting conditions on the responses of the waffle slab and the effect of compressive strength of the concrete on the behavior of the slab under the effects of blast were also studied. The explosive mass and its distance from the slab were the other parameters considered in this study. The effect of reinforcement size on the behavior of the slab under blast was also investigated. The following items can be mentioned as the important results of this research:

- Comparing the results of this study as a numerical simulation in ABAQUS software with the results of experimental studies, it is evident that the investigation of blast effects on the slab in numerical simulation had desirable accuracy and this method of study can be a good substitute for experimental methods which require a great deal of precision, time and cost.
- The investigations in this research illustrate that under the same conditions of materials such as concrete and reinforcement and their volume, the waffle slab shows less displacement and better behavior than those of conventional reinforced concrete slab under blast load. The increase in moment of inertia in the waffle slab is one of the

most important reasons for better behavior under the blast load.

- Under the same conditions of volume of concrete and reinforcement materials, the results show that the geometrical dimensions of the molds have little effect on the slab responses under the blast load.
- Based on the studies on the effects of the slab support conditions, in the case where the slab is fixed at all four sides a better response under the blast load compared to the case with two fixed sides is achieved. The important conclusion of this study is that changing the type of support from the fixed type to the pinned type does not have much effect on the slab responses, which could be due to the high blast loading rate. Because the slab failure under blast will occur rapidly and locally in the center of the slab and the support does not have enough time to show its effects on the slab response.
- As the compressive strength of concrete increases, the slab response also improves as the slab center displacement decreases with increasing concrete compressive strength. But the slope of the ratio of changes from C45 concrete grade upwards gradually decreases.
- Investigations on the effect of mass and distance of the explosive show that for a given distance from the blast point to the center of the slab, as the mass of the explosive increases, the destruction effects on the slab increase. Also, for a given mass of explosive, as the blast point distance to the slab shortens, the slab center displacement and slab demolition effects increase, which is conceivable. Two scenarios in this study have been investigated for a given amount of mass-distance scale. The first scenario is with a mass of 0.25 kg at a distance of 2 m and the second scenario with a mass of 1 kg at a distance of 3.1748 m that the mass-distance scale for both scenarios is 3.1748. But the interesting conclusion is that the second scenario leads to higher displacement and consequently more slab damage. This result means that for the identical mass-distance scale, the mass value has a greater effect on the slab behavior than the distance value from the blast point to the slab.
- Studies on the effect of reinforcement size on the behavior of the waffle slab subjected to the blast show that with increasing rebar size, the displacement of the center of the slab decreases. But its impact is not significant compared to concrete, indicating that reinforcement is less effective than concrete on the waffle slab responses subjected to blast.

6. References

Abdollahzadeh, G.R., Jahani, E. and Kashir, Z. (2017). "Genetic programming-based formulation to predict compressive strength of high strength concrete", *Civil Engineering Infrastructures Journal*, 50(2), 207-219.

Augustsson, R. and Harenstam, M. (2010). "Design of reinforced concrete slab with regard to explosion", M.Sc. Thesis, Department of Civil and Environmental Engineering, Chalmers University of Technology, Göteborg, Sweden.

Chen, W., Hao, H. and Chen, S. (2015). "Numerical analysis of prestressed reinforced concrete beam subjected to blast loading", *Materials and Design*, 65, 662-674.

Eltehawy, E. (2009). "Effect of using ferro-cement on the mechanical properties of reinforced concrete slab subjected to dynamic loads", *Aerospace Sciences a Aviation Technology*, ASAT-13, 26-28.

Johnson, G.R. and Cook, W.H. (1983). "A constitutive model and data for METALS subjected to large strain, high strain rates and high temperatures", *Proceedings of the Seventh International Symposium on Ballistics, The Hague, The Netherlands*, 541-548.

Kheyroddin, A., Sharbatdar, M.K. and Farahani, A. (2019). "Effect of structural height on the location of key element in progressive collapse of RC structures", *Civil Engineering Infrastructures Journal*, 52(1), 41-58.

LS-DYNA. (2006). "Theory manual", Compiled by John O. Hallquist, Livermore Software Corporation, Livermore, California.

Meng, Q., Wu, Ch., Su, Y., Li, J., Liu, J. and Pang, J. (2019). "A study of steel wire mesh reinforced high performance geopolymer concrete slabs under blast loading", *Journal of Cleaner Production*, 210, 1150-1163.

Pandey, A.K., Kumar, R., Paul, D.K. and Trikha, D.N. (2006). "Non-linear response of reinforced concrete containment structure under blast loading", *Nuclear Engineering and Design*, 236, 993-1002.

Rezaie, F., Fakhradini, S.M. and Ghahremannejad, M. (2018). "Numerical evaluation of progressive collapse potential in reinforced concrete buildings with various floor plans due to single column removal", *Civil Engineering Infrastructures Journal*, 51(2), 405-424.

Shuaib, M. and Daoud, O. (2015). "Numerical modelling of reinforced concrete slabs under blast loads of close-in detonations using the lagrangian approach", *Journal of Physics; Conference Series*, 628 (1), 1-8.

Tavakoli, H.R. and Kiakojouri, F. (2015). "Threat-independent column removal and fire-induced progressive collapse: Numerical study and comparison", *Civil Engineering Infrastructures Journal*, 48(1), 121-131.

Wang, W., Zhang, D., Lu, F., Wang, S.C. and Tang, F. (2013). "Experimental study and numerical simulation of the damage mode of a square reinforced concrete slab under close-in explosion", *Engineering Failure Analysis*, 27, 41-51.

Xu, K. and Lu, Y. (2006). "Numerical simulation study of spallation in reinforced concrete plates subjected to blast loading*", Computers and Structures*, 84, 431-438.

Yang, F., Feng, W., Liu, F., Jing, L., Yuan, B. and Chen, D. (2019). "Experimental and numerical study of rubber concrete slabs with steel reinforcement under close-in blast loading", *Construction and Building Materials*, 198, 423-436.

Zahrai, S.M. and Ezoddin, A.R. (2014). "Numerical study of progressive collapse in intermediate moment resisting reinforced concrete frame due to column removal", *Civil Engineering Infrastructures Journal*, 47(1), 71-88.

Zhao, C.F. and Chen, J.Y. (2013) "Damage mechanism and mode of square reinforced concrete slab subjected to blast loading", *Theoretical and Applied Fracture Mechanics*, 63-64, 54-62.

Zhao, Ch., Lu, X., Wang, Q., Gautam, A., Wang, J. and Mo, Y.L. (2019). "Experimental and numerical investigation of steel-concrete (SC) slabs under contact blast loading", *Engineering Structures*, 196, 1-13.

Civil Engineering Infrastructures Journal 2021, 54(2): 381-403
DOI: 10.22059/CEIJ.2021.304150.1684

RESEARCH PAPER

Dynamic Material Flow Analysis of Cement in Iran: New Insights for Sustainability of Civil Infrastructures

Hosseinijou, S.A.[1]* and Mansour, S.[2]

[1] Assistant Professor, Department of Industrial Engineering, Faculty of Engineering, Golestan University, Gorgan, Iran.
[2] Professor, Department of Industrial Engineering and Management Systems, Amirkabir University of Technology, Tehran, Iran.

Received: 09 Jun. 2020; Revised: 15 Jan. 2021; Accepted: 08 Feb. 2021

ABSTRACT: In this article, a Dynamic Material Flow Analysis (DMFA) model is presented that characterizes the stocks and flows of cement from 1963 to 2063 in Iran. Using cement consumption data for the period of 1963-2018 an attempt is made to provide reliable estimates of the present as well as future cement in-use stocks and discards (from 2019 to 2063) to relevant stakeholders such as the Ministry of Road and Urban Development, Department of Environment, public and private utilities, and the construction and cement industries. Based on a normal lifetime distribution, a flow dynamic model is developed for each cement end-use category including buildings, infrastructures and others. Each sub model is simulated with 9 scenarios made from combinations of 3 scenarios for future cement consumption growth rate and 3 scenarios for the mean lifetime of the structures. For the base scenario, the model-derived estimate of in-use cement stock and cumulative discard for the year 2063 is 2191 million metric tons (Mt) and 1856 Mt, respectively. Such a great discard should be considered in policy making for better life cycle management of cement in Iran. The main finding of the paper is that by increasing the mean lifetime of the structures (especially buildings), the amount of cumulative cement discard in 2063 can be drastically decreased (generally over 50%) and this decrease will not be affected considerably by the cement consumption growth rate in the future. So this can be a reliable strategy for the sustainable life cycle management of infrastructures in Iran.

Keywords: Cement Discard, Cement Life Cycle, Dynamic Modeling, Material Flow Analysis (MFA), Normal Lifetime Distribution, Structures.

1. Introduction

According to Horvath (2004), optimum performance, extended useful life, minimum life-cycle costs, and minimal environmental life-cycle impacts, including the minimum use of virgin raw materials, are the main characteristics of sustainable infrastructure systems. The rate of accumulation of new stock, its characteristics in terms of material use and service life, and the renovation of existing stock are key determinatives of infrastructure sustainability.

* Corresponding author E-mail: sa.hosseinijou@gu.ac.ir

Cement is one of the most extensively used construction material for buildings and infrastructures in Iran. Better management of cement stock in the form of buildings, highways, bridges, and other infrastructures built up over the past years can influence the stocks and flows of cement discard in the future. The first step to do this is quantifying the stock of cement in-use. Static and dynamic modeling are the two basic approaches to quantifying stocks. In the dynamic approach, material inflows to the system boundary under consideration are categorized into different end-uses (for example the amount of cement used for residential, commercial, and public buildings). Each of the end-uses is assigned a service lifetime. The lifetime determines the delay between the material inflows and material outflows in form of discards. The difference between the material inputs and discards is the net addition to in-use stock. The static approach provides a single snapshot of stocks and flows, whereas the dynamic model can be used to characterize the net addition or depletion of stocks over time. Characterization of stocks over time can also be used to estimate future discards or emissions. Such information is useful to formulate end-of-life strategies and management systems (Kapur and Keoleian, 2009).

The general paradigm of modeling of dynamic MFA is either stock dynamic or flow dynamic. Flow dynamic models are based on the basic assumption that the inflow and outflow of material stock is its main driving force. The future amount of inflow is either assumed or estimated using socio-economic variables by different techniques; while the amount of outflow is calculated by a delay process using an assumed lifetime distribution. The other type of modeling approach is stock dynamics driving. Its basic assumption is that the stock of service units is the driver for the material flows. The stock can be calculated by assigning a 'development pattern', 'stock expansion rate' or can be formulated as a function of population and its lifestyle. The outflow of materials and its associated obsolete service units is determined by the delay process, while the inflow of materials and its associated new add-in service units is calculated to maintain the development pattern of stock in use (Müller et al., 2006)

The purpose of this study is to characterize the stock and flow of cement from 1963 to 2063 in Iran. In this research, a flow dynamic driving model is developed for cement to characterize the stock and flows of cement from 1963 to 2063 in Iran. Thus the model has a retrospective and prospective approach. The driving force of the model is the cement inflow that is determined from 1963 to 2018 from the existent cement consumption statistics and extrapolated for the period 2019-2063 by a constant consumption growth rate (for different scenarios). A normal distribution function is used for the life time of different end uses. The information derived from the model is important for different stakeholders in Iran's infrastructure to make decisions about buildings and infrastructures more sustainable.

2. Literature Review

Table 1 presents a literature review of the most related dynamic MFA for construction materials and thus does not cover the wide range of dynamic MFA papers. The review is structured in three parts (the first row of Table 1); model type, model features and case study. In model type, it is showed that the general paradigm of modeling of dynamic MFA is either stock dynamic or flow dynamic. Flow dynamic driving, as applied in Kleijn et al. (2000), Kapur et al. (2008), Cao et al. (2017) and Miller (2020) assumes that the material stock is driven by its inflow and outflow. Stock dynamics driving approach has been presented in Müller et al. (2004), Müller (2006), Bergsdal et al. (2007), Sartori et al. (2008), Hu et al. (2010a), Huang et al. (2013) and Cao et al. (2018).

Table 1. Literature review of the most related dynamic MFA for construction materials

Reference	Type of model	Model features					Case study	
	Stock / Flow dynamic	Lifetime distribution	Retrospective / Prospective	Recycling/ Renovation	Environmental impacts	Scenario analysis/ Sensitivity analysis/ Uncertainty analysis	Material/ Substance	Country
Kapur et al. (2008)	Flow dynamic	Gamma, Weibull, LogNormal	Retrospective	Recycling	-----	No scenario, Monte Carlo method for uncertainty considerations	Cement (all sectors)	USA
Hu et al. (2010a)	Stock dynamic	Normal	Retrospective and prospective	Recycling	CO_2 emissions, net steel use	Material intensity, mean life time, floor area, recycling	Steel and iron in residential buildings	China
Huang et al. (2013)	Stock dynamic	Normal	Retrospective and prospective	Recycling	CO_2 emissions, iron ore, limestone, solid waste	Mean life time, recycling	Steel, glass, wood, gravel, sand, lime, brick, cement in buildings	China
Müller (2008)	Stock dynamic	Normal	Retrospective and prospective	----	----	Mean life time, material intensity, floor area	Concrete in dwelling stock	Netherland
Müller (2004)	Stock dynamic	Normal	Retrospective and prospective	----	Energy supply, waste	----	----	Swiss
Bergsdal et al. (2007)	Stock dynamic	Normal	Retrospective and prospective	----	----	Material intensity, mean life time	Concrete and wood in dwelling stock	Norway
Sartori et al. (2008)	Stock dynamic	Normal	Retrospective and prospective	Renovation	----	Person per dwelling, size of the dwelling, population, the interval of renovation	The stock of floor area (no material)	Norway
Cao et al. (2017)	Flow dynamic	Normal, Weibull	Retrospective: 1920-2013	----	----	Parameters of life time distribution, production data, sector split ratio	Cement in building, infrastructure and agriculture	China
Cao et al. (2018)	Stock dynamic	Weibull	Retrospective and prospective: 1985-2100	----	----	Parameters of life time distribution, Material intensity , Floor area, urbanization rate, population	Cement, steel, wood, brick, gravel, sand in the housing sector	China
Miller (2020)	Flow dynamic	Gamma, Weibull, LogNormal	Retrospective:	Recycling	-----	No scenario, Monte Carlo method for uncertainty considerations	Cement (all sectors)	USA
This paper	Flow dynamic	Normal	Retrospective and prospective: 1963-2063	----	----	Mean life time, consumption growth rate	Cement (all sectors)	Iran

In columns with header "model feature" different aspects of modeling are determined including: the type of life time distribution, time dimension, considering recycling and/or renovation in the model, considering environmental impacts, and scenario analysis, sensitivity analysis, and uncertainty analysis. The lifetime distribution function most frequently used in the area of dynamic MFA for construction material is a normal distribution. Most reviewed articles in Table 1 used a retrospective and prospective approach i.e. models the stock and flow both for the past and future. Some of them used only the retrospective approach and does not include any forecasting for the future. Few studies consider recycling, renovation and environmental impacts as features of the model. The scenario analysis or sensitivity analysis is a common part of almost all papers. The life time distribution and material intensity are the two main factors for a scenario or sensitivity analysis. In the last two columns, the specifications of the case study are presented which include the type of material or substances and the spatial scale of the case study. Some papers consider only a substance such as cement and others investigate a combination of construction materials such as concrete, steel, glass, wood etc. Finally, all of the papers presented in the table include a case study at the national level. The last row of Table 1 shows the characteristics of this research. The details of the model will be presented in the next section.

The main focus of the model is twofold: 1) Estimating the in-use cement stock for the present as well as future. This estimate will provide a foundation for policy design for better management of this stock to postpone its discard and reduce demand for new cement; 2) Estimating cumulative cement discard (or waste) for the present and the future. Such estimation would be critical to better design of demolition waste management strategies.

There are many studies in the context of Construction and Demolition (C&D) waste management that are related to this research. In fact, one of the main aspects of the researches in dynamic MFA for construction materials is to estimate the stock of waste. Some studies only estimate the waste of demolition as the main outflow of the dynamic MFA model (e.g. Muller, 2006; Kapur et al., 2008). Some papers estimate both construction and demolition waste. For example Huang et al. (2013) estimated demand for materials and environmental impacts of buildings in China from 1950 to 2050 based on the dynamic MFA. They studied the effect of lengthening the lifetime of buildings and enhancing materials recycling on reducing demand for raw material, generation of solid waste and CO_2 emissions. Hu et al (2010b) studied the construction and demolition flow of housing floor areas and the consumption and waste flows of concrete for Beijing from 1949 through 2050. Their findings indicated that C&D waste generation in the near future strongly depends on the lifetime of the buildings. They concluded that if the buildings lifetime can be extended, sever demolition pressure can be postponed or even reduced totally. It is worth noting that only in the stock dynamic models it is possible to calculate C&D waste generation.

As mentioned before, in the stock dynamic models, the stock of service units (buildings and infrastructures) is the driver for the material flows. So, the flow of all related materials (construction materials and waste) can be tracked and calculated. But in the flow dynamic models that material stock is driven by its inflow, only the flow of a single substance (for example cement or steel) can be tracked and thus all related C&D waste cannot be calculated. Only waste from the mentioned substance can be estimated after stock useful life.

There are also some researches in C&D waste literature that are based on the static MFA. One can refer to Condeixa et al. (2017), Wiedenhofer et al. (2015), Surahman et al. (2017), Wang et al. (2018)

and Huang et al. (2018). An analytical review of different methods for quantifying construction and demolition waste can be found at Wu et al. (2014). This research, from the viewpoint of waste context, only considers the demolition waste, i.e., the only waste in the model developed is the outflow of in-use cement stock which is derived by the lifetime of the stock. Even the only demolition waste in our model is cement discard. Other wastes materials arising from demolition are not the output of the model. This is because our model is a flow dynamic substance flow analysis model that tracks the flow of cement and ignores other related construction material in the building lifecycle. No construction waste is also calculated and thus this research is not completely fitted to the C&D waste context. So the literature review table was confined to the most related papers in the context of dynamic MFA.

3. Methodology and Data

3.1. Cement Life Cycle

The generic life cycle of cement has three life stages of production (including extraction of raw material), use, and waste management at the end of life. Figure 1 shows a generic view of cement life cycle. At every stage of the life cycle there can be material exchanges with the lithosphere, environment, and material imports and exports.

3.2. Goal, Scope and Features of the Model

The model described below does not include the production and end of life stage of the mentioned life cycle. It means that the capacity constraints of the production and different scenarios of the end of life are not considered in the model. Thus the model is an open loop one and does not include reverse flows (recycling). Repair and renovation will not also be considered in the model. The model uses the historical and extrapolated data of cement inflow to estimate the stock of cement discards. The stock of cement in-use is the other result of this calculation process.

The time scope of the model consists of two parts. The first part is the interval 1963-2018 when the historical data of cement consumption is used as the driver of the model. The second part is the interval 2019-2063 when the extrapolated data of cement consumption under different scenarios are used to estimate the stock of in-use and discards.

The model is disaggregated to different cement end-uses including “buildings” (residential, commercial and public), “infrastructures” (roads, bridges, highways, water and wastewater infrastructures, etc.) and “other” uses (farms, parks, stadiums, mines, etc). The main reason for such classification is its suitability for data gathering about cement end-use market share. Cement consumption growth rate, the mean and standard deviation of lifetime distribution are the main parameters of the model that directly affect the calculated stock. As will be described later, different scenarios for these parameters are used to better predict the future stock of cement in-use and discard. Because of the lack of data about the most appropriate life time distribution of different end uses, a normal distribution function is used for all of them.

3.3. Basic Structure of the Model

The model presented herein represents a Dynamic Material Flow Analysis (DMFA) of cement. It is based on the flow dynamics approach. Figure 2 illustrates the main aspects of the model. Processes are illustrated by rectangles, flows by ovals, and drivers and determinants by hexagons. Arcs represent influences between variables. The stock of in-use cement is denoted by M and the net stock accumulation by dM/dt. The input flow to the stock is given by dM_{in}/dt, while the output flow is represented as dM_{out}/dt. Determinants are denoted as F(t) for cement consumption, and L for the end-use lifetime (i.e. life time of buildings, infrastructures and others).

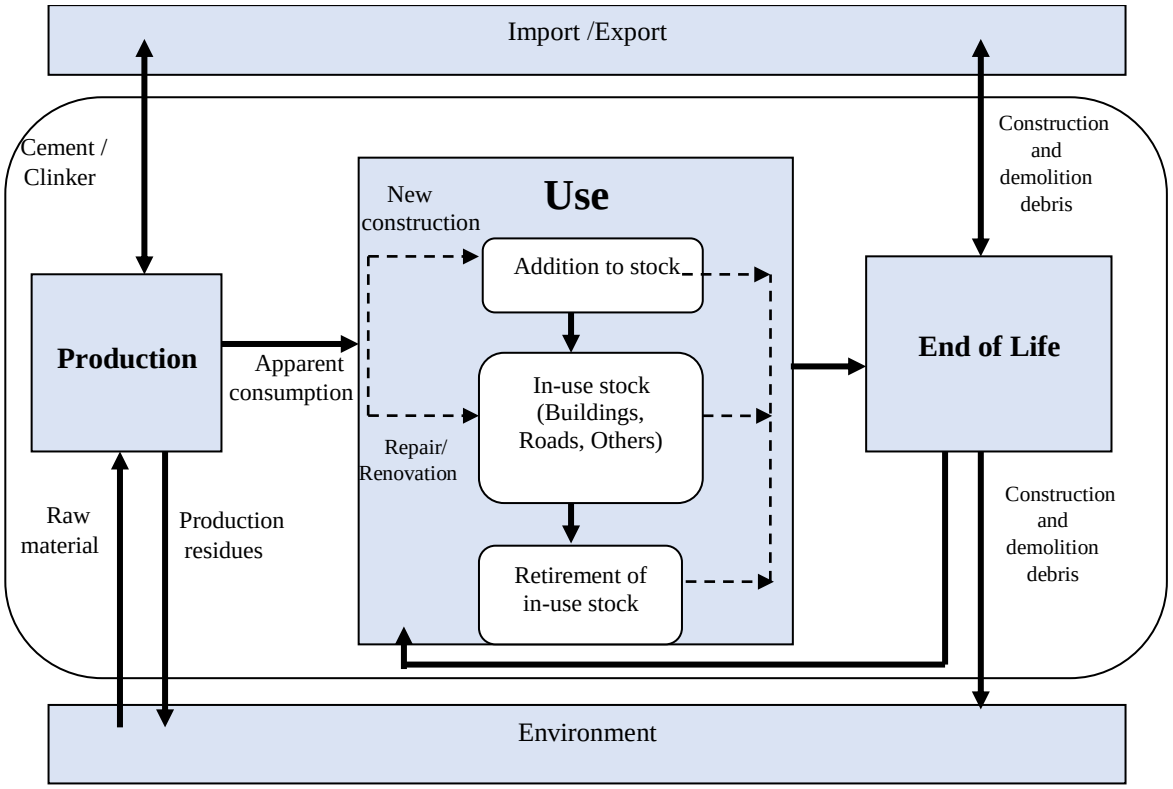

Fig. 1. Generic cement life cycle (adopted from Kapur et al., 2008)

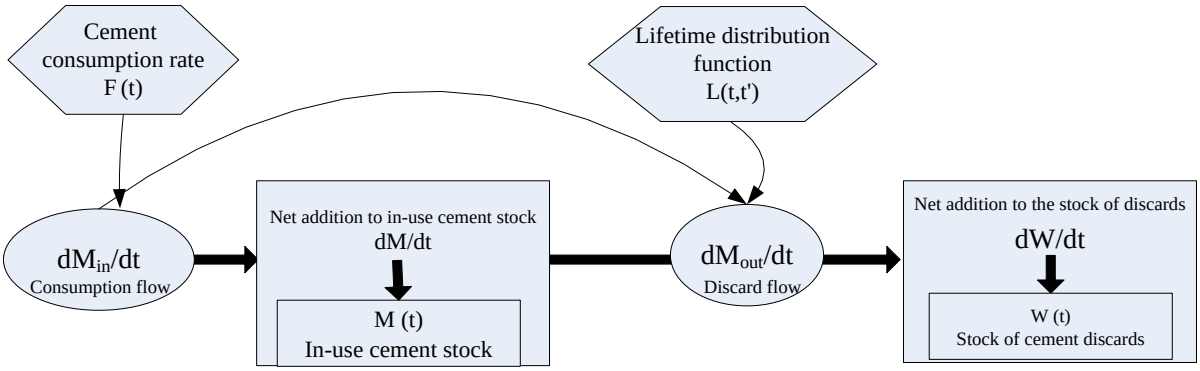

Fig. 2. Basic cement flow dynamic model

3.4. Model Formulation

According to Hu et al. (2010a), the flow dynamic model with some modifications can be described mathematically with a system of five differential equations as follows:

Eq. (1) defines the driver of the model (that is the cement inflow). The stock of in-use cement is driven by the cement consumption (here F(t)).

Eq. (2) defines the delay character of the cement stock in use. The outflow of the cement stock is determined by the previous inflow by delaying it by an assumed service lifetime. Since different infrastructures may have different service lifetimes before they are demolished, a lifetime distribution L(t, t') is used in Eq. (2), representing the probability that the structure units entering service at the time t' are going to be removed from the stock at the time t.

Eq. (3) defines a normal lifetime distribution L(t,t') for the model, with mean lifetime μ and standard deviation σ. Eq. (4) represents that the cement stock in the system can be calculated according to the material inflow and outflow. Finally, Eq. (5) describes that net addition to the stock of cement discards is equal to discard flow considering no outflow from this stock (for example by recycling).

It is worth noting that a discretized version of this continuous-time differential equation system should be used in practice.

Since the yearly data for cement consumption are available and because of the wide time range of this analysis it is rational to consider one year as the time step for the discrete form model. Such a model was formulated in Microsoft Excel and used for calculations.

$$\frac{\mathrm{dM_{in}(t)}}{\mathrm{dt}} = F(\mathrm{t}) \quad (1)$$

$$\frac{\mathrm{dM_{out}(t)}}{dt} = \int_{t_0}^{t} \mathrm{L(t,t')}.\frac{\mathrm{dM_{in}(t')}}{\mathrm{dt}}\,\mathrm{dt'} \quad (2)$$

$$\mathrm{L(t,t')} = \frac{1}{\sigma\sqrt{2\pi}}.\mathrm{e}^{-\frac{(\mathrm{t}-\mathrm{t}'-\mu)^2}{2\sigma^2}} \quad (3)$$

$$\frac{dM(t)}{dt} = \frac{\mathrm{dM_{in}(t)}}{\mathrm{dt}} - \frac{\mathrm{dM_{out}(t)}}{dt} \quad (4)$$

$$\frac{dW(t)}{dt} = \frac{\mathrm{dM_{out}(t)}}{dt} \quad (5)$$

in which $M(t)$: is the stock of in-use cement (million metric tons), $\frac{dM_{in}(t)}{dt}$: is the rate of inflow to the stock of in-use cement (million metric tons/year), $\frac{dM_{out}(t)}{dt}$: is the rate of outflow from the stock of in-use cement (discard flow) (million metric tons/year), $\frac{dM(t)}{dt}$: is the rate of net addition to the stock of in-use cement (million metric tons/year), $W(t)$: is the stock of cement discard (million metric tons), $\frac{dW(t)}{dt}$: is the rate of net addition to the stock of cement discard (million metric tons/year), $F(t)$: is the cement consumption rate, $L(t,t')$: is the lifetime distribution representing the probability that the structure units entering service at the time t' are going to be removed from the stock at the time t, σ: is the standard deviation of lifetime of infrastructure (year) and μ: is the mean of lifetime of infrastructure (year).

3.5. Scenario Planning and Simulation

There is large uncertainty in the main parameters of the model i.e. lifetime distribution parameters and cement consumption rate. The prediction of cement consumption rate for the interval 2019-2063 consists of inevitable uncertainty. Concluding from some researches on the perspective of Iran cement industry (The Global Cement Report, 2017; Edwards, 2017; Namazi and Bastami, 2019) three scenarios for the growth of cement consumption rate that are most likely in the future include high (5%), medium (3%) and low (1%) which is depicted in the first row of Table 2. From another way it is reasonable to consider three scenarios for the mean lifetime of cement end-use: short, medium and long lifetime. The values of the mean lifetime for different end-uses are provided in the first column of Table 2. Symbols μ_B, μ_I, μ_O stand for mean lifetime of buildings, infrastructures and other end-use. The mean lifetime data are derived from various sources such as industry reports, research studies and government surveys. The combination of these values results in 9 scenarios for the model (S1-1 to S3-3). These scenarios are demonstrated in Figure 3 which includes three sub-models according to different end-uses. These three sub-models will be run separately and then aggregated stocks of cement in-use and cement discard are calculated by summing of corresponding stocks of these sub-models. Because of the lack of data and any estimation, for all scenarios, the standard deviation of lifetime is considered to be 10 years, *i.e.* $\sigma = 10$. All sub-models formulated and simulated in Microsoft Excel.

Notably, the current trend in cement consumption in Iran implicates the low growth rate in cement consumption. In another way the short lifetime scenario represents the current situation in Iran. So S1-3 can be considered as the base scenario that represents the possible future if no significant changes will happen for the cement consumption growth rate and the average lifetime of structures.

3.6. Cement Consumption Data

Figure 4a shows the consumption of cement in Iran over the last 56 years (1963-2018). Over this period, the cumulative cement consumption in Iran was approximately 1137 Mt (beyond 1Gt). As seen in Figure 4a, both flow and stock of

cement consumption have doubled approximately from 2005 to 2013. This is because of the large development of the cement production industry in Iran at this period and also considerable growth of construction both in the private and public sectors of Iran's economy. For example, a national project for constructing residential building for low income families called "Maskan Mehr" was performed at this period that included the construction of above 2 million units of residential buildings. Such projects considerably increased the consumption of cement in Iran. There is also a fall in cement consumption in 2012 as seen in Figure 4a. The cause of this fall is the economic recession in Iran and the consequent recession in the construction industry.

There is no reliable data on cement consumption before 1963 in Iran so it is eliminated from this analysis. It is worth noting that cement consumption in this analysis refers to internal consumption and exclude cement export. This is because of the goal of this study, i.e. estimating the in-use cement stock and the stock of cement discard in Iran. Figure 4b demonstrates three scenarios (introduced in Section 2.5) for the future cement consumption in Iran for the period 2019-2063. Considering the recent economic recession in Iran, the scenario with low cement consumption growth is more probable for near future. However, for the sake of comparative analysis and scenario-based planning, and the relatively wide time horizon of the study, scenarios with medium and high consumption growth are also considered in this study.

Cement consumption was divided into various end-use markets. Based on available data these markets in Iran were divided into three parts: buildings (residential, commercial, public), civil infrastructures (such as roads, highways, bridges, tunnels, dams, etc.), and others (farms, stadiums, mining, defense, etc.). Figure 5 shows the cement end-use market share in Iran in recent years based on available resources (Dorafshani, 1996; RHUDRC, 2019).

The building sector has the largest portion of the cement market (60%). Civil infrastructures with 28% have the second rank and other uses include the remaining 12 % of ultimate cement consumption. There is no historical data about the cement end-use market share during the last 56 years (1963-2018). There is also no estimation of this market share in the future. This research deals with this problem by assuming that the cement end-use market share does not change radically over the next several decades. So, the cement market share in recent years is used for the entire time horizon of the model i.e. 1963-2063. Future studies may improve the result of this study by providing an accurate estimate of future cement end-use market share.

4. Results and Discussion

4.1. Estimate of Stock of in-Use Cement and Cumulative Cement Discards in 2018

Table 3 and Figure 6 show cumulative cement consumption, stock of in-use cement and cumulative cement discards in 2018 for different lifetime scenarios. Since the cement consumption data for the period of 1963-2018 is based on real data so there is no scenario on cement consumption and the results are shown based on only lifetime scenarios. According to these results, cumulative cement consumption in 2018 was about 1137.55 Mt (Million metric tons) while the estimated stock of in-use cement differs from 946.42 Mt in the short lifetime scenario to 1108.46 Mt in the long lifetime scenario. This means that because of the lack of data on the real lifetime of buildings, infrastructures and other end-use of cement, there is no certainty about the real stock of in-use cement at 2018 but it is estimated to be around 1000 Mt (or 1Gt (rigatoni)). Also, the cumulative discard of cement varies from 191.13 in the short lifetime scenario to 29.09 Mt in the long lifetime scenario indicating there is large uncertainty in the present stock of cement discard in Iran.

Table 2. Different scenarios for mean lifetime and growth in consumption rate

Scenarios for growth in consumption rate / Lifetime scenarios	High consumption growth (5%)	Medium consumption growth (3%)	Low consumption growth (1%)
short lifetime ($\mu_B = 30, \mu_I = 40, \mu_O = 20$)	S 1-1	S 1-2	S 1-3 (Base scenario)
medium lifetime ($\mu_B = 40, \mu_I = 50, \mu_O = 30$)	S 2-1	S 2-2	S 2-3
long lifetime ($\mu_B = 50, \mu_I = 60, \mu_O = 40$)	S 3-1	S 3-2	S 3-3

Table 3. Cumulative cement consumption, in-use and discards (million metric tons) at 2018 for different lifetime scenarios

Lifetime scenarios	End-use category	Consumption	In-use	Discard
Short lifetime ($\mu_B = 30, \mu_I = 40, \mu_O = 20$)	Buildings	682.53	561.10	121.43
	Infrastructure	318.51	293.84	24.68
	Others	136.51	91.48	45.02
	Aggregated	**1137.55**	**946.42**	**191.13**
medium lifetime ($\mu_B = 40, \mu_I = 50, \mu_O = 30$)	Buildings	682.53	629.65	52.88
	Infrastructure	318.51	310.63	7.89
	Others	136.51	112.22	24.29
	Aggregated	**1137.55**	**1052.50**	**85.05**
long lifetime ($\mu_B = 50, \mu_I = 60, \mu_O = 40$)	Buildings	682.53	665.63	16.90
	Infrastructure	318.51	316.90	1.61
	Others	136.51	125.93	10.58
	Aggregated	**1137.55**	**1108.46**	**29.09**

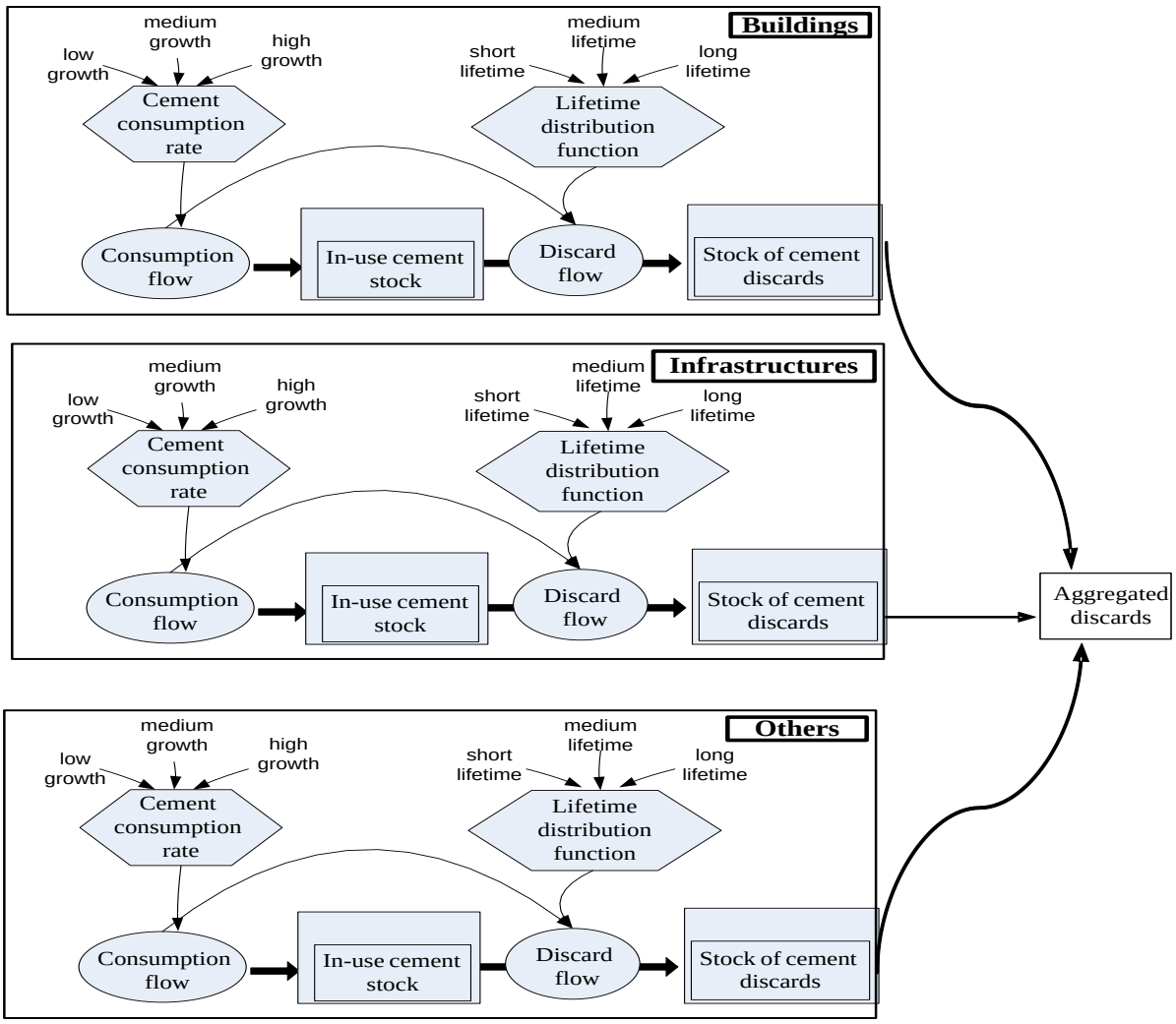

Fig. 3. Three sub-models (each one includes 9 scenarios) for cement flow dynamic model

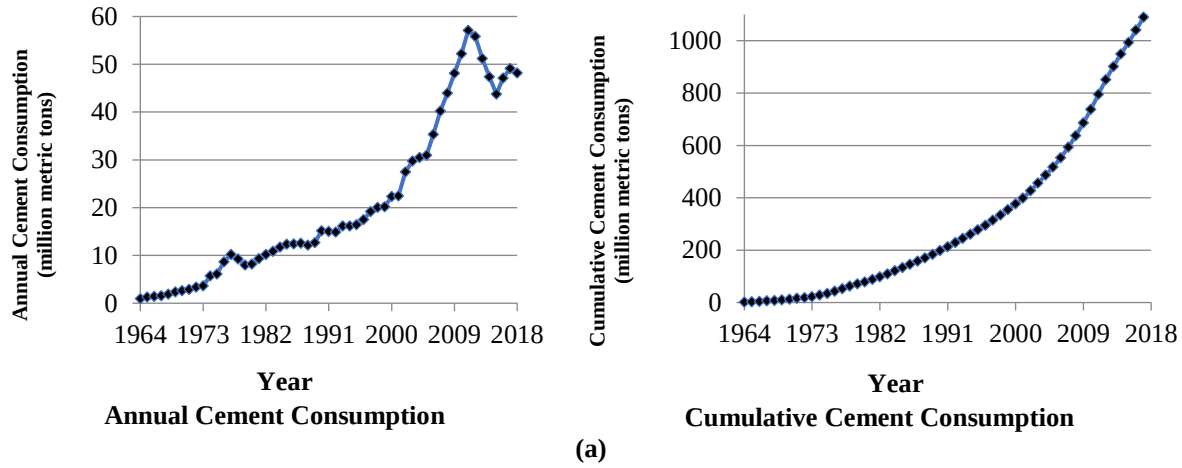

(a)

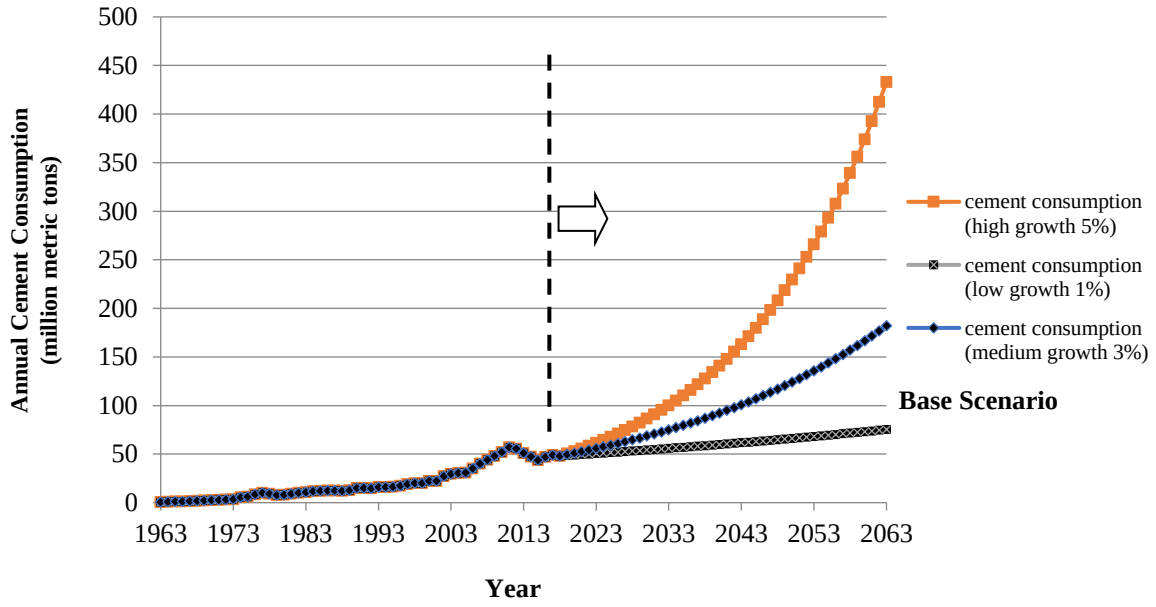

(b)

Fig. 4. Historical data and future projection for cement consumption in Iran: a) Annual and cumulative consumption of cement in Iran over the last 56 years (million metric tons) (Data source: Iran Cement Statistics, 2019; Ahmadi and Karimi, 2015; Heibati and Farzin, 2005); and b) Three scenarios for annual future cement consumption in Iran (2019-2063)

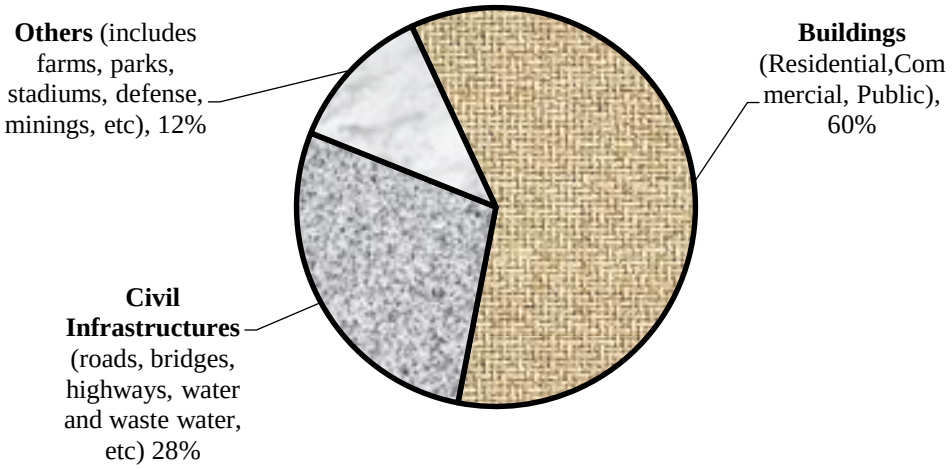

Fig. 5. Recent cement end-use market share in Iran

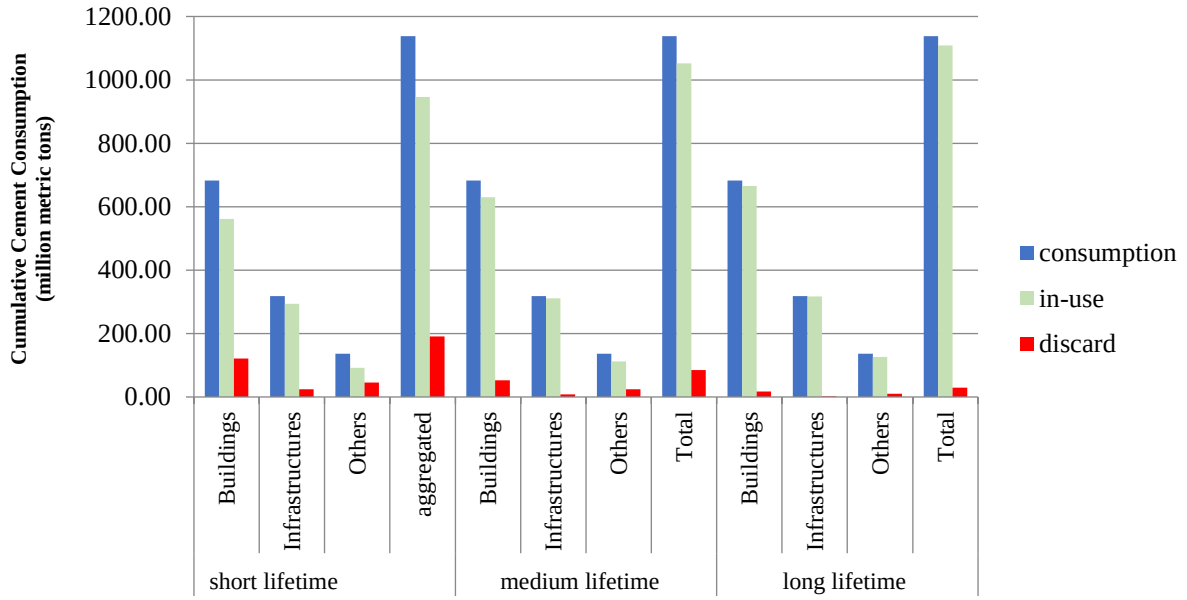

Fig. 6. Cumulative cement consumption, stock of in-use cement and cumulative cement discards at 2018 for different lifetime scenarios (million metric tons)

4.2. Estimate of the Final Stock of in-Use Cement In 2063

Table 4 and Figure 7 show an estimate of the stock of in-use cement in 2063 for different scenarios. As seen in the scenario S3-1, the highest rate of growth in cement consumption and the longest lifetime of cement products (building, infrastructures and others) have led to the largest stock of in-use cement (above 8 Gt) which is almost eight times of stock of in-use cement in 2018. In contrast, in the base scenario S1-3, the lowest rate of growth in cement consumption and the shortest lifetime of cement products have led to the smallest stock of in-use cement (above 2 Gt) which is almost twice the stock of in-use cement in 2018. As seen in Figure 7, the key factor causing larger differences in the final stock of in-use cement is the rate of growth in cement consumption.

Table 4. In-use cement stock (million metric tons) at 2063 for different scenarios

Cement consumption scenarios / **Lifetime scenarios**	**High consumption growth (5%)**	**Medium consumption growth (3%)**	**Low consumption growth (1%)**
	S 1-1	S 1-2	S 1-3 (**Base scenario**)
Sshort lifetime ($\mu_B = 30, \mu_I = 40, \mu_O = 20$)	in-use$_B$ = 4043.22 in-use$_I$ = 2143.50 in-use$_O$ = 655.72 Aggregated = 6842.45 S 2-1	in-use$_B$ = 2227.57 in-use$_I$ = 1239.46 in-use$_O$ = 345.50 Aggregated = 3812.53 S 2-2	in-use$_B$ = 1259.16 in-use$_I$ = 747.54 in-use$_O$ = 185.05 Aggregated = 2191.75 S 2-3
Medium lifetime ($\mu_B = 40, \mu_I = 50, \mu_O = 30$)	in-use$_B$ = 4593.22 in-use$_I$ = 2313.22 in-use$_O$ = 808.64 Aggregated = 7715.09 S 3-1	in-use$_B$ = 2655.98 in-use$_I$ = 1392.54 in-use$_O$ = 445.51 Aggregated = 4494.03 S 3-2	in-use$_B$ = 1601.87 in-use$_I$ = 887.64 in-use$_O$ = 251.83 Aggregated = 2741.35 S 3-3
Long lifetime ($\mu_B = 50, \mu_I = 60, \mu_O = 40$)	in-use $_B$ =4956.90 in-use $_I$ =2427.93 in-use $_O$ =918.64 Aggregated =8303.47	in-use $_B$ =2984.01 in-use $_I$ =1504.29 in-use $_O$ =531.20 Aggregated = 5019.50	in-use $_B$ =1902.09 in-use $_I$ =996.92 in-use $_O$ =320.37 Aggregated = 3219.38

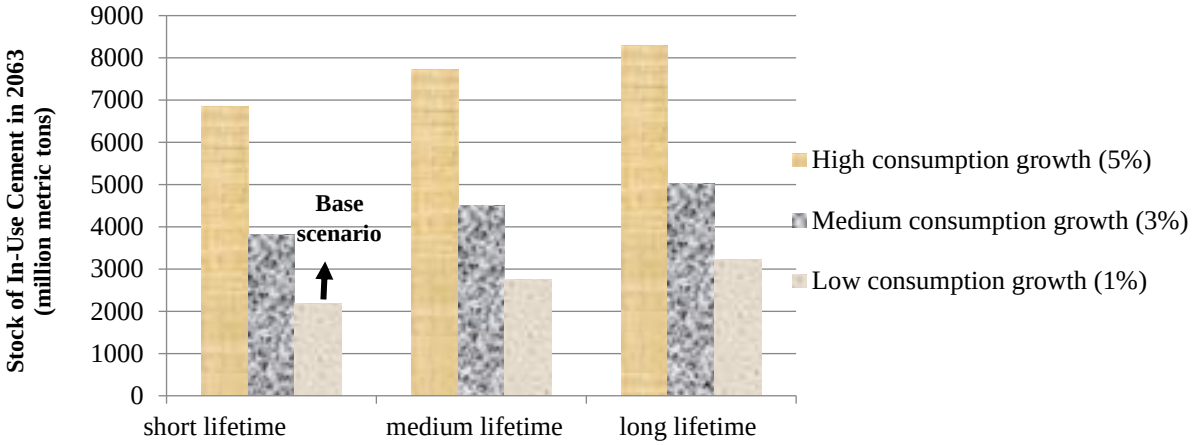

Fig. 7. Thestock of in-use cement in 2063 for different scenarios

4.3. Final Stock of Cement Discards at 2063

Table 5 and Figure 8 show cumulative cement discards until 2063 for different scenarios. (cd denotes cumulative discard). As seen in scenario S1-1, the highest rate of growth in cement consumption and the shortest lifetime of cement products (building, infrastructures and others) have led to the largest stock of aggregated cement discard (above 2 Gt). In contrast, in the scenario S3-3 the lowest rate of growth in cement consumption and the longest lifetime of cement products have led to the smallest stock of aggregated cement discard (less than 1 Gt).

As seen in Figure 8, the amount of cement consumption growth is more affected in the short lifetime scenarios meaning that the key factor influencing the cement discards is the lifetime of structures. This indicates that by increasing the mean lifetime of structures (i.e. building, civil infrastructures and etc.) the amount of cumulative cement discards until 2063 can be drastically decreased and this decrease will not be affected considerably by the consumption growth rate. Furthermore, it is interesting that by averagely making the mean lifetime of the structures one and a half time, the amount of cumulative cement discards until 2063 will be reduced almost to one third (from 2377 in the scenario S1-1 to 879 in the scenario S3-3).

Table 5. Cumulative cement discards (cd) (million metric tons) until 2063 for different scenarios

Cement consumption scenarios / **Lifetime scenarios**	**High consumption growth (5%)**	**Medium consumption growth (3%)**	**Low consumption growth (1%)**
	S 1-1	S 1-2	S 1-3 (**Base scenario**)
Short lifetime ($\mu_B = 30, \mu_I = 40, \mu_O = 20$)	cd_B = 1448.76 cd_I = 438.09 cd_O = 450.68 Aggregated = 2377.52	cd_B = 1300.52 cd_I = 413.65 cd_O = 356.31 Aggregated = 2070.48	cd_B = 1166.47 cd_I = 394.63 cd_O = 295.02 Aggregated = 1856.12
	S 2-1	S 2-2	S 2-3
Medium lifetime ($\mu_B = 40, \mu_I = 50, \mu_O = 30$)	cd_B = 938.76 cd_I = 268.37 cd_O = 297.75 Aggregated = 1504.89	cd_B = 886.38 cd_I = 263.95 cd_O = 260.10 Aggregated = 1410.44	cd_B = 845.63 cd_I = 260.27 cd_O = 233.29 Aggregated = 1339.19
	S 3-1	S 3-2	S 3-3
Long lifetime ($\mu_B = 50, \mu_I = 60, \mu_O = 40$)	cd_B =575.09 cd_I =153.67 cd_O =187.75 Aggregated = 916.50	cd_B = 565.62 cd_I = 153.21 cd_O = 177.28 Aggregated = 896.11	cd_B = 557.72 cd_I = 152.82 cd_O = 169.13 Aggregated = 879.67

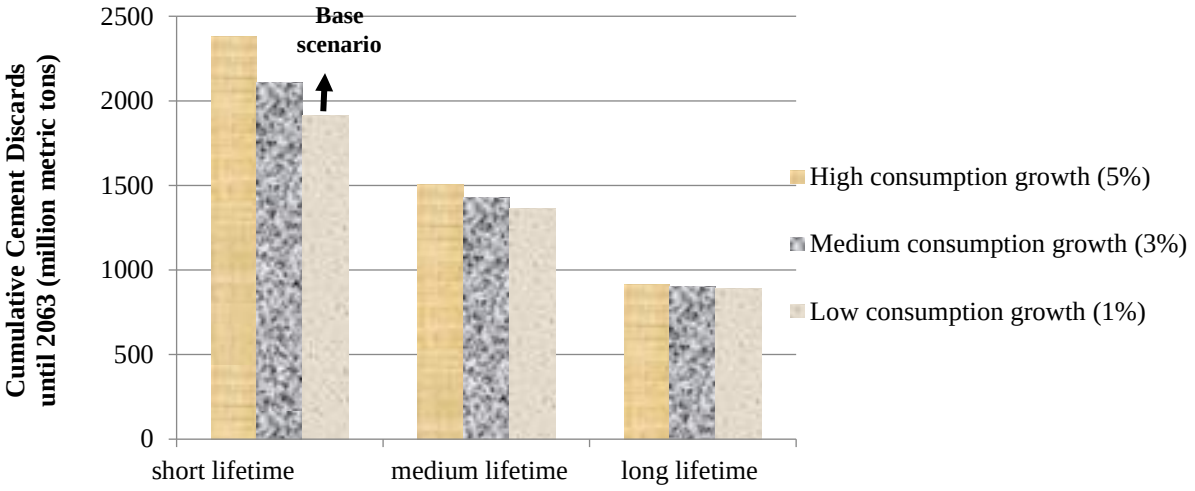

Fig. 8. Aggregated cumulative cement discards until 2063 for different scenarios

Buildings account for the largest portion of cement discards. This is because of the largest share of building in the cement end-use market. Note that in our classification, the category "Buildings" include residential, commercial and public buildings. However, by increasing the average lifetime of buildings it is possible to decrease cement discard from this sector. Cement discards from infrastructures and other end-uses are almost on the same scale.

Note that the model presented in this paper assumes that cement discards exit the economy completely at the end of the product service life. Sometimes this is not an actual assumption because old buildings or structures may be not completely demolished and a part of the structure (such as the foundation) remains in use. In other cases, some abandoned structures and buildings come back into use with an additional service life after appropriate repair and renovations measures. In the field of industrial ecology, the portion of the in-use stock of materials that have been put out of service but not demolished completely is referred to as "hibernating stocks". There is not reliable data or estimate about hibernating stock of cement in Iran and it cannot be determined with the presented model. It is necessary to perform empirical research in this regard to estimate the size of hibernating stocks. If hibernating stocks can be estimated, then those estimates should be subtracted from the estimated discard of this study to drive the true cement discards.

4.4. Past and Future Trends of Cumulative Aggregated Cement Consumption, Discards and in-Use

Cumulative aggregated cement consumption, discards and in-use for all scenarios are depicted in Figure 9. In scenarios with the short lifetime (S1-1, S1-2, S1-3) the model derived estimate of in-use cement stock for the year 2019 is 982 Mt (near 1Gt). This indicates that 83% of the cement utilized during the last half-century is still in use. For scenario S1-1, an estimate of in-use cement stock for 2063 is 6842 Mt. This is almost 7 times of in-use stock in 2018 and indicates that 74% of the cement utilized during the period 1963-2063 will be in use in 2063. However, for scenarios S1-2 and S1-3, an estimate of in-use cement stock for 2063 is 3670 and 2031 Mt respectively. Thus the portions of in-use cement from total cement consumption in 2063 for these scenarios are 64% and 52% respectively.

To understand the effect of structures lifetime on the stock of in-use cement it is helpful to compare the results from scenario S1-1 with S3-1. In both scenarios the growth rate of cement consumption is 5% but the mean lifetime of structures at scenario S3-1 is almost one and a half time of the corresponding lifetime in scenario S1-1. The result is that the portion of in-use

cement from total cement consumption in 2063 for S3-1 is 90%. Comparing this value with 74% for scenario S1-1, it is found that by increasing the mean lifetime of the structures, a larger fraction of total cement consumption will be in use and in other words, a smaller fraction of total cement consumption will be discarded.

4.5. Past and Future Trends of Annual Cement Consumption and Discards

Figure 10 shows cement consumption and discards (aggregated and sectoral) in each year for all scenarios. It is worth noting that to provide more resolution in charts of Figure 10 their vertical axes are depicted in different scales. As seen in the scenario S1-1, the annual aggregated cement discard in 2063 is above 100 Mt. From an environmental point of view this is the worst case. The portion of buildings from this stock of cement discard is over 60%. The great value of annual cement discard in this scenario originated from the bigger rate of cement consumption growth and the lower lifetime of structures in contrast with other scenarios. However, by decreasing the cement consumption growth rate and increasing the average lifetime of structures, annual cement discard will be reduced considerably. From an environmental point of view, the scenario S3-3 is the best where the annual cement discard in 2063 is slightly above 40 Mt. This addressed a reduction of near 60% comparing with the corresponding value in the scenario S1-1.

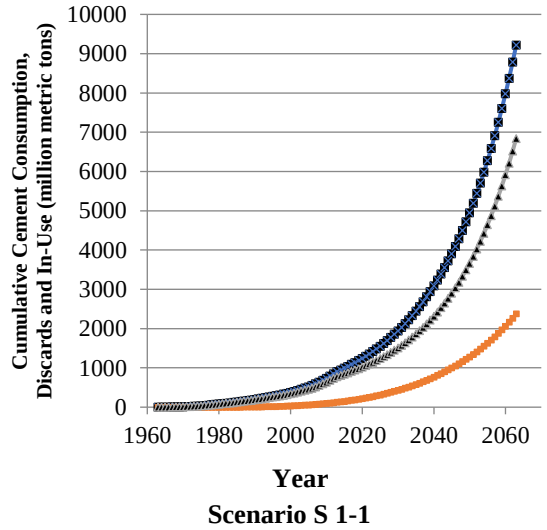

Scenario S 1-1

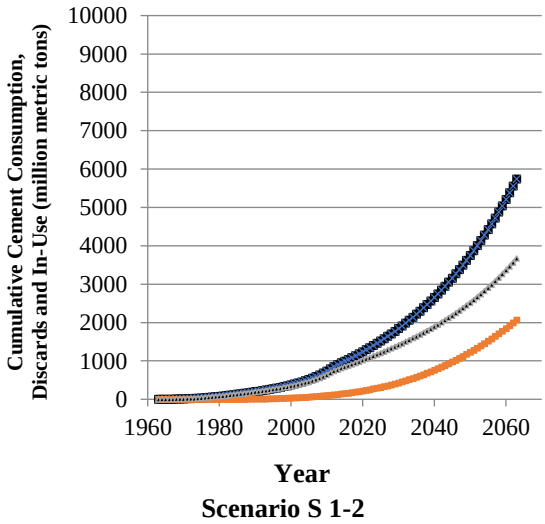

Scenario S 1-2

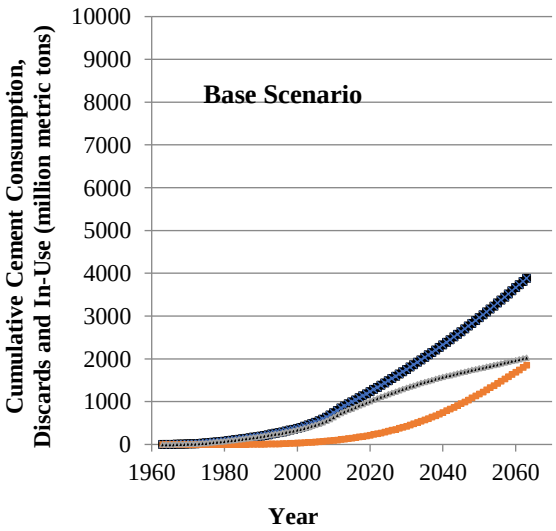

Scenario S 1-3

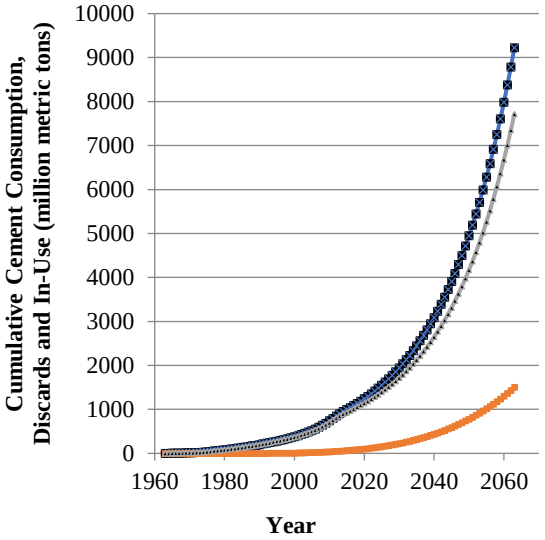

Scenario S 2-1

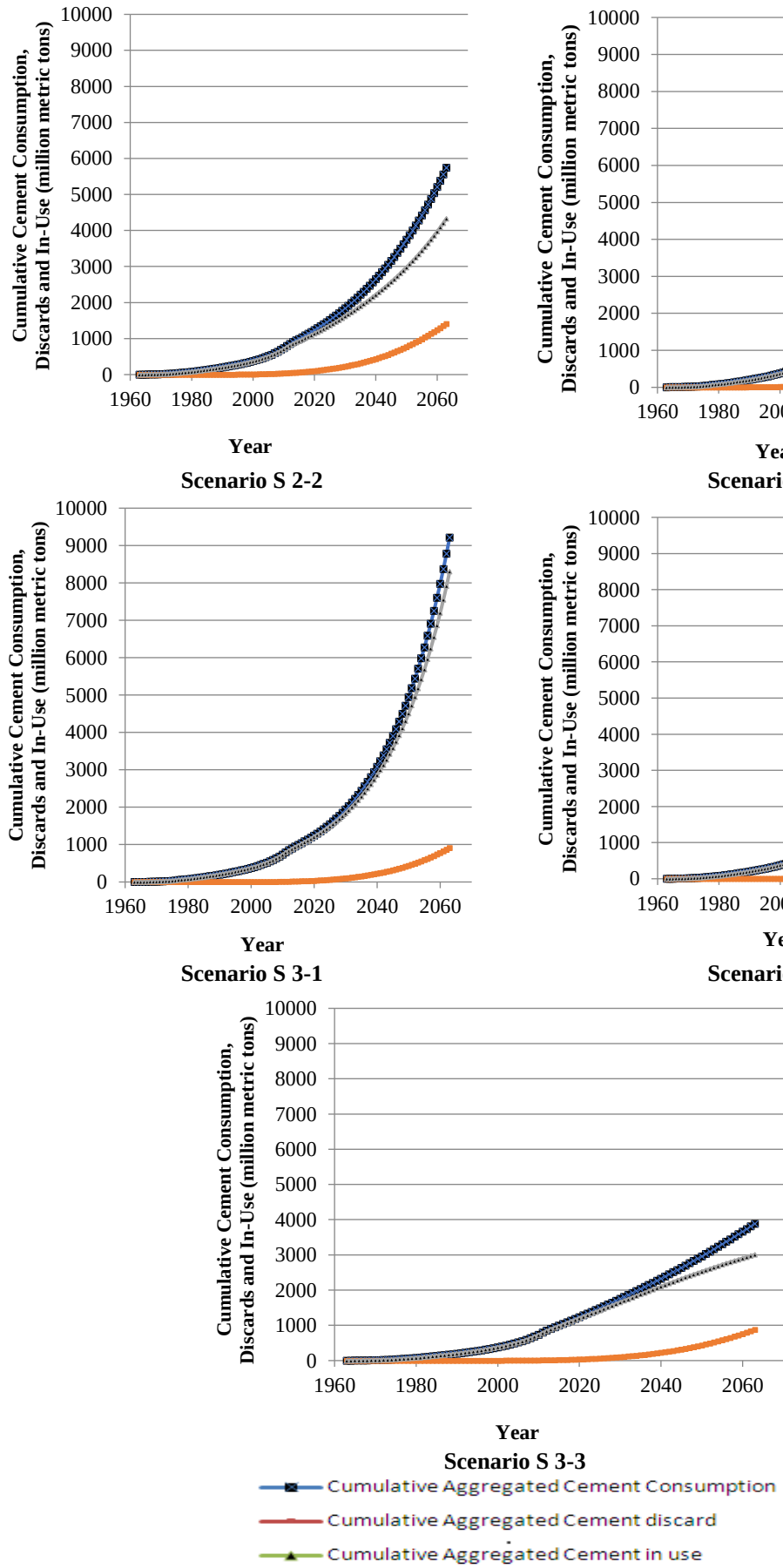

Fig. 9. Cumulative aggregated cement consumption, discards and in-use for all scenarios

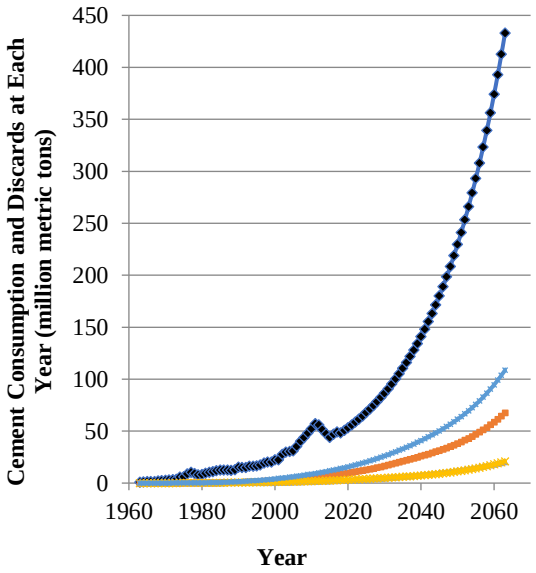

Scenario S 1-1

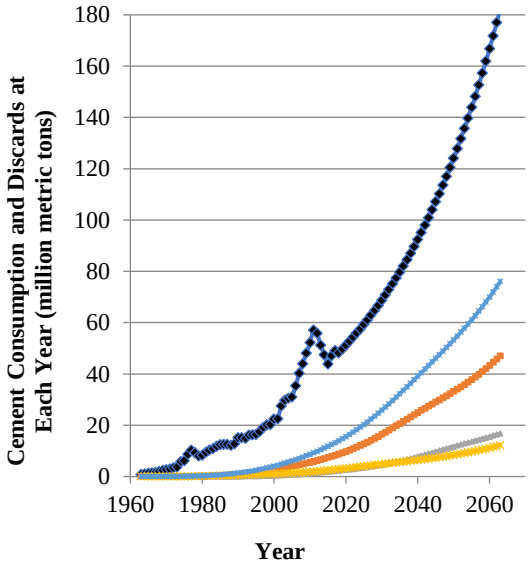

Scenario S 1-2

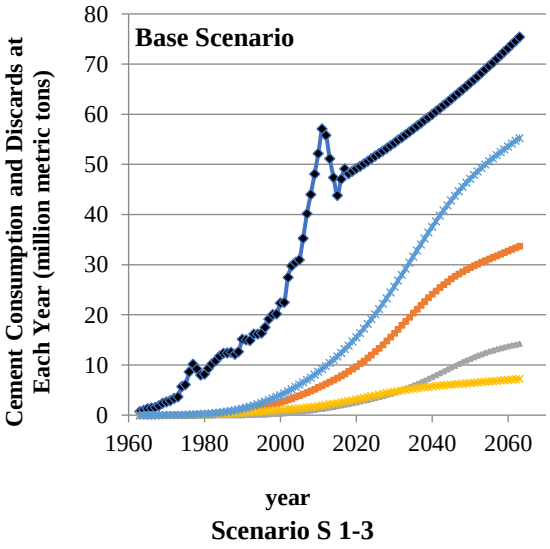

Scenario S 1-3

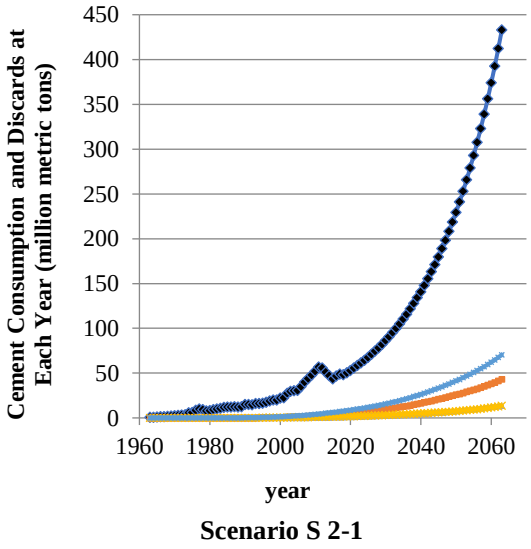

Scenario S 2-1

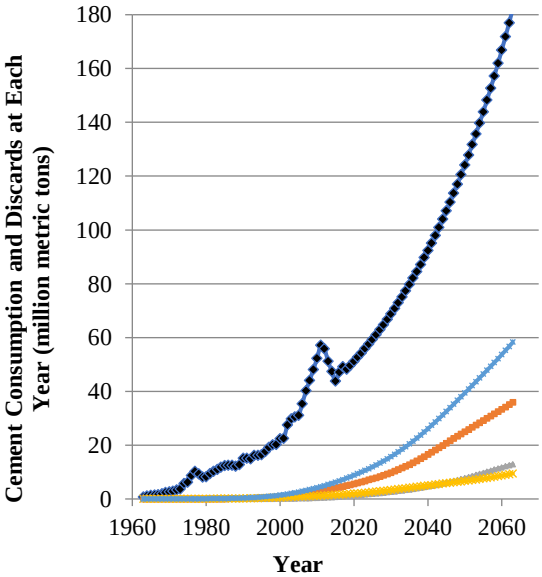

Scenario S 2-2

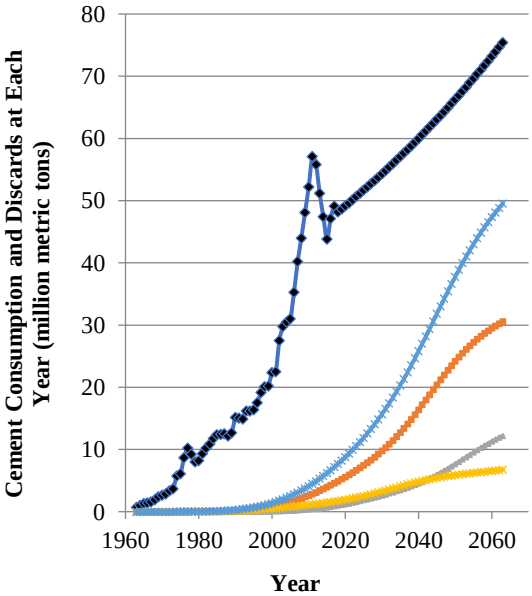

Scenario S 2-3

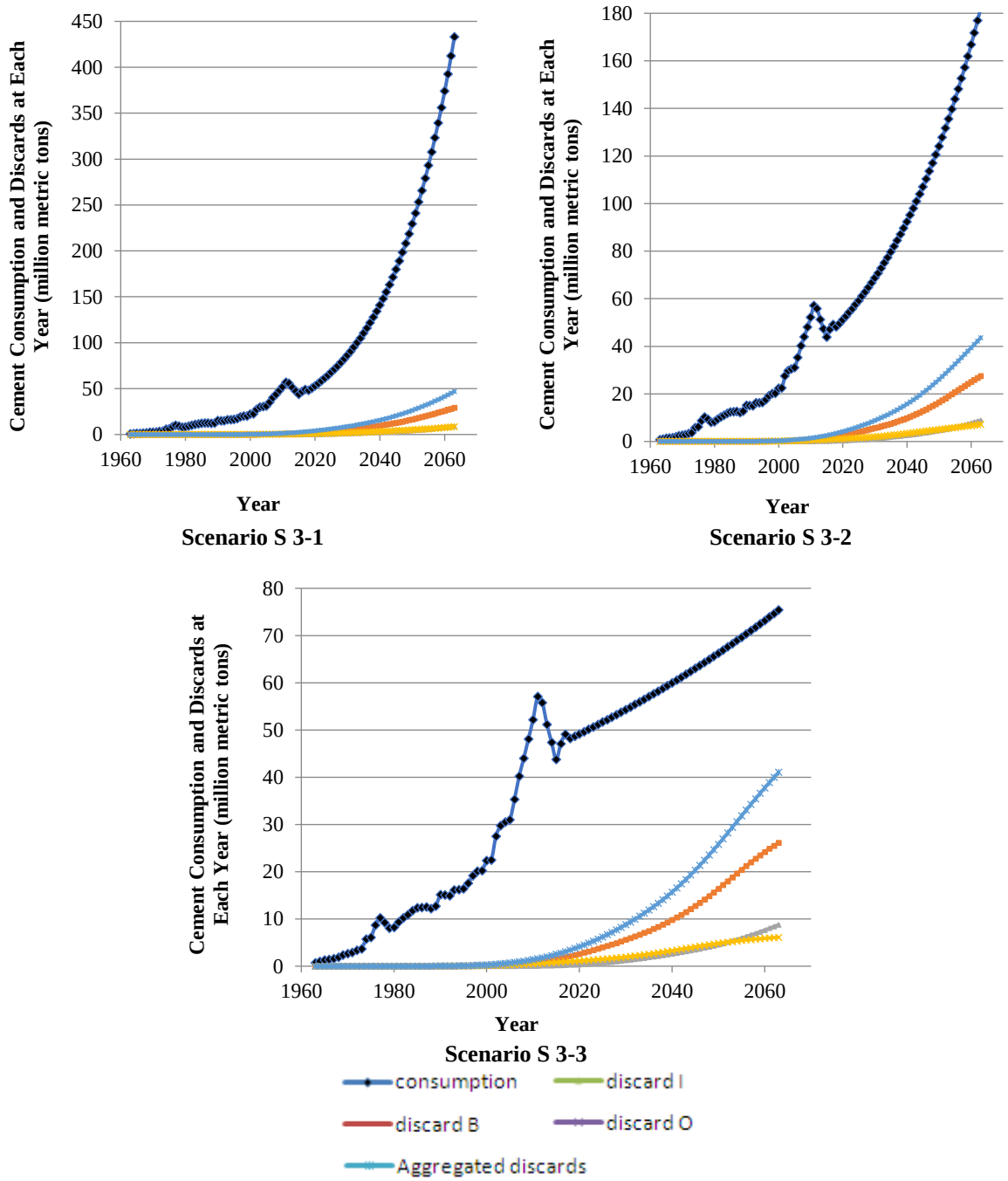

Fig. 10. Cement consumption and discards (aggregated and sectoral) at each year for all scenarios

4.6. Age Distribution of the Cement Discards for the Building Sector

Age distributions of cement discards for the building sector are demonstrated in Figure 11. In this context "age" means the time delay between entering a stock of cement into use and discarding it from usage. Three scenarios are selected for comparison. The normal distribution of the lifetime of buildings is graphically seen as assumed in the model formulation. Different average lifetimes of these scenarios are seen in these charts. In scenario S1-1, the biggest stock of cement discard that belongs to age category 20-25 years is 286 Mt. The biggest stock of cement discard in scenario S2-1 (belonging to the age category 35-40) is 180 Mt and the biggest stock of cement discard in scenario S3-1 (belonging to the age category 45-50) is 115 Mt. These findings indicate that longer lifetime of buildings results in smaller stock of cement discard in the time horizon of this study.

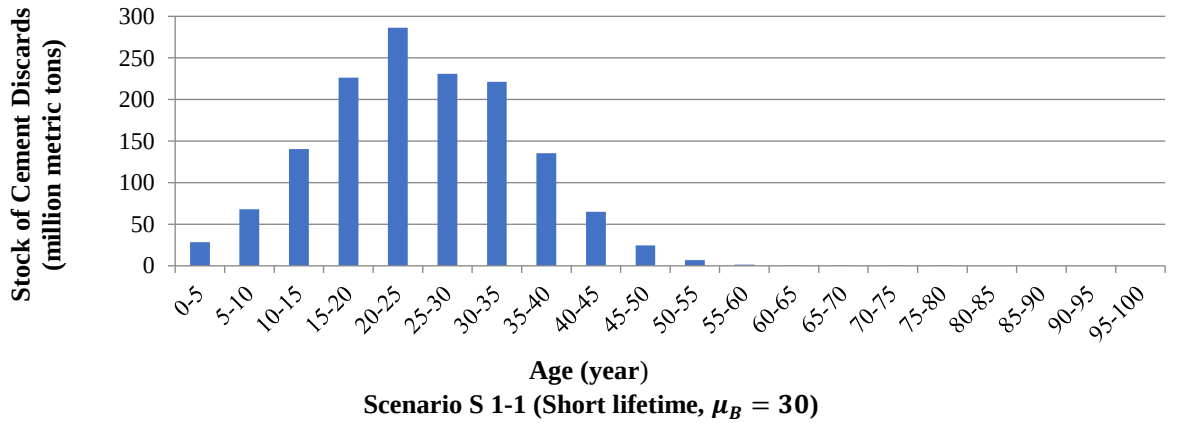

Scenario S 1-1 (Short lifetime, $\mu_B = 30$)

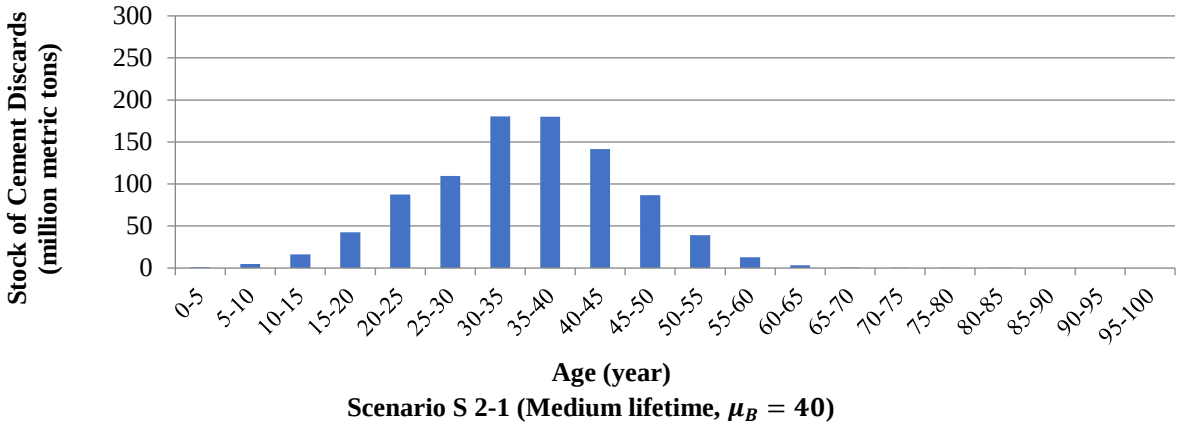

Scenario S 2-1 (Medium lifetime, $\mu_B = 40$)

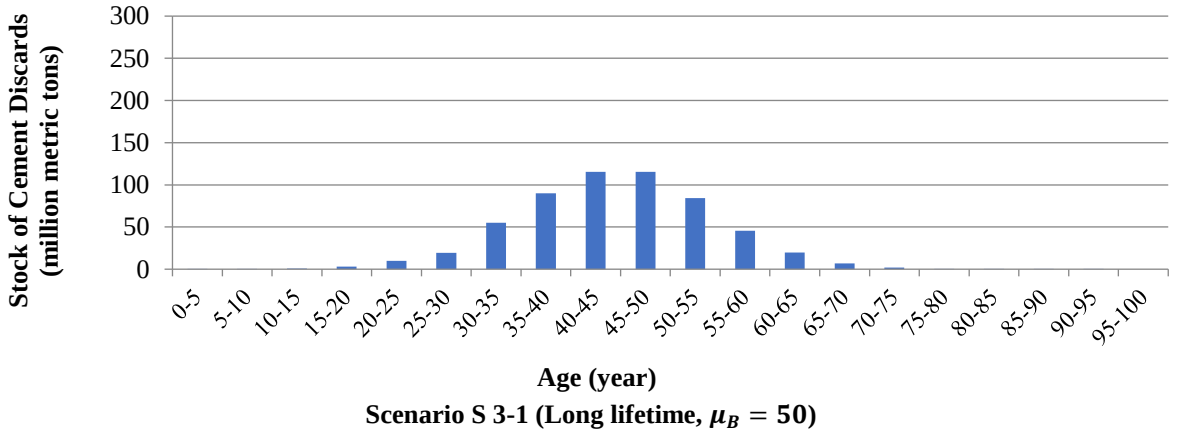

Scenario S 3-1 (Long lifetime, $\mu_B = 50$)

Fig. 11. Age distribution of cement discards for building sector

4.7. Other Results

Total cement discards originating from cement consumption at year t is presented in Figure 12. Three scenarios are selected for comparison. In the scenario S1-1 there are two peaks in the aggregated discard curve; one in 2010 and the other in 2030; meaning that the largest stock of cement discard originates from cement consumed at these times. But at scenarios S2-1 and S3-1 aggregated discard curve has one peak in 2010. The cause of second peak (i.e. 2030) in scenario S1-1 is the shortness of structures lifetime. In this scenario, the average of mean lifetimes among three sectors of cement end-uses is 30 years and a large portion of cement consumed at 2030 will be discarded until 2063 (i.e. the end of the time horizon of the study). But in scenarios S2-1 and S3-1, the average of mean lifetimes is 40 and 50 years respectively and a major portion of cement consumed in 2030 will be discarded after 2063 and hence has been excluded from this

study. It is notable that the cause of not seeing any peak before 2010 is the value of annual cement consumption in this interval that is lower than consumption in 2010. Briefly the stock of cement consumed in 2010 is large enough and has enough time to be discarded until 2063 (in all scenarios) so formed a peak in all three curves in Figure 12.

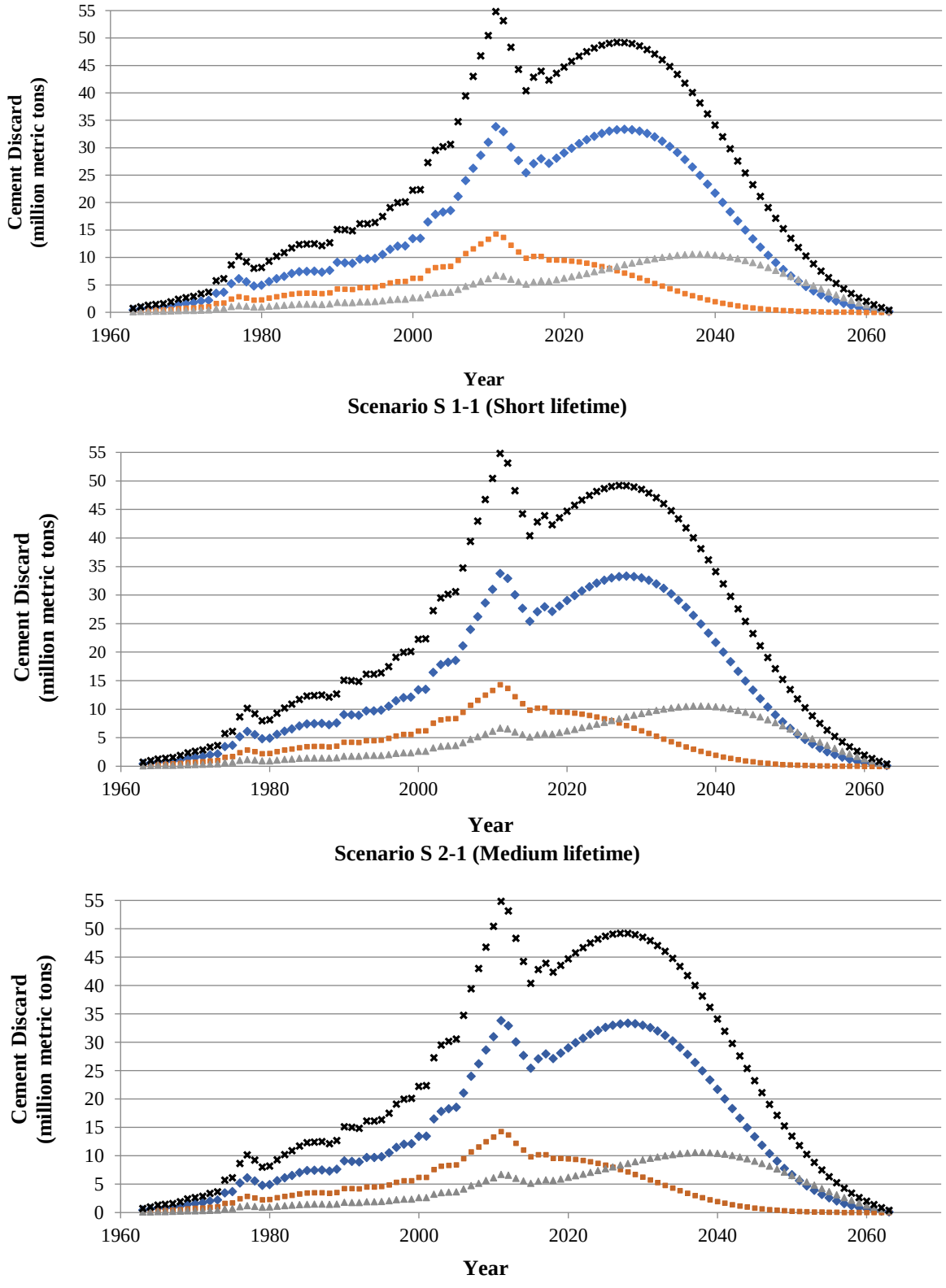

Fig. 12. Cement discard originating from cement consumption at each year

4.8. Strategic Recommendations for the Sustainability of Buildings and Civil Infrastructures

4.8.1. Prolonging the Lifetime of Buildings and Infrastructures to Increase the Longevity of in-Use Cement Stock and Reduce Cement Demand and Cement Waste

Findings in previous sections have some clear implications and advice for different stakeholders of cement industries in Iran. The building sector has the largest portion of the cement end-use market in Iran. However, buildings in Iran have a lower average lifetime in contrast with global norms (RHUDRC, 2019). As findings show, by increasing the mean lifetime of the buildings, the amount of cumulative cement discards until 2063 in this sector can drastically be decreased from 1167 Mt in the base scenario to 557 Mt in scenario 3-3. In scenario 3-1 (with high cement consumption growth rate) cumulative cement discards until 2063 is 575 Mt. This show that the decrease in cumulative cement discards will not be affected considerably by the cement consumption growth rate in the future. Thus designing and implementing initiatives to increase the mean lifetime of the buildings is a reliable strategy to decrease cement discards in the long term future.

From an environmental point of view performing initiatives to increase the mean lifetime of structures (especially buildings) is a valuable act. The cement industry is an energy-intensive industry and accounts for 15 % of industrial energy consumption and 4% of total energy consumption in Iran (Alihosseini et al., 2009). Furthermore, the cement industry is a pollutant one and emits one million tons of CO_2 to produce one million tons of cement. According to third Iranian communication to the United Nations framework convention on climate change (UNFCCC), with the production of about 34,432 Gg of CO_2, the cement industry is responsible for about half of process-based CO_2 emission in Iran (Department of Environment, 2017).

By increasing the mean lifetime of the structures, a smaller fraction of total cement consumption will be discarded. Thus there would be a lower need for new cement production (at least for domestic consumption) and this decrease energy consumption and CO_2 emission in cement industries. The direct benefit of a decrease in cement discard is that a lower amount of disposed material will be accumulated in the environment. This is more important because the recycling process of construction material including cement and concrete is not well developed still in Iran. These findings are in agreement with the research done by Miller (2020) in the USA. Miller showed that if cement longevity could increase by 50%, material resource demand and GHG emissions from concrete production will reduce 14% in the United States.

Findings in section 4.7 show that if the lifetime of the buildings and infrastructures can be almost doubled, the rise of the second waste peak will be pushed to the next half of the century. Therefore, for mid-term waste reduction, the most important strategy is to prolong the lifetime of the buildings and infrastructures. The first way is to ensure a greater service life for the new construction through the improvement of construction techniques and better urban planning. The second way is to enhance the existing building stock management by, for instance, regular renovation and rehabilitation.

4.8.2. Enhancing the Recycling of Concrete to Reduce Disposed Cement in the Environment

The dynamic MFA for the cement in the Iranian economy establishes a base to understand the mechanism of future generation of cement waste in Iran and the potential of various waste management strategies. It indicates that cement waste generation in the future strongly depends on the lifetime of the buildings and infrastructures. Therefore, as a mid-term

strategy, the main focus should be on prolonging the service life of the buildings whenever it is possible. However, all the scenarios demonstrate that the dramatic rise of cement waste generation will arrive sooner or later (note that cumulative cement discard at 2063 for different scenarios ranges from 879 Mt to 2377 Mt). Because this large amount of cement waste is unavoidable, concrete recycling should be emphasized to restrict the pressure on landfills and reduce impacts on the environment. Thus, it seems a suitable long-term strategy for Iran to increase concrete recycling capability and invest in enhancing concrete recycling technology, promoting high recyclability design, and so on. This is the main strategy to prevent the city's landfill capacity being used up completely by huge amounts of demolition waste. Suggestion for improving the recyclability of cement-based product has been provided in many studies in the context of construction and demolition (C&D) waste management such as Kapur et al. (2008), Hu et al. (2010b), Bergsdal et al. (2007b) and Huang et al. (2013).

4.8.3. Controlling the Growth of Cement Consumption in the Construction Industry

It is clear that prolonging the average lifetime of the in-use cement stock and reducing the cement intensity of buildings and infrastructures would be the top priority policies to reduce cement consumption in the foreseen future. Using supplementary cementitious materials (SCMs) is a way to reduce cement intensity that is attracting attention in the global research community. Askarinejad (2017) proposed three different methods of nanofabrication, using ultrasound irradiation, solvothermal /hydrothermal process and microwave irradiation, that were used for activation of two types of SCMs. Optimizing the use of cement by adoption of material efficiency strategies, would led to reduce demand throughout the entire construction value chain, helping to cut CO_2 emissions from cement production. Lower cement demand can be achieved through actions such as optimizing the use of cement in concrete mixes, using concrete more efficiently, minimizing waste in construction, and maximizing the design life of buildings and infrastructure (RHUDRC, 2019).

There are several additional means to benefit concrete buildings and infrastructure through increasing material efficiency. Improving yield loss during concrete manufacture, where possible, and reducing over-ordering of material for construction projects also can be considered as material efficiency improvement measures that could help in environmental impact mitigation. In current practice in Iran, 340 kg of cement are used to produce one cubic meter of concrete. The compressive strength of the resulting concrete is less than 25 MP. It is far from the planned 50 MP compressive strength for concrete (RHUDRC, 2019). Engineering concrete in such way to provide necessary properties with less material can reduce material flows associated with the concrete as well as structural systems needed to support the concrete. Eghbali et al. (2019) performed a study on the problem of material loss/construction waste in the Iranian building industry considering the impact of critical shortcomings in the stages of design, construction and supervision as the main phases of construction process. They concluded that construction project managers, engineers, contractors and workers in Iran believe that from 40 to 100 percent of construction wastes can be reduced using prefab construction methods. So, prefabrication would be considered as a solution to waste reduction in the Iranian building industry.

5. Conclusions

To the best of our knowledge, it is the first time a research was conducted to simulate the dynamic material flow of cement in Iran. The model developed in this research was a flow dynamic one and had a

retrospective and prospective approach. It was an open-loop model and ignored capacity constraints of the production and different scenarios of end of life. Like many other studies in this area a normal lifetime distribution was adopted for all structures. Different scenarios for the mean lifetime of structures and cement consumption growth were designed and simulated. Results showed a considerable and reliable impact of prolonging the lifetime of structures (especially buildings) on decreasing future cement discards. Furthermore, for long-term strategies, suggestions for enhancing the recycling of concrete to reduce disposed cement in the environment were offered. Controlling the growth of cement consumption in the construction industry by reducing cement intensity of buildings and infrastructures and minimizing construction waste are also recommended.

For future studies it is recommended to add a production-export sub-model with parameters such as export growth rate and production growth rate to assess the effect of cement production capacity, which is under installation in the near future. Considering recycling in the model aid to partition the estimated total discards into the landfill and recycling reservoirs and makes the model more realistic. Another direction for future research is incorporating other lifetime distribution functions such as Weibull and gamma in the model and investigating their effects on the results. Considering emissions such as CO_2 and other environmental impacts in the model provide a platform to assess the environmental effects of cement production, consumption and discards for the future. Finally, an important suggestion for the future researches may be expressed as developing a stock dynamic model in which the stock of service units is the driver for the material inflows.

6. References

Ahmadi, R. and Karimi, A. (2015). "Statistical analysis of production, consumption and universal trade of the cement industry of Iran in comparison with the world's main countries", *Iranian Journal of Official Statistics Studies* 26(1), 107-128, (in Persian).

Alihosseini A., Abbaszadeh A. and Bastani, D. (2009). "Necessity of revision in energy consumption and the ways to reduce energy consumption in cement industry", *Environment, Science and Technology*, 16(93), 75-83, (in Persian).

Askarinejad, A. (2017). "Using different methods of nanofabrication as a new way to activate supplementary cementitious materials, A review", *Civil Engineering Infrastructures Journal*, 50(1), 1-19.

Bergsdal, H., Brattebø, H., Bohne, R.A. and Müller, D.B. (2007). "Dynamic material flow analysis for Norway's dwelling stock", *Building Research and Information*, 35(5), 557-570.

Cao, Z., Shen, L., Liu, L., Zhao, J., Zhong, S., Kong, H. and Sun, Y. (2017). "Estimating the in-use cement stock in China: 1920–2013", *Resources, Conservation and Recycling*, 122, 21-31.

Cao, Z., Shen, L., Zhong, S., Liu, L., Kong, H. and Sun, Y. (2018). "A probabilistic dynamic material flow analysis model for Chinese urban housing stock", *Journal of Industrial Ecology*, 22, 377-391.

Condeixa, K., Haddad, A. and Boer, D. (2017) "Material flow analysis of the residential building stock at the city of Rio de Janeiro", *Journal of Cleaner Production*, 149, 1249-1267.

Department of Environment (2017). "Islamic republic of Iran's third national communication to United Nations framework convention on climate change (UNFCCC)", Iran National Climate Change Office, Available at: http://unfccc.int/sites/default/files/resource/ Third National communication IRAN.pdf.

Dorafshani, A. (1996). "Studying cement industry of Iran (1968-1994)", M.Sc. Thesis, Shaid Beheshti University, Tehran, Iran, (in Persian).

Edwards P. (2017). "The cement sector of Iran", *Global Cement Magazine*, Pro Global Media, available at: https://www.globalcement.com/ magazine/articles/1022-the-cement-sector-of-iran.

Eghbali, S., Azizzadeh Araee, R. and Mofrad Boushehri, A. (2019). "Construction Waste Generation in the Iranian Building Industry", *Civil Engineering Infrastructures Journal*, 52(1), 1-10.

Heibati, F. and Farzin, A. (2005) "The estimation of cement demand in Iran based on time series models", *Journal of Economics Research*, 5(19), 181-210, (in Persian).

Horvath, A. (2004). "Construction materials and the environment", *Annual Review of Environment and Resources*, 29, 181-204.

Hu, M., van der Voet, E. and Huppes, G. (2010 b). "Dynamic material flow analysis for strategic construction and demolition waste management

in Beijing", *Journal of Industrial Ecology* 14(3), 440-456.

Hu, M., Pauliuk, S., Wang, T., Huppes, G., van der Voet, E. and Müller, D.B. (2010a). "Iron and steel in Chinese residential buildings: A dynamic analysis", *Resources, Conservation and Recycling*, 54(9), 591-600.

Huang, T., Feng S., Tanikawa, H., Fei, J. and Han, J. (2013). "Materials demand and environmental impact of buildings construction and demolition in China based on dynamic material flow analysis", *Resources, Conservation and Recycling*, 72, 91-101.

Huang, W., Huang, Y., Lin, S., Chen, Z., Gao, B. and Cui, S. (2018). "Changing urban cement metabolism under rapid urbanization, A flow and stock perspective", *Journal of Cleaner Production*, 173, 197-206.

Iran Cement Statistics (2019). Available at: http://www.irancement.com/new_site_12_7_88/ENGLISH/e-statistics.html, accessed at 2019.

Kapur, A. and Keoleian, G.A. (2009). *Dynamic modeling of material stocks: A case study of in-use cement stocks in the United States*, A book chapter in: Ruth, M., Davidsdottir, B. Changing stocks, Flows and Behaviors in Industrial Ecosystems, Edward Elgar Pub, 40-53.

Kapur, A., Keoleian, G.A., Kendall, A. and Kessler, S.E. (2008). "Dynamic modeling of in-use cement stocks in the United States", *Journal of Industrial Ecology*, 12(4), 539-556.

Kleijn, R., Huele, R., and Van der Voet, E. (2000). "Dynamic substance flow analysis: The delaying mechanism of stocks with the case of PVC in Sweden", *Ecological Economics*, 32(2), 241-254.

Miller, S.A. (2020). "The role of cement service-life on the efficient use of resources", *Environmental Research Lett*er, 15, 024004

Müller, D.B., Bader, H.P. and Baccini, P. (2004). "Long-term coordination of timber production and consumption using a dynamic material and energy flow analysis", *Journal of Industrial Ecology*, 8(3), 65-87.

Müller, D.B. (2006). "Stock dynamics for forecasting material flows, A case study for housing in The Netherlands", *Ecological Economics*, 59, 142-156.

Namazi, F. and M. Bastami. (2019). "Pathology of underlying problems in cement industry of Iran", Islamic Parliament Research Center of The Islamic Republic of IRAN, Report Serial Number 16305, (in Persian).

Road, Housing and Urban Development Research Center (RHUDRC). (2019). "Comprehensive document on concrete perspective", Available at: https://www.bhrc.ac.ir/Portals/0/PDF-Word/dastresi/1404.pdf, accessed at 2019, (in Persian).

Sartori, I., Bergsdal, H., Müller, D.B. and Brattebø, H. (2008). "Towards modeling of construction, renovation and demolition activities: Norway's dwelling stock, 1900-2100", *Building Research and Information*, 36(5), 412-425.

Surahman, U., Higashi, O. and Kubota, T. (2017). "Evaluation of current material stock and future demolition waste for urban residential buildings in Jakarta and Bandung, Indonesia: Embodied energy and CO_2 emission analysis", *Journal of Material Cycles and Waste Management*, 19, 657-675.

The Global Cement Report™. (2017). 12th Edition, Available at: https://www.cemnet.com/Publications/Item/176633/Global-cement-report-12.html.

Wang, Y., Chen, P.C., Ma, H.W., Cheng, K.L. and Chang, C.Y. (2018). "Socio-economic metabolism of urban construction materials: A case study of the Taipei metropolitan area", *Resources, Conservation and Recycling*, 128, 563-571.

Wiedenhofer, D., Steinberger, J.K., Eisenmenger, N. and Haas, W. (2015). "Maintenance and expansion: Modeling material stocks and flows for residential buildings and transportation networks in the EU25", *Journal of Industrial Ecology* 19(4), 538-551.

Civil Engineering Infrastructures Journal 2021, 54(2): 405-421
DOI: 10.22059/CEIJ.2021.302094.1672

TECHNICAL NOTE

Comparison of Nonlinear Dynamic Analysis of Time History and Endurance Time Method in Tall Structures with Frame-Wall System

Mohammadizadeh, M.R.[1]* and Jafarzadeh, A.[2]

[1] Associate Professor, Department of Civil Engineering, University of Hormozgan, Bandar Abbas, Iran.
[2] M.Sc., Islamic Azad University, Bandar Abbas Branch, Bandar Abbas, Iran.

Received: 03May 2020; Revised: 29 Sep. 2020; Accepted: 14 Dec. 2020

ABSTRACT: In this study, the seismic response of tall concrete structures with a special dual frame-wall concrete system is investigated using the endurance time method, and the results are compared with nonlinear time history analysis results. For this purpose, first, appropriate analytical models including buildings with concrete framed-wall system and 20, 30, and 40 stories are modeled non-linearly in PERFORM 3D software, and then, main nonlinear time history analyses are carried out for seven ground motions (accelerogram) further from the fault based on the FEMA P695 code and the endurance time accelerogram of (in) series. The results of the analysis are compared using indices (shear, relative displacement, and acceleration). The results indicate that the endurance time method is accurate in two indices of shear and acceleration, but the accuracy of the relative displacement index of the floor decreases as the number of stories of the structure increases.

Keywords: Dual Concrete Lateral Resistant System, Endurance Time Method, Nonlinear Time History Analysis, Tall Structure.

1. Introduction

The growth and development of new tall structures began in the 80s of the nineteenth century with commercial and residential applications. Structurally, a tall structure is one which its height imposes special considerations or a structure with a period of more than 0.7 seconds. Due to the high number of degrees of freedom and the complexity in the behavior of tall structures, the analysis of tall structures requires the methods that predict the actual behavior of these structures with acceptable accuracy and the least time possible. Endurance time method is a seismic analysis that allows engineers and researchers to obtain the most information from the state of the structures with the lowest computational cost. This warrants provision of a scientific documentation of the precision of this method in the field of seismic design of which unknowns and uncertainties are an integral part, in order to take a step towards the better introduction of this method. It is necessary to create a nonlinear model and to perform nonlinear analysis of the time history in order to design tall structures. Endurance time method can be used to reach more comprehensive responses in less

* Corresponding author E-mail: mrzmohammadizadeh@yahoo.com

time compared to the natural accelerogram method.

One of the most efficient lateral resistant systems used in tall structures is the wall frame system. In recent years, studies have been carried out on structures with a lateral resistant frame-wall system (Memari et al., 2000; Kim et al., 2007; Shin et al., 2010; PEER, 2010). Mali et al. (2010) have reported details of the nonlinear modeling of structures with lateral resistant concrete frame-wall system. Using the idea of the cardiac test, Estekanchi et al. (2004) presented the idea of endurance time method for the first time. Estekanchi et al. (2007) also showed the application of the endurance time method in seismic analysis within the linear range. In that research, the generation of acceleration functions related to the endurance time method and results of the modeling of multiple frame analysis were examined. Estekanchi et al. (2008) compared the failure indices in the methods of time histories and endurance time. Riyahi and Estekanchi (2010) compared the methods of time history and endurance time in the study of steel frames. Valamanesh and Estekanchi (2010) and Valamanesh (2010) presented a method for three-dimensional analysis using the time-endurance method and examined the accuracy of this method in the three-dimensional analysis of moment frames in the elastic range. Estekanchi et al. (2011) applied the endurance time method in seismic assessment of steel frames to examine the adequacy of this method for these structures.

Also, Foyouzat and Estekanchi (2016) examined concerning application of rigid-perfectly plastic spectra in improved seismic response assessment by the endurance time method which played a great role in strengthening and expanding it. For other investigations related to the endurance time method (one can refer to Basim and Estekanchi, 2015; He et al., 2015; Guo et al., 2016; Tafakori et al., 2017; Bai et al., 2019; Li et al., 2019; Seyed Kolbadi et al., 2020).

No research has been conducted yet to investigate the structural response using the endurance time method in tall structures. So, in this research, the seismic response of tall concrete structures with a lateral resistant frame-wall system using nonlinear analysis of time history and endurance time methods has been investigated. Therefore, the buildings with a special resistant moment frame system and shear core with 20, 30 and 40 stories including coupling shear wall in one direction are analyzed using the powerful 3D Perform software with 7 different accelerogram records. The buildings are designed in accordance with the ACI 318 (2014) regulations for specific norms and indices such as story drift, story shear and the acceleration of stories are calculated.

2. The Concept of the Endurance Time

The concept of the endurance time method can be excellently explained with a hypothetical experiment. For example, the structural performance of three different structures with unspecified characteristics is evaluated against earthquakes. In this evaluation, these three structures are placed on a shake table. The experiment begins with vibrational stimulation that intensifies as the time passes, and the structure response increases with the passage of time and subsequently the amplitude of the stimulation increases, and the state of the structure changes from linear and undamaged mode to a partial failure mode, to yield points of some components and ultimately reaches dynamic instability level subsequent to entering into the nonlinear region and increasing of the structure response amplitude.

The values of the failure indices can be graphed directly versus time, for example, the maximum relative displacement of the stories is plotted in Figure 1. As it can be seen, in general, the range of failure indices in frame A is higher than others and it is lower than the rest of them in frame B. As a result, it can be said that the performance of

the B structure is more favorable than the other two structures at different intensities. It is also possible to conclude from the response curves that frames A, C and B reach the failure mode after 8, 13 and 18 seconds, respectively.

As a result, regarding these time periods and the corresponding intensity of the structure stimulation, it is possible to achieve the extent of the failure of the structures and the maximum period of time that they are able to withstand the load imposed by increasing acceleration function. If these three structures are three different designs for one purpose and their performance level and the soil type of the region are the same, it can be concluded that the structure B has a more favorable performance than the other two structures. In this case, if the acceleration function is capable of meeting the requirements of the design in accordance with regulations, the target time can be set for a standard structure to be allowed to fail to the specific degree at that time. In the endurance time method, the incremental changes of acceleration are considered linear in time. In Figure 1a, the acceleration function-time graph is illustrated. As shown in Figure 1a, the duration of the acceleration function and its intensity increase over time. Figure 1b illustrates the behavior of the frames examined under increasing acceleration function and Figure 1c shows the response of different structures to this acceleration function in time.

3. Modeling and Design of Buildings

For the purpose of this study, three concrete buildings with a special dual resistant lateral system (the resistant lateral system includes a special moment frame with a shear wall, each able to withstand at least 25% and 50% of the earthquake load, respectively) are considered and the number of stories are selected to be 20, 30, and 40. In the design of these buildings, the ACI318-14 regulations have been used. The structures have been modeled in three dimensions and analyzed through ETABS2016 software by spectral dynamic analysis using the 2800 Standard Design (2014) spectrum of Iran (to consider the effect of earthquake force). The 2800 standard design spectrum of Iran is illustrated in Figure 2.

In all buildings, the height of the stories is the same and equal to 3.4 meters, as shown in Figure 3. The dead and live loads distributed on the floors are considered to be 6 KN/m^2 and 2 KN/m^2, respectively. The characteristic strength of steel and concrete is considered to be F_y = 400 Mpa and F_c = 30 Mpa. Regarding the construction of buildings in areas with high relative risk, the acceleration coefficient of the design (A) is assumed to be (0.3). The experimental period is calculated from the following Eq. (1):

$$T = 0.05H^{3/4} \quad (1)$$

where T and H: are period and height of the structure, respectively.

The soil of the region is assumed to be of type ш and the behavioral coefficient of the resistant lateral dual system is based on the fourth edition of the code for calculating earthquake load in Iran (the standard 2800). Therefore, the buildings are designed according to the regulations of the seismic design of the mentioned code. Tables 1-3 show the designed sections of different stories separately for each building.

4. Nonlinear Structural Modeling

In the nonlinear modeling of structures in the PERFORM software (Powell and Graham, 2011), the beam- column elements with joints on both ends of the element and fiber elements (referred to in ASCE41-13, 2013) have been used for elements of the beam, column and wall, respectively. In the modeling of wall elements, a combination of concrete and steel fibers (single-dimensional fiber threads) has been used, as shown in Figure 4. The number and distribution of fibers at the wall section must be optimized. It should be noted that

the use of few fibers or ones with inappropriate distribution cannot properly model the behavior of the wall.

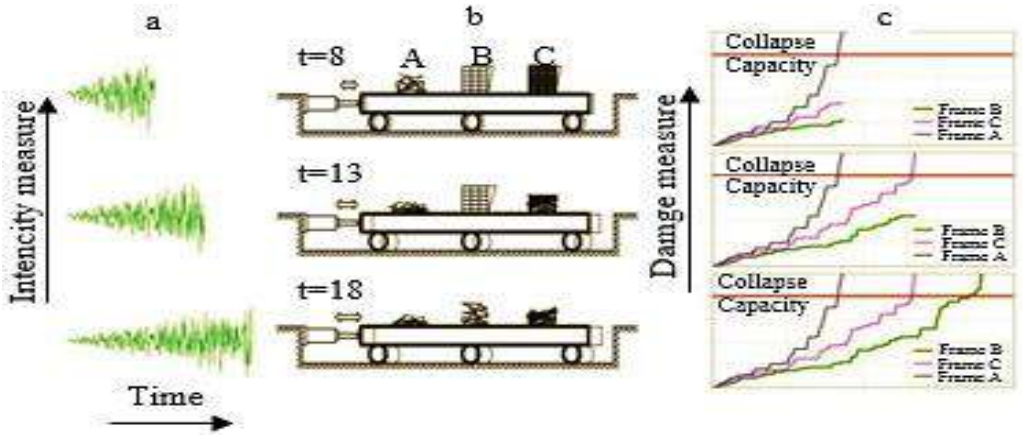

Fig. 1. The concept of endurance time in the form of hypothetical experiment (Valamanesh, 2010)

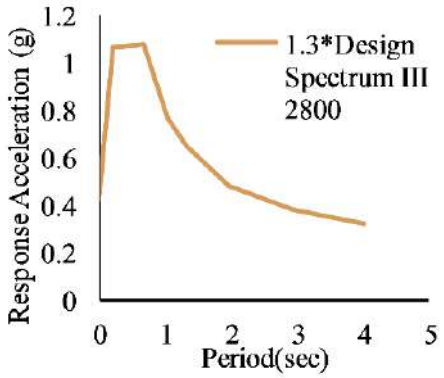

Fig. 2. The 2800 standard design spectrum (Standard 93-2800)

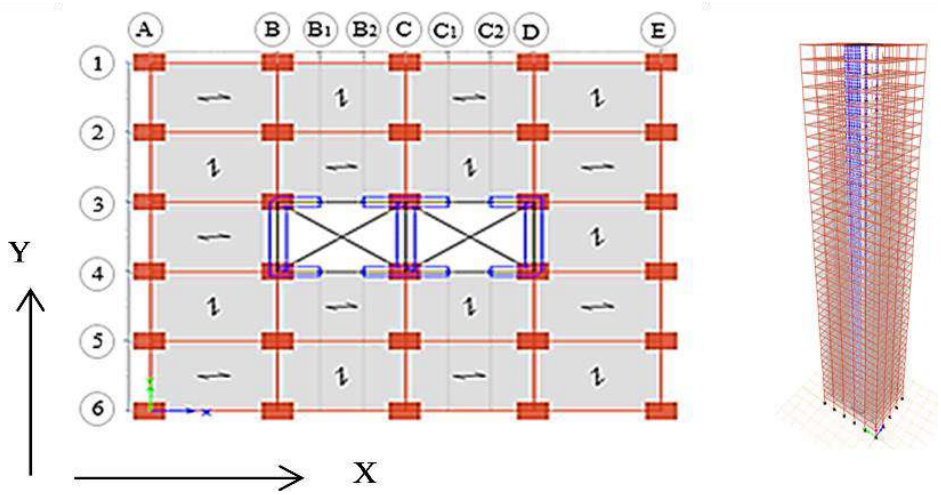

Fig. 3. Plans for buildings with 20, 30 and 40 stories as well as the 3D form

Table 1. Designed sections of the 20-story building

Story	Column			Beams									Wall
				Beam			Collector			Coupling			
	ID	b	h	ID	b	h	ID	b	h	ID	b	h	
1-3	C95×95	95	95	B 60×80-1	80	60	CB 80×80-1	80	80	CPB 160×90-1	90	160	W60
4-6	C85×85	85	85	B 60×80-2	80	60	CB 80×80-2	80	80	CPB 160×90-2	90	160	W40
7-10	C70×70	70	70	B 60×60-1	60	60	CB 70×60-1	70	60	CPB 160×90-3	90	90	W30
11-14	C60×60	60	60	B 60×60-2	60	60	CB 70×60-2	70	60	CPB 150×60	60	60	W25-1
15-20	C50×50	50	50	B 60×50	60	50	CB 50×70	50	70	CPB 130×50	50	50	W25-2

Table 2. Designed sections of the 30-story building

Story	Column			Beams									Wall
				Beam			Collector			Coupling			
	ID	b	h	ID	b	h	ID	b	h	ID	b	h	
1-3	C 110×110	110	110	B 70×90	90	70	CB 90×90	90	90	CPB 170×100	100	170	W70
4-7	C 95×95	95	95	B 60×80-1	80	60	CB 80×80-1	80	80	CPB 160×90-1	90	160	W60
8-12	C 85×85	85	85	B 60×80-2	80	60	CB 80×80-2	80	80	CPB 160×90-2	90	160	W40
13-18	C 70×70	70	70	B 60×60-1	60	60	CB 70×65-1	70	65	CPB 160×90-3	90	160	W30
19-24	C 65×65	65	65	B 60×60-2	60	60	CB 70×65-2	70	65	CPB 150×60	60	150	W25-1
25-30	C 50×50	50	50	B 60×50	60	50	CB 40×70	40	70	CPB 140×50	50	140	W25-2

Table 3. Designed sections of the 40-story building

Story	Column			Beams									Wall
				Beam			Collector			Coupling			
	ID	b	h	ID	b	h	ID	b	h	ID	b	h	
1-3	C 150×150	150	150	B 100×100	100	100	CB 100×120-1	120	100	CPB 170×100-1	100	170	W80
4-8	C 135×135	135	135	B 90×90	90	90	CB 100×120-2	120	100	CPB 170×100-2	100	170	W70
9-14	C 115×115	115	115	B 70×90	90	70	CB 80×100-1	100	80	CPB 160×90-1	90	160	W60
15-20	C 95×95	95	95	B 60×80-1	80	60	CB 80×100-2	100	80	CPB 160×90-2	90	160	W50
21-26	C 85×85	85	85	B 60×80-2	80	60	CB 80×100-3	100	80	CPB 160×90-3	90	160	W40
27-32	C 70×70	70	70	B 60×60	60	60	CB 70×65	65	70	CPB 150×60	60	150	W30
33-40	C 55×55	55	55	B 60×50	60	50	CB 40×70	70	40	CPB 140×50	50	140	W25

On the other hand, the use of a large number of fibers increases the cost of computing. The behavior of the fibers is simulated using a model that is assigned as material properties (the stress-strain curve of fiber material) and in the center of each wall element. (Thomsen et al., 2004; Birely et al., 2008). Inelastic modeling of moment frame systems includes modeling for bending members (beam and column) and joints. In these types of systems, inelastic deformation should occur in bending joints in the beams and columns. It should be noticed that fulfilling the minimum code requirements does not necessarily prevent the creation of a plastic joint in the column and the nonlinear deformations of the connection area in the column-beam joints. Therefore, non-linear models should include the points mentioned above unless the demand to capacity ratio is small enough to prevent it from occurring.

Typically, the beam-column elements are modeled using a central joint or fiber section. Although the fiber model generally has the ability to more accurately model the initial non-linear cracking effects in concrete and the distribution of concrete yielding, its ability in describing the failure associated with the sliding of the reinforcing bar in concrete connections and the local buckling and failure of the rebar is limited. Plastic joint models are often more applicable to describe the general behavior of force-deformation (moment-rotation), including the strain softening. Modeling concrete frames that consider seismic design requirements is somewhat more difficult than steel frames. The hardness of members is affected by the cracking of the concrete. The beam-column connection is affected by the cracking of the concrete and the rebar slipping. The response is also sensitive to the axial force after reaching the yield point while the columns and connections enter the plastic region.

ASCE41-13 and PEER/ATC72 have developed models and recommendations for determining the stiffness of the members, the features of the nonlinear joint of the member, and strategies for connection modeling, which are outlined in the following. The structural model should be able to simulate structural failure and collapse of the structure when the structure is under severe earthquake. Determining crucial failures and collapse modes is a key factor in the selection of nonlinear

analytical model.

The general view of the generated model for a frame is as follows: A beam-column element with a central nonlinear rotational joint at each end and a beam-column connection with limited length using five non-linear centralized springs to model the shear failure of the connection plate and the sliding of the reinforcement bar in each side of the connection. The modeling is schematically illustrated in Figure 5.

Since the probability of failure in the beam and column of the concrete moment frame is higher, the accurate modeling of the inelastic effect in the beam-column elements is essential in the collapse modeling. The centralized joint is selected due to its simplicity and the inherent limitations of the fiber model (using a fiber model in the simulation of the strain softening associated with the rebar buckling is difficult).

The fiber model represents the distribution of plasticity along the member and modeling can be done so that it stimulates the behavior caused by concrete failure from the initiation of the crack to concrete breakage. However, the existing steel models do not have the ability to represent the buckling behavior and the rebar failure. Because of such limitations, the available fiber model is not adequate enough to simulate the collapse. Despite the fact that a centralized joint model does not have the accuracy of the fiber model, it can be calibrated in such a way that it shows the failure issued from the buckling of the rebar and the failure of the rebar stirrup and results in the loss of concrete confinement (Mander et al., 1988).

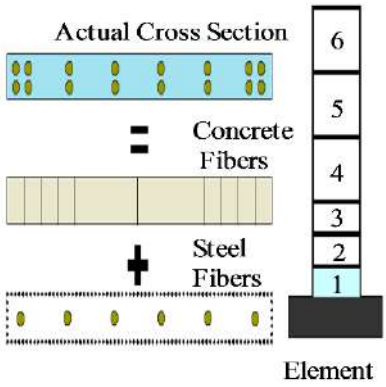

Fig. 4. Fiber modeling shear wall elements (PEER, 2010)

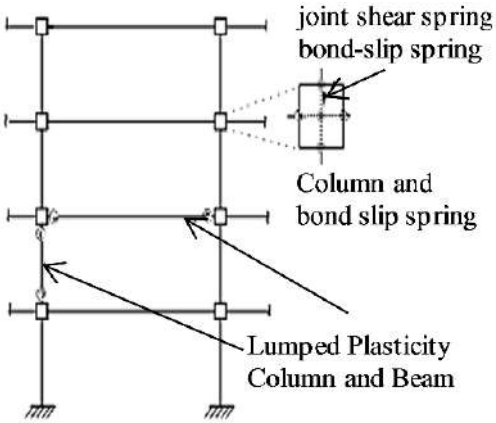

Fig. 5. Schematic representation of frame construction members (FEMA P695, 2009)

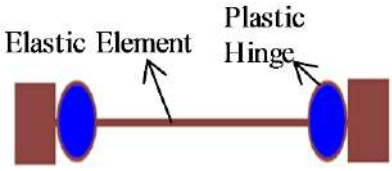

Fig. 6. Simple form of plastic joint (Hasleton et al., 2008)

Figure 6 depicts a simple view of a centralized joint model, and Figure 7 illustrates the moment-rotation behavior of the plastic joint. This model is composed of an elastic element with two plastic joints on both ends. The parameters required for defining the plastic joint behavior (Figure 7) include elastic hardness e_k, yield moment M_y, ultimate moment M_c, plastic rotation originated from the ultimate moment θ_{cap}^{pl}, and slope of the strain softening region K_c, which have been illustrated in Figure 7.

Eq. (2) has been developed and calibrated in order to obtain the yield moment of concrete member (Hasleton and Deierlein, 2007).

$$\frac{M_y}{bd^3} = \varphi_y \left(E_c * \frac{\xi^2}{2}\left(\frac{1+\delta'}{2} - \frac{\xi_y}{3}\right) + \frac{E_S(1-\delta)}{2}\left[(-\xi_y)\rho_1 + (\xi_y - \delta')\rho_2 + \frac{\rho_v}{6}(1-\delta')\right]\right)$$

$$\alpha = \frac{E_S}{E_C} \quad \xi_y = (\alpha^2 A^2 + 2\alpha B)^{\frac{1}{2}} - \alpha A \quad \varphi_y = \frac{f_{y1}}{E_s(1-\xi_y)d} \quad \rho_1 = \frac{A_s}{bd} \quad \rho_2 = \frac{A_s'}{bd} \quad \rho_v = \frac{A_{sw}}{bd}$$

$$s' = \frac{d'}{d} \qquad B = \rho_1 + \delta'\rho_2 + \frac{\rho_v(1+\delta')}{2} + \frac{N}{bdf_{y1}} \qquad A = \rho_1 + \rho_2' + \rho_v + \frac{N}{bdf_{y1}} \tag{2}$$

where M_y: is the single-axial yield moment, φ_y: is the yield curvature, f_{y1}: is the yield stress of tensile rebar, ε_y: is the neutral axis depth in yield, d': is the distance between the centroid of the steel under compression and the farthest compression fiber of section, N: is the axial load (positive in compression), α: is the modulus of elasticity coefficient, d: is the effective depth of section and b: is the compression flange width.

The hardness of the hardening region will be obtained after yield point by division of the maximum ultimate moment to the yield moment (Eq. (3)). Researches suggest that the hardening ratio depends on the axial force and tensile rebar ratio. According to Haselton et al. (2007), the ratio of the axial load and concrete strength are among the key factors in determination of the hardness ratio.

$$\frac{M_C}{M_y} = (1.25)(0.89)^{\upsilon}(0.91)^{0.01f_c'} \tag{3}$$

where M_C and M_y: are the maximum moment capacity and yield moment capacity, respectively.

Eq. (4) is presented for estimation of the plastic rotational capacity.

$$\theta_{cap,pl} = 0.12(+0.55a_{sl})(0.16)^{\nu}(0.0 + 40\rho_{sh})^{0.43} * (0.54)^{0.01f_c'}(0.66)^{0.1s_n}(2.27)^{10\rho} \tag{4}$$

where a_{sl}: is the probability of the rebar slipping, so that the zero value is considered impossible and the value of 1 is considered as possible for the above phenomenon. ρ_{sh} and ρ: are percentages of the longitudinal and transverse rebar, respectively and υ: denotes the axial load ratio.

In spite of the importance of the parameter θ_{pc} in estimating the collapse capacity, the amount of research carried out regarding its estimation is inadequate. The important parameters in the calculation of θ_{pc} are the axial load ratio υ and the transverse rebar ratio ρ_{sh}. In Eq. (5) the upper limit imposed by the lack of information is reliable. However, it may be rigorous for well-confined members.

$$\theta_{pc} = 0.76(0.031)^{\vartheta}(0.02 + 40\rho_{sh})^{1.02} \leq 0.1 \tag{5}$$

Nonlinear modeling parameters can be obtained by using laboratory results or by using the ASCE41-13. In the case of using the ASCE41-13 code, the rotation capacity of the member is obtained by two parameters of a and b. In Figure 8, the a and b parameters are a part of the deformation that occurs after the yield point and are referred to as plastic deformations. These parameters can be acquired using the

ASCE41-13.

The rotational capacity of the members is determined on the basis of the curvature capacity of the cross section and the length of the plastic joint. Such that, using the moment-curve analysis, the curvature corresponding to the yield point and ultimate curvature of the cross section are determined, and using the length of the plastic joint, the rotational capacity of the member is obtained.

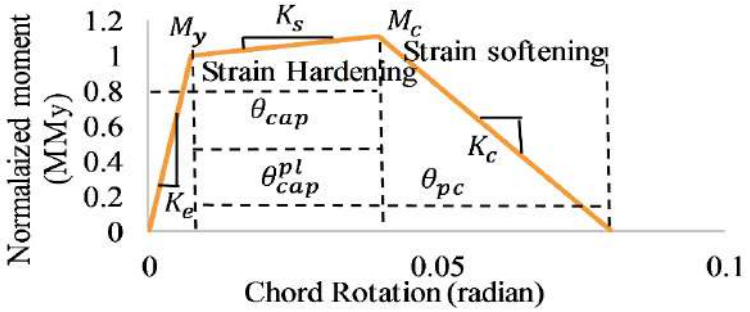

Fig. 7. Monotonic behavior of component model (FEMA P695, 2009)

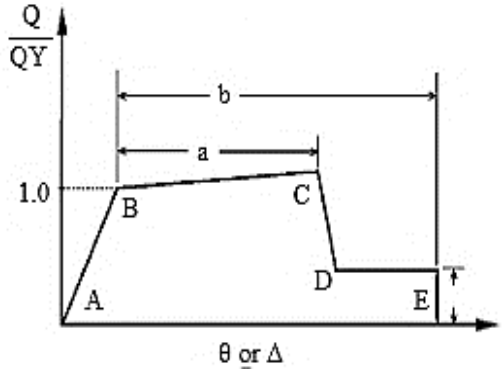

Fig. 8. The Force-Deformation of members' model (FEMA356, 2000)

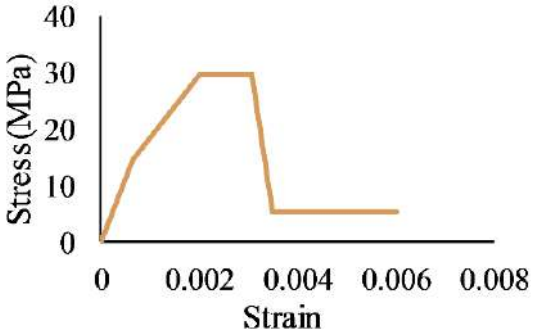

Fig. 9. Modeling of concrete behavior in software

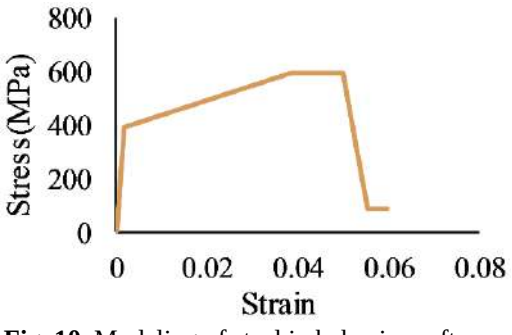

Fig. 10. Modeling of steel in behavior software

For the modeling of shear walls, it is necessary to introduce the stress-strain curves of steel and concrete. Therefore, the stress-strain curves of steel and concrete are shown in Figures 9 and 10, respectively.

5. Employed Accelerograms and Their Scaling Procedure

In this study, seven accelerations of the FEMA-P695 have been used, as given in Table 4, which are acquired from the PEER website. The fourth edition of Iran's 2800 standard is used as follows in order to scale the records.

5.1. Scaling of the Endurance Time Functions

In this study, the ETA20 in records of the endurance time function have been used for the non-linear analysis of the structures on hard soil types (FEMA P695, 2009). The spectrum of acceleration for 0 to 12 seconds of each pair of the functions is calculated separately, and the spectra of the square root of sum of squares is computed to scale the endurance time functions at hazard level 1. Then, to each of these three spectra, a scale coefficient is assigned in such a way that the area under them in the interval of 0.2 to 1.5 times the first vibrational mode period of the structure becomes equal to the area of the target spectrum. The target spectrum for scaling is considered to be the SRSS average spectrum of the acceleration spectra of the scaled natural accelerogram (7 records) at hazard level 1, for the main period of the structure. In the following, first, the SRSS of the response spectrum for three pairs of the scaled endurance time functions is obtained. Then, for each structure, the average response spectrum is obtained based on the target time, which is different for each structure.

Figures 11a-11c illustrate the comparison of the SRSS average response spectrum of the 7 scaled records (target spectrum) with the SRSS average spectrum of the scaled endurance time spectrum for structures of 20, 30 and 40 stories, respectively. Using the trial and error procedure, the target time for the 20, 30, and 40-story structures is calculated to be 12, 15, and 19 seconds, respectively. Because the target time of 12 seconds has been used for all of the structures, therefore, some scale coefficients should be used to match the response spectrum obtained from the endurance time method, for each structure with the target spectrum. These calculated coefficients are presented in Table 5.

6. Comparison of the Results of the Two Methods

In this section, the results related to drift of the stories (relative displacement of stories) as well as shear and acceleration of the stories have been examined based on the results of nonlinear analysis. The vertical axis shows the number of stories and the horizontal axis represents the maximum drift of stories (the average of the maximum drift responses of the 7 records is selected by the FEMA-P695). The comparison of maximum drift in the x, y directions for structures with 20, 30, and 40 stories is indicated in Figures 12-13, using both methods of time history analysis and the endurance time analysis, respectively. By comparing the results, it can be seen that by increasing the number of stories, the drift error of the stories will increase by about 20%. By comparing Figures 14 and 15, it can be seen that the acceleration error rate is 13, 15 and 15 percent in the structures of 20, 30 and 40 stories, respectively. The relative error in estimating the acceleration of stories in the endurance time method and time history analysis method does not change with elevation of the structure and the results of the two methods correspond to each other. Figures 16 and 17 illustrate the average of the results obtained in the 12th second of the nonlinear endurance time analysis for story shear, which is very consistent with the results of the nonlinear time-history analysis method, and with increasing the height of the structure, the accuracy of this method is not diminished.

Table 4. Records employed in this study (FEMA P695, 2009)

ID No.	PEER-NGA record information				Recorded motions	
	Rec. Sec	Lowest freq. (HZ)	File names-horizontal records		PGA (g)	PGV (cm/s)
1	767	0.13	RSN752_LOMAP_CAP000	RSN752_LOMAP_CAP090	0.53	35
2	1633	0.13	RSN1633_MANJIL_ABBAR-L	RSN1633_MANJIL_ABBAR-T	0.51	54
3	953	0.25	RSN953_NORTHR_MUL009	RSN953_NORTHR_MUL279	0.52	63
4	1787	0.04	RSN1787_HECTOR_HEC000	RSN1787_HECTOR_HEC090	0.34	42
5	1111	0.13	RSN1111_KOBE_NIS000	RSN1111_KOBE_NIS090	0.51	17
6	1485	0.05	RSN1485_CHICHI_TCU045-E	RSN1485_CHICHI_TCU045-N	0.44	115
7	1158	0.24	RSN1158_KOCAELI_DZC180	RSN1158_KOCAELI_DZC270	0.36	59

Table 5. Scale coefficients of the endurance time functions with SRSS average of the 7 scaled records

Record name	Scale factor 20 story	Scale factor 30 story	Scale factor 40 story
ETA20inx01	0.99	1.276	1.903
ETA20iny01	0.99	1.276	1.903
ETA20inx02	1.05	1.268	1.834
ETA20iny02	1.05	1.268	1.834
ETA20inX03	1.04	1.328	1.98
ETA20iny03	1.04	1.328	1.98

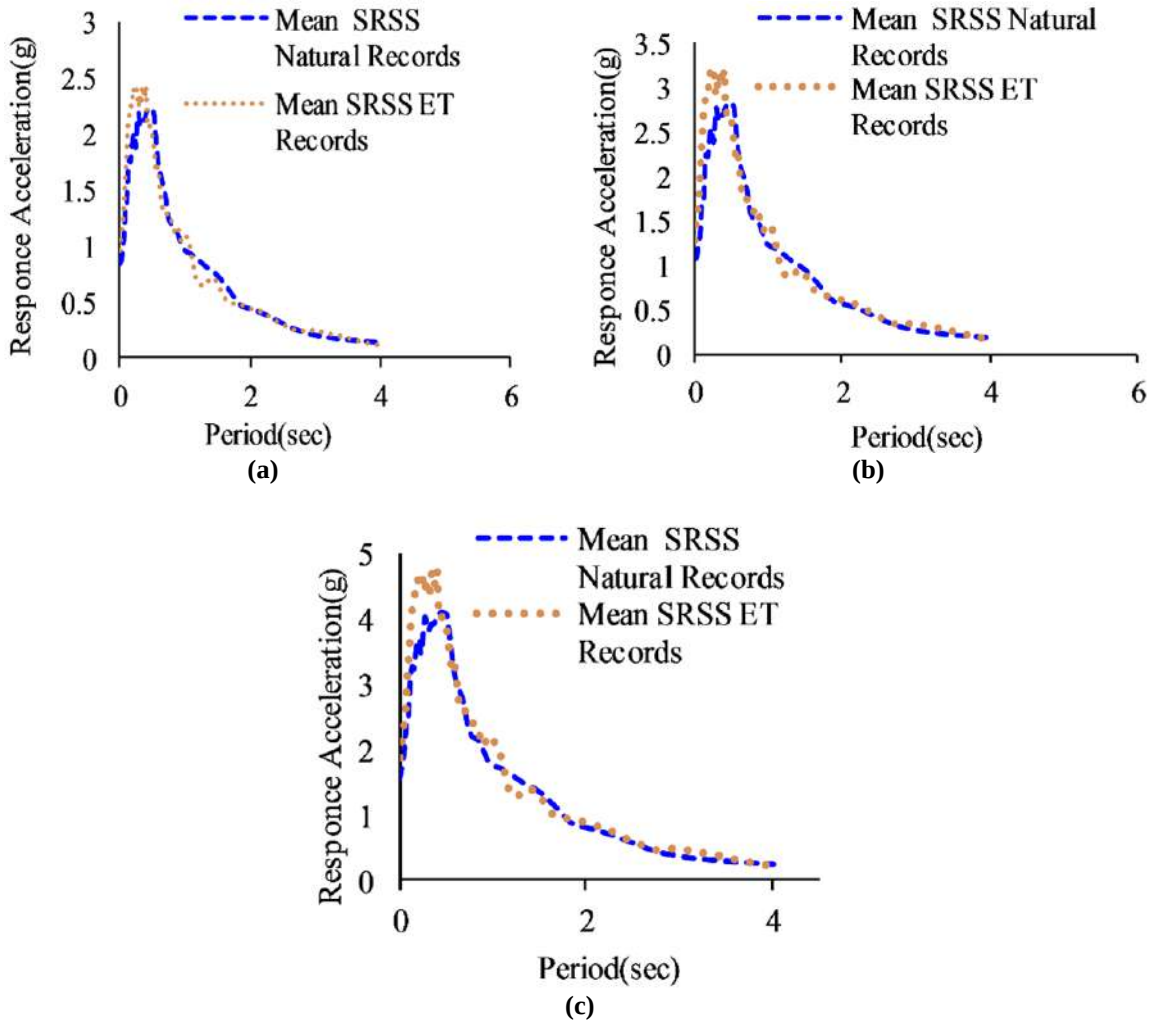

Fig. 11. Scaling of the endurance time functions with the average of the 7 scaled natural records for: a) 20-story; b) 30-story; and c) 40-story structure

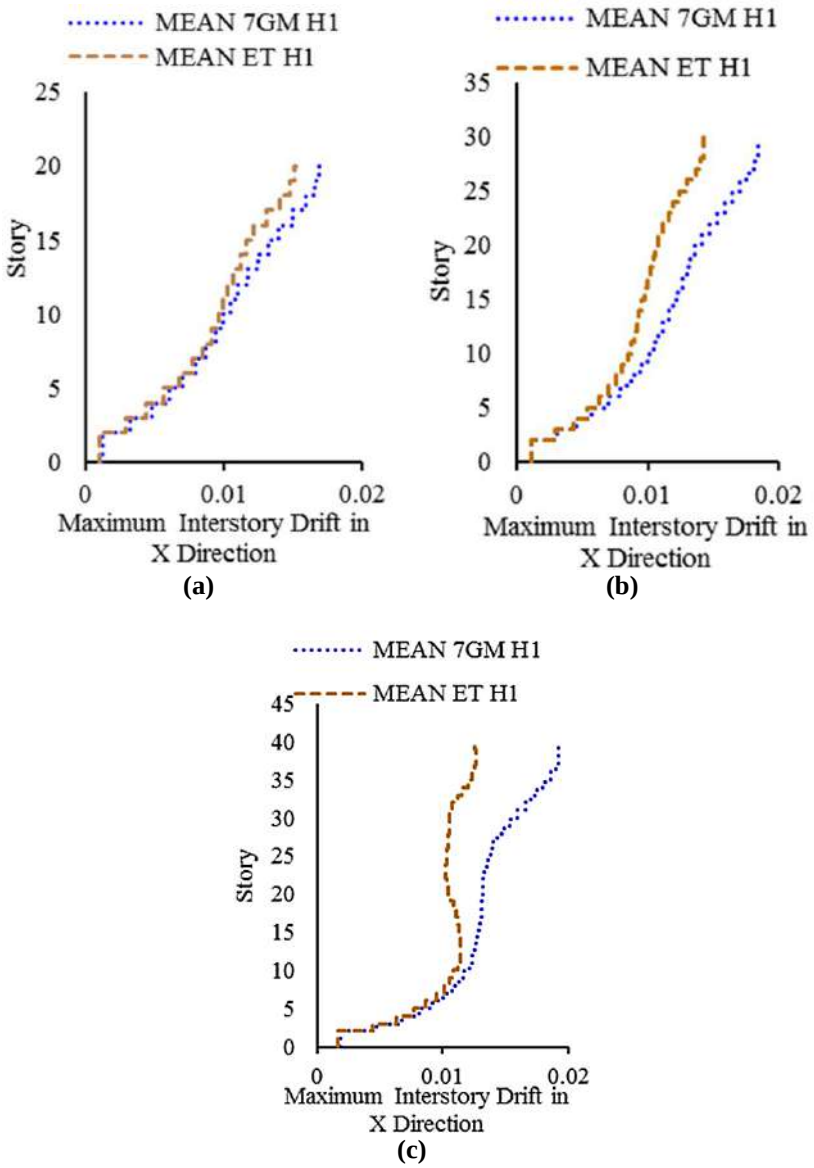

Fig. 12. Story drift in the X direction- Nonlinear time history analysis- 12th second of the endurance time for: a) 20-story; b) 30-story; and c) 40-story

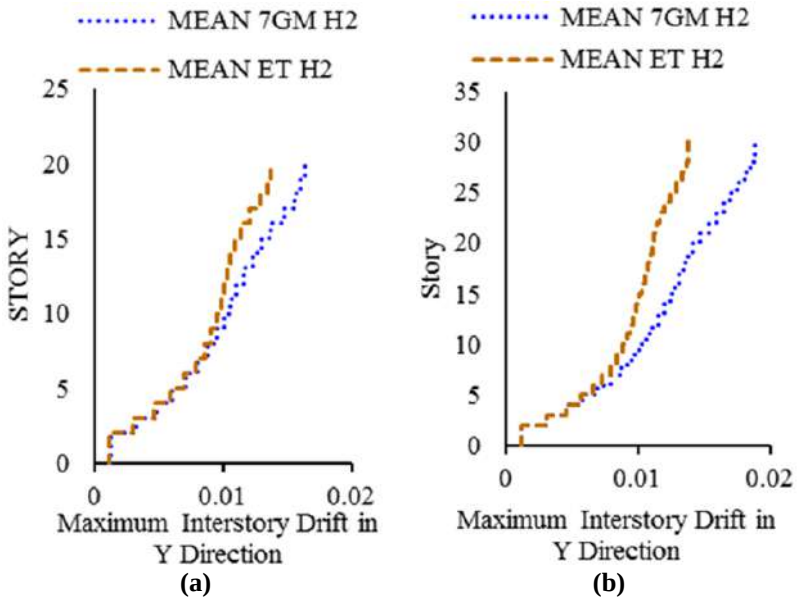

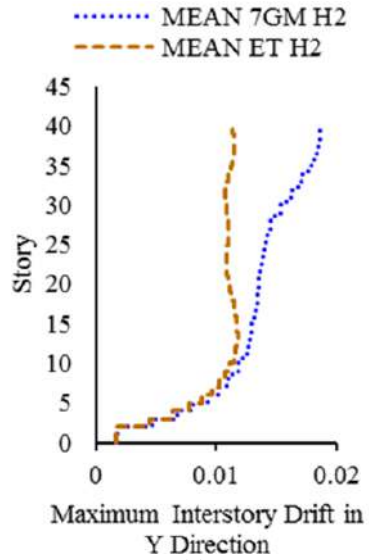

(c)

Fig. 13. Story drift in the Y direction- Nonlinear time history analysis 12th second of the endurance time for: a) 20-story; b) 30-story; and c) 40- story

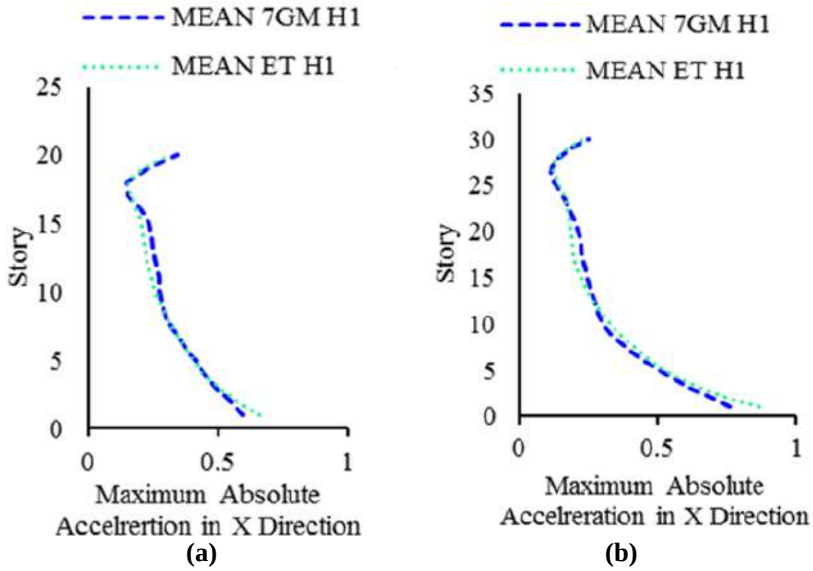

(a) **(b)**

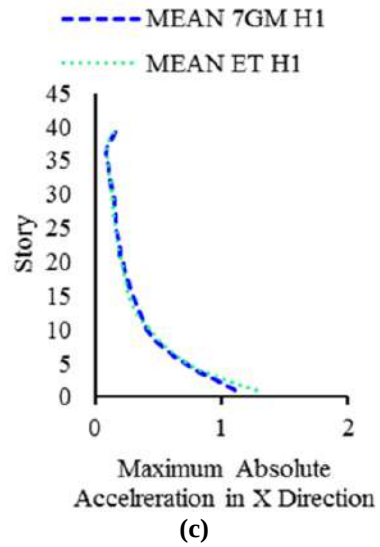

(c)

Fig. 14. Absolute acceleration in the X direction- Nonlinear time history analysis 12th second of the endurance time for: a) 20-story; b) 30-story; and c) 40-story

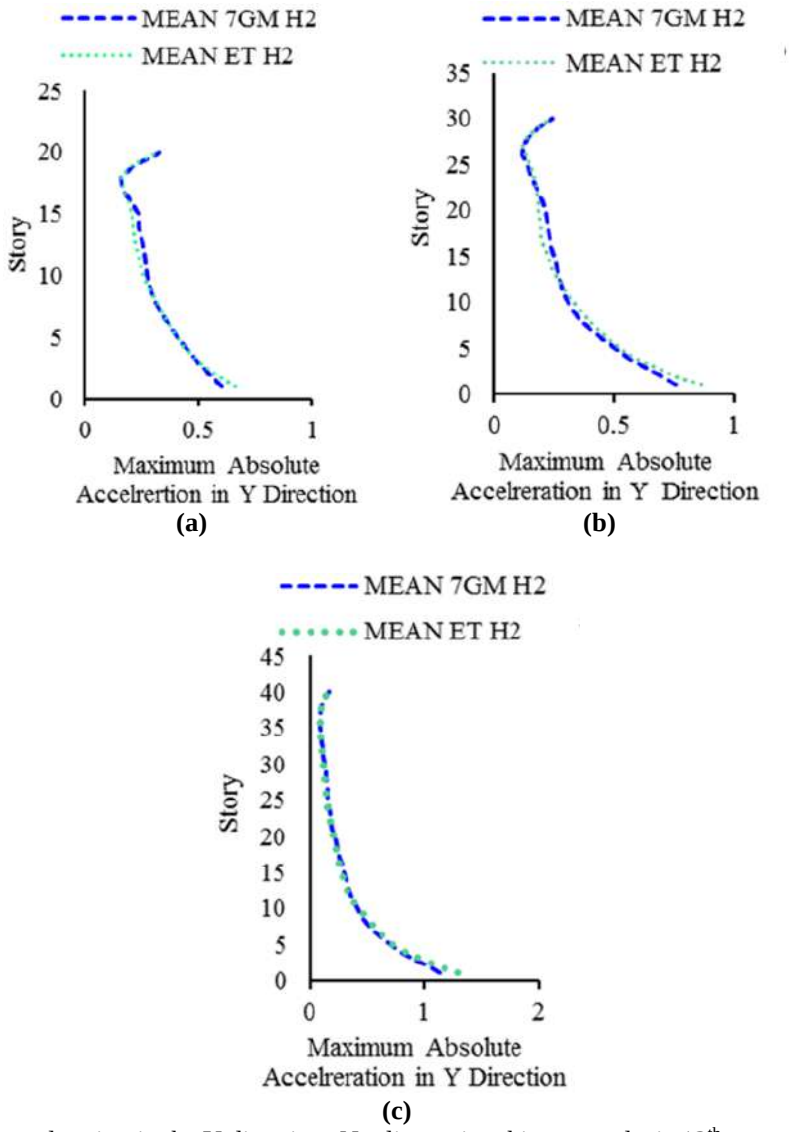

Fig. 15. Absolute acceleration in the Y direction- Nonlinear time history analysis 12th second of the endurance time for: a) 20-story; b) 30-story; and c) 40-story

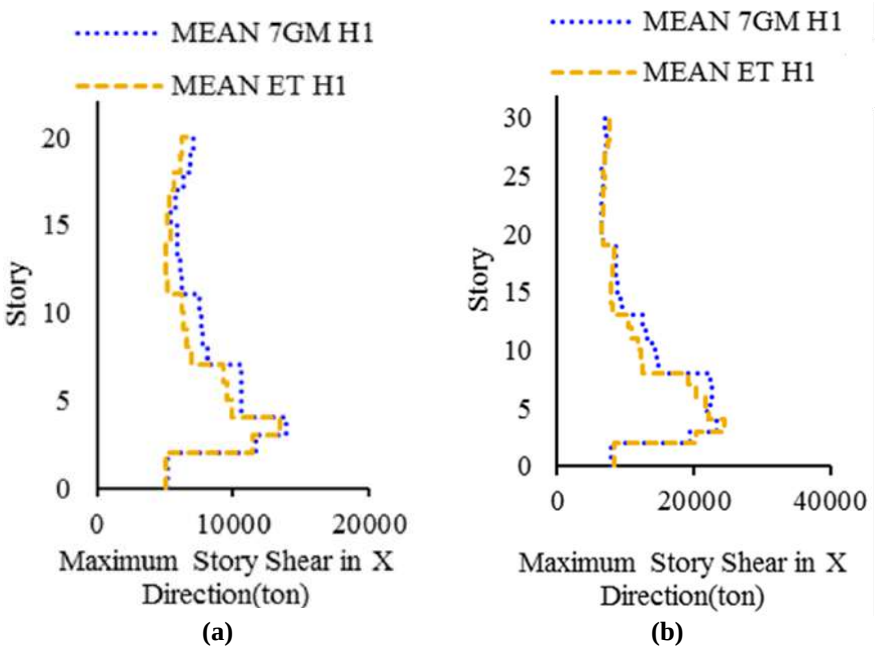

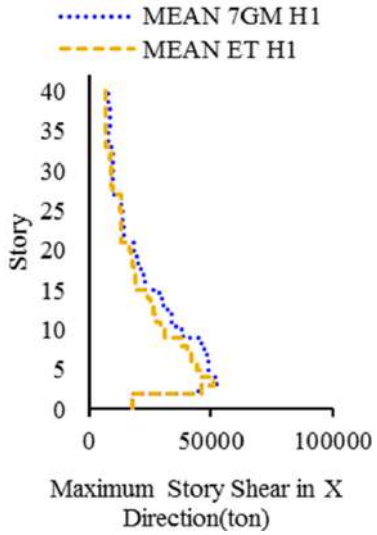

(c)

Fig. 16. Story shear in the X direction- Nonlinear time history analysis 12th second of the endurance time for: a) 20-story; b) 30-story; and c) 40-story

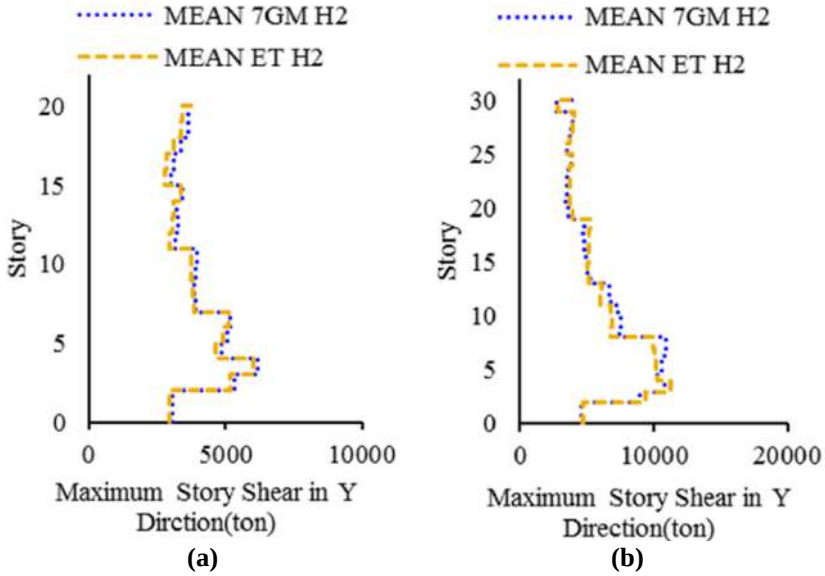

(a) **(b)**

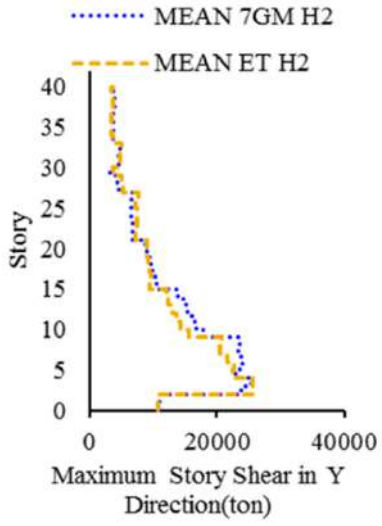

(c)

Fig. 17. Story shear in the Y direction- Nonlinear time history analysis 12th second of the endurance time for: a) 20-story; b) 30-story; and c) 40-story

7. Relative Error Analysis of the Endurance Time Method

In this research, three structural models for 20, 30 and 40 story-structures were investigated. The average of maximum responses (drift, shear and acceleration) of the buildings with different heights according to the results obtained from Figures 12-17 are presented in Table 6, in order to recapitulate the results. This table indicates the maximum error ratio of the endurance time method to the nonlinear time history analysis of the studied structures. The error rate of the two responses of shear and acceleration does not change much with the increase of the period of the structure, but the accuracy of the drift response is diminished. It seems that by reforming the records (which leads to an increase in the spectrum acceleration of the artificial records), it is possible to improve the accuracy of the story drift response in higher periods.

7.1. Comparison of Analysis Time in Endurance Time Methods and Nonlinear Time History

With regard to this matter that in tall structures with a large number of floors, the number of degrees of freedom increases significantly, so the analysis time using the time history method will be very long. One of the advantages of the endurance time method is the reduction of the analysis time compared to the time history method. In Table 7, the analysis time of a 20-story structure has been compared with the relevant earthquake accelerograms using endurance time and time history methods. The results show that the time of analysis in the endurance time method has a significant reduction compared to the time history method. The processor system related to the computer which the analyzes were performed, is Intel® Dou Core ™ 2, CPU 2.2 GHZ, 3GB RAM.

8. Conclusions

In this research, concrete frames with special dual structural system and different heights using PERFORM software were analyzed by two methods of endurance time and time history. In the analysis procedure, the geometric and material nonlinearities were taken into consideration. Comparing the results of the two methods, the following general results are obtained.

Table 6. Maximum relative error of the endurance time analysis method compared to the time history analysis method (percent)

Story shear		Absolute acceleration		Story drift		Indices
Y	X	Y	X	Y	X	structure
9	18	12.5	13	18	13	20 STORY
11	17	20	15	27	27	30 STORY
15	19	15	15	39	34	40 STORY

Table 7. Records analysis time

ID No.	File names-Horizontal records		Time(s) records	Time step	Analysis time (min)
1	RSN752_LOMAP_CAP000	RSN752_LOMAP_CAP090	39.99	0.005	400
2	RSN1633_MANJIL_ABBAR--L	RSN1633_MANJIL_ABBAR--T	53.5	0.02	135
3	RSN953_NORTHR_MUL009	RSN953_NORTHR_MUL279	29.98	0.01	150
4	RSN1787_HECTOR_HEC000	RSN1787_HECTOR_HEC090	45.3	0.01	230
5	RSN1111_KOBE_NIS000	RSN1111_KOBE_NIS090	40.95	0.01	200
6	RSN1485_CHICHI_TCU045-E	RSN1485_CHICHI_TCU045-N	89.995	0.005	900
7	RSN1158_KOCAELI_DZC180	RSN1158_KOCAELI_DZC270	27.18	0.005	325
8	ETA12inx01	ETA12iny01	12	0.01	75
9	ETA12inx02	ETA12iny02	12	0.01	75
10	ETA12inx03	ETA12iny03	12	0.01	75

- The results of the endurance time analysis on the overall behavior of the structure (drift, shear, and acceleration of stories) are in most cases in the range of minus one to plus one a standard deviation from the average of time history analysis and the maximum average error percentage of the endurance time method to the time history method for buildings of 20, 30 and 40 stories is 18, 27 and 39 percent, respectively.
- According to the results of the acceleration and shear responses for buildings with different heights, the difference between the results of the two methods of endurance time and time history is almost constant, which indicates the independence of the accuracy of the endurance time method from the seismic intensity and type of the analysis.
- Comparison of the story drifts calculated by nonlinear time history method indicates that with respect to the studied structures, the relative accuracy of the method is reduced by increasing the height of the structure. As the height of the structure increases, the period of the structure is increased. This can be due to the generation of series (in) records with mostly low frequency periods, which can be improved by generating appropriate records for drift response and tall structures.

9. References

ACI 318. (2014). "Building code requirements for structural concrete and commentary", American Concrete Institute, Farmington Hills, MI, USA.

American Society of Civil Engineers (ASCE). (2013). "Standard ASCE/SEI 41-13, Seismic evaluation and retrofit of existing buildings", Reston, Virginia, U.S.A.

Bai, J., Jin, S., Zhao, J. and Sun, B. (2019). "Seismic performance evaluation of soil-foundation-reinforced concrete frame systems by endurance time method", *Soil Dynamics and Earthquake Engineering*, 118, 47-51.

Basim, M.C. and Estekanchi, H.E. (2015). "Application endurance time method in performance-based optimum design of structures", *Structural Safety*, 56, 52-67.

Birely, A., Lehman, D., Lowes, L., Kuchma, D., Hart, C. and Marley, K. (2008). "Investigation of the seismic behavior and analysis of reinforced concrete structural walls", *Proceedings of the 14th World Conference on Earthquake Engineering*, Beijing, China.

Estekanchi, H.E., Vafaei, A. and Sadeghazar, M. (2004). "Endurance time method for seismic analysis and design of structures", *Scientia Iranica*, 11(4), 361-370

Estekanchi, H.E., Valamanesh, V. and Vafai, A. (2007). "Application of endurance time method in linear seismic analysis", *Engineering Structures*, 29(10), 2551-2562.

Estekanchi, H.E., Arjomandi, K. and Vafai, A. (2008). "Estimating structural damage of steel moment frames by endurance time method", *Journal of Constructional Steel Research*, 64(2), 145-155.

Estekanchi H.E., Riahi H.T. and Vafai A. (2011). "Application of endurance time method in seismic assessment of steel frames", *Engineering Structures*, 33(9), 2535-2546

FEMA. (2000). "Prestandard and commentary for the seismic rehabilitation of buildings", Federal Emergency Management Agency, Report FEMA-356, Washington, DC.

FEMA P695. (2009). "Quantification of building seismic performance factors", Applied Technology Council and Federal Emergency Management Agency, US.

Foyouzat M.A. and Estekanchi H.E. (2016). "Application of rigid-perfectly plastic spectra in improved seismic response assessment by Endurance Time method", *Engineering Structures*, 111, 24-35.

Guo, A., Shen, Y., Bai, J. and Li, H. (2017). "Application of the endurance time method to the seismic analysis and evaluation of highway bridges considering pounding effects", *Engineering Structures*, 131**,** 220-230.

Haselton, C.B., Goulet, C.A., Mitrani-Reiser, J., Beck, J.L., Deierlein, G.G., Porter, K.A., Stewart, J.P. and Taciroglu, E. (2008). "An assessment to benchmark the seismic performance of a code-conforming reinforced-concrete moment-frame building", PEER Report, 2007/1, Pacific Earthquake Engineering Research Center, Berkeley, CA.

Haselton, C.B., Deierlein, G.G. (2007). "Assessing seismic collapse safety of modern reinforced concrete moment frame buildings", John A. Blume Earthquake Engineering Center Technical Report 156, Stanford University.

He, H., Wei, K., Zhang, J. and Qin, S. (2015). "Application endurance time method to seismic fragility evaluation of highway bridges considering scour effect", *Oil Dynamics and Earthquake Engineering*, 136, 106243.

Kim, T. and Foutch, D.A. (2007). "Application of FEMA methodology to RC shear wall buildings governed by flexure", *Engineering Structures*, 29(10), 2514-2522.

Li, S., Liu, K., Liu, X., Zhai, C. and Xie, F. (2019). "Efficient structural seismic performance evaluation method using improved endurance time analysis", *Earthquake Engineering and Engineering Vibration*, 18(4), 795-809.

Malley, J.O., Dierlein, G., Krawinkler, H., Maffei, J., Pourzanjani, M., Wallace, J. and Heintz, J. (2010). "Modeling and acceptance criteria for seismic design and analysis of tall buildings", Applied Technology Council, PEER/ATC-72-1.

Mander, J.B., Priestley, M.J.N. and Park, R. (1988). "Theoretical stress-strain model for confined concrete", *Journal of Structural Engineering*, 114(8), 1804-1826.

Memari, A.M., Motlagh, A.Y. and Scanlon C, A. (2000). "Seismic evaluation of an existing reinforced concrete framed tube building based on inelastic dynamic analysis", *Engineering Structures*, 22(6), 621-637.

PEER. (2010). "Guidelines for performance-based seismic design of tall buildings", Pacific Earthquake Engineering Research Center, College of Engineering, University of California, Berkeley, USA.

PERFORM, C. (2011). *3D user manual (v5. 0.1)*, Berkeley, CA: Computer and Structures Inc, USA.

Riahi, H.T. and Estekanchi, H.E. (2010). "Seismic assessment of steel frames with the endurance time method", *Journal of Constructional Steel Research*, 66(6), 780-792.

Shin, M., Kang, T.H.K. and Grossman, J.S. (2010). "Practical modelling of high-rise dual systems with reinforced concrete slab-column frames", *The Structural Design of Tall and Special Buildings*, 19(7), 728-749.

Standing Committee on the Revision of the Regulations for the Design of Buildings against Earthquake. (2014). "Building regulations for building against earthquake", Standard 93-2800, Tehran, Iran.

Seyed Kolbadi, S.M., Piri, H., Keyhani, A., Seyed Kolbadi, S.M. and Mirtaheri, M. (2020), "Nonlinear seismic performance evaluation of flexural slotted connection using endurance time method", *Shock and Vibration*, 2020(4), 1-15.

Tafakori, E., Pourzeynali, S. and Estekanchi, H.E. (2017). "Probabilistic seismic loss estimation via endurance time method", *Earthquake Engineering and Engineering Vibration*, 16(1), 233, 245.

Thomsen IV, J.H. and Wallace, J.W. (2004). "Displacement-based design of slender reinforced concrete structural walls experimental verification". *Journal of structural engineering*, 130(4), 618-630.

Valamanesh, V. and Estekanchi, H.E. (2010). "A study of endurance time method in the analysis of elastic moment frames under three-directional seismic loading", *Asian Journal of Civil Engineering (Building and Housing)*, 11(5), 543-562.

Valamanesh, V. (2010). "3D nonlinear seismic analysis of structures by endurance time method", Ph.D. Thesis, Faculty of Civil Engineering, Sharif University of Technology, Tehran, Iran.

Reviewers

The Editorial Board of the Civil Engineering Infrastructures Journal (CEIJ) would like to express sincere thanks to all reviewers of papers submitted to CEIJ during 2020 and 2021 for their time and efforts in evaluating papers for this journal.

Aboutalebi Esfahani, M.
University of Isfahan
Aghabayk, K.
University of Tehran
Aghayan, I.
Shahrood University of Technology
Ahmadi, A.
Isfahan University of Technology
Akansel, V.
Mugla Sitki University
Akbarimehr, D.
Amirkabir University of Technology
Akbarzadeh, A.
Water Research Institute
Akbarzadeh Bengar, H.
University of Mazandaran
Akhound Ali, A.M.
University of Ahvaz
Albayati, A.H.
University of Baghdad
Albayrak, U.
Eskisehir Osmangazi University
Ali, Y.
Queensland University of Technology
Alipour, R.
Shahrekord University
Asadi, N.
University of Zanjan
Askari, F.
International Institute of Earthquake Engineering and Seismology
Aslani, F.
University of Western Australia
Azhari, M.
Isfahan University of Technology
Babaei, M.
University of Zanjan
Bahadori, H.
Urmia University
Basaligheh, F.
Shahrood University of Technology
Beheshti-Aval, S.B.
K.N.Toosi University of Technology
Bosch, J.
University of Akron
Broumand, P.
Shahrood University of Technology
Cai, K.
RMIT University
Colangelo, F.
University of Naples
Chalioris, C.
Democritus University of Thrace
Dabiri, H.
University of Camerino
Derakhshani, A.
Shahed University
Edrisi, A.
K.N. Toosi University of Technology
Farina, I.
Parthenope University of Naples
Farzane, O.
University of Tehran
GhalandarZade, A.
University of Tehran
Ghobadi, M.H.
Bu-Ali Sina University
Golchin, B.
Mohaghegh Ardabili University
Haji Agha Bozorgi, A.
University of Tehran
Hamedi, G.H.
University of Gilan
Hamidiya, M.J.
Shahid Beheshti University
Hashemi, H.
Shahid Beheshti University
Hashemy Shahdany, S.M.
University of Tehran
Hayati, P.
Iran University of Science and Technology
Huang, X.
Southeast University
Jalili Qazi Zadeh, M.R.
Shahid Beheshti University
Julien, P.Y.
Colorado State University
Kalantary, F.
K.N. Toosi University of Technology
Karakan, E.
Kilis 7 Aralik University
Karakouzian, M.
University of Nevada
Karami Mohammadi, R.
K.N. Toosi University of Technology
Karbhari, V.
University of Texas

Kavand, A.
University of Tehran
Kavianpour, M.R.
K.N.Toosi University of Technology
Kenai, S.
Saad Dahlab University
Kerachian, R.
University of Tehran
Khabiri, M.M.
Yazd University
Khanmohmmadi, M.
University of Tehran
Khavandi Khiavi, A.R.
University of Zanjan
Kheyroddin, A.
Semnan University
Khodadadi, A.
Tarbiat Modares University
Kwan, A.K.H.
The University of Hong Kong
Lantsoght, E.
Delft University of Technology
Lashkari, A.
Shiraz University of Technology
Li, J.
California Baptist University
Maadi, S.
University of Glasgow
Madani, S.H.
Graduate University of Advanced Technology
Maghoul, P.
University of Manitoba
Mahinroosta, R.
Charles Sturt University
Mahmoudi, M.
Shahid Rajaee Teacher Training University
Maleki, M.
Bu-Ali Sina University
Mirghasemi, A.A.
University of Tehran
Mishra, D.K.
Hong Kong University of Science and Technology
Moghadas Nejad, F.
Amirkabir University of Technology
Monjurul Hasan, M.
Dhaka University of Engineering and Technology
Moosazadeh, S.
Urmia University
Mousavi, S.R.
Sistan and Baluchestan University
Najma, A.R.
York University
Navidjouy, N.
Urmia Medical Sciences University
Nazif, S.
University of Tehran
Nourani, V.
Tabriz University
Nouri, Gh.
Kharazmi University
Ouhadi, V.R.
Bu-Ali Sina University
Pan, X.
Zhejiang University of Technology
Prongmanee, N.
Kasetsart University
Rabczuk, T.
Ton Duc Thang University
Rafiee, R.
University of Tehran
Rastegar, M.M.
K.N.Toosi University of Technology
Roozbahany, A.
University of Tehran
Saadeghvaziri, M.A.
New Jersey University of Technology
Safavi, H.R.
Isfahan University of Technology
Salehi, S.
IA University, Garmsar Branch
Salvalaggio, M.
University of Padova
Samadzad, M.
University of Tehran
Sert, S.
Sakarya University
Seyed Ardakani, S.M.
Ohio Northern University
Seyedi Hosseininia, E.
Ferdowsi University of Mashhad
Seyedpoor, S.M.
Shomal University
Shahir, H.
Kharazmi University
Shao, Y.
Southwest Petroleum University
Shekarchi Zadeh, M.
University of Tehran
Shi, X.
Southeast University
Soroushian, A.
International Institute of Earthquake Engineering and Seismology
Tabesh, M.
University of Tehran
Tariverdilo, S.
Urmia University
Tavakoli, H.R.
Babol Noshirvani University of Technology
Thom, N.
University of Nottingham

AIMS AND SCOPE

Since the College of Engineering (Former Faculty of Engineering, FOE) of the University of Tehran has renewed its policy toward scientific publication, the Civil Engineering transaction of the well- built 45 years old Persian journal of *"Nashrieh Daneshkadeh Fanni"* is to be published in English and as separate independent journal with the name of ***Civil Engineering Infrastructures Journal***.

Civil Engineering Infrastructures Journal is an international journal which publishes high quality scientific papers in all areas of engineering and management of civil infrastructures. The civil infrastructures include, but are not limited to: buildings, bridges, dams, transportation systems, geotechnical structures, underground constructions, water distribution systems, offshore platforms, pipelines, ocean structures, airports and power plants.

The scope of this journal encompasses, but is not restricted to the following aspects of engineering and management of infrastructures:

- Mathematical modeling
- Computational and experimental methods
- Environmental Impact assessment
- Passive defense and security issues
- Monitoring and assessment
- Construction and design for durability
- Deterioration modeling and aging
- Failure analysis
- Field testing
- Financial planning
- Inspection and diagnostics
- Life-cycle analysis and prediction

- Maintenance, rehabilitation, repair and replacement strategies
- Non-destructive testing
- Optimization of maintenance and management
- Specifications and codes
- Reliability and risk management
- Supervisory Control and Data Assimilation (SCADA)
- Automation and Robotics in Construction
- Smart civil infrastructure Systems
- Sustainable civil infrastructure systems
- Case studies

Audiences of ***Civil Engineering Infrastructures Journal*** are researchers and practitioners as well as people working in infrastructure design, construction, maintenance and operation. Papers considered for publication must contain a clear and well-defined engineering component and make a significant contribution to the engineering and management of civil infrastructures. All articles submitted to this journal will undergo a rigorous peer review by anonymous independent experts.

Additional information can be obtained from:

Civil Engineering Infrastructures Journal
College of Engineering,
University of Tehran
P.O. Box: 11155- 4563
Tehran, Iran
Tel/ Fax: +98-21-88956097
Web Site: www.ceij.ir
Email: ceij@ut.ac.ir

University of Tehran
College of Engineering

Copyright Transfer Agreement

In order to protect the author(s), from the consequences of unauthorized use, the publisher requests that all author(s) sign the appropriate statement below:
The author(s) undersigned hereby approves submission of this work and all subsequent revisions for publication and transfers, assigns, or otherwise conveys copyright ownership to the Civil Engineering Infrastructures Journal (CEIJ). I (we) acknowledge that i) the submitted material represents original material, ii) does not infringe upon the copyright of any third party, and iii) that no part of the work has been published or under consideration for publication elsewhere unless and until it is rejected by Civil Engineering Infrastructures Journal (CEIJ). I (we) agree to indemnify the publisher against any loss or damages arising out of a breach of this agreement. In the event that my (our) submission is not published, copyright ownership shall revert to the author (s).

Manuscript Title:

Corresponding Author

Author:
Date: Signature;

Author:
Date: Signature:

Author:
Date: Signature:

Author:
Date: Signature:

Please submit the signed agreement with the final manuscript to:
Civil Engineering Infrastructures Journal (CEIJ)
School of Civil Engineering
College of Engineering, University of Tehran
Enghelab Ave., P.O. Box: 11155-4563, Tehran, Iran.
Tel: 88956097
Fax: 66498981
E-mail: ceij@ut.ac.ir
Website: www.ceijournal.com

CIVIL ENGINEERING INFRASTRUCTURES JOURNAL (CEIJ)

is indexed and abstracted in the bibliographical databases including:

Web of Science (ESCI)
http://science.thomsonreuters.com

Scopus
https://www.scopus.com

Islamic World Science Citation Center;
http://www.isc.gov.ir

Directory of Open Access Journals (DOAJ)
https://doaj.org

Google Scholar
https://scholar.google.com

General Impact Factor (GIF)
http://generalimpactfactor.com

Scientific Indexing Services (SIS)
http://www.sindexs.org

International Institute of Organized Research (I2OR)
http://www.i2or.com

Information Matrix for the Analysis of Journals (MAIR)
http://miar.ub.edu

ROAD: the Directory of Open Access scholarly Resources
http://road.issn.org

Scientific World Index
http://www.sciwindex.com

International Innovative Journal Impact Factor (IIJIF)
http://www.iijif.com

Science library index
http://scinli.com

Journal Factor
http://www.journalfactor.org

Open Academic Journals Index (OAJI)
http://oaji.net

Electronic Journals Library (EZB)
https://rzblx1.uni-regensburg.de

Systematic Impact Factor (SIF)
http://www.sifactor.org

COSMOS IMPACT FACTOR
http://www.cosmosimpactfactor.com

Polish Ministry of Science and Higher Education (MSHE)
https://journals.indexcopernicus.com

Magiran
http://www.magiran.com

Scientific Information Database (SID); Iran;
http://www.Sid.ir

Ministry of Science, Research and Technology of Iran has granted the Science and Research (Elmi-Pajouheshi) credit to CEIJ according to the letter No. 3/252445 at 25 Feb. 2012.

College of Engineering

Civil Engineering Infrastructures Journal

Volume 54, Number 2, December 2021

CONTENTS:

Civil Engineering Infrastructures Journal (CEIJ)

Volume 54, Number 2, December 2021